Neutron Transport in the Sudbury Neutrino Detector

Matthew Jeremy Lyon

Balliol College, Oxford University

Thesis submitted in partial fulfilment of the requirements

for the degree of Doctor of Philosophy

at the University of Oxford

Michaelmas Term, 1996

This work is dedicated to

Florence White,
5th October 1898 - 29th September 1993,

and to

Rory David Boyer,
26th January 1974 - 12th October 1995.

Abstract

The Sudbury Neutrino Observatory (SNO), a heavy water Čerenkov detector, is a solar neutrino telescope which is currently under construction. The Čerenkov photons will be detected by a Hamamatsu R1408 photomultiplier and concentrator whose angular performance has been measured and found to behave in accordance with the computer simulation of Lay, giving a concentration factor of $1.6 \rightarrow 1.7$ in water.

Photodisintegration of the deuteron is a principal background in SNO. A phenomenological cross section for this process in the $0 \rightarrow 25$MeV energy region, accurate to better than 2% over most of the range, is presented. A neutron transport code has been adapted for use in the SNO Monte Carlo, and an extensive verification procedure carried out which confirmed its suitability for n-transport calculations in SNO.

The n-transport capability of the SNO Monte Carlo has been used to determine the probability that neutrons from the $\nu_x + d \rightarrow n + p + \nu_x$ neutral current neutrino reaction are detected above a threshold of 60 PMT hits as a function of the concentration of the $MgCl_2$ additive in the SNO D_2O. The probability initially rises steeply with salt concentration but then levels off, being $8.9 \pm 0.1\%$ without salt and $41.0 \pm 0.3\%$ in an 0.1% salt solution, $44.6 \pm 0.4\%$ at 0.2%, $46.7 \pm 0.4\%$ at 0.3%, and $47.7 \pm 0.4\%$ at 0.4%. The Monte Carlo has also been used to simulate a single year of SNO data taking assuming the MSW effect and a simple analysis presented to show that the ratio of the neutral current and charged current event rates (normalised to their standard solar model values) will be 2.7 ± 0.2 without salt, 3.0 ± 0.1 in an 0.1% salt solution, 2.7 ± 0.1 at 0.2%, 2.8 ± 0.1 at 0.3%, and 2.9 ± 0.1 at 0.4%. An 0.1% solution is recommended as the minimum salt concentration that should be used in the SNO experiment.

This Thesis

In this thesis, the work done by the author in developing the SNO experiment's Monte Carlo, SNOMAN, will be described in some detail. The author has undertaken three projects for which he is solely responsible; the first to measure the angular performance of the SNO PMT and concentrator, with which to test a Monte Carlo model developed by Lay (Chapter 3), and which is part of a paper by Lay and Lyon [96] accepted for publication in NIM; the second to investigate the cross section for the d(γ,n)p interaction for use in the SNOMAN program (Chapter 5); and the third to select, install, develop, test, and use a neutron transport code for the SNOMAN program (Chapters 6 $\rightarrow$ 9). This neutron transport code will be used by the whole SNO collaboration to predict the background and response of the detector to neutral current events, and hence will be a cornerstone in the analysis of detector data.

The development of a neutron transport code for SNOMAN and the testing that accompanied it, which now serves as a verification of the code, took approximately 12 months. There are two reasons for the length of time that was taken. The first is that SNOMAN is a very different program from MCNP, the program from which the neutron transport code was taken; consequently the use of MCNP in SNOMAN was not just a matter of 'plugging it in' (to SNOMAN). The second reason for the long time taken is the extremely comprehensive nature of the testing that was carried out on SNOMAN once it was n-transport capable. These issues are covered in detail in Chapters 7 and 8.

The author has also done additional work, described in Chapter 4, on the design of a facility for the long term monitoring of the performance and water tolerance of individual detector components. The design of the facility was undertaken in collaboration with N. Jelley, who also commissioned the construction work; the calculations that were used in assessing the feasibility of the design were carried out by this author.

Acknowledgements

Many individuals have aided me in the completion of this thesis. My supervisor, Nick Jelley, has been a constant source of encouragement and direction throughout the 3 years it has taken to prepare this work. Nick West has been of great assistance to me in helping me tackle my difficulties with SNOMAN, and has always amazed me with his vast knowledge of all things digital, and the speed with which he works. Dave Wark's enthusiasm and knowledge of the subject of neutrino physics have served to remind me, on the occasions when it has been necessary, why I have been doing the work that is now complete.

Thanks are especially due to everyone who has read my thesis, all of whom have been able to provide me with an ample supply of constructive criticism. They are John Rees, Nick Jelley, Dave Wark, and last but not least, Mike Bowler.

Mike Lay and Norm Taplin, formerly both my fellow students, deserve a special mention; Mike for introducing me to EGS4 and for providing the impetus to the experimental work that I completed in my first year, and Norm for providing and setting up the electronic equipment for the operation of the bin. Norm has also been an unstoppable source of humour, which helps! Thanks also to Peter Trent for providing a better perspective.

A special mention is due to Sarah Knight, who has lately been a source of unending support, and to whom I am soon to be married. Thank you all!

Terminology

Throughout this thesis the author has used a number of shorthand notations. The most important and frequent are;

1. the acronym **SNO** which refers to the Sudbury Neutrino Observatory; and,
2. the term **PMT** which refers to a photomultiplier tube; and,
3. the terms **NHIT** or **NHITs** which refer to the number of photomultiplier tubes registering a hit in a 100ns event window in the SNO detector; and,
4. **n**, **p**, **d**, and **t** which, in the context of a nuclear reaction, refer to a neutron, a proton, a deuteron, or a tritium nucleus, respectively; and,
5. ν_e, ν_μ, and ν_τ, which refer to the electron neutrino, the muon neutrino, and the tau neutrino, respectively; and,
6. ν_x which refers to a neutrino of any of the three flavours; electron, muon, or tau; and,
7. the term **β-γ decay** which refers to the decay of a nucleus such as ^{208}Tl, where a β decay to an excited state of ^{208}Pb is followed by the prompt emission of γ radiation which ceases when the ^{208}Pb nucleus reaches the ground state; and,
8. the term **macroscopic cross section** which refers to an inverse mean free path, λ, where $\lambda = \sum_i n_i \sigma_i$, and the n_i are number densities and the σ_i are usually neutron-nucleus interaction cross sections (the σ_i are also known as **microscopic cross sections**); and,
9. the term **CC** which refers to the **C**harged **C**urrent interaction $\nu_e + d \rightarrow p + p + e^-$; and,
10. the term **ES** which refers to the **E**lectron **S**cattering interaction $\nu_x + e^- \rightarrow \nu_x + e^-$; and,
11. the term **NC** which refers to the **N**eutral **C**urrent interaction $\nu_x + d \rightarrow \nu_x + p + n$; and,
12. the term **IN** which refers to **I**nternal **N**eutron events, or neutron events that are distributed uniformly throughout the SNO heavy water; and,
13. the term **EN** which refers to **E**xternal **N**eutron events, or neutron events external to the SNO heavy water.

Contents

Chapter 1

Solar Neutrino Physics

1.1 Introduction to the Solar Neutrino Problem

Neutrinos are weakly interacting spin $\frac{1}{2}$ particles that are generated in the core of the Sun during the processes of nuclear fusion and β-decay which provide the energy with which the Sun shines. Due to the fact that neutrinos only interact weakly with matter, those that are generated in the solar core can pass directly out from the sun, and therefore provide physicists with a unique opportunity to study its interior.

In 1968 Davis *et al.* reported the first results from the Homestake solar neutrino experiment [1][2]. There, ν_e were captured by ^{37}Cl atoms in a tank of perchloroethylene (C_2Cl_4) to give ^{37}Ar. The Homestake experiment is ongoing, and the most recent result is a capture rate of [3];

$$\text{Observed rate} = (2.56 \pm 0.16\,(\text{stat.}) \pm 0.14\,(\text{sys.}))\,\text{SNU}\ , \tag{1.1}$$

where 1 SNU (Solar Neutrino Unit) is equal to 10^{-36} captures per target atom per second. The predicted capture rate is [30];

$$\text{Predicted rate} = (9.3^{+1.2}_{-1.4})\,\text{SNU}\ , \tag{1.2}$$

where the error represents an estimate of the 1σ theoretical error (see Refs. [25], and [30]).

Another detector, the Kamiokande detector in Japan [4][7][8], has also reported a deficit in the observed flux of solar neutrinos (Kamiokande II and III average) [9];

$$\frac{\Phi_{\text{Observed}}}{\Phi_{\text{Predicted}}} = 0.424 \pm 0.029\,(\text{stat.}) \pm 0.05\,(\text{sys.})\ . \tag{1.3}$$

The Kamiokande detector is a water Čerenkov instrument, and was the first detector to verify that the Sun was the source of the neutrino signal.

The SAGE [14][15] and GALLEX [10][11] experiments are radiochemical experiments similar in principle to the Homestake chlorine detector, but utilising the $^{71}\text{Ga}(\nu_e,e^-)^{71}\text{Ge}$ reaction in gallium. The threshold for this reaction is much lower than that of the similar $^{37}\text{Cl}(\nu_e,e^-)^{37}\text{Ar}$ reaction in Homestake, being 0.2332MeV rather than 0.814MeV. This low threshold makes possible the detection of the low-energy high-flux pp neutrinos. Both experiments confirm the shortfall in neutrino flux; the GALLEX result being [13];

$$\Phi_{\text{Observed}} = (70 \pm 7)\,\text{SNU}\,(\text{sys.+stat.})\ , \tag{1.4}$$

whilst the SAGE result is [17];

$$\Phi_{\text{Observed}} = 72^{+12\,+5}_{-10\,-7}\,\text{SNU}\ (\text{stat./sys.}). \tag{1.5}$$

These results are to be compared to the theoretical expectation, for which a representative value is [30] (1σ theoretical errors);

$$\Phi_{\text{Expected}} = 137^{+8}_{-7}\,\text{SNU}\ . \tag{1.6}$$

The difference between the observed and predicted rates is known as the solar neutrino problem. The experimental field of solar neutrino physics began in order to observe directly the products of the

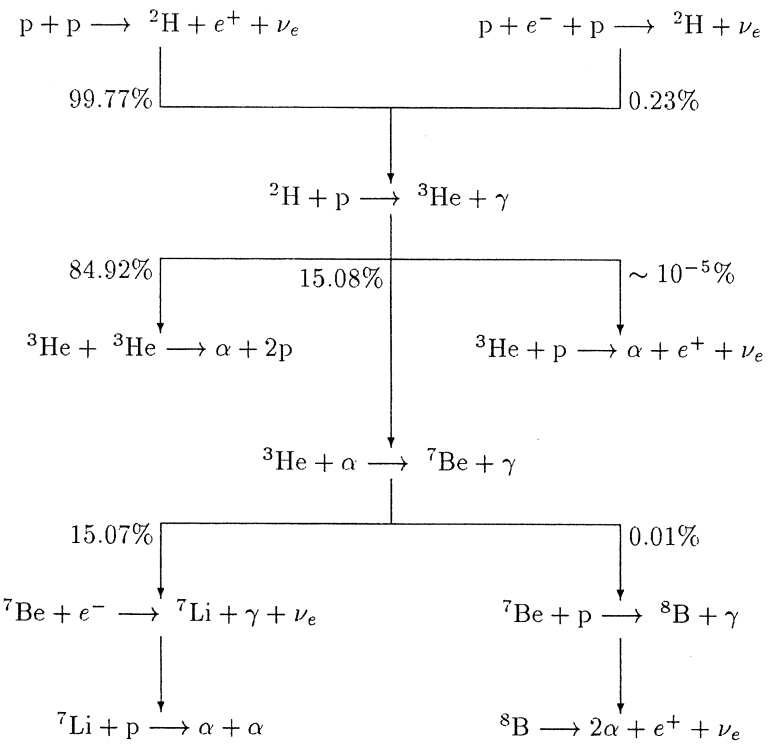

Figure 1.1: Schematic diagram of the pp chain [25].

nuclear reactions that occur in the Sun. The unexpected deficit in the number of neutrinos observed compared to the number predicted has led to further exciting experimental and theoretical work in an attempt to explain the discrepancy. The remainder of this chapter will give an overview of the theoretical understanding and experimental activity which is the field of solar neutrino physics, concluding with a brief look at the future of the field.

1.2 Energy Generation and Neutrino Production in the Solar Interior

Nuclear fusion is the source of the energy with which the Sun supports itself and shines. The proton-proton chain, which is illustrated in Figure 1.1 and details about which are contained in Table 1.1, generates $\sim 98.5\%$ of the energy produced by the sun, the CNO cycle contributes the remainder ($\sim 1.5\%$). The overall consequence of the pp chain can be represented as;

$$4\mathrm{p} + 2e^- \rightarrow \alpha + 2\nu_e + 4\gamma \ , \ Q = 27.7\mathrm{MeV} \ , \tag{1.7}$$

where the bulk of the thermal energy supplied by the burning of 4 protons to form a helium nucleus ultimately emerges from the surface of the Sun in the form of light. Very little of the energy supplied by the process of nuclear fusion is carried off by the neutrinos. As a result, the flux of the neutrinos at the earth can be crudely estimated by the expression;

$$\Phi = \frac{L_\odot}{13\mathrm{MeV}} \times \frac{1}{4\pi D^2} = 6.5 \times 10^{10}\mathrm{cm}^{-2}\mathrm{s}^{-1} \ , \tag{1.8}$$

where $L_\odot$ is the luminosity of the Sun, and D is the Earth-Sun distance, and the energy contribution to the solar luminosity from one pp termination has been approximated as 13MeV per neutrino. The flux estimate is remarkably accurate given its crude nature; the standard solar model prediction for the total neutrino flux is $\Phi = (6.56 \pm 0.07) \times 10^{10}\mathrm{cm}^{-2}\mathrm{s}^{-1}$ [30]. The estimate given neglects all the physics required to determine the energy spectrum of neutrinos from the Sun, and hence all the physics that might determine the event rate in a given solar neutrino experiment. The neutrino energy spectrum is

Reaction	Reaction Name	Termination (%)	τ (yr)	E_ν (MeV)
$p + p \rightarrow {}^2H + e^+ + \nu_e$	pp	100	10^{10}	≤ 0.420
$p + e^- + p \rightarrow {}^2H + \nu_e$	pep	0.4	10^{12}	1.442
${}^2H + p \rightarrow {}^3He + \gamma$		100	10^8	
${}^3He + {}^3He \rightarrow \alpha + 2p$		85	10^5	
${}^3He + {}^4He \rightarrow {}^7Be + \gamma$		15	10^6	
${}^7Be + e^- \rightarrow {}^7Li + \nu_e$	^{7}Be	15	10^{-1}	0.861 or 0.383
${}^7Li + p \rightarrow 2\alpha$		15	10^{-5}	
${}^7Be + p \rightarrow {}^8B + \gamma$		0.02	10^2	
${}^8B \rightarrow {}^8Be + e^+ + \nu_e$	^{8}B	0.02	10^{-8}	≤ 15
${}^8Be \rightarrow 2\alpha$		0.02		
${}^3He + p \rightarrow {}^4He + e^+ + \nu_e$	hep	0.00002	10^{12}	≤ 18.77

Table 1.1: pp cycle statistics [26]. The termination % is the fraction of all terminations in the pp cycle that include the listed reaction. $\tau = 1/\lambda$, where λ is the reaction rate constant in solar conditions. E_ν is the energy of the emitted neutrino, where applicable.

a consequence of the rates of the individual reactions that make up the pp chain. The rates of these reactions can only be estimated by constructing a detailed physical model of the solar interior. It is these solar models that are the subject of the next section.

1.3 Standard Solar Models

A Standard Solar Model (SSM) is a solar model that most of the community accepts contains no surprising or unusual physical input parameters, assumptions, or evolution equations. Many such models have now been constructed; the solar models used to predict the neutrino flux from the sun have been refined from those used in the modelling of stellar evolution. A SSM makes the following basic assumptions [26] about the sun, which is a hydrogen burning main sequence star;

1. That the Sun is a spherically symmetric body undergoing no *significant* rotation.

2. That the Sun is in a state of hydrostatic equilibrium, where the internal pressure in the Sun counterbalances gravity;

$$\frac{dP}{dr} = -\frac{Gm(r)\rho(r)}{r^2} \ , \tag{1.9}$$

where P is the pressure at a radius r in the Sun, $m(r)$ is the mass contained within a sphere of radius r, and $\rho(r)$ is the density of matter at r. The Sun is in hydrostatic equilibrium if this equation is valid for all r. This is known to be an excellent approximation, because if hydrostatic equilibrium is not maintained, the Sun should collapse in a free-fall time of less than an hour. The pressure internal to the sun is just that of an ideal ionised gas, with contributions from radiation pressure and electron degeneracy;

$$P(r) = \frac{a}{3}T^4 + \frac{k\rho T}{\mu m_{\rm H}}(1 + D) \ , \tag{1.10}$$

where $a = 8\pi^5 k^4/15c^3h^3$, and the term $aT^4/3$ arises from radiation pressure, whilst $k\rho T/\mu m_{\rm H}$ is the thermal pressure and $(1 + D)$ are the corrections from ionisation (calculated using the theory of Debye and Hückel, [131]), electron degeneracy and screening. μ is the mean molecular reduced mass of the gas.

3. Energy generation in the Sun is primarily due to nuclear reactions, with a small contribution due to gravitational expansion or contraction. The luminosity generated in a spherical shell of radius r is given by;

$$\frac{dL_r}{dr} = \rho(4\pi r^2)\left(E_{\rm nuclear} - T\frac{dS}{dt}\right) \ , \tag{1.11}$$

where S is the stellar entropy.

4. Energy transport in the Sun occurs by radiation (photons and neutrinos) or by convective motion only. Radiative energy transfer by photons dominates convective transfer in the solar core, and hence the energy transport is given by

$$L_r = -4\pi r^2 \frac{ac}{3} \frac{1}{\kappa\rho} \frac{dT^4}{dr} \ . \tag{1.12}$$

κ is the total opacity, and it is the sum of the radiative and conductive opacities, $\kappa^{-1} = \kappa_{\rm rad}^{-1} + \kappa_{\rm cond}^{-1}$. The dominance of radiative transfer in the solar interior makes the calculation of radiative opacity an important step in the construction of any solar model.

5. That the Sun was in a state of chemical homogeneity when it was formed. Since that time, changes to the composition in the Sun have occurred only as a result of nuclear reactions or the radial diffusion of elements.

6. Mass loss from the sun is neglected, as are the effects of the solar magnetic field.

7. No unknown physics plays any significant role in the Sun.

Helium and heavy element diffusion [22] [23] have only recently been included in any solar model, and significantly affect both the computed neutrino fluxes and the helioseismological frequencies (see Table 1.4). Helioseismological analyses of measured p-mode oscillation frequencies [21] provide an accurate test of the sound velocity in the solar interior. Bahcall and Pinsonneault [30] have included diffusion in their model, and their results agree very well with the observed p-mode oscillation data in the solar core [33].

In addition to the assumptions about pressure, energy generation, energy transfer, and chemical nature in the stellar core, the conditions at the outer edge of the star must also be specified. The boundary conditions that are used represent a great simplification of the actual conditions. This is because the outer regions of the Sun are strongly influenced by convection and by turbulence, processes which are poorly understood in a solar context. In practice, it is sufficient to assume that the outer regions are in convective equilibrium, and to apply well known approximate temperature-pressure relations. Bahcall [25] has demonstrated that the difference between the crudest and the most exact models of the convective region of the Sun is about 2% in the solar neutrino fluxes, and additionally Bahcall and Glasner [29] have demonstrated that a change in the depth of the convective zone by a factor of 5 changes the ^{8}B flux by less than 7%, and the ^{7}Be flux by less than 4%.

1.3.1 Input Data

In the previous section, the physical assumptions that are used in constructing SSMs were described. To complete the picture of a SSM, the more important input parameters will be outlined.

Fusion Cross Sections

The nuclear reactions that take place in the solar interior do so at energies much lower than those for which cross sections are measured in the laboratory. It is therefore necessary to extrapolate the cross sections to low energies. At these low energies, the Coulomb barrier plays a significant part in determining the rates for nuclear fusion. One common parameterisation for exothermic reactions is;

$$\sigma(E) = \frac{S(E)}{E} e^{-2\pi\eta} \ , \text{ where } \eta(E) = \frac{\alpha z Z}{v/c} \ , \tag{1.13}$$

where the exponential arises from the Gamow penetration factor for the penetration of the Coulomb barrier. $S(E)$ contains the small energy dependence of the matrix element, whilst the factor $1/E$ represents the dependence of many low-energy cross sections upon the de Broglie wavelength. Table 1.2 contains values for the parameters used in a recent solar model [26]. The cross sections so obtained by extrapolation from MeV energies to zero energy are convoluted with the Maxwell-Boltzmann thermal energy distribution to obtain the fusion rate in a solar model. Note that the rate of the pep reaction is proportional to that of the pp reaction, and hence is nearly solar model independent. The constant of proportionality varies by less than 10% between solar models.

Reaction	Q (MeV)	$\langle q_{\nu_e} \rangle$	S_0 / keV b	dS/dE	t
^{1}H(p, $e^+\nu_e$)^{2}H	0.420	0.265	$4.07(1 \pm 0.051)E-22$	$4.52E-24$	10^{10}
^{1}H(pe^-, ν_e)^{2}H	1.442	1.442	*		10^{12}
^{2}H(p, γ)^{3}He	5.494		$2.5E-04$	$7.9E-06$	10^{-8}
^{3}He(^{3}He, 2p)^{4}He	12.860		$5.15(1 \pm 0.17)E+03$	-0.9	10^5
^{3}He(^{4}He, γ)^{7}Be	1.586		$0.54(1 \pm 0.06)$	$3.1E-04$	10^6
^{7}Be(e^-, ν_e)^{7}Li	0.862	0.862	*		10^{-1}
	0.384	0.384			
^{7}Li(p, α)^{4}He	17.343		$52(1 \pm 0.5)$	0	10^{-5}
^{7}Be(p, γ)^{8}B	0.137		$0.0243(1 \pm 0.22)$	$-3E-05$	10^2
^{8}B(e^+, ν_e)^{8}Be	17.980	6.710			10^{-8}
^{3}He(p, $e^+\nu_e$)^{4}He	19.795	9.625	$8E-20$		10^{12}

Table 1.2: Reaction parameters for the p-p chain [26]. The errors are estimated 3σ errors. Q is the Q-value of the reaction, $\langle q_{\nu_e} \rangle$ is the average neutrino energy, S_0 the cross section factor at zero energy, and t is the mean lifetime of the target nucleus in the solar interior. A * indicates that the cross section is not extrapolated in the usual manner but can be calculated accurately using weak interaction theory and the local physical conditions of the stellar plasma.

Element	Abundance
C	8.55 ± 0.05
N	7.97 ± 0.07
O	8.87 ± 0.07
Ne	8.08 ± 0.06
Na	6.33 ± 0.03
Mg	7.58 ± 0.05
Al	6.47 ± 0.07
Si	7.55 ± 0.05
P	5.45 ± 0.04

Element	Abundance
S	7.21 ± 0.06
Cl	5.5 ± 0.3
Ar	6.52 ± 0.10
Ca	6.36 ± 0.02
Ti	5.02 ± 0.06
Cr	5.67 ± 0.03
Mn	5.39 ± 0.03
Fe	7.50 ± 0.04
Ni	6.25 ± 0.04

Table 1.3: Primordial heavy elemental abundances in the Sun [20]. The numerical entries are the logarithms of the abundances normalised to $\log N = 12$ for hydrogen. The heavy element abundance is $Z/X = 0.0245$, where Z is the fraction of the solar mass accounted for by heavy elements ($Z > 2$) and X is the fraction of the solar mass accounted for by hydrogen.

Elemental Abundances

Stellar elemental abundances are obtained from two sources; meteorites and the solar photosphere. In the past the two sources have given discrepant results, but as the atomic data has improved the abundances determined from the solar atmosphere have approached those obtained from meteorites, resulting in the consensus view that meteoritic values correctly represent the primordial elemental abundances in the Sun.

The assumed abundances of the heavy elements in the primordial Sun significantly influence the calculated neutrino fluxes [30]. Most importantly, the heavy elements contribute to the radiative opacity, which in its turn affects the temperature profile in the solar interior, and hence the rates of neutrino production (many of the rates are strongly dependent on the solar core temperature [31]). Table 1.3 contains a recent determination of the heavy element abundances [20].

The Radiative Opacity

The calculation of the opacity is believed by most not to be a major source of uncertainty in the solar neutrino fluxes because in the centre of the sun, where most of the solar neutrinos are produced and the temperature is $> 10^7$K, more than half the opacity arises as a result of photon scattering on free electrons and inverse bremsstrahlung in the presence of completely ionised hydrogen and helium, processes which

Neutrino Production Reaction	Neutrino Fluxes / 10^{10}cm^{-2} s^{-1}		
	Bahcall and Pinsonneault [30]	Bahcall and Ulrich [25]	Turck-Chiéze *et al.* [35]
^{1}H(p, $e^+\nu_e$)^{2}H	$5.91(1.00^{+0.01}_{-0.01})$	$6.0(1 \pm 0.02)$	$5.98(1 \pm 0.03)$
^{1}H(pe^-, ν_e)^{2}H	$1.40 \times 10^{-2}(1.00^{+0.01}_{-0.02})$	$1.4 \times 10^{-2}(1 \pm 0.05)$	1.30×10^{-2}
^{7}Be(e^-, ν_e)^{7}Li	$5.15 \times 10^{-1}(1.00^{+0.06}_{-0.07})$	$4.7 \times 10^{-1}(1 \pm 0.15)$	4.18×10^{-1}
^{8}B($e^+\nu_e$)^{8}Be	$6.62 \times 10^{-4}(1.00^{+0.14}_{-0.17})$	$5.8 \times 10^{-4}(1 \pm 0.37)$	$3.83 \times 10^{-4}(1 \pm 0.26)$
^{13}N($e^+\nu_e$)^{13}C	$6.18 \times 10^{-2}(1.00^{+0.17}_{-0.20})$	$6.1 \times 10^{-2}(1 \pm 0.5)$	6.27×10^{-2}
^{15}O($e^+\nu_e$)^{15}N	$5.45 \times 10^{-2}(1.00^{+0.19}_{-0.22})$	$5.2 \times 10^{-2}(1 \pm 0.58)$	5.60×10^{-2}
^{17}F($e^+\nu_e$)^{17}O	$6.48 \times 10^{-4}(1.00^{+0.15}_{-0.19})$	$5.2 \times 10^{-4}(1 \pm 0.46)$	

Table 1.4: Neutrino fluxes for a selection of reactions and solar models. The model of Bahcall and Pinsonneault [30] includes helium and heavy element diffusion.

can be calculated relatively easily.

Rogers and Iglesias [19] have provided an opacity code to replace that of Los Alamos, which was previously used in most standard solar models. Their code indicates increases in opacity by up to a factor of 4 at low temperatures (large solar radii) largely due to the rich spectrum of transitions in the M shell of iron. The importance of iron as a contributor to the astrophysical opacity was overlooked because the fractional mass content of iron in stellar plasmas is only about 10^{-5}. New experimental techniques have been developed involving laser heated iron samples; these experiments produce results which are in good agreement with the theoretical opacity.

The new opacity code of Rogers and Iglesias (the OPAL code) [19] improves the agreement between the SSM and the observed solar p-modes [21]. This is demonstrated by Bahcall *et al.* [33], where it is shown that SSMs without the OPAL code cannot reproduce the calculated speed of sound for $r > 0.75R_\odot$.

1.3.2 Iteration

A SSM is a sequence of models, beginning with a main sequence star that is of homogeneous composition. Successive models are calculated by allowing for changes in composition and the evolution of other parameters. Each model involves a time step of the order of $5 \times 10^8 \rightarrow 10^9$ years and the model is typically iterated through $5 - 10$ epochs representing a total time of $t_\odot = 4.55 \times 10^9$ years.

In practice, an initial guess is made for a small number of parameters and the solar model is iterated in time until the properties of the solar model match the observed properties of the Sun, such as the solar age, mass, luminosity, radius, p-mode oscillations, and surface heavy element abundance. Bahcall and Ulrich [25] guess the initial values of X, the initial hydrogen abundance, and S, an entropy like variable.

No mention has been made so far of pre-main sequence solar evolution. This is because solar models are remarkably insensitive to the process, indeed Bahcall and Glasner [29] have calculated that different scenarios for pre-main-sequence evolution change the predicted rates for solar neutrino experiments by less than $\sim 1\%$.

1.3.3 Neutrino Fluxes

The neutrino fluxes from a number of solar models are included in Table 1.4. The fluxes from [30] are depicted in Figure 1.2. The figure shows that the majority of the neutrino flux from the sun is due to pp neutrinos, which have an endpoint of ~ 0.4MeV, below the threshold for detection of all the solar neutrino experiments except the gallium experiments.

The uncertainty represented by the differences in the neutrino fluxes between different solar models arise principally from the following sources (overleaf);

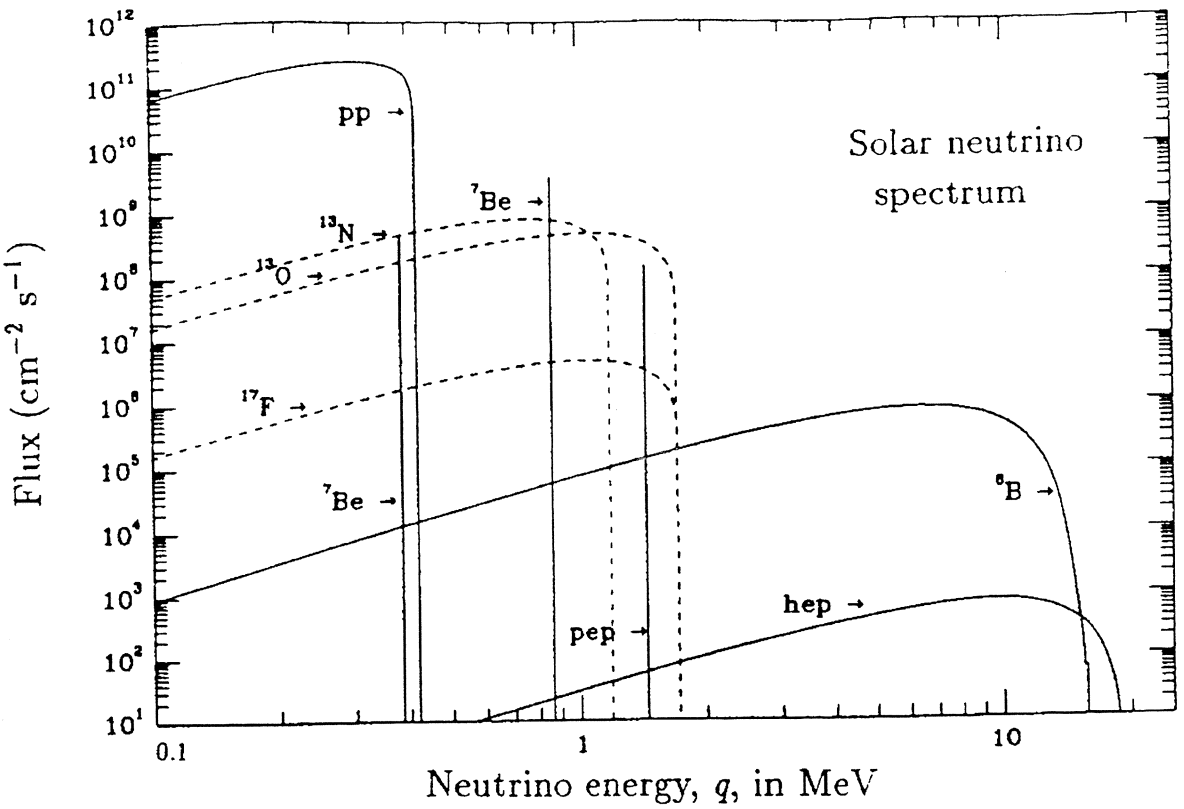

Figure 1.2: The solar neutrino flux as a function of energy. The units are number cm^{-2} s^{-1} MeV^{-1} for the continuous sources and number cm^{-2} s^{-1} for the discrete sources [26].

1. differences in the equation of state, specifically the inclusion or lack thereof of the Debye-Hückel corrections;
2. differences in the calculated solar opacity, stemming partly from differences in the assumed elemental abundances; and,
3. differences in the values of S_0 for the ^{3}He+^{3}He and the ^{7}Be$(p,\gamma)^8$B reactions. The extrapolation from laboratory energies down to zero energy is complicated by the effects of electron screening.

One result of the standard solar models is that the ^{7}Be and ^{8}B neutrinos are fantastically sensitive to the core temperature of the sun. Bahcall and Ulmer have evaluated 1000 numerical solar models similar to their best standard solar model, and derive the following relationships [31];

$$\Phi\left(^7\mathrm{Be}(e^-,\nu_e)^7\mathrm{Li}\right) \sim T^{10} \ , \tag{1.14}$$

and

$$\Phi\left(^8\mathrm{B}(e^+\nu_e)^8\mathrm{Be}\right) \sim T^{24} \ . \tag{1.15}$$

The sensitivity of these neutrino fluxes to the core temperature of the sun begs the question of how any two standard solar models agree at all. It has been pointed out that solar neutrino fluxes are strongly constrained by the luminosity of the sun, which is evident in the following heuristic argument; if;

$$L_\odot \propto T_c^4 \ , \tag{1.16}$$

and;

$$\Phi_\nu \propto T_c^n \ , \tag{1.17}$$

then;

$$\frac{\Delta\Phi_\nu}{\Phi_\nu} = \frac{n}{4}\frac{\Delta L}{L} \ , \tag{1.18}$$

and hence

$$\frac{\Delta\Phi_\nu}{\Phi_\nu} = \frac{0.01n}{4} , \tag{1.19}$$

where the relations $L_\odot \propto T_c^4$ and $\Delta L/L = 0.01$ have been assumed, and $\Phi_\nu \propto T_c^n$ represents the power-law dependence of a neutrino flux on the temperature of the solar core. This argument shows that the calculated neutrino fluxes are constrained to some extent by the observed luminosity of the sun, but it does not place any constraint upon changes in the physics of neutrino production which do not effect observable changes in the solar luminosity. Hence, Bahcall and Pinsonneault have reported that their model and that of Turck-Chièze *et al.* agree at the 1% level when the same input parameters are used to calculate the event rate in the Homestake detector, but solar models where the ^{7}Be(p,γ)^{8}B cross section is $\frac{1}{2}$ the theoretical expectation are not ruled out.

The standard solar model has evolved a great deal over the past decade. The current state-of-the-art solar models are capable of reproducing all of the observable properties of the sun except the neutrino fluxes. The standard solar model also reproduces the theoretical relationship between the mass and the photon luminosity of stars that is in agreement with observation over 2 orders of magnitude. In addition, it successfully accounts for the distribution of known stars in the Hertzsprung-Russell diagram (a luminosity-temperature graph), most of which is empty. Having established a framework for the prediction of neutrino fluxes at the earth, the next section will describe the terrestrial experiments that have been used to detect these fluxes.

1.4 The Detection of Solar Neutrinos by Terrestrial Experiments

A number of solar neutrino experiments have now reported results. The first solar neutrino experiment was a radiochemical chlorine experiment conducted by Davis *et al.* . That experiment reported a deficit in the expected number of neutrinos. Subsequent experiments have been conducted which have different sensitivities to the neutrino energy spectrum, and all have reported a deficit.

1.4.1 The Chlorine Experiment

The Homestake detector of Davis *et al.* [1][2], Figure 1.3, contains 390000 litres of liquid tetrachloroethylene, C_2Cl_4, containing 520 tonnes of chlorine in a horizontal tank. Solar neutrinos are detected through the reaction

$$\nu_e + {}^{37}\mathrm{Cl} \rightarrow e^- + {}^{37}\mathrm{Ar} , \tag{1.20}$$

which has a threshold of 0.814MeV. The 0.814MeV threshold permits the detection of all neutrino sources except the pp neutrinos. The system is located 4850 feet underground in order to reduce the production of ^{37}Ar from (p,n) reactions by protons formed in cosmic-ray muon interactions. The rate of ^{37}Ar production in the liquid by cosmic-ray muons is estimated to be 0.1 ^{37}Ar atoms per day. Total ^{37}Ar production from all backgrounds is less than 0.2 ^{37}Ar atoms per day, which is well below the rate of solar neutrino production.

Neutrino detection depends upon the effective removal of the ^{37}Ar atoms from the tank of tetrachloroethylene, and subsequent observance of the decay of the ^{37}Ar in a small proportional counter. The argon extraction procedure is calibrated for each run by the introduction of known quantities of isotopic alternates, either ^{36}Ar or ^{38}Ar, into the tank. The tank is then purged with helium. The extraction of argon from the tank has been experimentally demonstrated to be exponential, with the fraction of the gas remaining in the tank equal to $e^{-\alpha V}$, where V is the total volume of helium that has been passed through the tank, and α is a constant. The mean value of α is 7.645 ± 0.519 megalitres^{-1}, and has shown no indication of any variation since 1970. The tank is typically swept with 390 kilolitres of helium, giving a tank extraction efficiency of 95%. The argon gas is removed from a charcoal trap through which the helium/argon mixture is passed, and purified by gas chromatography. Its volume is measured. The purified argon gas is then put into a very small proportional counter, and the ^{37}Ar decays are followed for $\sim$ 1 year. At the end of 1 year, the gas is removed from the counter and its volume measured again. The isotopic content of the gas is then determined by mass spectroscopy. The fraction of the gas recovered, corrected for the tank extraction efficiency, is called the gas processing efficiency. The mean value of the gas processing efficiency is (95.8 ± 0.7)%, and has shown no variation since 1970.

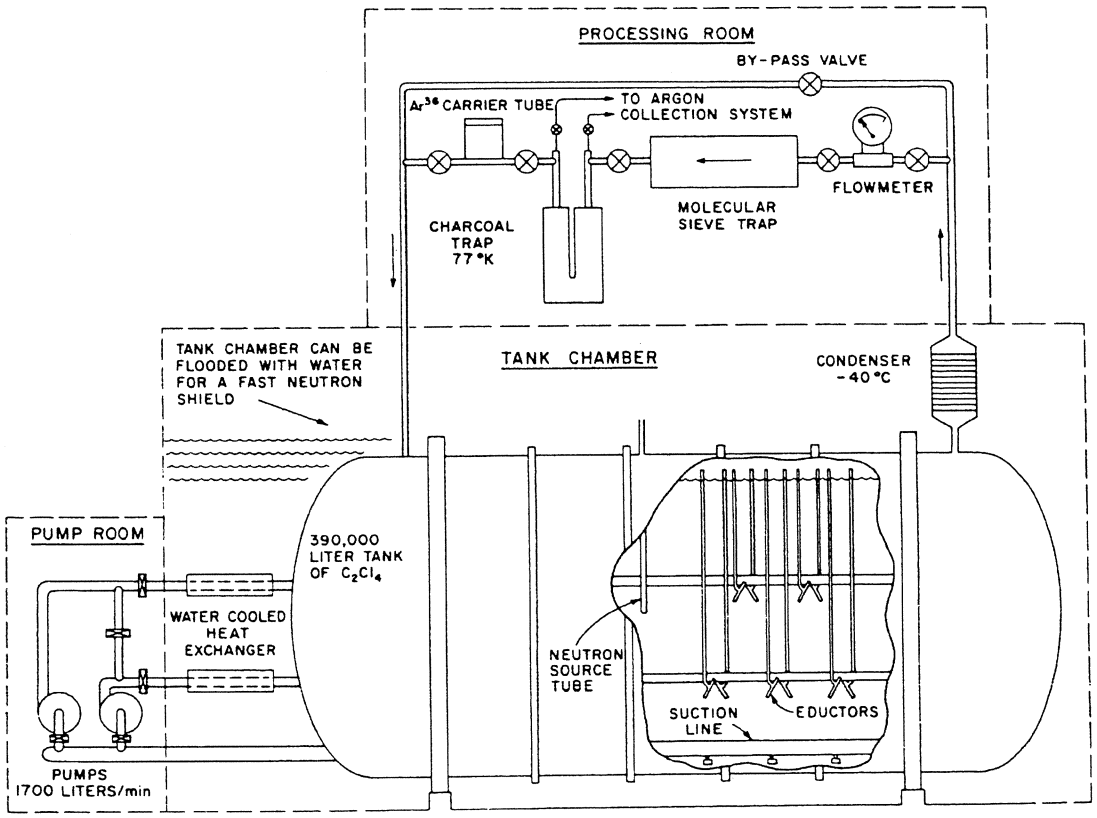

Figure 1.3: The Homestake chlorine experiment [1].

The argon sample is counted in a small proportional counter with an active volume 3cm long and 0.5cm in diameter. A small amount of methane is added to the argon to improve the counting characteristics of the gas. The counter is shielded from external radiations by a cylindrical iron shield 30cm thick lined with a ring of 5cm diameter proportional counters for registering cosmic-ray muons. The argon counter is held in a well of a 12.5cm square sodium-iodide scintillation counter located inside the ring counters. Events in anticoincidence with both the scintillator and the muon veto shields are recorded and filtered to eliminate unwanted signals and electrical noise. It is in this way that the decay of the atoms of ^{37}Ar are observed via K-shell electron capture with a characteristic mean-life of 50.5 days. There are dead regions and regions of very low detection efficiency within the proportional counter volumes, and these counters are calibrated by introducing a known quantity of ^{37}Ar into the counters and observing the number of resultant decays to obtain their efficiency.

The cosmic ray background has been measured by the use of a ^{39}K target in a potassium hydroxide solution, KOH. The potassium is converted by cosmic rays from ^{39}K to ^{37}Ar. The quantity of ^{37}Ar produced is then measured. The potassium target detectors were compared with portable perchloroethylene detectors at shallow depths before being used at the full depth of the chlorine detector. These measurements give a cosmic ray background of 0.055 ± 0.015 ^{37}Ar per day, in agreement with analytic extrapolations from lesser depths.

There have been other systematic tests of the extraction technique (see [2]). The flux estimates have also been found to be grossly constant as a function of time, yielding 2.52 ± 0.41 SNU for the period $1970-77$, 2.27 ± 0.30 SNU for the period $1977-85$, and 2.78 ± 0.35 SNU for the period $1986-93$. Figure 1.4 shows another breakdown of the results as a function of time. The time averaged flux is [3];

$$\text{Observed rate} = (2.56 \pm 0.16\,(\text{stat.}) \pm 0.14\,(\text{sys.}))\,\text{SNU}\ , \tag{1.21}$$

Estimates of the theoretical rates are available in Table 1.5. It is clear that even in the most optimistic of scenarios, the difference between theory and experiment is about 2σ. Note that Bahcall and Pinsonneault [30] are the only group to have included helium and heavy element diffusion in their solar model, and as a result they are the only group which can reproduce the observed p-mode oscillations.

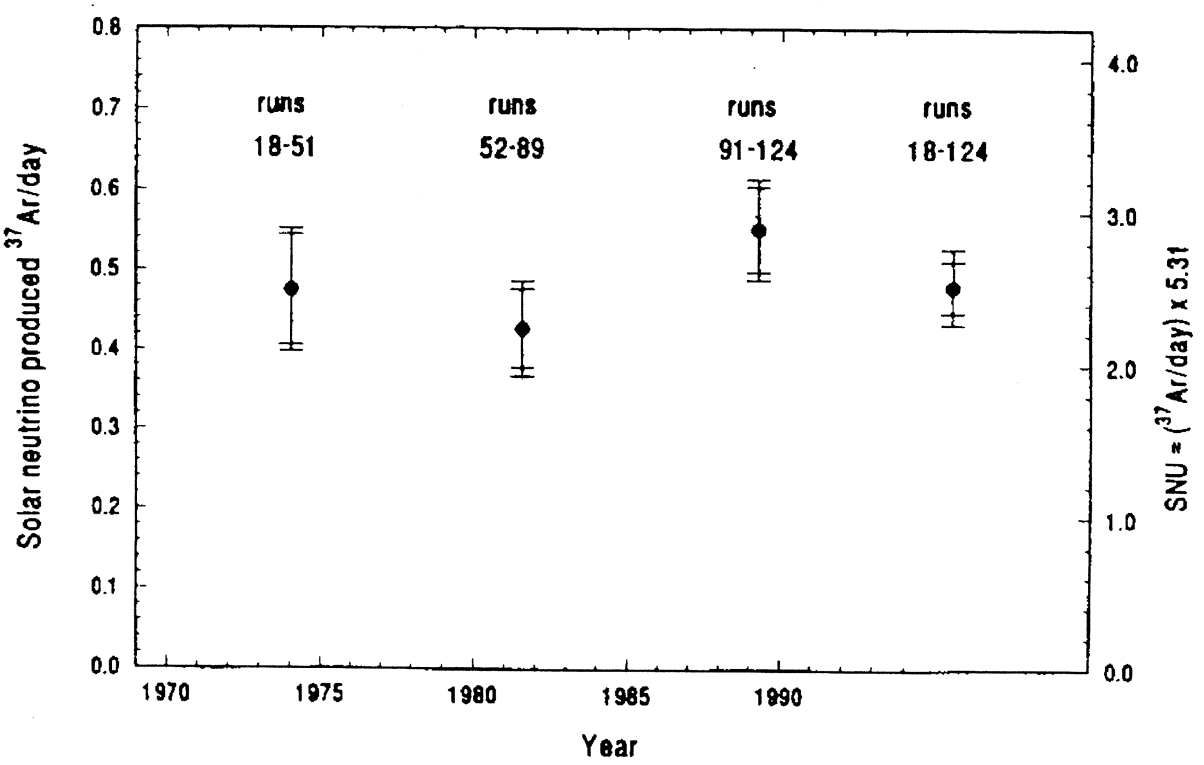

Figure 1.4: The event rate in the chlorine detector as a function of time [2].

Neutrino Source	Capture Rates		
	Bahcall and Pinsonneault [30]	Bahcall and Ulrich [25]	Turck-Chiéze and Lopes [35]
^{1}H(p, $e^+\nu_e$)^{2}H	0.0	0.0	0.0
^{1}H(pe^-, ν_e)^{2}H	0.22	0.23	0.22
^{7}Be(e^-, ν_e)^{7}Li	1.24	1.12	1.10
^{8}B($e^+\nu_e$)^{8}Be	7.36	6.15	4.63
^{13}N($e^+\nu_e$)^{13}C	0.11	0.102	0.063
^{15}O($e^+\nu_e$)^{15}N	0.37	0.34	0.21
^{17}F($e^+\nu_e$)^{17}O	...	0.0034	0.0028
Total (SNU)	$9.3^{+1.2}_{-1.4}$	$7.9(1 \pm 0.33)$	6.36 ± 1.4

Table 1.5: The contributions to the predicted event rates in the chlorine detector from the several solar neutrino sources. All rates are given in SNU.

1.4.2 The Kamiokande Experiment

The Kamiokande experiment [4][7] is an imaging water Čerenkov detector. Solar neutrinos are detected through neutrino-electron scattering, $\nu_e e \rightarrow \nu_e e$, and the measurement of the initial position and vector momentum of the recoiling electron. The scattering angle is small ($\theta_e \leq 2m_e/T_e$) so that the direction of the incident neutrino is usually preserved in the direction of the recoiling electron. The detector has an angular resolution of 28° at 10MeV, mainly limited by the multiple scattering of the electron in water. This angular resolution makes it possible to point the incident neutrinos back to the sun, if that is their origin. In addition, the observed electrons yield information about the energy spectrum of the incident ν_e and the temporal distribution of the events.

The detector is located 1000m underground (2700m water equivalent) in the Kamioka metal mine in Japan. The Kamiokande detector consists of an inner main detector and an outer anticounter. The inner

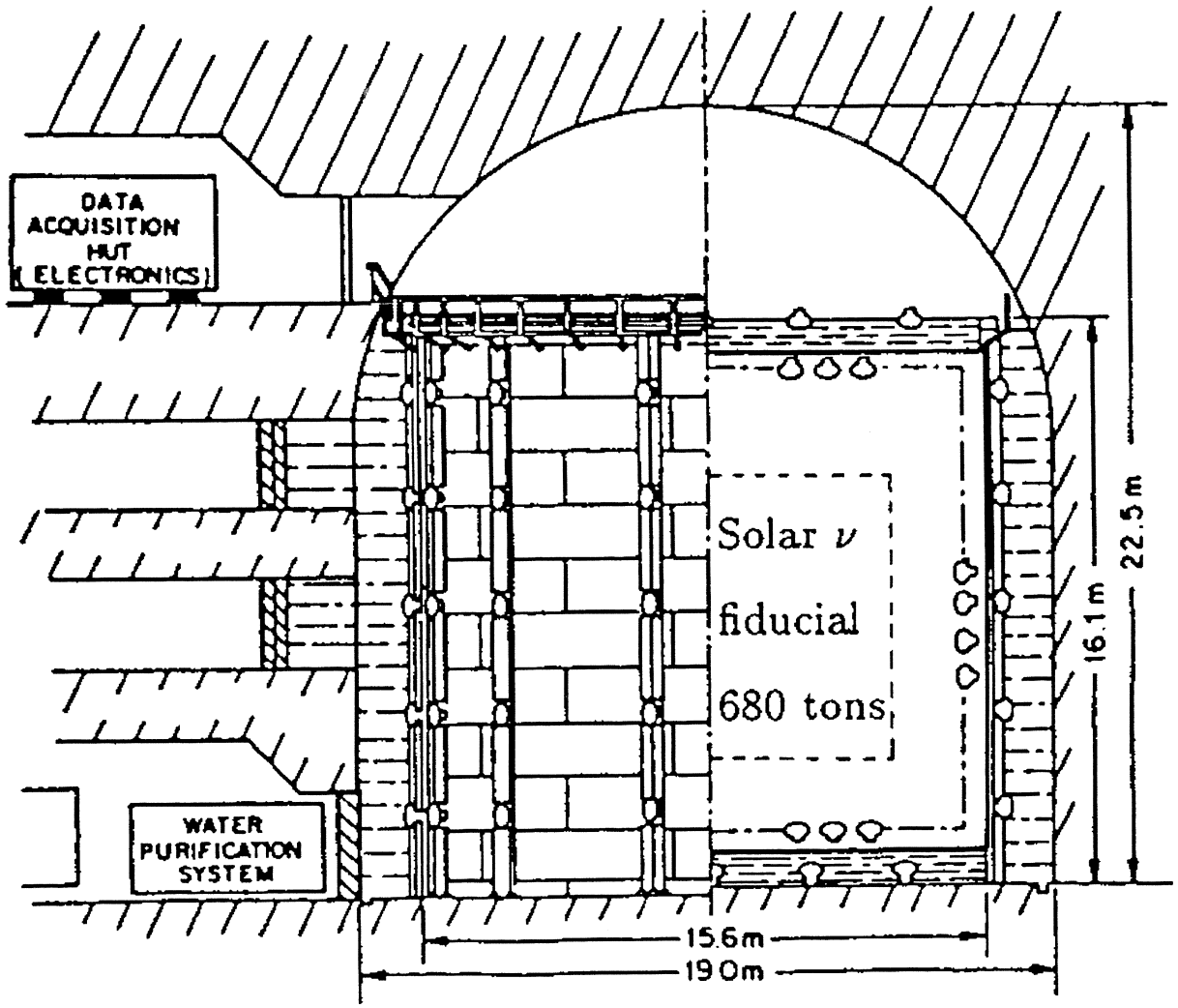

Figure 1.5: Schematic of the Kamiokande II Solar Neutrino Detector [5].

main detector is contained in a cylindrical steel tank and has a cylindrical volume 14.4m in diameter and 13.1m in height, containing 2142 metric tonnes of water. A total of 948 photomultiplier tubes, each with a 50cm diameter photosensitive area, cover 20% of the entire inner surface of the tank. The fiducial mass for the ^{8}B solar-neutrino measurement is 680 tonnes, with boundaries 2.0m from the containing walls. A schematic of the Kamiokande II detector (the original detector was used to search for proton decay) can be seen in Figure 1.5.

The anticounter that surrounds the detector is a 4π solid-angle water Čerenkov detector whose total mass is 1800 tonnes. 123 photomultiplier tubes look into the anticounter, whose inner surface is covered by aluminium sheets to obtain good light collection efficiency.

The water in the detector is maintained at high purity. This is because metal ions such as iron, nickel, and cobalt, as well as organic molecules, can reduce water transparency due to their absorptivity. In addition, at low energies the detector trigger rate is dominated by radioisotopes present in the water. The uranium and radium content in the tank is less than 10^{-3}pCi per liter.

The Kamiokande II trigger system is designed to collect all events above approximately 6MeV with almost no dead time. The trigger efficiency as a function of total energy is obtained from Monte Carlo generated events. The trigger accepts 6.7MeV electrons with a 50% efficiency, and 9.2MeV electrons with a 90% efficiency. The trigger rate is $\sim$ 1Hz with a 6.1MeV threshold, of which 0.37Hz is due to cosmic ray muons, and the remainder is presumed to be due to radioactivity in the water and in the detector materials.

The energy, position, and direction of an event in the detector are calibrated using three sources. A Cf-Ni 9MeV γ-ray source was placed at the centre of the detector and produced γ ray spectra for calibration. The Monte Carlo was tuned to reproduce the peak of the calibration spectra to within 1%. The shape and the width of the energy spectrum was well reproduced by the Monte Carlo. The calibration source was moved to positions in the detector other than the centre, and the Monte Carlo reproduced the position of the peak in the spectra to within 2%. The stability of the gain of the detector was also monitored using the γ-ray source. The gain is stable to within $\pm$2% over the four years of operation from 1987 to 1990. The energy resolution is approximated by the function $\sigma(E_e)/E_e = 0.63/\sqrt{E_e}$.

Stopping muons were also used to calibrate the Kamiokande II detector. They were sampled and compared to the Monte Carlo simulation of the well known muon decay spectrum (the Michel spectrum). Comparison of the Monte Carlo and the data shows that the peak of the spectrum differs by less than 2%. In addition to the direct comparison of muon events, spallation events resulting from through going muons were also used to calibrate the detector. The Monte Carlo was used to generate the ^{12}B and ^{12}N events that result from spallation, and again, the difference in the position of the peak of the energy spectrum of events identified in the detector as spallation and those simulated by the Monte Carlo was less than 2%. As a result of the three calibrations, the absolute energy calibration is estimated to be accurate to 3%.

Position resolution was also obtained using the Cf-Ni 9MeV γ-ray source, and timing calibration was achieved using a laser source whose light was channelled through a diffuser, making it reasonably isotropic. Timing calibration was carried out for every PMT.

The detector was operated with an analysis threshold of 7MeV. With this threshold the Kamiokande detector is only sensitive to about 50% of the ^{8}B neutrinos. The Kamiokande II detector was the first detector to confirm the solar origins of its neutrino signal. The characteristic forward peak of the neutrino-electron scattering is shown in Figure 1.6. The neutrino image of the Sun is shown in Figure 1.7. Once again, the number of events recorded by the Kamiokande II detector is in disagreement with the theoretical predictions [9];

$$\frac{\Phi_{\text{Observed}}}{\Phi_{\text{Predicted}}} = 0.424 \pm 0.029\,(\text{stat.}) \pm 0.05\,(\text{sys.})\ . \tag{1.22}$$

1.4.3 The Gallium Experiments; SAGE and GALLEX

SAGE (formerly the Soviet-American Gallium Experiment, but now the Russian-American Gallium Experiment) and GALLEX (a European collaboration) are radiochemical experiments similar in principle to the chlorine experiment described earlier. The detection of solar neutrinos proceeds via the reaction;

$$\nu_e + {}^{71}\text{Ga} \rightarrow e^- + {}^{71}\text{Ge}\ ,\ E_{\text{min}} = 0.2332\text{MeV}\ . \tag{1.23}$$

Once created, the germanium must then be extracted and counted before the neutrino flux through the detector can be determined. The low threshold of a gallium detector renders it sensitive to all the neutrino sources, including the pp neutrinos, which have an endpoint of 420keV.

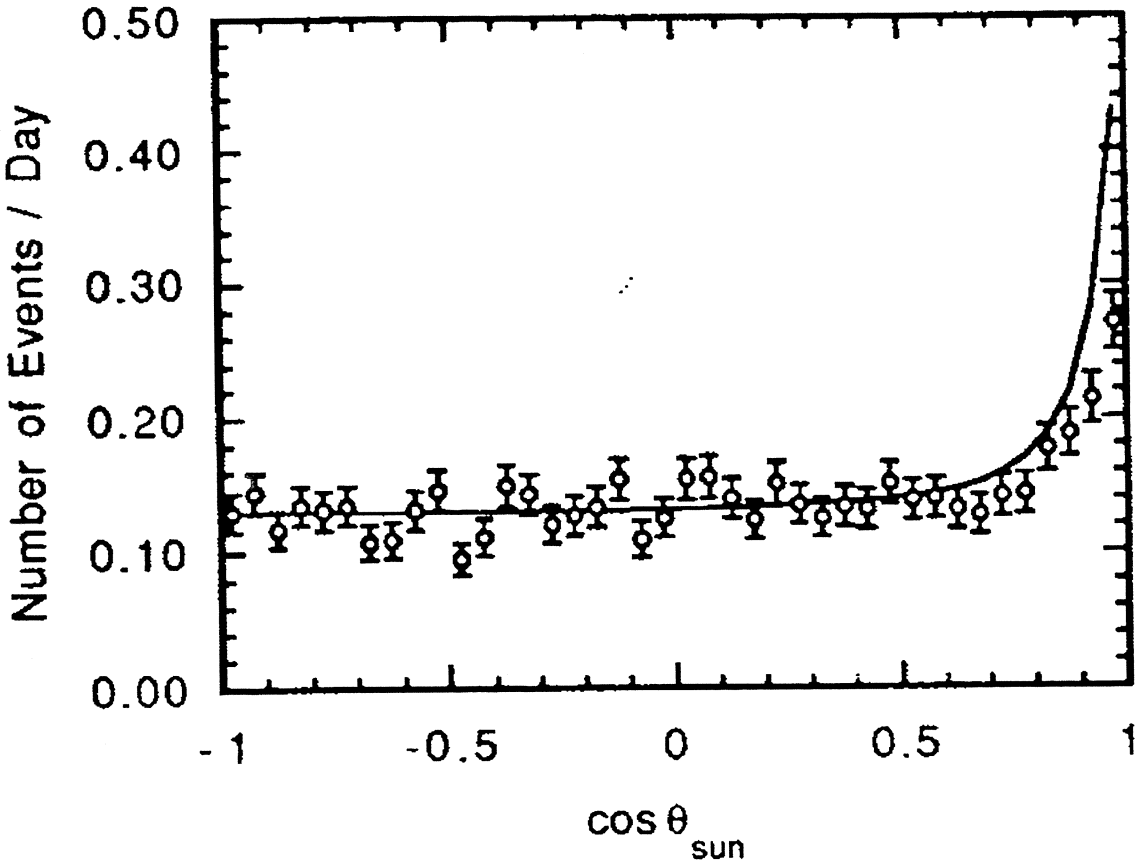

Figure 1.6: The angular distribution of events in the Kamiokande detector [7]. θ_{sun} is the angle from the solar core/ Kamiokande axis. The solid curve is the SSM prediction.

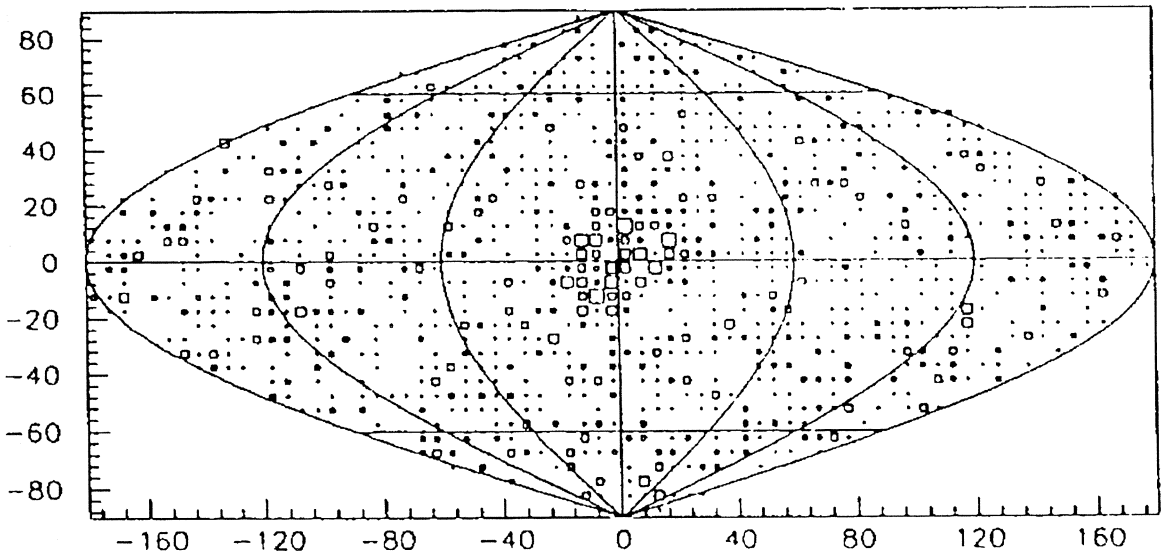

Figure 1.7: The neutrino image of the Sun in a celestial coordinate system with the Sun at the centre [7].

SAGE [14][15] is situated 3.5km from an entrance driven into the side of Mount Andyrchi in the Baksan mountains, and has overhead shielding of approximately 4700m water equivalent. The SAGE experiment initially contained 30 tonnes of liquid gallium, but this was later increased to 55 tonnes. The gallium was contained in Teflon-lined containers each holding approximately 7 tonnes of liquid. The main chamber of the laboratory is 60m long, 10m wide and 12m high. It is lined with 60cm of low activity concrete in order to reduce neutron and γ-ray backgrounds from the surrounding rock.

Each measurement of the solar neutrino flux begins with the addition of approximately 160μg of natural Ge carrier to each of the four reactors holding the gallium. After a typical exposure interval of 3−4 weeks the Ge carrier and any ^{71}Ge atoms that have been produced by neutrino capture are chemically extracted from the gallium. The efficiency of the extraction of the germanium carrier is measured at two stages during the extraction process using atomic absorption analysis. The overall extraction efficiency is typically $80 \pm 6\%$. The germanium exits from the chemical extraction process in the form of the gas germane, GeH_4, which is then mixed with a measured quantity of xenon and is inserted into a low background proportional counter. The proportional counter with an active volume of 0.75cm^3 is placed in the well of a NaI detector inside a large passive shield and counted for $2 - 3$ months.

^{71}Ge decays by electron capture to the ground state of ^{71}Ga with an 11.4 day half-life. The low-energy K- and L-shell Auger electrons and x-rays produced during electron shell relaxation in the resulting ^{71}Ga atom are detected by the proportional counter. With a typical counter-gas mix, 37% of the decays are observed in the Ge K peak at 10.4keV and 34% in the L peak at 1.2keV. Because of higher backgrounds in the L peak, only the K peak was initially used in the analysis of the experimental data. Both the K and L peaks were used from SAGE III onward. Pulse shape discrimination was used to separate the signal from the background. The counters were calibrated at 1-month intervals using an external ^{55}Fe source, which illuminates the central part of the counter through a thin side window. The results of this frequent calibration were checked by filling a proportional counter with $^{71}GeH_4$, together with the standard counter gas.

The data analysis selects events within the ^{71}Ge K peak which have no NaI activity in coincidence. A maximum likelihood analysis is then carried out to fit the time distribution of the events to an 11.4 day half-life and a flat background. The total count rate in the counters between 0.7 and 13.0keV is approximately 2.0 counts per day, with 0.1 counts per day in the ^{71}Ge K peak. The total production rate in the 30 tonnes of liquid gallium of all germanium activities from external neutron, internal radioactivity and cosmic-ray muons is calculated to be less than 2.5% of the standard solar model production rate.

Recently, the SAGE experiment has confirmed its extraction efficiency using a ^{51}Cr source [16]. ^{51}Cr decays to ^{51}V via electron capture with a half-life of 27.7 days and neutrino energies of 751keV (90% branch) and 426keV (10% branch). A 320keV γ-ray accompanies the 10% branch. The source consisted of a 513g of 92% enriched ^{50}Cr metal rods encased in a tungsten shield which in turn is welded inside a stainless steel casing. The source was fabricated and irradiated at a fast-breeder reactor in Kazakhstan. The source was used to irradiate the gallium contained within the SAGE detector, and the standard extraction and counting procedure followed. The final result was the ratio of measured ^{71}Ge production to that expected from the source strength. The ratio was $0.93^{+0.15}_{-0.17}(1\sigma)$. The result is consistent with the claimed extraction efficiency.

The observed flux in the SAGE detector is [17];

$$\Phi_{\text{Observed}} = 72^{+12+5}_{-10-7}\,\text{SNU (stat./sys.)}. \tag{1.24}$$

The GALLEX [10][11] experiment is located in the Laboratori Nazionali del Gran Sasso. The target is 30.3 tonnes of gallium containing 12 tonnes of ^{71}Ga in the form of an 8.13 molar aqueous solution acidified to a 2 molar solution with HCl. The expected event rate of 132SNU yields 14 atoms of ^{71}Ge in the target after $\sim$ 3 weeks of exposure.

The extraction of the ^{71}Ge is different from that used in the SAGE experiment, but again leads to the counter-gas, GeH_4, which is again counted in a proportional counter. The GALLEX experiment has also used a radioactive ^{51}Cr neutrino source to confirm their estimated extraction efficiency [12]. In the first observation of low energy neutrinos from a terrestrial source they confirmed that there were no significant experimental artifacts or unknown errors at the 10% level that are comparable to the 40% deficit in the observed solar neutrino flux. The event rate for the GALLEX experiment is [13];

$$\Phi_{\text{Observed}} = (70 \pm 7)\,\text{SNU (sys.+stat.)}\ , \tag{1.25}$$

Once again, the event rates observed in the gallium experiments, SAGE and GALLEX, are seriously at odds with the theoretical predictions. The expected contributions to the experimental rate from all solar sources are shown in Table 1.6.

Neutrino Source	Capture Rates		
	Bahcall and Pinsonneault [30]	Bahcall and Ulrich [25]	Turck-Chiéze and Lopes [35]
$^1\mathrm{H}(p, e^+\nu_e)^2\mathrm{H}$	69.7	70.8	71.1
$^1\mathrm{H}(pe^-, \nu_e)^2\mathrm{H}$	3.0	3.01	2.795
$^7\mathrm{Be}(e^-, \nu_e)^7\mathrm{Li}$	37.7	34.4	30.6
$^8\mathrm{B}(e^+\nu_e)^8\mathrm{Be}$	16.1	14.1	10.77
$^{13}\mathrm{N}(e^+\nu_e)^{13}\mathrm{C}$	3.8	3.77	2.36
$^{15}\mathrm{O}(e^+\nu_e)^{15}\mathrm{N}$	6.3	6.03	3.66
$^{17}\mathrm{F}(e^+\nu_e)^{17}\mathrm{O}$	...	0.06	...
Total (SNU)	137^{+8}_{-7}	132^{+20}_{-17}	122.5 ± 7

Table 1.6: The contributions to the predicted event rates in the gallium detectors from the several solar neutrino sources. All rates are given in SNU.

1.5 The Definiteness of the Solar Neutrino Problem

In the preceding sections the standard solar model used to predict the neutrino fluxes in terrestrial experiments has been discussed. The experiments used to detect the solar neutrino flux have also been described. The discrepancy between the theoretical estimate of the neutrino flux at the earth, and the experimental measurement of that flux must be due to one or more of the following statements;

1. the standard solar model is wrong;
2. the experiments are wrong; or,
3. electron neutrinos produced in the sun do not arrive at the earth.

That the experiments are wrong is now very difficult to credit. There are now four experiments utilising three wholly independent techniques, each with different sensitivities to the solar neutrino spectrum. All the experiments produce results that are lower than the results predicted by the standard solar model.

Several authors have argued that in the light of the experimental results there is no simple fix for the standard solar model. Following on from the great sensitivity of the neutrino fluxes to the core temperature of the sun (see Section 1.3.3) it was suggested that a cool sun might be responsible for the deficit in the neutrino fluxes, particularly the ^{8}B neutrino flux. Castellani *et al.* [36] have shown that standard solar models that have been altered so as to produce lower core temperatures have an unchanged temperature profile, at least for $R/R_\odot < 0.7$, and hence that the model can be parameterised by the reduced core temperature alone. No core temperature can be found, however, to reproduce the experimental results.

Bahcall has argued [28] that there are two solar neutrino problems. These will now be summarised using the 1994 SSM predictions and experimental data presented by Bahcall in [28]. Since the publication of that paper, the numbers given in this summary have changed slightly, but conclusions remain the same. The first arises because, assuming that the ^{8}B neutrino spectrum from the sun is the same as that in the laboratory, then the capture rate in the Homestake chlorine detector from the ^{8}B neutrinos in the Kamiokande experiment should be $(3.21^{+0.24}_{-0.23}(\mathrm{stat.}) \pm 0.39(\mathrm{sys.}))$SNU. The observed rate in the chlorine detector is $((2.55 \pm 0.17(\mathrm{stat.}) \pm 0.18(\mathrm{sys.}))$SNU, which implies that the rate for neutrinos from all other solar sources to which the chlorine detector is sensitive is negative, or consistent with zero;

$$\mathrm{Rate}(\mathrm{pep}, {}^7\mathrm{Be}, \mathrm{CNO}) = (-0.66 \pm 0.52)\mathrm{SNU}\ . \tag{1.26}$$

This negative rate is independent of any solar model. The rate is constrained to be positive definite, and adopting a Bayesian approach with a flat prior gives an upper limit of 0.68 SNU at the 95% confidence level. This is less than the predicted SSM ^{7}Be flux alone! The 'second' solar neutrino problem arises from the low observed rate in the gallium experiments, SAGE and GALLEX. In an earlier section (Section 1.2) the close link between the observed solar luminosity and the pp neutrino flux has been described. As a result of this constraint, all standard solar models predict the same pp neutrino event rate in the gallium experiments, $(\sim 74 \pm 1)$SNU. Using this prediction and the observed rate of ^{8}B neutrinos in the

Kamiokande experiment, a limit on the ^{7}Be neutrino flux in the chlorine experiment can now be derived from the observed event rates in the gallium experiments ($\sim (77 \pm 10)$ SNU). That limit is;

$$\text{Rate}(^7\text{Be}) \leq 19\,\text{SNU}\ , 95\% \ . \tag{1.27}$$

Once again this limit is lower than the ^{7}Be flux predicted by most standard solar models, which is (34 ± 4)SNU. To summarise; the first solar neutrino problem is the discrepancy between Homestake and Kamiokande, the second the fact that the event rate in the gallium experiments is consistent with the well constrained pp neutrino flux alone.

Parke [37] has a particularly striking analysis to demonstrate the discrepancy between the standard solar model and the experimental results. His analysis shows that even were one of the terrestrial solar neutrino experiments wrong, a solar neutrino problem would still exist. Parke requires few assumptions;

1. that the pp solar cycle is the dominant energy source in the Sun;
2. that the sun is in quasi-equilibrium;
3. that neutrinos are unaffected in their passage from the Sun to the Earth; and,
4. that the neutrino interaction cross sections assumed in the results of the terrestrial experiments are correct.

The pp solar cycle can be summarised as;

$$\begin{aligned} 4\text{p} + 2e^- &\rightarrow {}^4\text{He} + 2\nu_e^{\text{pp}} \ , & (1.28)\\ &\rightarrow {}^4\text{He} + \nu_e^{pp} + \nu_e^{^7\text{Be}} \ , & (1.29)\\ &\rightarrow {}^4\text{He} + \nu_e^{pp} + \nu_e^{^8\text{B}} \ . & (1.30) \end{aligned}$$

where the total energy release in any one of these terminations is 26.731MeV, and the ν_e^{pp}, $\nu_e^{^7\text{Be}}$, and $\nu_e^{^8\text{B}}$ on average have 0.265MeV, 0.861MeV, and 7MeV respectively.

If the solar luminosity is constant over a timescale of a few 10^6 years, then a relationship exists between the neutrino flux and that luminosity;

$$L_\odot = 13.1(\Phi^{\text{pp}} - \Phi^{^7\text{Be}} - \Phi^{^8\text{B}}) + 25.6\Phi^{^7\text{Be}} + 19.5\Phi^{^8\text{B}} \ . \tag{1.31}$$

Normalising the fluxes to those of Bahcall and Pinsonneault [30] such that $\phi^i = \Phi^i/\Phi_{\text{BP}}$, where $\Phi_{\text{BP}}^{\text{pp}} = 6.0 \times 10^{10}\text{cm}^{-2}\ \text{s}^{-1}$, and $\Phi_{\text{BP}}^{^7\text{Be}} = 4.9 \times 10^{9}\text{cm}^{-2}\ \text{s}^{-1}$, and $\Phi_{\text{BP}}^{^8\text{B}} = 5.7 \times 10^{6}\text{cm}^{-2}\ \text{s}^{-1}$, and dividing out the luminosity;

$$1 \simeq 0.913\phi^{\text{pp}} + 0.071\phi^{^7\text{Be}} + 4 \times 10^{-5}\phi^{^8\text{B}} \ . \tag{1.32}$$

The contributions of the three neutrino fluxes to the chlorine, Kamiokande, and gallium experiments are;

$$\begin{aligned} S_{\text{Cl}}^* &= 6.2\phi^{^8\text{B}} + 1.2\phi^{^7\text{Be}}\,\text{SNU} \ , & (1.33)\\ S_{\text{K}}^* &= \phi^{^8\text{B}}\Phi_{\text{BP}}^{^8\text{B}} \ , & (1.34)\\ S_{\text{Ga}}^* &= 14\phi^{^8\text{B}} + 36\phi^{^7\text{Be}} + 71\phi^{\text{pp}}\,\text{SNU} \ , & (1.35) \end{aligned}$$

where a * is used to indicate a theoretical quantity. The luminosity constraint of Equation 1.32 may be used to eliminate the pp flux from the rate for the gallium experiments;

$$S_{\text{Ga}}^* = 14\phi^{^8\text{B}} + 30\phi^{^7\text{Be}} + 78\text{SNU} \ . \tag{1.36}$$

Combining the results from the two gallium experiments, and then the statistical and systematic errors of the experiments in quadrature, the results from the three types of experiment are;

$$\begin{aligned} S_{\text{Cl}} &= (2.55 \pm 0.25)\text{SNU} \ , & (1.37)\\ S_{\text{K}} &= (0.51 \pm 0.072)\Phi_{\text{BP}}^{^8\text{B}} \ , & (1.38)\\ S_{\text{Ga}} &= (74 \pm 9.5)\text{SNU} \ . & (1.39) \end{aligned}$$

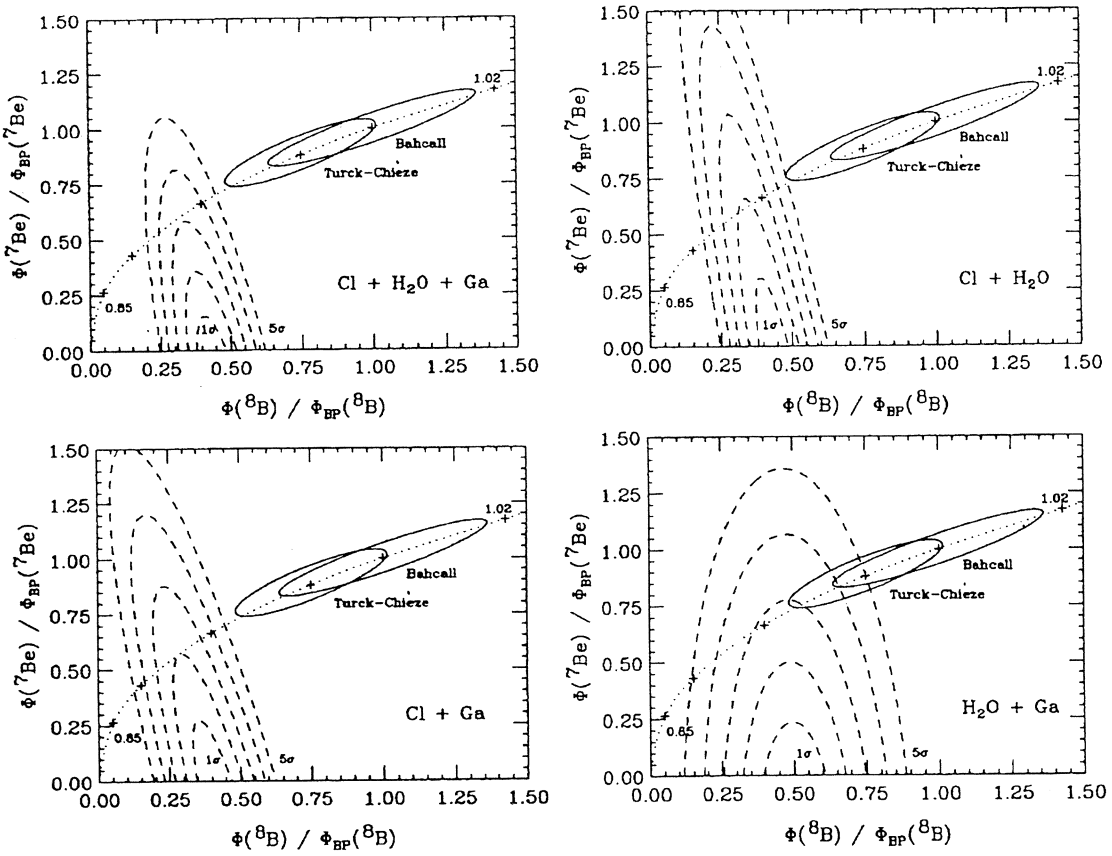

Figure 1.8: The discrepancy between the standard solar models and the experimental data is now clear. See text for details. Data taken from Parke [37].

Equations 1.33, 1.34 and 1.36 and 1.37 $\rightarrow$ 1.39 were then used to fit the neutrino flux quantities $\phi^{^7\mathrm{Be}}$ and $\phi^{^8\mathrm{B}}$, with the necessary constraint $\phi^{^7\mathrm{Be}} \geq 0$. Figure 1.8 shows the $1 \rightarrow 5\sigma$ contours for the fit to the two neutrino fluxes obtained by Parke [37] using four combinations of the experimental data, and the location of the fluxes from two standard solar models. The dotted line on the plots corresponds to the relation $\phi^{^7\mathrm{Be}} = (\phi^{^8\mathrm{B}})^{8/18}$. The exponents 8 and 18 were thought to represent the dependence of the ^{7}Be and ^{8}B neutrino fluxes on the core temperature of the Sun at the time Parke's paper was written. The line is intended to represent a solar model whose core temperature has been allowed to be free in order to fit the observed experimental data. The upper-left plot shows the fit obtained using the experimental data from all three experiments. The upper-right plot shows that obtained from the chlorine and the Kamiokande experiments alone. The lower-left plot shows the fit obtained from the chlorine and gallium experiments, and the lower-right plot shows the fit obtained from the Kamiokande and gallium experiments alone.

Figure 1.8 shows that even if the data from any one type of experiment is excluded, the discrepancy between the standard solar model and the experimental results is 3σ. This relatively small disagreement only occurs if the chlorine data is excluded. If either the Kamiokande data or the gallium data is excluded then the disagreement between the standard solar model and experiment is very much greater. Note that the 'solar model' with a free core temperature is excluded at at least the 2σ level by any two experiments, and at the 3σ level if all three types of experiment are correct.

The standard solar models now reproduce all the observable data about the Sun, including the p-mode oscillations, and it is increasingly unlikely that the solution to the SNP lies in the discovery of a common error or that some important physics has been left out of such models. The three arguments presented in this section, by Castellani *et al.* [36], Bahcall [28], and Parke [37], are intended to demonstrate that there is no simple astrophysical fix available for the solar neutrino problem, nor will the SNP vanish if just one of the terrestrial experiments that has been carried out is incorrect. In the next section some plausible and implausible solutions to the solar neutrino problem will be put forward.

1.6 Solutions to the Solar Neutrino Problem

Solutions to the solar neutrino problem fall into two categories. They are either astrophysical, proposing some general change to the standard solar model that would result in the production of fewer neutrinos, or they arise from particle physics, in which case the number of neutrinos generated by the Sun is assumed to be given correctly by the standard solar model, and some process alters the number of detectable neutrinos between their generation in the Sun and the observation of the neutrino flux at the Earth.

1.6.1 Astrophysical Solutions

Nonstandard solar models range from the unlikely to the ridiculous. In the low Z model, heavy elements which contribute to the opacity in the core of the sun were presumed not to be present there. As a result, radiation escaped the core of the Sun more easily, and it had a lower temperature, and hence lower neutrino fluxes. The model can be rejected on the grounds that it could not reproduce the observed p-mode oscillations, and that there is no known mechanism for depleting the solar core of the heavy elements. Along similar lines, an iron-precipitation model has been proposed. In this model, iron and iron-like elements precipitate out of the plasma in the solar core, and hence no longer contribute to the opacity there, resulting in a lower core temperature just as occurs in the low-Z model. There is no evidence that heavy elements should precipitate out of a stellar plasma. A rapidly-rotating core model has also been proposed. In this model the rapid rotation of the core of the Sun reduces the thermal pressure required to support the star against gravity. The model requires an angular velocity in the core of the Sun which is at least 3 orders of magnitude faster than that at the surface. This model can be discarded on the basis of the p-mode oscillation data which indicates that the angular velocity of the Sun is remarkably uniform with depth. Strong magnetic field models have also been put forward and rejected. Another non-standard solar model is the mixed-up Sun. The neutrino flux increases with the age of the sun as the core temperature rises to compensate for the gradual depletion of hydrogen in the core. In a mixed-up sun, the hydrogen in the core is continually being replaced by mixing, and the temperature remains low. This model founders because there is no known mechanism to keep the Sun's composition homogeneous over its entire lifespan. Other suggested possible non-standard solar models include turbulent diffusion, thermal instabilities (but numerical calculations have shown the standard model to be stable against thermal instabilities) or hydrodynamic phenomena, mass loss, and a central black hole (where a significant fraction of the observed solar luminosity would be supplied by accretion onto a central black hole). These models are discussed by Bahcall [26].

Many of these models rely on a reduction of the core temperature of the Sun, which does not resolve the SNP by itself [36][37]. In addition the new data from observation of the p-mode oscillations in the Sun is sufficiently accurate to eliminate most non-standard solar models. These facts have led Bahcall to remark that non-standard solar models cannot provide a solution to the solar neutrino problem [32][33].

1.6.2 Particle Physics Solutions; Neutrino Oscillations

Several solutions that fall into the realm of particle physics have been proposed. WIMPs (Weakly Interacting Massive Particles) have been proposed as a simultaneous solution to both the solar neutrino problem and the astrophysical problem of missing mass. WIMPs might form a solution to the solar neutrino problem by accreting in the solar core. Once there, if they have the right properties, they modify the energy transport in the solar core. The proposed WIMP provides another mechanism for energy transport from the solar core, and hence has an effect on the neutrino fluxes similar to lowering the opacity. No known particle has the necessary properties to solve the SNP. The most stringent of the requirements is that the scattering cross section be large compared to a typical weak interaction cross section, and that the annihilation cross section be small compared to the scattering cross section ($\sigma_{\text{annihilation}} \leq 10^{-4}\sigma_{\text{scattering}}$). No WIMP has yet been found.

Neutrino flavour oscillations are a natural solution to the solar neutrino problem. Current terrestrial experiments are essentially only sensitive to electron neutrinos, which means that if the ν_e produced in the sun undergo flavour oscillations on the way to the Earth, they would not be detected in another state, such as ν_μ or ν_τ. Vacuum oscillations occur if the weak neutrino production eigenstates are not the same as the vacuum propagation eigenstates. Matter enhanced oscillations are an extension of the idea of vacuum oscillations; in matter all neutrinos suffer neutral current scattering, but only electron neutrinos also undergo charged current scattering. In this way the propagation of electron neutrinos through matter is different from that of the other neutrino flavours, which can enhance the flavour oscillations.

Another possibility has arisen in response to the published results of the LSND experiment [46]. It is the possibility that neutrinos oscillate into at least one sterile flavour, sterile in the sense that the ν_{sterile}

does not interact detectably either in the terrestrial solar neutrino experiments, or in particle accelerators (LEP). This speculative solution has been proposed because otherwise the scenario of flavour oscillations is unable to account for the experimental results. The LSND results are controversial [47], and the sensitivity of the KARMEN experiment [48] will be improved to investigate the LSND result. Sterile neutrinos are extremely difficult to detect experimentally. No further speculation about sterile neutrinos will take place here.

Vacuum Oscillations

Vacuum oscillations [40] occur when the weak flavour eigenstates in which neutrinos are created are not the same as the mass eigenstates in which they are propagated. Consider the restricted case of just two neutrino flavours, ν_e and ν_μ. The mass eigenstates, ν_1 and ν_2, evolve in time according to the usual quantum mechanical prescription; $\nu_k(t) = \nu_k(0)e^{-iE_k t}$, $k = 1, 2$. The flavour eigenstates can be written in the mass basis as orthogonal combinations of mass eigenstates;

$$\begin{pmatrix} \nu_e \\ \nu_\mu \end{pmatrix} = \begin{pmatrix} \cos\theta & \sin\theta \\ -\sin\theta & \cos\theta \end{pmatrix} \begin{pmatrix} \nu_1 \\ \nu_2 \end{pmatrix} , \tag{1.40}$$

and hence the wavefunction of what started as an electron neutrino at time $t = 0$ can be written at time t as;

$$\nu_e(t) = \nu_1 \cos\theta e^{-iE_1 t} + \nu_2 \sin\theta e^{-iE_2 t} . \tag{1.41}$$

The projection of this state onto the electron neutrino flavour eigenstate yields the probability amplitude for finding electron neutrinos. The square modulus of this probability amplitude is the probability of an electron neutrino remaining an electron neutrino;

$$P(\nu_e \to \nu_e; t) = 1 - \sin^2 2\theta \sin^2 \frac{(E_2 - E_1)t}{2} , \tag{1.42}$$

and the corresponding probability for the electron neutrino to oscillate into a muon neutrino is;

$$P(\nu_e \to \nu_\mu; t) = \sin^2 2\theta \sin^2 \frac{(E_2 - E_1)t}{2} . \tag{1.43}$$

If the momentum of the electron neutrino is much greater than the neutrino mass eigenvalues, then the argument $(E_2 - E_1)/2$ can be written $\pi D/L$, where D is the distance travelled by the neutrinos (assuming a velocity of c), and $L = 4\pi p/\Delta m^2$. The approximate relation $E_k = p + m_k^2/2p$ has been used. L is the oscillation length. The survival probability oscillates between 0 and $\cos^2 2\theta$ as D goes from one integer multiple of L to the following half-integer multiple. For $D \gg L$, we replace the distance dependent factor by its average value, which is $\frac{1}{2}$, and the survival probability is then entirely dependent on the mixing angle θ. The survival probability is lowest for maximal mixing, where $\theta = \pi/4$, and $P(\nu_e \to \nu_e; t) = \frac{1}{2}$. In a three flavour basis, the principle behind these results remains the same, and the averaged survival probability is $\frac{1}{3}$ rather than $\frac{1}{2}$.

The vacuum oscillations solution to the solar neutrino problem is not favoured. This is because the mixing angles required to solve the solar neutrino problem are much larger than the mixing angles found in the quark sector. The MSW effect, which will be discussed next, does not suffer from this theoretical prejudice.

The MSW Effect: Matter Enhanced Oscillations

The Mikheyev-Smirnov-Wolfenstein (MSW) effect was developed by Mikheyev and Smirnov [38] from an idea originally proposed by Wolfenstein [39]. That idea was matter enhanced neutrino oscillations. When neutrinos pass through matter, they undergo coherent forward scattering from ordinary matter, and therefore acquire a refractive index. All flavours scatter through exchange of a neutral Z^0 boson, but only the electron neutrino also scatters via the charged $W^\pm$ boson. Due to the additional scattering interaction, the electron neutrino will have a different refractive index from the other flavours, and hence will acquire a relative phase in its passage through matter.

The effective Hamiltonian for the interaction of electron-neutrinos with electrons in matter is written;

$$H_{\text{effective}} = \frac{G_F}{\sqrt{2}} (e^\dagger \gamma_4 \gamma_\mu (1 + \gamma_5) \nu_e)(\nu_e^\dagger \gamma_4 \gamma_\mu (1 + \gamma_5) e)^\dagger . \tag{1.44}$$

In the rest frame of the electron the expression for the effective Hamiltonian, identifying the squared-modulus of the electron wavefunction as the number density of electrons, becomes;

$$H_{\text{effective}} = \sqrt{2} G_F N_e \ . \tag{1.45}$$

The ultra-relativistic vacuum propagation Hamiltonian for the vacuum eigenstates can be written;

$$i\frac{d\nu_k}{dt} = \left(p + \frac{m_k^2}{2p}\right)\nu_k \ . \tag{1.46}$$

Expressing the ν_k eigenstates in the flavour basis, retaining only terms that result in phase differences between the flavour eigenstates, and adding the effective matter oscillation Hamiltonian, the flavour Hamiltonian is;

$$i\frac{d}{dt}\begin{pmatrix}\nu_e\\ \nu_\mu\end{pmatrix} = \begin{pmatrix} \frac{m_1^2\cos^2\theta + m_2^2\sin^2\theta}{2p} + \sqrt{2}G_F N_e & \frac{m_2^2 - m_1^2}{2p}\cos\theta\sin\theta \\ \frac{m_2^2 - m_1^2}{2p}\cos\theta\sin\theta & \frac{m_1^2\sin^2\theta + m_2^2\cos^2\theta}{2p} \end{pmatrix}\begin{pmatrix}\nu_e\\ \nu_\mu\end{pmatrix} \ . \tag{1.47}$$

The solution for a constant density has the same form as that for the case of vacuum oscillations alone;

$$P(\nu_e \to \nu_e; D) = 1 - \sin^2 2\theta_M \sin^2(\pi D/L_M) \ , \tag{1.48}$$

where;

$$\sin^2 2\theta_M = \frac{\sin^2 2\theta}{\sin^2 2\theta + (L/L_0 - \cos 2\theta)^2} \ , \tag{1.49}$$

$$L_M = \frac{L}{\sqrt{\sin^2 2\theta + (L/L_0 - \cos 2\theta)^2}} \ , \tag{1.50}$$

$$L = \frac{4\pi p}{\Delta m^2} \ , \tag{1.51}$$

$$L_0 = \frac{\sqrt{2}\pi}{G_F N_e} \ . \tag{1.52}$$

This formula for the mixing angle in matter has two important properties. Firstly, no matter how small the neutrino mixing angle is, maximal mixing in matter is reached when $L/L_0 = \cos 2\theta$. Secondly, when maximal mixing is achieved, the oscillation length is now much greater than that in vacuo; $L_M = L/\sin 2\theta$. Note that in regions of high density such that $N_e \gg \Delta m^2/2\sqrt{2}G_F p$, the matter oscillations are suppressed rather than enhanced. The oscillation resonance is shown in Figure 1.9.

In the solar interior, the density of neutrinos decreases away from the core of the sun. Qualitatively, for solar neutrinos with a given energy E, a layer may exists inside the Sun in which resonant oscillations can take place. This layer is characterised by a critical density, ρ_c;

$$\rho_c \sim 10^7 \frac{\Delta m^2}{E}\cos 2\theta \ . \tag{1.53}$$

Electron neutrinos passing through a region where the electron density varies slowly from $\rho > \rho_c$ to $\rho < \rho_c$ will be almost completely converted to muon neutrinos, assuming they are next in the neutrino mass hierarchy, and that the τ mass is too heavy for resonant conversion in the sun. This is the adiabatic MSW effect. The change of state is illustrated in Figure 1.10. For the case of solar neutrinos, the solar central density of 150g cm^{-3} and the hydrogen fraction of 36% imply that there will be a critical value of $E_\nu/\Delta m^2$ of 10MeV/10^{-4}eV^2, above which all the electron neutrinos convert to muon neutrinos. Below this critical value, the central density of the sun is less than ρ_c and no conversion takes place. If the ratio of $E/\Delta m^2$ is much greater than that required to produce neutrino oscillations in the solar core, then the conversion will take place in the outer layers of the sun where the electron density is falling exponentially. In this case the conversion will not be complete, and the rate of conversion will fall with increasing neutrino energy. This is the non-adiabatic MSW effect. A plot of survival probability is shown in Figure 1.11, where the the effect of resonant conversion can be anticipated by sliding a window in $E/\Delta m^2$ from low E (below the threshold for adiabatic conversion) to high E, the window being bounded at its lower limit by an experimental threshold, and at its upper limit by the upper limit of the neutrino energy spectrum.

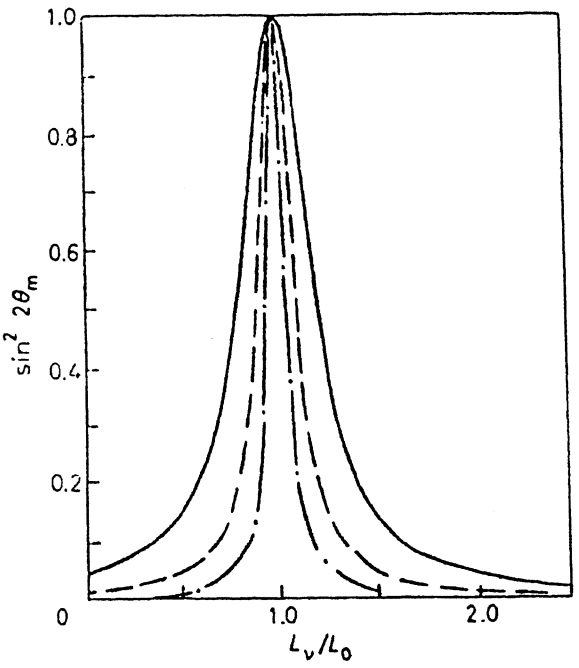

Figure 1.9: The dependence of the oscillation depth, $\sin^2 2\theta_M$, on L/L_0, for $\sin^2 2\theta = 4 \times 10^{-2}$ (solid line), $\sin^2 2\theta = \times 10^{-2}$ (dashed line), $\sin^2 2\theta = 2.5 \times 10^{-3}$ (dashed-dot line). The plot is taken from [38].

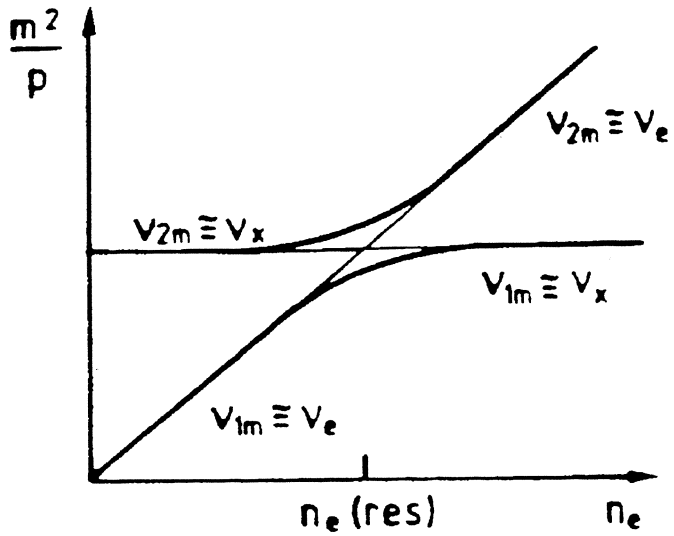

Figure 1.10: A ν_e created in a region of high density (the core of the sun) converts to a ν_μ upon travelling to regions of lower density.

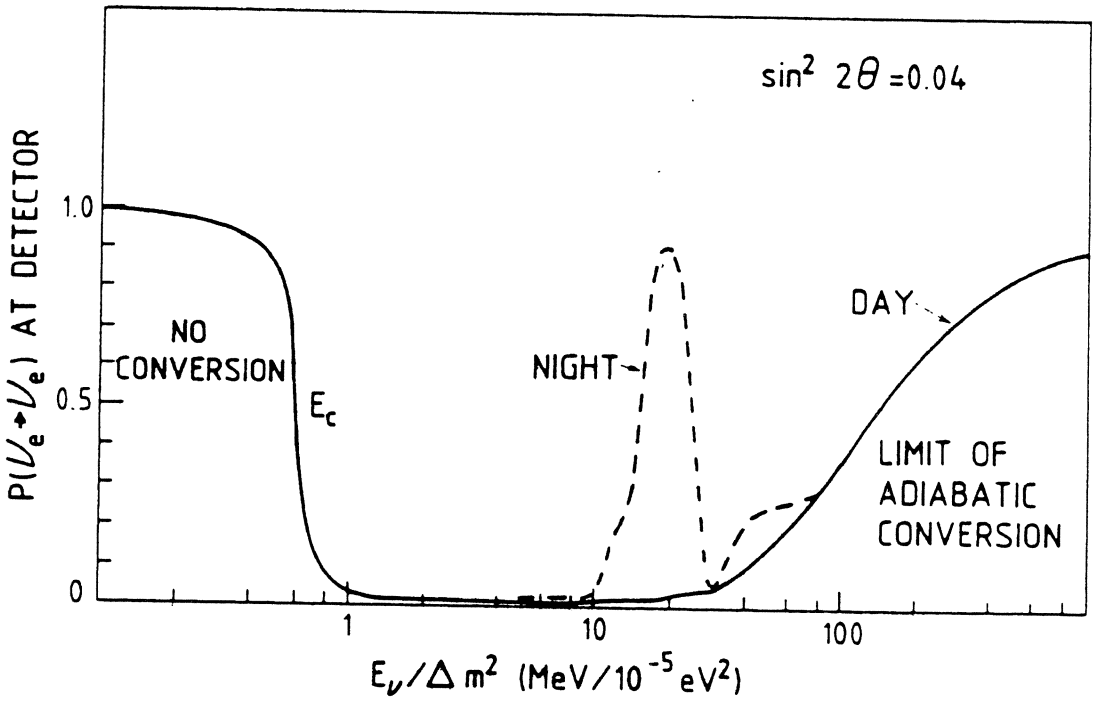

Figure 1.11: The fraction of ν_es created in the sun which reach the detector unchanged is shown as a function of $E/\Delta m^2$ for $\sin^2 2\theta = 0.04$ [83]. For some values of $E/\Delta m^2$, a significant day-night effect can be observed.

The Earth is a large body of reasonably constant electron density. Matter enhanced oscillations may occur in the Earth, giving rise to a day/night effect. These effects are particularly important when $\sin^2 2\theta > 0.04$ and $\Delta m^2 \sim 10^{-5}\text{eV}^2$. The day/night effect is shown in Figure 1.11. Figure 1.12 shows the allowed and excluded regions in the Δm^2, $\sin^2 2\theta$ phase space from the experimental results reported so far.

1.7 The Future of Solar Neutrino Physics

The standard solar model now reproduces the observable properties of the Sun, other than the neutrino fluxes, very well. The evidence against non-standard solar models or an astrophysical solution to the solar neutrino problem is mounting as the number of solar observables a solar model must reproduce rises. Four terrestrial solar neutrino experiments exist, using three different targets. The experimental results, taken at face value, suggest an energy dependent suppression of the neutrino flux at the Earth. The MSW effect is a natural physical solution to the SNP, requiring only that neutrinos, which have been thought massless until now, have a small mass, and that the weak eigenstates of neutrino production are not the mass eigenstates of neutrino propagation.

The future of solar neutrino physics lies in conducting experiments which can demonstrate the existence or non-existence of neutrino oscillations, particularly the MSW effect, and hence indicate whether the solution to the SNP lies in the realm of particle physics or astrophysics. To this end, the next generation of solar neutrino experiments is intended to make the following measurements;

1. a measurement of the ratio of the ^{8}B electron neutrino flux to the flux of all neutrino types. If this ratio is not one, then it will provide clear evidence for flavour oscillations;

2. a measurement of the spectral shape of the ^{8}B neutrinos. A distortion from the expected shape could provide evidence for the MSW effect;

3. an accurate measurement of the time dependence of all the neutrino fluxes. A day-night time

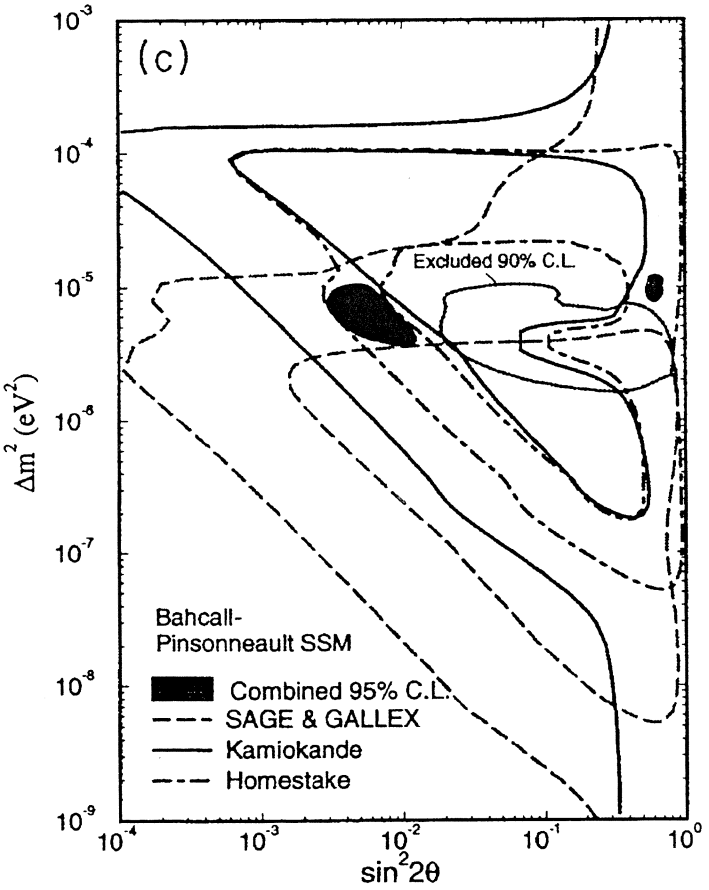

Figure 1.12: The MSW exclusion plot, showing the regions allowed and excluded by the experimental results [6].

dependence would indicate electron neutrino regeneration in the Earth. A minimal seasonal variation is expected due to the elliptical orbit of the Earth - greater variations would indicate vacuum oscillations or might be the result of a neutrino magnetic moment; and,

4. a measurement of the ^{7}Be neutrino flux, to determine its MSW suppression.

All the future solar neutrino detectors have the property that they will collect as many solar neutrino events in two months as have been observed in the previous 25 years of experimentation!

The Super Kamiokande detector is a 50000 tonne water Čerenkov detector with a fiducial volume of 23000 tonnes. Observing it are 11200 50cm diameter photomultiplier tubes with a coverage of about 40%. The PMTs are mounted in a frame about 3m inside the walls of the cylindrical container, so the inner volume monitored by the PMTs is about 32000 tonnes. The detector inner volume is surrounded by an anticounter with 1800 PMTs. The energy threshold in Super Kamiokande is intended to be 5MeV, lower than in its predecessor (7MeV), and the energy resolution will also be improved (14% at 10MeV instead of 20%). Neutrinos will be detected at a rate of 27 per day, assuming a 5MeV threshold. The Super Kamiokande detector began taking data with an analysis energy threshold at 7MeV on April the 1st of 1996. The first results are eagerly awaited.

The results from the first four solar neutrino experiments (chlorine, Kamiokande, and the gallium experiments, SAGE and GALLEX) suggest that the flux of the ^{7}Be electron neutrinos is very much less than the standard model prediction. The Borexino detector [18] has been designed to have a low enough threshold to observe the 0.86MeV ^{7}Be neutrinos directly. The detector is envisaged to be a 300 tonne liquid scintillator in an acrylic vessel surrounded by a 2m thick water shield. The fiducial volume will be viewed by 1700 20cm diameter PMTs fitted with reflectors, which will provide an effective photocathode coverage of $\sim$ 50%. The detector will have a threshold of 250keV, and is primarily sensitive to elastic scattering by the ^{7}Be neutrinos. The rate in the detector will be high ($\sim$ 50 events per day with the

planned energy threshold). Contamination by radioisotopes in the Borexino detector must be kept to an extremely low level, lower even than acceptable levels in the SNO detector. This is because the ^{7}Be neutrino energy is very close to that obtained from the decay of the naturally occurring radioisotopes of uranium, thorium, potassium, and carbon. ^{238}U and ^{232}Th concentrations of 10^{-16}g/g are required, with ^{40}K at the 10^{-14}g/g level. The Borexino detector is planned to be active in 1999.

An iodine detector is planned to be situated in the Homestake mine, near the ongoing chlorine based detector. One 23 tonne module has already been placed in the mine, and five more are to be installed. The iodine radiochemical detector will be very similar in principal to the chlorine detector upon which it is based, however the sensitivity provided by ^{127}I is about 10 times higher per ton than that provided by Cl, and includes a larger ^{7}Be sensitivity. In addition, the detection signature of ^{127}Xe is more distinct than that of ^{37}Ar, and should therefore have a lower inherent background.

The ICARUS collaboration plans to install the first 600 tonne module of their detector in Gran Sasso in 1999. It will observe the neutrino-electron elastic scattering reaction, and electron-neutrino absorption on argon via the emitted recoil electron. The ultimate objective of the ICARUS collaboration is to use up to 5000 tonnes of liquid argon for the detection of proton decay and long baseline neutrino experiments.

HERON (HElium ROton detection of Neutrinos) is intended to observe about 20 events per day in a 10 tonne liquid helium module. The events are from the pp and ^{7}Be neutrino flux. The HERON project has operated small prototype detectors and observed the production of rotons from an ^{241}Am source.

The Hellaz collaboration has been operating a small prototype gaseous helium time projection chamber to demonstrate the feasibility of detecting the pp neutrino spectrum. Ultimately, the collaboration hope to operate two 4 tonne detectors which would provide 2500 pp and 1500 ^{7}Be elastic scattering neutrino events per year.

The Sudbury Neutrino Observatory is a 1000 tonne heavy-water Čerenkov detector that will simultaneously measure charged and neutral event rates in order to determine both the electron neutrino flux and the total neutrino flux through the detector, as well as measuring the ^{8}B electron neutrino energy spectrum. The author of this thesis has worked on aspects of the SNO experiment for 3 years, and a more complete description of the SNO experiment will be given in the next chapter.

The field of solar neutrino physics has grown considerably in the last $10 - 15$ years. This growth in the field reflects the fact that for neutrinos of very low mass ($< 10^{-6}$eV), the observation of neutrino oscillations in solar neutrino experiments is the only plausible method for confirming that neutrinos have mass at all.

Chapter 2

The Sudbury Neutrino Observatory

The main aims of the Sudbury Neutrino Observatory (SNO) experiment are;

1. to measure the charged current to neutral current event rate ratio, and hence infer the ratio of the electron neutrino flux to the total neutrino flux through the detector;
2. to measure the charged current energy spectrum, and to look for possible distortions in that spectrum due to neutrino oscillations.

The simultaneous measurement of the charged and neutral current rates is a measurement which can only be made in the SNO detector. The significance of this measurement cannot be overstated; if the electron neutrino flux is less than the total neutrino flux (a charged current to neutral current ratio of less than 1) then neutrino flavour oscillations will have been observed.

To achieve these aims, the SNO experiment requires a high count rate (large active volume), and low background rates (high material purities). This is typical of next-generation solar neutrino experiments. Much of the data contained in the chapter is extracted from the SNO Proposal documents [83][84], and the reader is referred to them for additional information.

2.1 The Design of the Detector

The SNO detector is situated in shaft number 9 of the INCO nickel mine in Sudbury, Ontario. The shaft is the second deepest continuous shaft in the western world, making it an ideal site for a neutrino experiment because of the impressive overburden of rock that shields the observatory from cosmic rays. The experiment is housed in a purpose-excavated section of the mine which is separated from the active mining operation by air-locks. Schematics of the mine showing the SNO experiment are shown in Figure 2.1 and Figure 2.2. The cavity housing the experiment is 30m high and 21.4m in diameter. It is 2070m below the surface, and a distance 1200m from the mine shaft. The site for the experimental cavity has been chosen in hanging wall rock since it is composed of norite, which has lower uranium and thorium content than the rock making up the footwall, and because its homogeneous nature simplified the construction of the cavity.

The SNO detector is a water Čerenkov detector containing 1000 tonnes of heavy water as the target material. A schematic cross section of the detector is shown in Figure 2.2. The heavy water is better than reactor grade; it contains 99.92% D_2O by mass. The low hydrogen content reduces the probability that a neutron will capture on hydrogen in the heavy water ($\sigma_c = 330$mb) rather than deuterium ($\sigma_c = 0.46$mb) to $\sim 37\%$. It will be contained within a spherical shell of acrylic (the acrylic vessel) whose average thickness is ~ 5.5cm and whose inner diameter is 12m. The acrylic vessel is constructed from rectangular tiles and it is being bonded in situ. It is transparent to ultraviolet light (a 5MeV γ-ray just inside the acrylic vessel produces $\sim \frac{3}{4}$ of the number of PMT hits of a 5MeV γ-ray just outside it). At the time of writing, 1st November 1996, the upper half of the vessel has been constructed. The acrylic vessel will be suspended from the support platform constructed 30m above the cavity floor by 10 VECTRAN ropes. The support platform will also house the detector's data acquisition electronics and calibration equipment. The vessel will be surrounded and observed by approximately 9600 photomultiplier tubes (PMTs) equipped with light concentrators, positioned approximately isotropically about the D_2O target. The light concentrators increase the effective photocathode coverage to $\sim 60\%$ and serve to prevent light generated by radiations in neighbouring PMTs from being detected. The vertical component of the Earth's magnetic field has been reduced to $\leq 0.2\mu$T by coils built into the wall of the cavity. This

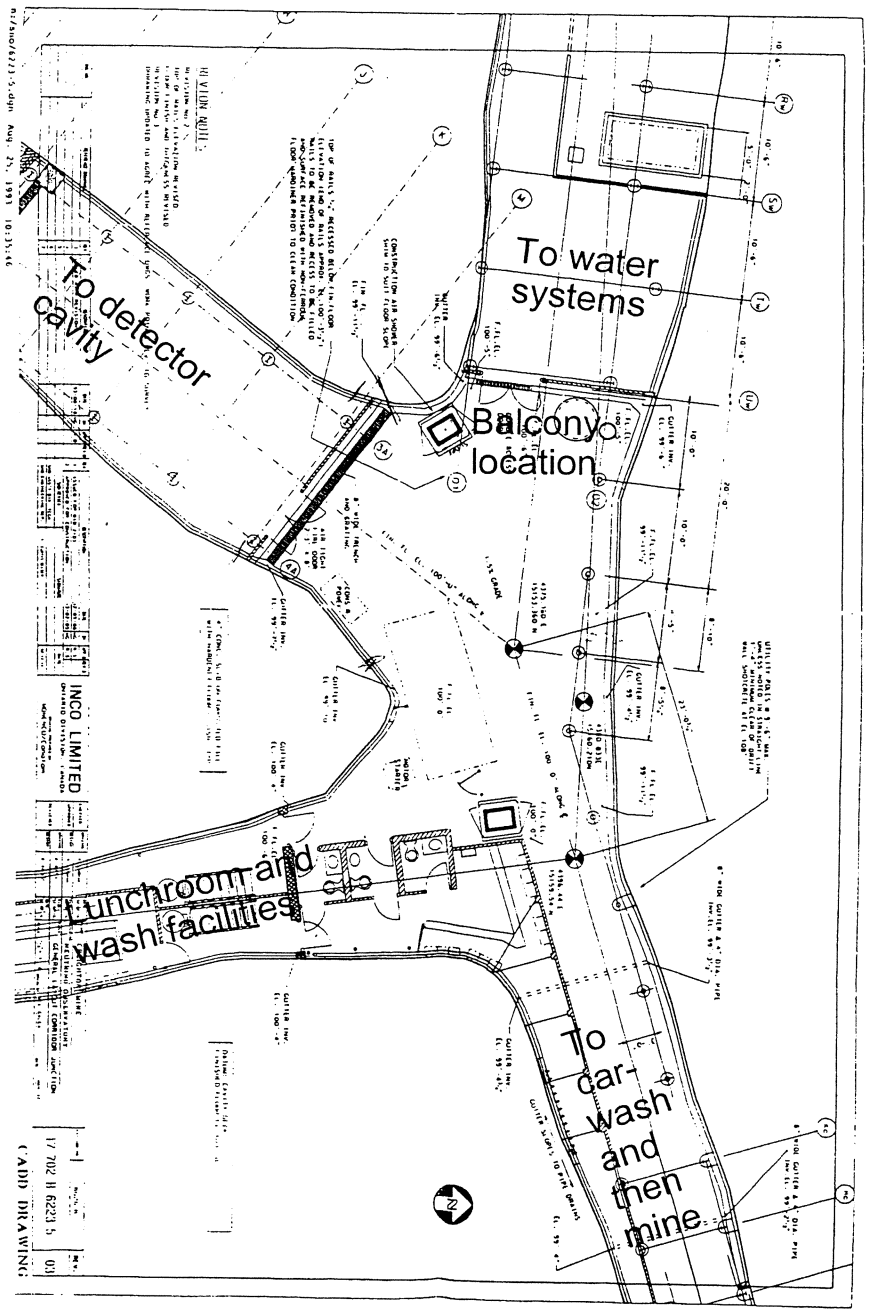

Figure 2.1: Map showing the internal layout of the SNO experiment. The map is centred on the 'Picadilly Circus' location.

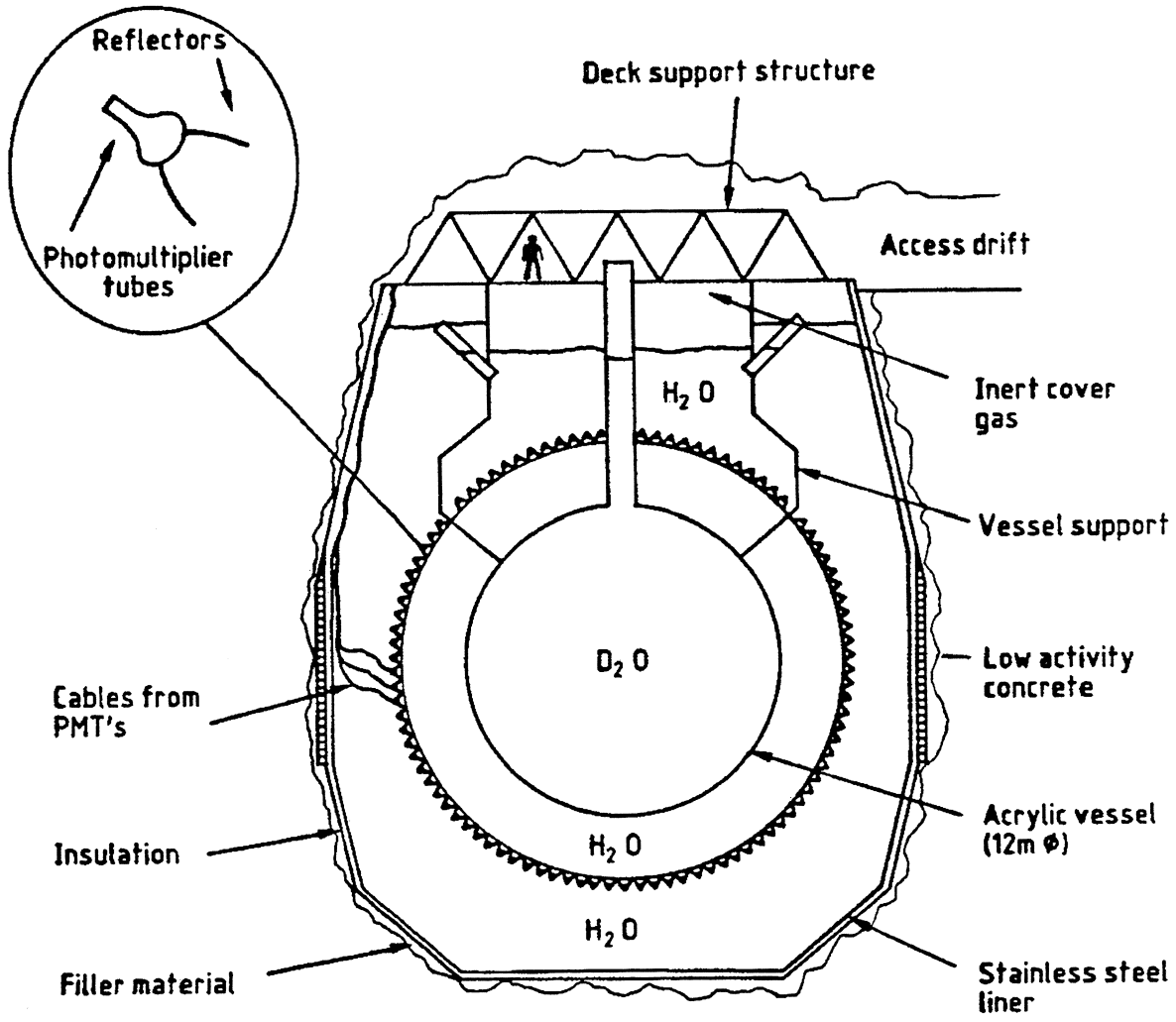

Figure 2.2: Schematic cross section of the SNO detector.

minimises the effect of a PMT's orientation upon its performance. The PMTs and the concentrators are discussed in detail in Chapter 3. The PMTs are held in place by the PSUP (the PMT support structure), and are a radial distance of $\sim$ 2.5m from the acrylic vessel. The upper half of the PSUP has been constructed, and the PMTs within it have been cabled.

During the detector's operation, the whole cavity will be immersed in 7300 tonnes of ultrapure light water, which will both support the weight of the acrylic vessel and form a radiation shield. The water will be maintained at 10°C to reduce PMT noise, inhibit biological activity, and keep the D_2O near its density maximum. The role of the light water as a shield is twofold; it will shield the PMTs from neutrons and γ-rays emanating from the rock wall 3m from the PSUP that encloses the cavity containing the experiment, and it will shield the heavy water from the same radiations emitted from radioisotopes in the PMTs and PSUP, and the PMT glass envelopes in particular. The PSUP is designed as a $> 99.99\%$ impermeable membrane to ensure a constant water flow, from the acrylic vessel side outward. This is intended to carry contaminants leached from the PSUP away from the acrylic vessel.

2.1.1 The Detector Response

The 9600 PMTs that observe the SNO detector are sensitive to Čerenkov radiation emitted by high energy electrons within the PMT sphere. A signal or background event that is reported by the PMTs in the SNO detector is usually one of 3 types (overleaf);

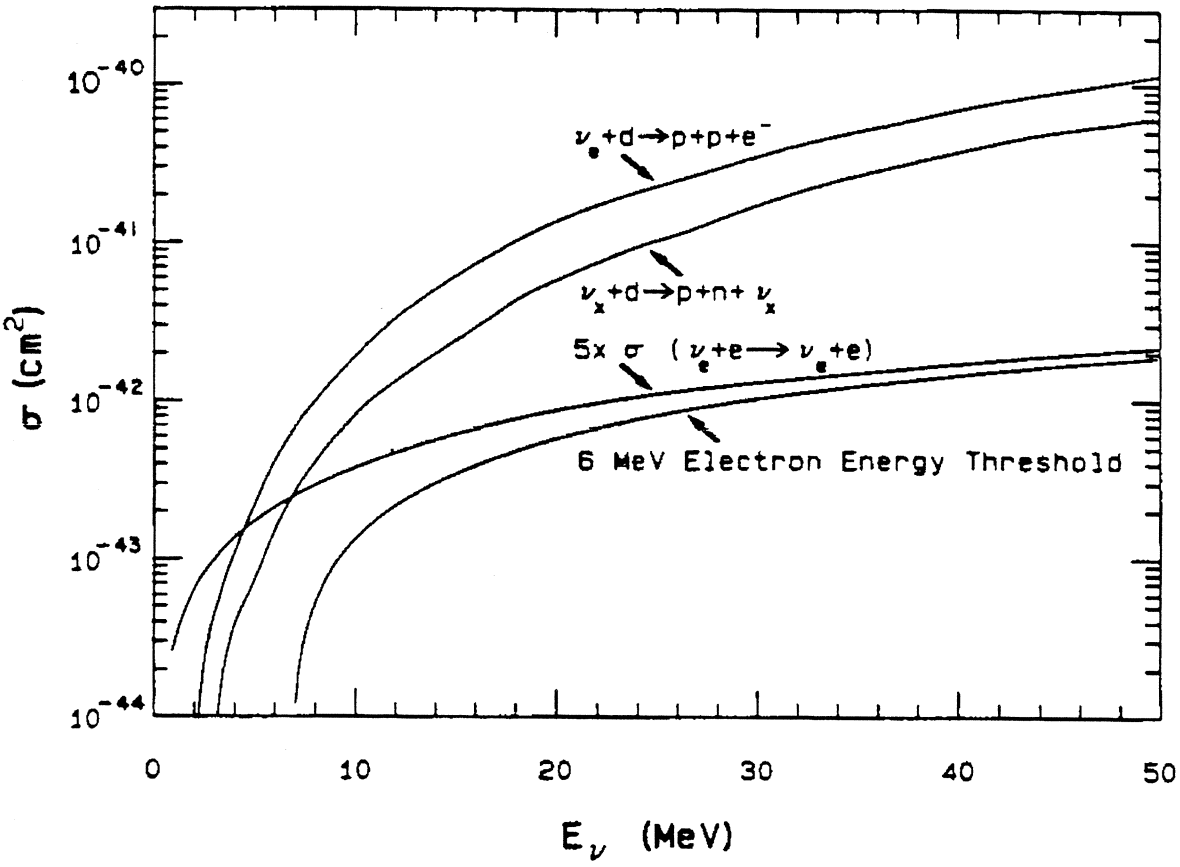

Figure 2.3: The cross sections for the principal reactions in the SNO experiment.

1. Čerenkov radiation from a high energy electron; or,
2. a high energy γ-ray which produces one or more high energy electrons, mainly through Compton scattering; or,
3. a combination electron/γ-ray event (β-γ events are common in the SNO detector).

Muon events also occur. The emission of Čerenkov radiation will be discussed in Section 2.4.1. The hardware threshold in the SNO detector will be set as low as the resulting rate of data acquisition permits; it is thought that a hardware threshold between 10 and 20 hit PMTs can be achieved. It is known that an analysis threshold of 60 hit PMTs (a 60 hit threshold) is essentially background free for any reasonable estimate of the background rates in SNO (see Section 2.5 for a discussion of the backgrounds in the SNO detector).

Event fitting is an important mechanism for the identification and rejection of backgrounds. Fitting an event is complicated by the timing jitter of the PMTs ($\sim$ 1.5ns, see Chapter 3), the scattering of photons en route to the PMTs (Rayleigh scattering and Fresnel scattering are the dominant effects but Mie scattering - scattering from small particles in the water - has yet to be quantified), and a noise rate in each PMT of 1 $\rightarrow$ 2kHz. Current event fitters are capable of achieving a position resolution of about 30cm and a direction resolution of about 30° with Monte Carlo data [122]. Event fitting and event classification have been extensively discussed [122][59][57][58].

2.2 Signals of the Solar Neutrino Flux

Neutrinos interact in the detector through the weak charged and neutral currents. The cross sections for the principal interactions are shown in Figure 2.3. The rates for these interactions in SNO for a number of proposed solutions to the solar neutrino problem are shown in Table 2.1. The diagnostic power of the SNO detector, with its capability to observe both neutral current and charged current events is evident, as is the advantage to be gained by the addition of salt to the heavy water in the detector.

Scenario	d(ν_e, e^-p)p	e^-(ν_x, ν_x)e^-	d(ν_x, ν_xn)p	
Raw Rate	14200	5970	5480	
SSM	8832	1206	474	2413*
SSM / 3	2944	402	158	804*
MSW	3400	535	474	2413*

Table 2.1: The expected event rates in 1 year in the SNO detector. The raw rate is the SSM rate in the SNO detector, regardless of detector efficiency or thresholds. The SSM rate is the raw rate, subject to a 60 hit threshold and a 7 meter fiducial volume. SSM / 3 is the scenario in which the solution to the SNP is astrophysical, subject to the same cuts. The MSW effect shows the expected rate for the most likely MSW solution. The cuts have again been applied. The * indicates the number of neutral current events passing the NHIT and fiducial cuts when 2 tonnes of $MgCl_2$ is added to the D_2O. The rates were calculated using data from [83] and work by Brice [122]. The neutron capture probabilities implied in this table will be discussed in Chapter 9.

2.2.1 The Charged Current (or CC) Interaction

Electron neutrinos from the sun can be detected in SNO through a charged current interaction;

$$\nu_e + \mathrm{d} \rightarrow \mathrm{p} + \mathrm{p} + e^- \ . \tag{2.1}$$

The threshold for this interaction is 1.44MeV. The light mass of the electron and the distribution of possible kinematic final states mean that the electron's energy is essentially $E_{\nu_e} - 1.44\mathrm{MeV}$. In addition the direction of the electron is correlated to the direction of the incident neutrino with an angular distribution given by $f(\theta) = 1 - \frac{1}{3}\frac{v}{c}cos\theta$. The charged current reaction will be detected through the Čerenkov radiation emitted by the electron in the final state. The cross section for the interaction of ^{8}B neutrinos, averaged over the neutrino energy spectrum from the standard solar model, is [43];

$$\langle\sigma(^8\mathrm{B})\rangle = 1.15 \times 10^{-42}\mathrm{cm}^2 \ , \tag{2.2}$$

whilst the cross section for hep neutrinos averaged over the SSM neutrino energy spectrum is [43];

$$\langle\sigma(\mathrm{hep})\rangle = 2.97 \times 10^{-42}\mathrm{cm}^2 \ . \tag{2.3}$$

2.2.2 The Electron Scattering (or ES) Interaction

Neutrinos of all flavours can be detected in SNO when they undergo electron scattering;

$$\nu_x + e^- \rightarrow \nu_x + e^- \ . \tag{2.4}$$

This reaction can be identified because the struck electron is predominantly scattered in the forward direction, as was observed in the Kamiokande detector (see Chapter 1). The cross section is [34];

$$\frac{d\sigma}{dE_e} = \frac{2G_v^2 m_e^2}{\pi\hbar^4}\left[g_L^2 + g_R^2\left(1 - \frac{E_e}{E_\nu}\right)^2 - g_L g_R \frac{E_e}{E_\nu^2}\right] \ , \tag{2.5}$$

where E_e is the final state energy of the electron, E_ν is the initial energy of the incident neutrino, $g_L = \pm\frac{1}{2} + \sin^2\theta_W$, $g_R = \sin^2\theta_W$, and $\sin^2\theta_W = 0.23$. Electron neutrinos take the upper sign in g_L, muon and tau neutrinos take the lower. Radiative corrections, of the order of several percent, have been neglected. The electron direction in the final state is closely correlated to the neutrino direction in the initial state; at 5MeV 90% of the electrons are within a cone of half angle $\sim 15°$ about the initial neutrino direction, at 10MeV the opening half angle of the cone has fallen to $\sim 7°$ [24]. The electron scattering cross section is higher for electron neutrinos than for muon or tau neutrinos ($\sigma_{\mathrm{ES}}(\nu_e) \sim 7\sigma_{\mathrm{ES}}(\nu_\mu, \nu_\tau)$) because electron neutrinos may scatter through the exchange of a $W^\pm$ boson, as well as through the usual Z^0 channel (see Figure 2.4). Electron scattering will be detected through the Čerenkov radiation emitted by the scattered electron.

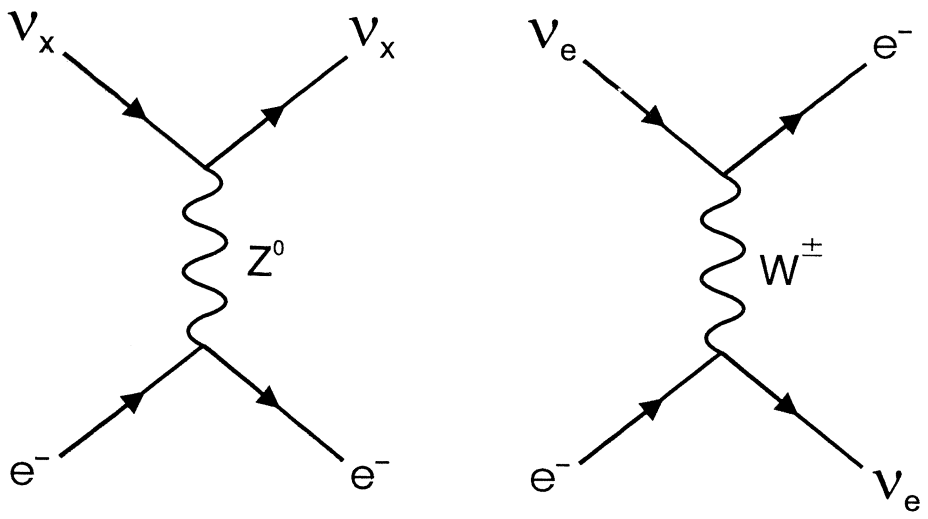

Figure 2.4: Neutrinos of all flavours can scatter from electrons via the exchange of the Z^0 boson, but only electron neutrinos can scatter via the exchange of a $W^{\pm}$ boson.

Reaction	Doi *et al.* [42]	Ying *et al.* [43]	Bahcall *et al.* [44]
$\langle\sigma(^8\mathrm{B})\rangle$	$4.65 \times 10^{-43}\mathrm{cm}^2$	$4.44 \times 10^{-43}\mathrm{cm}^2$	$4.1(1 \pm 0.1) \times 10^{-43}\mathrm{cm}^2$
$\langle\sigma(\mathrm{pep})\rangle$	$1.21 \times 10^{-42}\mathrm{cm}^2$	$1.24 \times 10^{-42}\mathrm{cm}^2$	$1.15(1 \pm 0.1) \times 10^{-42}\mathrm{cm}^2$

Table 2.2: Theoretical estimates of the neutral current cross section, averaged over the SSM neutrino energy spectrum.

2.2.3 The Neutral Current (or NC) Reaction

Neutrinos of all flavours are capable of the disintegration of the deuteron via the exchange of the Z^0 boson;

$$\nu_x + \mathrm{d} \rightarrow \nu_x + \mathrm{p} + \mathrm{n} \; . \tag{2.6}$$

The threshold for the neutrino disintegration of the deuteron is 2.22MeV. The 3 neutrino flavours are all equally likely to disintegrate the deuteron; the reaction is flavour blind. Estimates of the reaction cross section are contained in Table 2.2. None of the products of the neutral current reaction are directly observed in the SNO detector. The reaction is observed indirectly through the capture of the neutron after thermalisation has taken place. The thermalisation of the neutron eliminates any correlation between the initial state neutrino energy and direction and those of the neutron. An observable capture will take place on either chlorine or deuterium (an (n,γ) capture), or in ^{3}He proportional counters (an (n,p) capture).

The neutral and charged current cross sections for the deuteron disintegration are subject to an uncertainty of $\sim$ 10%. Details about the charged current cross section can be found in Bahcall and Ulrich [25] or Bahcall and Ellis [85], while the calculation of the neutral cross section and its error has been carried out by Bahcall *et al.* [86]. The $\sim$ 10% uncertainty of the cross sections is due to the difficulty of evaluating the nuclear matrix elements involved in the calculation. In the aforementioned papers, the errors on the cross sections are estimated in part by repeating the calculation using a number of different nuclear potential models. In [86], Bahcall, Kubodera and Nozawa demonstrate that the ratio of the cross sections is much better determined than either of the cross sections themselves. They do this by demonstrating that the ratio varies very little with their choice of nuclear potential models (and hence nuclear wavefunctions). The ratio of these two cross sections is remarkably free of error, and Bahcall *et al.* [86] estimate that error to be $\pm$0.5%.

Deuterium (n,γ) Capture

In the initial phase of operation, the detector will be in its simplest configuration, that of pure D_2O. In this mode of operation only about 30% of the neutrons will capture on deuterium, yielding a single 6.5MeV γ-ray;

$$n + d \rightarrow t + \gamma \ , \tag{2.7}$$

and of those capturing on deuterium, only 30% are detectable above a 60 hit threshold. Neutrons not capturing on deuterium capture mainly on hydrogen (60%, (n,γ), E_γ = 2.2MeV) and ^{16}O (5%, (n,γ), $E_\gamma = 3.271, 0.870$MeV) and ^{17}O (4%, (n,α)), none of which produce enough Čerenkov radiation to be observed in SNO above a 50 hit detector threshold. The capture estimates given here and in the next section will be justified in Chapter 9.

Chlorine (n,γ) Capture

Once the operation of the detector has stabilised (meaning that acceptable levels of water purity have been reached, and transient radioactivity subsided) and a pure D_2O data set has been taken, either salt or the neutral current detectors will be put into the heavy water. In the salt option, 2 tonnes of $MgCl_2$ will be dissolved in the heavy water (see Chapter 9). Chlorine has a high thermal (n,γ) capture cross section of 33.34b which yields an average of 2.6 γ-rays with a total energy of 8.6MeV. When 2 tonnes of $MgCl_2$ is distributed uniformly throughout the D_2O, 86% of the NC neutrons capture on chlorine or deuterium, in the ratio 27.4:1, and 45% of such captures lead to 60 hits or more in the detector. The (n,γ) captures on both D and Cl are observed through the Čerenkov radiation emitted by high energy electrons that have been produced by γ-rays from the capture interaction itself. The dominant interaction for high energy γ-rays is Compton scattering, but pair production and the photoelectric effect also take place.

A neural net technique has been used to categorise events in the SNO detector [122]. The pattern recognition algorithm upon which this technique relied has been shown to be able to distinguish, on a statistical basis, events in the detector involving just one high energy electron and events involving more than one. The reason for this has been understood; single electron events have a hit pattern which is less isotropic that multiple electron events [59]. The sensitivity of this technique to systematic effects is as yet not fully investigated, nor has it been demonstrated that the distributions required can be obtained by calibration; however it seems likely from the Monte Carlo studies that it will be possible to distinguish distributions of charged current events (single electron events) and neutron capture in salt (multiple electron events).

The ^{3}He Proportional Counters

The ^{3}He proportional counters, or 'neutral current detectors', nickel cylinders containing a ^{3}He-xenon-methane counter gas, detect neutrons via the reaction;

$$^3He + n \rightarrow p + {}^3H, \ Q = 0.764\text{MeV} \ . \tag{2.8}$$

The cross section for this reaction is 5327b. The counters are 5cm in diameter, and will be hung throughout the detector on a 1m grid; they are buoyant and anchored to the floor of the detector. The array contains $\sim$ 900m of nickel tubing, 0.4mm thick. Pulse shape discrimination will be used to eliminate the background from α and β particles. The overall efficiency for the identifiable capture of a neutron in the proportional counters is $\sim$ 42%. The major advantage of the introduction of neutral current detectors into the heavy water over the introduction of salt is that the NC detectors are able to identify neutrons with a unique signature. The major disadvantages are the possible introduction of uranium and thorium into the detector as part of the detectors, and the reduced sensitivity of the detector to the charged current interaction (the NC detectors slightly block the passage of Čerenkov photons to the PMTs in a position dependent way). Neutral current detectors and the salt option are complementary methods for determining the neutral current rate in the SNO detector, and it is proposed that both will be used.

The Poison Option

Figure 2.5 shows the shape of the ν_e energy spectrum for two favoured MSW scenarios. The difference in shape is negligible above $\sim$ 7.5MeV. Below 5MeV, the β-γ background in the SNO detector will render any measurement impossible. These limits define a window of opportunity. Assuming that the β-γ background is not significant in the 5 $\rightarrow$ 7.5MeV region, the major background to the measurement of

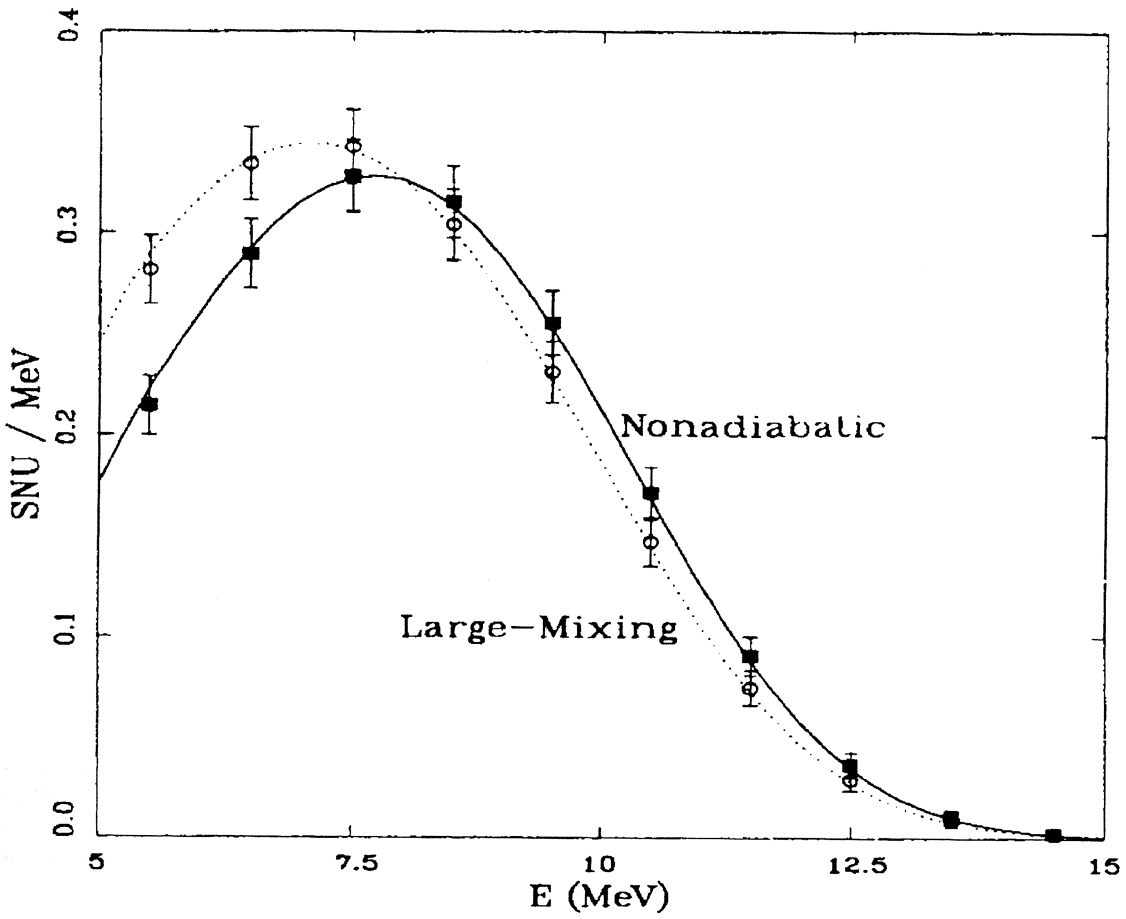

Figure 2.5: The ν_e energy spectrum for two favoured MSW scenarios.

the shape of the charged current energy spectrum is the neutral current interaction. The NC energy spectrum is approximately Gaussian, and peaks at $\sim$ 5.5MeV with 2 tonnes of $MgCl_2$ added to the D_2O (the great majority of neutron captures are then the $^{35}Cl(n,\gamma)^{36}Cl$ reaction), and at $\sim$ 4.5MeV otherwise (in the absence of chlorine in the detector, n-captures are only detected via the $^2H(n,\gamma)^3H$ reaction).

To reduce the neutral current event rate in the detector, the addition of a neutron poison, $LiNO_3$, has been proposed [60]. $LiNO_3$ is known as a neutron poison because ^6Li possesses a very large (n,α) cross section of 946.6b, and this reaction does not produce Čerenkov light in the detector. Moorhead *et al.* estimate that 300kg of 95% ^6Li enriched lithium nitrate would have to be added to the heavy water to reduce the incidence of $d(n,\gamma)t$ reactions to $\frac{1}{100}$ the rate of (n,γ) reactions on deuterium in pure D_2O. This would allow the most sensitive measurement of the CC energy spectrum, but no measurement of the charged to neutral current ratio would be possible, and the detector's sensitivity to a supernova event would be severely reduced. The poison option would be operated for the order of 1 year. Its usefulness will be dependent on the background rate in the $5 \rightarrow 7.5$MeV energy range; a high rate in this range will obscure the shape of the CC energy spectrum, and make it impossible to distinguish one MSW solution from another.

2.3 Supernova Neutrinos

"Massive stars ($\geq 8M_\odot$) do not die quietly, but with dramatic and violent explosions" [51]. The total optical radiation emanating from a type II supernova event (stellar core collapse) is $\sim 10^{49}$ ergs. The kinetic energy of expanding debris carries away $\sim 10^{51}$ ergs. The neutrino burst energy dwarfs both the optical and the kinetic energy releases; the burst carries away $\sim 10^{53}$ ergs. For the few millisecond duration of the neutrino burst, the neutrino luminosity of the supernova can rival that of the total optical

D_2O	Standard Model	MSW	Vacuum Osc.
$d(\nu_e, e^-)pp$	82	121	82
$d(\overline{\nu}_e, e^+)nn$	67	67	78
$d(\nu_e,\nu_e)np$	35	53	35
$d(\overline{\nu}_e, \overline{\nu}_e)np$	37	37	42
$d(\nu_\mu, \nu_\mu)np$	100	100	95
$d(\nu_\tau, \nu_\tau)np$	100	84	100
$e^-(\nu_e, \nu_e)e^-$	4.4	4.3	4.4
$e^-(\overline{\nu}_e, \overline{\nu}_e)e^-$	1.1	1.1	1.1
$e^-(\nu_\mu, \nu_\mu)e^-$	1.2	1.2	1.2
$e^-(\nu_\tau, \nu_\tau)e^-$	1.2	1.2	1.2
$O(\nu_e, e^-)F$	1.2	4.0	1.2
$O(\overline{\nu}_e, e^+)N$	1.4	1.4	2.1
Total in D_2O	431	475	443

H_2O	Standard Model	MSW	Vacuum Osc.
$p(\overline{\nu}_e, e^+)n$	331	331	348
$e^-(\nu_e, \nu_e)e^-$	7.8	7.7	7, 8
$e^-(\overline{\nu}_e, \overline{\nu}_e)e^-$	1.9	1.9	2.0
$e^-(\nu_\mu, \nu_\mu)e^-$	2.1	2.1	2.1
$e^-(\nu_\tau, \nu_\tau)e^-$	2.1	2.1	2.1
$O(\nu_e, e^-)F$	2.1	7.2	2.1
$O(\overline{\nu}_e, e^+)N$	2.6	2.6	3.8
Total in H_2O	350	355	368

Total	781	830	811

Table 2.3: Number and type of interactions in the SNO detector expected from a supernova at a distance of 10kpc [53]. The SNO detector has been assumed to operate with 100% efficiency and above a 5MeV threshold.

emission of the observable universe. Averaging over many millennia, the neutrino luminosity of the galaxy is comparable to its optical luminosity.

The SNO experiment is capable of detecting neutrinos from a supernova. The rate of supernova explosions in the milky way is low ($(10^{-1} \rightarrow 10^{-2})$/yr [51]), and so an event is unlikely during the lifetime of the SNO detector. Should a supernova event occur however, it is possible that a stringent limit might be placed on the ν_τ mass (the current limit is $m_{\nu_\tau} < 24$MeV, 95% C.L. [50]).

For τ neutrino masses in the range 50eV $< m_{\nu_\tau} <$ 100keV, the τ neutrino signal would be delayed by a time between 3s and $\sim$ half a year. Such a delay would be readily measurable in SNO [83]. For τ masses greater than 200keV, the τ neutrino burst would be a year later than the optical signal and spread over half a year, making it difficult to detect against the solar neutrino background ($\sim$ 18 events per day).

For τ neutrino masses in the range 20eV $< m_{\nu_\tau} <$ 50eV, the ratio of the neutral to charged current rate in the SNO detector is sensitive to the ν_τ mass [52] , but the analysis of the supernova burst event for the extraction of the ν_τ mass would be complicated were neutrino oscillations to occur in the supernova itself.

Table 2.3 shows the number and type of interactions expected in SNO in response to a supernova event at 10kpc. Note that 10 ν_e events are expected in SNO within the first 5ms in the absence of the MSW effect. Were $\nu_e \rightarrow \nu_\mu$ oscillations to occur in the supernova, these events would not be seen, and a considerable hardening of the ν_e spectrum is expected; the mean ν_e energy rises 8MeV from 14MeV for the $d(\nu_e,e^-)pp$ interaction [53].

SN1987A was detected in the IMB [54] and Kamiokande [55] detectors. A partial list of what was learned from the 20 observed neutrino events is presented in order to illustrate the importance of the observation of neutrinos from a stellar core collapse [51];

1. $\Phi(\nu_e) \sim (5.0 \pm 2.5) \times 10^9 \text{cm}^{-2}$;
2. $L_{\nu_e} \sim 4 \times 10^{52}$ ergs s^{-1} at early times ($t <$ 1s);

Event	Response (NHITs)	Width (%)
5 MeV e^-	51.82	17.3
10 MeV e^-	105.3	22.9
$^{35}Cl(n,\gamma)^{36}Cl$	60.89	22.3

Table 2.4: Detector response for named event classes [64]. Events were uniformly distributed throughout the D_2O and isotropic in direction.

3. the characteristic signal decay time was $\tau \sim 4$s;
4. the radius of the core was 50 ± 20km, close to the calculated radius of a neutron star;
5. the total electron neutrino luminosity was $(4 \pm 1) \times 10^{52}$ ergs;
6. the total neutrino luminosity was $(2 \pm 1) \times 10^{53}$ ergs; this is the first measurement of the binding energy of a neutron star;
7. the gravitational mass of the young neutron star is $\sim (1.35 \pm 0.15) M_{\odot}$.

Naturally, many of the estimates listed are model dependent.

2.4 The Energy Response of the SNO Detector

2.4.1 Čerenkov Radiation

Čerenkov radiation [45] is emitted by a charged particle moving through a medium faster than the local phase velocity of light. The number of Čerenkov photons emitted per unit distance per unit wavelength by a charged particle is;

$$\frac{d^2N}{dxd\lambda} = \frac{2\pi\alpha Z^2}{\lambda^2}\left(1 - \frac{1}{n^2\beta^2}\right) , \tag{2.9}$$

where α is the fine structure constant, Z is the charge of the charged particle in motion, $\beta = v/c$, and n is the refractive index of the medium. The photons are emitted at the Čerenkov angle;

$$\cos\theta_c = \frac{1}{\beta n(\omega)} . \tag{2.10}$$

The emission of Čerenkov light is uniform in the azimuthal angle due to rotational symmetry. The threshold kinetic energy for the production of Čerenkov radiation by electrons is 272keV in the heavy water, 275keV in the light water, and 183keV in the acrylic vessel. In water, the Čerenkov angle is $\sim 42°$. Approximately 220 Čerenkov photons are emitted per MeV for electrons in the 5 to 15MeV range at wavelengths between 250 and 600nm.

2.4.2 Energy Response

Lay [64] has simulated electrons and γ-rays between $1 \rightarrow 20$MeV in energy, distributed uniformly and isotropically throughout the heavy water in SNO. The simulations were completed using the SNOMAN program, which will be discussed in a later chapter (Chapter 7). The NHIT spectrum (NHIT is the number of tubes reporting a hit in a detector event) is shown in Figure 2.6. In the figure it is evident that the NHIT response of the detector to γ-rays is less than its response to electrons of the same energy. The cause is twofold; a γ-ray must retain some of its energy when it Compton scatters an electron; and each electron scattered is invisible in the SNO detector below the Čerenkov threshold. Also shown in the figure is the detector's response to chlorine and deuterium events. The poor response to chlorine is a result of the multiplicity of the chlorine γ cascade. In general, the detector's energy response is linear over the energy range of interest in the SNO experiment, recording about 10.5 hits per MeV. The response is low at low energies because of the effects of the Čerenkov threshold and low at high energies because the probability of striking the same PMT twice is no longer negligible [64]. The variation in the number of PMT hits recorded for an event of fixed energy is expected to be dominated by statistics, although systematic variations due to electron position and direction do occur. Assuming a mean of $N(E)$ counts

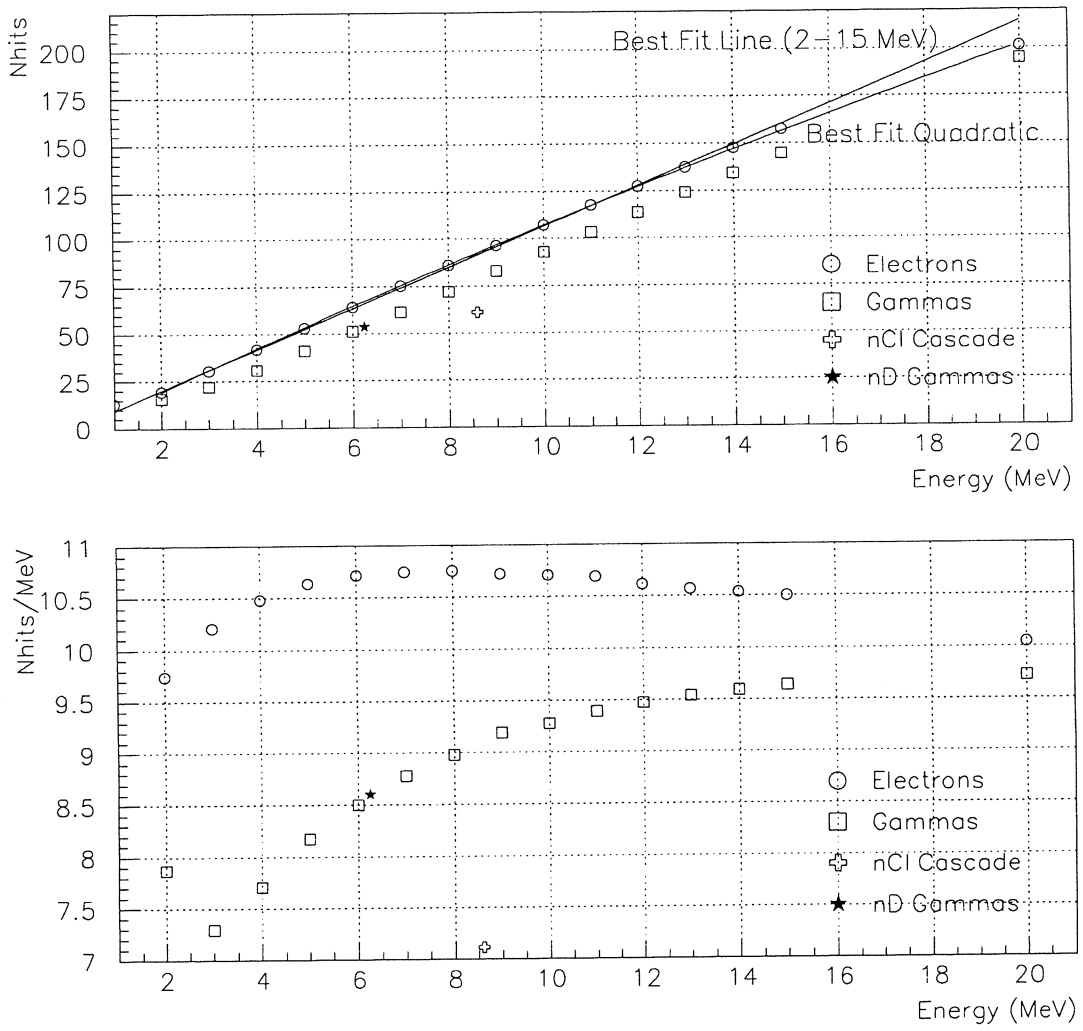

Figure 2.6: The NHIT spectrum as a function of event energy for a variety of event classes, and the NHITs / MeV for the same classes [64]. See text for explanation.

Radius	Fitted Values	
(cm)	NHITs	Width
0	50.63	8.50
100	50.92	8.67
200	51.81	8.60
300	52.69	8.83
400	53.67	9.07
500	53.71	9.12
550	53.36	9.09
590	52.98	9.06
599	50.51	8.36

Table 2.5: Mean and width of the Gaussian fitted to NHITs as a function of radial position in the detector [64]. There is an 0.1% error on the NHIT mean, and a 1% error on the width.

Material		^{238}U g/g	^{232}Th g/g
Light Water	Target	1.5×10^{-14}	2.2×10^{-14}
	Estimate	$\sim 1 \times 10^{-13}$	$\sim 1 \times 10^{-14}$
Acrylic Vessel	Target	3.0×10^{-12}	2.5×10^{-13}
	Estimate	$\sim 1 \times 10^{-12}$	2.5×10^{-13}
Heavy Water	Target	4.5×10^{-14}	3.0×10^{-15}
	Estimate	$\sim 3 \times 10^{-14}$	$\sim 3 \times 10^{-15}$

Table 2.6: Target and estimated levels of radionuclide purity in the inner volumes of the SNO detector. The target levels are from the SNO proposal document [83] [84, Annex 12]. The estimates were obtained from [49].

the uncertainty will therefore be $\sim \sqrt{N(E)}$. Table 2.4 shows the result of fitting a Gaussian to the NHIT distribution of the named events. Table 2.5 shows the radial dependence of the NHIT spectrum for 5MeV electrons. The detector response is seen to vary by about 6% over the volume of the D_2O.

2.5 Backgrounds in the SNO Detector

2.5.1 Cosmic Rays

The depth of the SNO detector is 2070m, or about 6000m water equivalent shielding. At this depth, the only surviving cosmic ray components are muons and neutrinos. The muon flux through the SNO detector and other neutrino observatories is shown in Figure 2.7. Muon induced ^{16}O spallation products such as ^{8}B, ^{12}B, and ^{12}N are 13 $\rightarrow$ 16MeV β emitters with half-lives of 10 $\rightarrow$ 800ms. These have been observed in Kamiokande II, where 1% of the muons produced spallation products above a 10MeV threshold. The situation in the SNO detector is much more favourable; SNO is at greater depth than Kamiokande, and the muon flux in SNO is 24 per day, with 1.5 muons expected to produce detectable spallation events above 5MeV. Events in the SNO detector will be vetoed for a short time following the observation of a cosmic ray to reduce the effects of spallation.

2.5.2 Radionuclide Backgrounds

The main obstacles to achieving the objectives for which the SNO detector has been designed are its internal backgrounds. The most serious of these are the radioactive decays of naturally occurring potassium, thorium, and uranium in or inside the PSUP region. The presence of these radionuclides in the detector has two main effects;

1. low energy events are generated in the detector which mask the low energy part of the charged current spectrum, which limits the range over which spectral distortions can be studied. The spectral distortions are greatest at low energies.

2. γ-rays with energies greater than 2.2MeV can photodisintegrate the deuteron in the d(γ,n)p reaction, which releases a free neutron in the D_2O.

Only the uranium and thorium decay chains contain radionuclides that decay to γ-rays with sufficient energy to photodisintegrate the deuteron (2.2MeV). The ^{232}Th and ^{238}U decay schemes are shown in Appendix A. The ^{232}Th decay chain has a 36% branch to ^{208}Tl, which in turn β-γ decays to an excited state of ^{208}Pb. This decays to the ground state via a 2.614MeV γ-ray. The ^{238}U decay chain leads to ^{214}Bi, which has a $\sim$ 2% branch to β-γ decays where $E_\gamma > 2.2$MeV. The majority of the decays in the ^{238}U and ^{232}Th chain result in the emission of a 4 $\rightarrow$ 6MeV α particle. α particles at these energies are not a background inside the PSUP region of the SNO detector because they do not produce Čerenkov light; however (α,pγ) reactions, and neutron capture following (α,n) reactions on Si, Al, Mg, and Na and others in the rock wall of the cavity are both sources of γ-rays of up to 10MeV in energy. 3m of light water shielding reduces the flux of these γ-rays at the PSUP to the level of a few per day above 5MeV. The neutron flux from the cavity wall is entirely absorbed by the light water shield.

The SNO detector has been built from materials which have been carefully selected to limit the background radiation generated in the detector. Inside the PSUP region there is 1668 tonnes of light

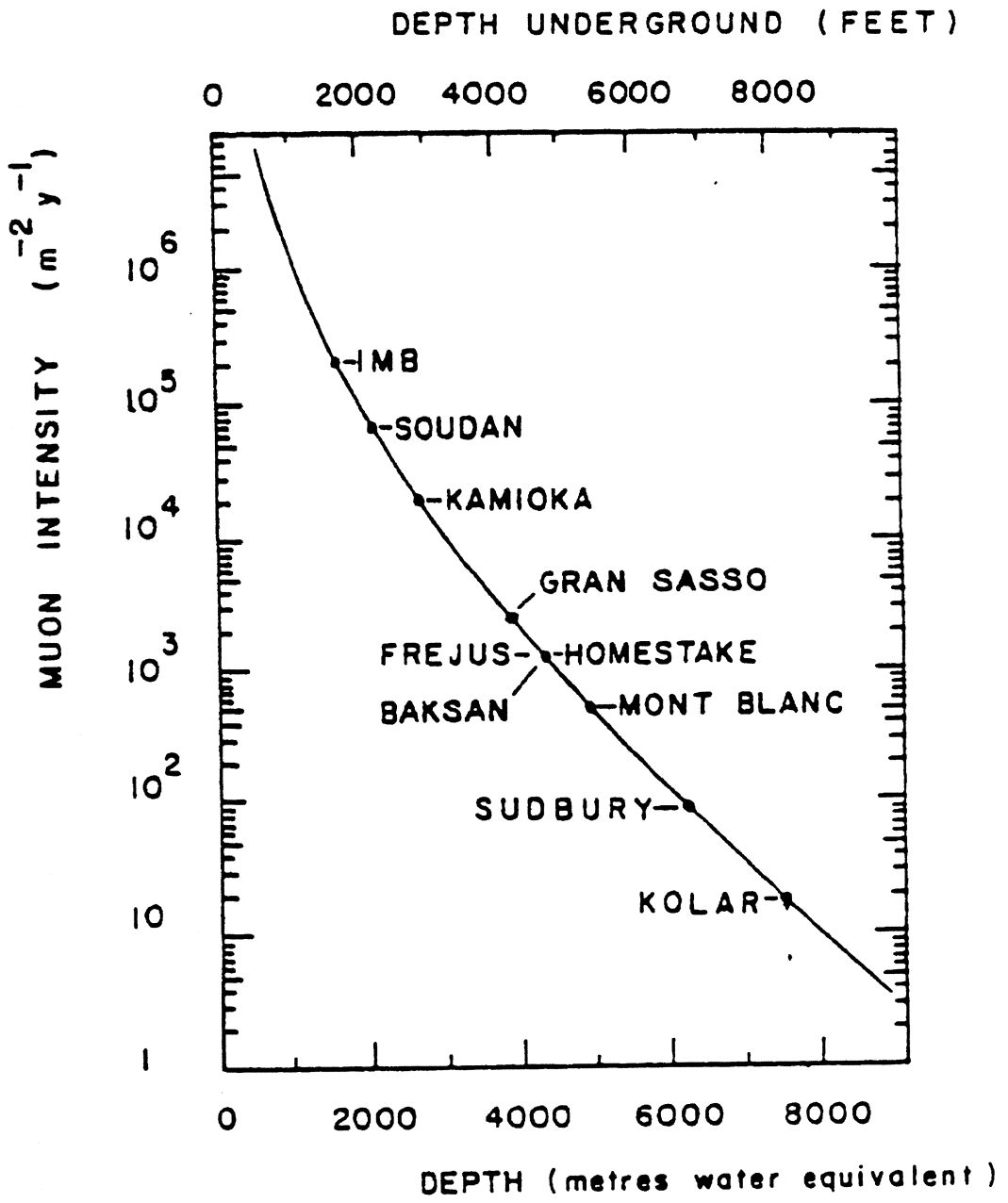

Figure 2.7: The cosmic ray muon flux for the Sudbury detector and other existing underground laboratories.

Assay Source	^{40}K	^{238}U	^{232}Th
University of Guelph	25.9 ± 5.6	47.6 ± 4.8	19.9 ± 2.5
Birkbeck College	20.3 ± 2.9	38.8 ± 4.6	10.1 ± 1.5

Table 2.7: Radionuclide concentrations in Schott 8246 glass (10^{-9} g/g).

water, 1000 tonnes of heavy water, and 30 tonnes of acrylic. These material volumes are directly observed by the SNO PMT array, and therefore the most stringent purity requirements in the detector apply to them. The target levels of radioisotope purity for ^{238}U and ^{232}Th are shown in Table 2.6, accompanied by recent estimates of their purity. The target levels for contamination in the the heavy water and the acrylic were set to reduce the rate of photodisintegration of the deuteron to 1 per day per medium for ^{238}U and ^{232}Th. This rate is to be compared to the standard solar model prediction of about 18 neutrons per day. The target for the light water is more stringent than that of 1 photodisintegration per day per nuclear species; it arises because of the need to reduce the radionuclide decay rate in the vicinity of the PMTs. The current best estimates of the d(γ,n)p rate for the sources listed in Table 2.6 are given in Chapter 9.

A major source of β-γ events in the detector are the PMTs. Most of the components of the PMTs are shielded from the light water to some extent, the exception being the PMT glass. Although the glass (Schott 8246) has been specially selected for its low activity for use in the SNO experiment, it is still active by SNO standards. Table 2.7 shows the concentrations of ^{40}K, ^{238}U and ^{232}Th in the glass.

Figure 2.8 shows the relative magnitudes of the SNO signals and dominant backgrounds. The background wall is the background rate arising from β-γ decays; it is the rate of these events that sets the effective threshold for any analysis of the SNO detector.

2.6 Water Condition

Pure water is an effective solvent; therefore to maintain water purity in the SNO detector requires the use of a water purification system. The light water system consists of four semi-independent functional groups, shown in Figure 2.9.

The pretreatment stage is used to purify the water from the source provided to the SNO experiment by the INCO mine authority. The pretreatment includes basic filtration, the addition of chemicals to complex specific elements for later removal by filtering, de-aeration, and reverse osmosis. The pretreatment removes iron, calcium, and magnesium from the water. Using high pressure across a semi-permeable membrane, the reverse osmosis removes > 99% of ionised salts, colloids, and organic molecules.

During normal operation light water will be extracted from the SNO cavity at a rate of about 270 litres per minute. 50% of this flow will return to the recirculation loop to be purified and degassed. The first stage of water purification is a bank of ultraviolet lamps at 185nm wavelength. These break apart large organic compounds, which are then extracted using mixed bed ion exchange columns. The ion exchange columns remove residual ions to yield 18.3MΩ ultra-pure light water. The next stage is the removal of radon from the water in a purpose-built degassing apparatus. The water then passes through an ultraviolet steriliser ($\lambda = 254$nm) to kill biological contaminants. Finally, the water is passed through a 1μm filter and a heat exchanger before returning to the detector cavity. The remaining 50% of the water is extracted from the cavity and passed through an ultrafiltration device before being chilled to 8°C in the second heat exchanger. It is then returned to the cavity. The treatment of heavy water is similar in principle, but it is complicated by the need to avoid degrading its isotopic purity, which is 99.92%. Mechanisms for the introduction and removal of $MgCl_2$ have been developed. The ultimate limit upon the maximum salt concentration is set by the desalination process - the final product is limited to a 120 tonne 5% concentration solution of brine, implying an absolute maximum salt concentration of 0.6% in 1000 tonnes of D_2O.

2.6.1 Assaying the Water in the SNO Detector

A number of assay techniques have been developed to allow the radionuclide content of the SNO water systems to be measured. These are;

1. the extraction of ^{222}Rn by vacuum degassing, followed by α counting in a Lucas cell (an acrylic cell lined with a ZnS scintillator);

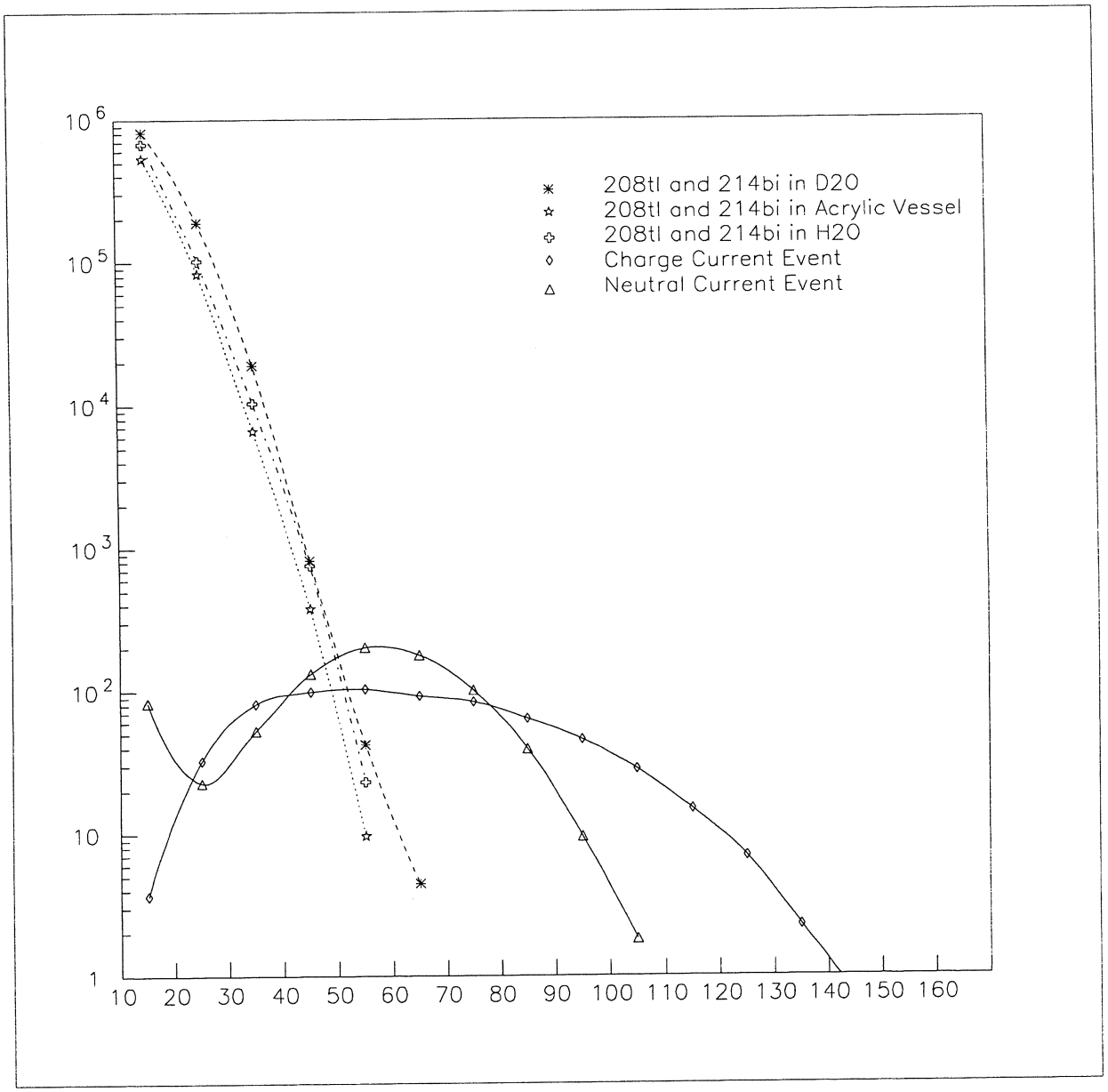

Figure 2.8: SNO detector signal and backgrounds [56]. The units are yr^{-1} (vertical axis) and NHITs (horizontal axis). The CC and ES energy spectra assume a neutrino flux equal to $\frac{1}{3}$ that of the SSM, whilst the NC energy spectrum assumes the SSM rate and that 2 tonnes of salt has been introduced into the D_2O.

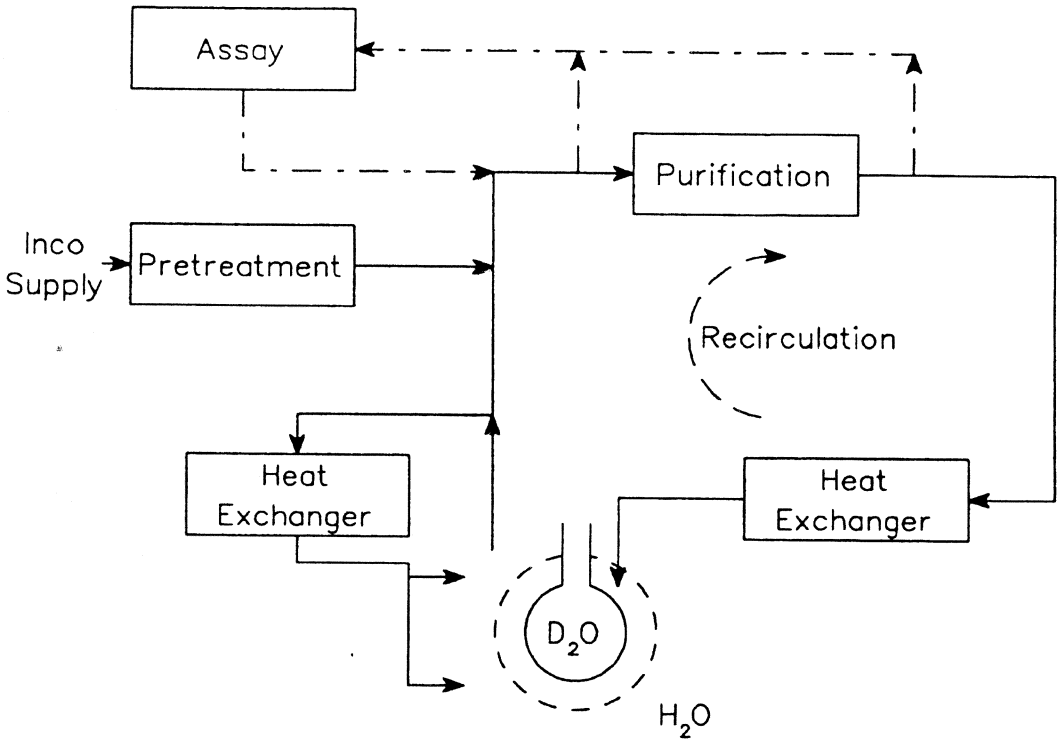

Figure 2.9: Schematic diagram of the SNO light water circulation loop.

2. the extraction of ^{224}Ra and ^{226}Ra using manganese dioxide beads, followed by the emanation and α counting of the radon daughters ^{220}Rn and ^{222}Rn;

3. Concentration of a ^{212}Pb-EDTA complex by reverse osmosis, followed by the precipitation of lead chromate to make a thin source for β-α coincidence counting;

4. Extraction of ^{224}Ra, ^{226}Ra, ^{228}Th and ^{212}Pb by seeded ultrafiltration, followed by β-α coincidence counting using a liquid scintillator counter.

The redundant nature of the assay techniques is deliberate; the SNO experiment is dependent on an accurate measurement of concentrations of the water contaminating nuclides. With the exception of the chemical assays of ^{212}Pb (method 3 and part of 4), secular equilibrium over a period of days must be assumed to infer the concentration of the photodisintegration capable nuclides ^{214}Bi and ^{210}Tl from the concentrations of the assayed nuclei. This is an undesirable feature of the chemical assay techniques that can be checked by comparing the measured energy dependence of the β-γ background wall to the Monte Carlo in order to determine the level of radionuclide contamination internal to the detector. Additional techniques for recognising ^{214}Bi and ^{210}Tl in a 30 $\rightarrow$ 40 hit window using algorithm involving pattern recognition are also being investigated [57]. These techniques have proved themselves to be robust against certain systematic effects [58].

2.7 Data Acquisition and Calibration in SNO

A detailed description of the data acquisition system is beyond the scope of this discussion, and therefore only a brief description will be given here. Each PMT is connected to a preamplifier via a coaxial cable. Any charge deposited in the PMT and the time it was deposited are recorded in a circular buffer after analogue to digital conversion. A hit is declared if the charge deposited exceeds a PMT-specific threshold. A global trigger is declared if the number of PMTs hit within an event window of 100ns exceeds a minimum threshold; the level of this threshold will be set as low as possible to maximise the amount of data recorded from the detector. 100ns is slight longer that the light transit time from one side of the detector to the other, and the time width of the event window has been chosen so as to reduce the effects of light reflections.

Source	Energy	Comments
^{2}H(n,γ)^{3}H	$E_\gamma = 6.25$MeV	
^{35}Cl(n,γ)^{36}Cl	$E_\gamma = 8.6$MeV	$\overline{N}_\gamma = 2.6$
^{7}Li(α,γ)^{11}B	$E_\gamma = 10.3$MeV	
^{3}H(p,γ)^{4}He	$E_\gamma = 20$MeV	
^{11}B(p,γ)^{12}C	$E_\gamma = (11.7 + 4.4)$MeV	Requires 163keV protons.
$^{16}N \rightarrow e^- + \nu_e + {}^{16}$O	$Q = 10.4$MeV	26% B.R., $\tau = 7.13$s
	$Q = 4.3$MeV, $E_\gamma = 6.1$MeV	68% Branching ratio.
$^8Li \rightarrow e^- + \nu_e + {}^8$Be	$Q = 13.1$MeV	$\tau = 0.84$s
Fission of ^{252}Cf	$E_n \sim 1$MeV	$3 \rightarrow 4$ neutrons per fission.

Table 2.8: Some of the calibration sources planned for use in the SNO detector.

An understanding of the neutrino signals detected by the SNO experiment can only be gained through calibration. The first stage of calibration is to quantify the performance of the data acquisition electronics and the PMTs. The electronics calibration calibrates the charge and time ADCs and their circular buffers using test pulses; dead channels will be identified and the slope and offset of the ADCs determined.

A laserball calibration device exists which will enable the PMTs to be calibrated with respect to time and gain. The laserball is a diffuse source of laser light which can be used to emit light at wavelengths above 325nm, and which can be positioned within the D_2O and to a lesser extent the light water outside the acrylic. For the purposes of calibration, the laserball will be operated at low light intensities to prevent multiple PMT hits, and its intensity will be continuously monitored by a photodiode.

The extraction of the PMT quantum efficiencies using the light ball will be carried out in air, before the filling of the detector. This avoids the need to decouple the attenuation lengths of light water and heavy water from the measurements in order to learn the PMT quantum efficiencies. The calibration in air is a still a coupled problem, although a simpler one; measurement of the efficiency of light collection in a PMT for a single position of the calibration device measures the combined effect of the quantum efficiency of the PMT and the absorption of an acrylic panel. Measurements will be made with the laserball in a number of positions throughout the inner volume of the acrylic vessel to extract both a PMT's quantum efficiency and the absorption length in individual acrylic panels. The measurements will be made across all the wavelengths that the laserball can produce in order to assemble a wavelength dependent profile of the detector's light response. Note that what has been referred to here as quantum efficiency is in fact a convolution of a number of effects; the light collection efficiency of the PMT and reflector concentrator arrangement, the probability of liberating an electron from the photocathode of the PMT given a photon incident upon it (which is what is normally referred to as the absolute quantum efficiency), and the efficiency of the PMT for the detection of the liberated electron above a discriminator threshold. The measurements will be repeated once the detector has been filled with water.

Henceforth, it will be assumed that a successful DAQ and PMT calibration has been performed, and hence that differences in the timing and amplitude of signals reported from PMTs have been understood, and the attenuation lengths of the light water, the heavy water, and the panels of the acrylic vessel are known. A number of calibration sources are planned that will be introduced into the heavy water to determine the detectors response to electrons and γ-rays. A partial list of the sources is shown in Table 2.8. These sources will be used to obtain γ-ray and electron energy calibrations (the Monte Carlo prediction of the energy response was shown earlier). The electron response will have to be obtained from the ^{8}Li source and Monte Carlo as there is no source of monoenergetic electrons available at the detector site.

None of the data from the calibration sources will be used directly in interpreting data from SNO, for in every case the effect of the source upon the signal obtained in the detector must be assessed. For example, the high energy short half life ^{8}Li source is manufactured by neutron capture and then piped into a decay chamber in the D_2O through an umbilical cord. The assessments will make use of the Monte Carlo. Particularly demanding are the cases of the β decay calibration sources, where the electron may scatter before leaving the source, distorting the observed energy spectrum. Even after all the calibrations have been completed, the agreement between the Monte Carlo of the detector and the data will be flawed. Historically, both the IMB and Kamiokande experiments, water Čerenkov detectors similar to the SNO detector, required an overall normalisation to bring their Monte Carlos into agreement with experimental data. IMB applied a normalisation of 0.53, whilst Kamiokande used a factor of 0.85. The Small Test Detector, assembled to demonstrate the feasibility of low energy (solar)

neutrino water Čerenkov detectors, required a normalisation factor of 0.82 to reconcile the simulated and detected numbers of photoelectrons [83][84, Annex 15]. A similar correction is expected in SNO, where the physical explanation for it is that the absolute quantum efficiency of the photomultipliers in the detector is not known to better than 5%, and hence a correction in the range $0.95 \rightarrow 1.05$ is expected. This correction should only affect the overall factor determining the number of PMTs hit by an electron of known energy.

2.8 Discussion

The SNO detector is scheduled to be filled with water during the summer of 1997. The water fill will take approximately 3 months. The detector will then be operated in its most basic mode - containing D_2O only - probably for 6 months to 1 year. In this time, DAQ and PMT calibration and the chemical assays will become routine operations and the first data will be taken. Analysis of calibration and detector data will indicate whether the β-γ background wall can be accounted for by the assayed elements, and whether pattern recognition techniques are viable.

There are four modes of operation for the SNO detector aside from the basic pure D_2O option. These are;

1. a salt fill, where 2 tonnes of $MgCl_2$ is added to the heavy water to increase the detection efficiency for neutrons;

2. a poison fill, where 300kg of $LiNO_3$ is added to the heavy water to suppress any signal from neutron capture;

3. the neutral current detector run, which will both increase the efficiency of the detector for observing neutrons over that of pure D_2O and identify them with a unique signal; and,

4. a light water fill, which will be used to make systematic checks on the performance and backgrounds of the detector.

The light water fill can only take place after the heavy water has been removed from the acrylic vessel. This is because if the option of a light water fill was to precede the heavy water fill, at some point the acrylic vessel would have to be dried to avoid isotopic degradation of the heavy water, a condition which would require the immediate return of the D_2O to Atomic Energy Canada Limited (AECL). This is undesirable because the inner and outer surfaces of the acrylic vessel will dry faster than its interior, and hence shrink faster. This may lead to crazing and to structural weaknesses which would endanger the D_2O. The light water fill will therefore be the very last option.

The poison fill option may or may not take place. The major disadvantage of the poison fill is the detector's reduced sensitivity to supernovæ, which are thought to shine with approximately equal intensity in all the three neutrino flavours. There are two advantages to a poison fill. The first and most important is the measurement of the shape of the charged current energy spectrum, which can be used to distinguish MSW solutions. The success of this measurement is dependent on the background rate in the $5 \rightarrow 7.5$MeV range. The second is that the absence of any significant background from neutron capture allows a pure charged current data set to be collected with which to calibrate the statistical event recognition techniques. The poison option is unlikely to occur unless the background rate in the $5 \rightarrow 7.5$MeV energy range is low.

The neutral current detector run will take place. It is likely that it will be the last mode of operation in which the detector is operated with D_2O. This is because the NC detectors take about 3 months to insert into detector, and about 3 months to remove from it. The presence of NC detectors inside the acrylic vessel reduces the detector's energy resolution, and makes the systematic variation of detector performance with event position slightly stronger. Nevertheless, it provides a direct measurement of the rate of neutral current events in the detector. The salt fill will also take place. The salt fill and the NC run are complementary methods of determining the neutral current event rate in the detector. An analysis of data from the salt fill, or of data from a pure D_2O fill, depends heavily upon the calibration of the detector and upon the Monte Carlo. This is because the analysis of the salt run will use statistical techniques to determine the number of events in each event class. There are many event classes, such as the charged current class, the elastic scattering class, the internal and external neutron classes, and classes for each distinct background in the detector. Each class of events will have a different distribution in energy, position, direction, and other variables, many of which can only be learnt from the calibration

sources and Monte Carlo combined. Knowledge of each of these distributions is crucial to the success of the statistical analysis.

The SNO experiment is a technically challenging project, the success of which will determine whether the deficit of solar neutrinos observed in the previous solar neutrino experiments; Homestake, Kamiokande, SAGE, and GALLEX, is due to neutrino oscillations or an error in the understanding of the physical processes in the sun's core. An observation of neutrino oscillations would be the first observation of the effects of a non-zero neutrino mass. The SNO experiment may also be fortunate enough to observe a supernova explosion of a relatively nearby star. In that case, a stringent limit might be put upon the ν_τ mass.

Chapter 3

The Angular Response of the SNO Photomultiplier-Concentrator

3.1 Introduction and Purpose

A Monte Carlo model of the SNO photomultiplier tubes has been prepared by Lay [63]. The computational model will form an essential part of the SNO Monte Carlo. This chapter describes work done by the author in obtaining experimental results that were used to test the model. The results presented here have been compared to the Lay's model in a paper accepted for publication by Nuclear Instruments and Methods [96].

The aim of the experimental work was to measure the angular response and concentration factor of the photomultiplier-reflector arrangement that is to be used in the SNO detector. The measurements were made both in air and in water. The angular response was measured as a function of polar angle θ, and the assumption that the response is independent of the azimuthal angle ϕ was examined. These measurements were made both with and without a concentrator using an apparatus that was designed by Moorhead [92]. The ratio of results taken with and without the concentrator allow a concentration factor to be calculated as a function of θ. The dependence on ϕ was also examined.

3.2 The Photomultiplier and Concentrator Arrangement

The photomultiplier that will be used in the SNO experiment is the Hamamatsu R1408 20cm photomultiplier. The photomultiplier geometry is described by Lay [94]. The SNO concentrator was first investigated by Moorhead [92] and a detailed discussion of it is given by Doucas *et al.* [95].

The Hamamatsu R1408 was chosen for use in SNO because it possesses a number of important properties. These are examined in detail by Boardman [91], and only two results are given here. First, the Hamamatsu phototubes have a small transit time spread of $\Delta t \simeq 3$ns full width half maximum which is equivalent to a light transit distance in water of 67.6cm. This leads to a typical resolution in the SNO detector of $\pm \sim 25$cm for point events yielding Čerenkov light. Second, the Hamamatsu's counting efficiency is insensitive to small local magnetic fields of up to 40μT. This means that a PMT's efficiency will not vary significantly with a change of location in the SNO detector, in which the 55μT vertical field will be cancelled, leaving only a 15μT horizontal field. The Hamamatsu photomultiplier is also relatively cheap.

The concentrators used in SNO are non-imaging concentrators, made of a molded plastic support containing 18 dielectric coated aluminium segments arranged into something closely resembling a truncated Winston cone. The optical properties of a similar device (a 24 petal concentrator) and alternatives, have been studied in detail by Moorhead [92]. Other factors, such as water survival, robustness, weight, and price, also contributed to the final selection of the design of the SNO concentrator.

The SNO concentrators serve several purposes. They are designed to accept photons incident upon the concentrator at angles up to 56.4° from normal incidence; this increases the light collection from within the fiducial volume of the detector, whilst reducing light collection from outside it. This improves both the energy and position resolution of the detector. The improvement in energy resolution means that the β-γ background has a threshold of 5MeV rather than 6MeV [92], which has important consequences for the detection of the neutral current signal. The acceptance angle was chosen such that a fiducial volume 7m in radius is visible to all the PMTs. Moorhead [92] measured the concentration factor to be ~ 1.7

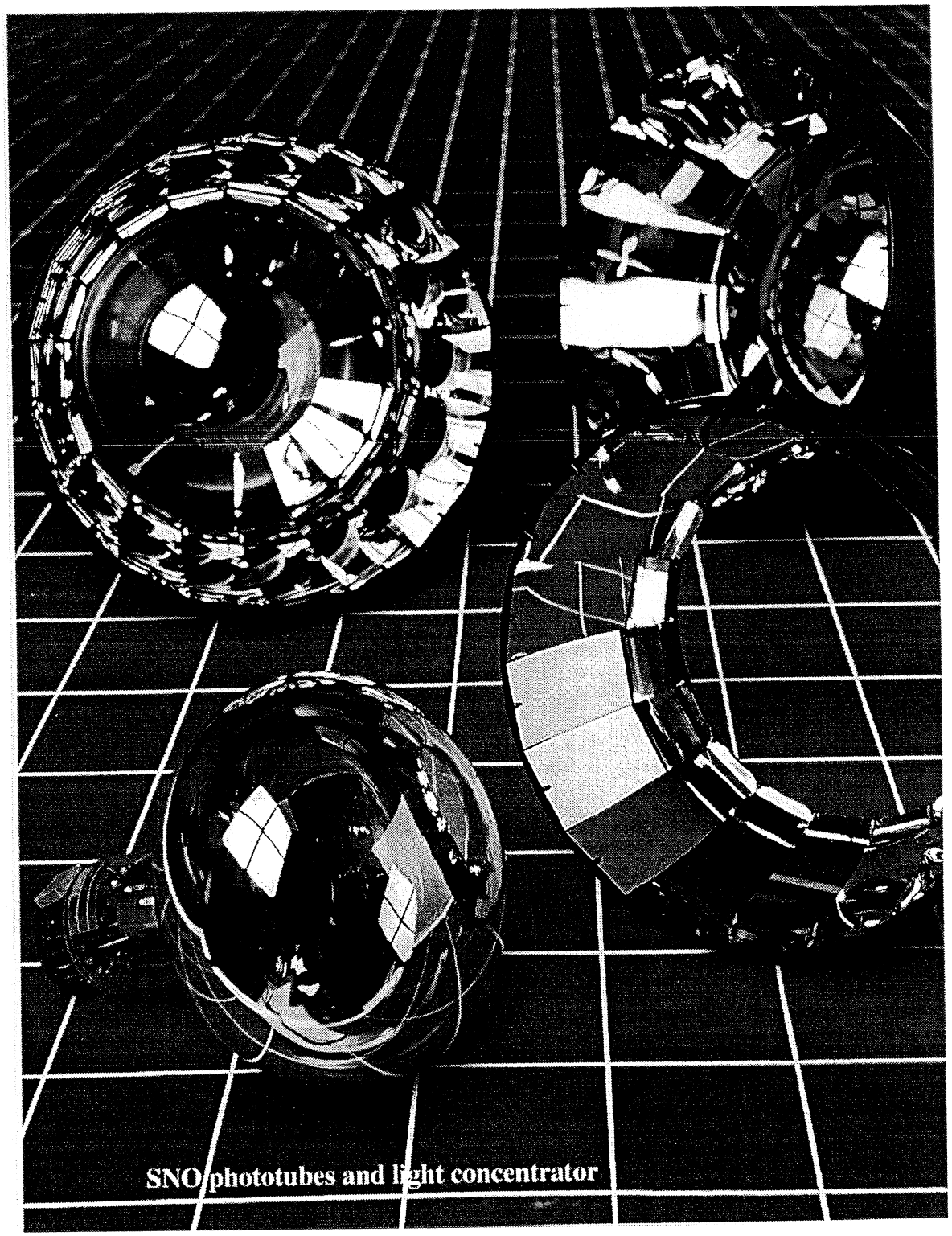

Figure 3.1: The Hamamatsu R1408 photomultiplier, and the SNO concentrator.

for the prototype concentrator. A theorem due to Liouville bars an increase in the density of particles in phase space in the absence of applied work, and so places a theoretical upper limit upon the improvement in light collection efficiency that can be achieved with a concentrator [92, Chapter 3]. The maximum concentration factor that can be achieved with an acceptance angle of 56.4° is 1.824 (C.F. $\propto 1/\sin^2\theta$) [95]. The design of the Winston cone is such that this is also the ratio of the normal area of the concentrator entrance aperture to the projected area of the photocathode. The measured concentration factor of the prototype (1.7) is lower than the ideal C.F. (1.824) because the reflectivity of the concentrator is less than 100%. Production concentrators have a measured concentration factor of ~ 1.7 at normal incidence and a reflectivity of $82 \pm 3\%$ [95], figures which are consistent both with the ideal C.F. and the illuminated normal areas of the photocathode and concentrator. Another important concern in the design of the concentrators was that they collect light uniformly from the fiducial volume of the SNO detector, thus avoiding distortions in the energy calibration as a function of position and direction.

3.3 Apparatus

The apparatus is shown in Figure 3.2. A black plastic container [92], known as the bin, houses the entire experiment. Light exiting from the Čerenkov source [91] at the focus of the mirror below is reflected upward in an almost parallel beam. This light is then incident upon the PMT or the PMT-concentrator arrangement. The PMT rig is free to rotate about a horizontal axis, so the parallel light from the mirror can be made incident upon the PMT rig at a non-zero polar angle. Changing the azimuthal angle of the PMT is more difficult, and only four azimuthal orientations can be achieved. These correspond to rotations of the PMT about the vertical axis of the bin through 0, $\pi/2$, π, and $3\pi/2$ radians.

The bin possesses a tight lid and this is sealed with black tape so as to reduce the quantity of external light that penetrates into the experiment. The Čerenkov source cannot see the PMT rig directly; it is housed in a 50mm diameter brass cylindrical shield which is closed at the top end. Čerenkov light from the source passes downward in a 45° cone. It is reflected nearly parallel by the mirror at the bottom of the bin, and then passes upward toward the PMT rig. A source blocker is available. This is a simple shield that, when moved into place below the Čerenkov source, prevents any Čerenkov radiation from being reflected by the mirror up to the PMT rig. This allows measurements of the dark current to be made.

The PMT is housed in a very nearly water-tight rig that protects the sensitive electronics at the base of the phototube from contact with water. The entire PMT rig can be immersed in water, and to this end, the bin itself is water-tight. When water is present in the bin, bubbles of gas can form on the surface of the mirror, and any impurities in the water can attenuate the Čerenkov light. To prevent these effects the water used in the experiment is degassed and passed through a membrane by reverse osmosis (the water is then known as RO water), removing larger particulate contaminants (> a few nm). The surfaces in the bin were washed with the RO water before measurements began. The mirror and the PMT glass received special treatment, being washed with de-ionised water (with a nominal purity of 18MΩ). De-ionised water leaves no residue when it evaporates, and so surfaces washed with the water have no distribution of particles with which to scatter light.

The R1408 was be operated under conditions as similar as possible to the operating conditions that will be encountered in the SNO detector. This means that the local magnetic field was reduced, and the PMT fitted with a SNO base and operated in single pulse mode with the voltage and discriminator levels set in the manner they will be set in the actual SNO experiment. Setting the voltage and discriminator levels entailed adjusting the high voltage supply until the PMT achieves a mean gain of 10^7, and then setting the discriminator to cut out signals that are less than those producing a quarter of the charge deposited by the average single photoelectron. The electronic arrangement used in the experiment is shown in Figure 3.3. It includes a calibrated pulse generator which was used to start the scalar counter and to stop it after a period of 5 seconds.

A flux gate magnetometer was used to measure the magnitude of the magnetic field due to the Earth at the PMT's experimental location. The field was found to be $\sim 40.5\mu$T. By positioning a set of Helmholtz coils at an angle of 23° to the vertical, facing south, and providing the coils with a current of 0.35A, the magnetic field experienced by the PMT was reduced to $\sim 0.6\mu$T, or 1.5% of the Earth's local field. With respect to the magnetic field conditions, the PMT operates in the same regime (maximal efficiency) in which it will be operating in the SNO experiment.

It is well known that the dark current in a PMT is enhanced by exposing the photocathode to light and declines rapidly after the application of EHT. The explanation for this behaviour is unclear [146], and one possible mechanism is the excitation of metastable states in the photocathode [147]. Whatever the

The PMT/Concentrator Performance Measurement Apparatus

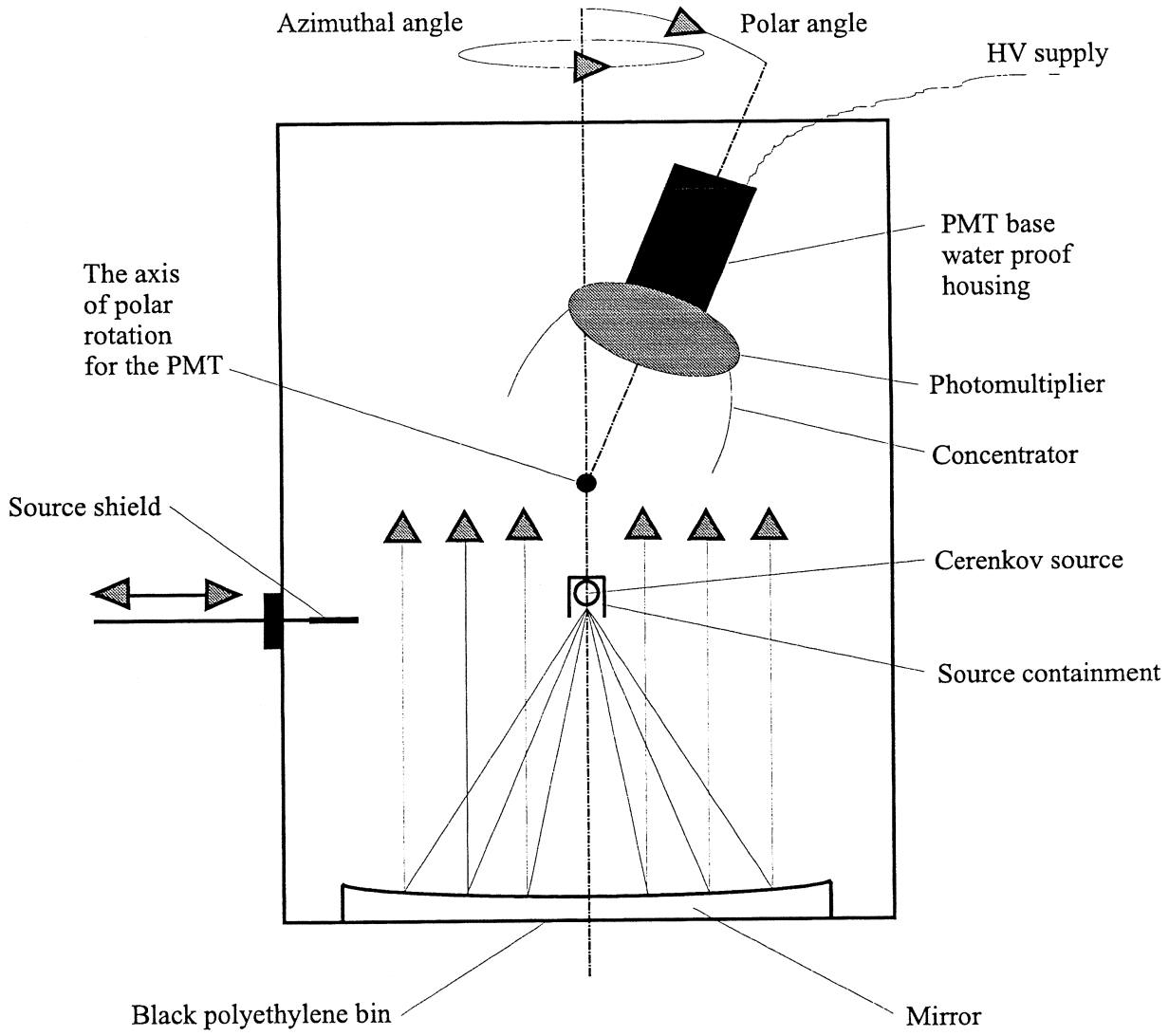

Figure 3.2: A schematic diagram of the experimental apparatus.

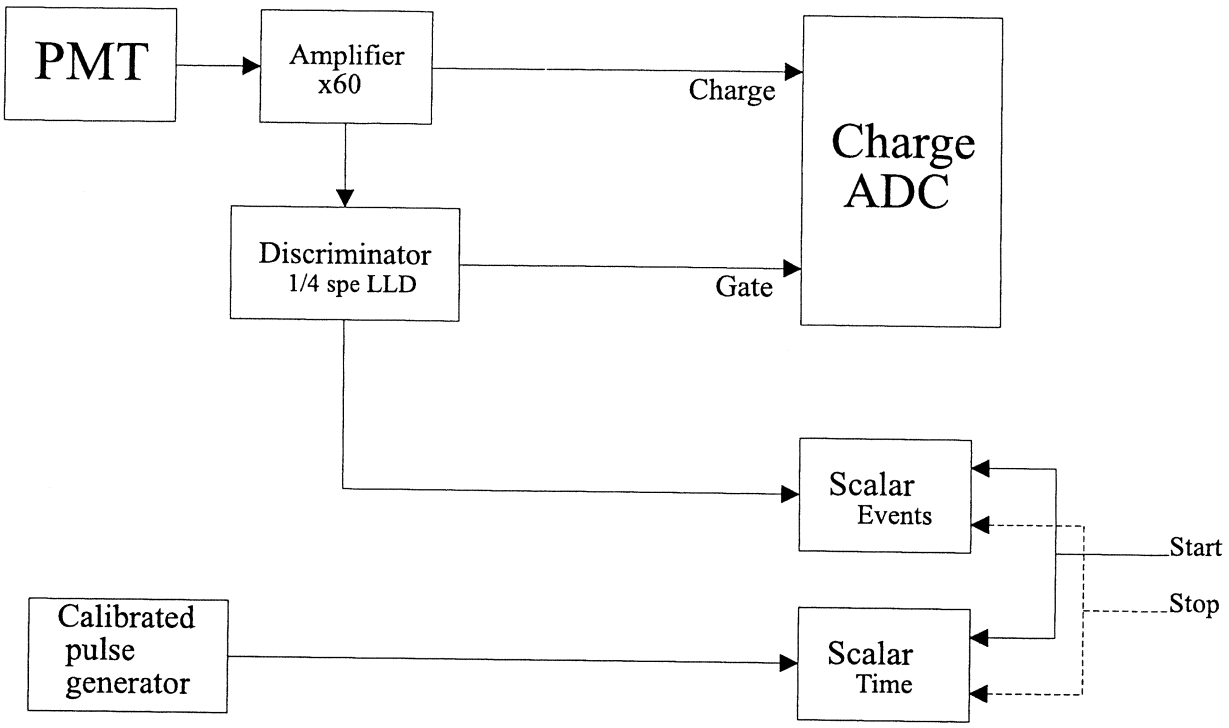

Figure 3.3: A schematic of the electronics used to gather data from the R1408 photomultiplier tube.

explanation, most PMTs require several hours of continuous operation to ensure a stable dark current, after which the principle source of noise is the thermionic current. To counter the effects of exposure to light, the PMT was allowed to operate under normal experimental conditions without exposure to light sources, until noise levels had returned to the nominal background level. To establish a nominal level of noise for the PMT, it was allowed to operate in the dark for several days before the experiment began. During the experiment itself, exposure to light was minimised during changeover operations, and the PMT was always allowed to quieten down through dark operation before measurements resumed.

In order to obtain a concentration factor for SNO's concentrators, it is necessary to take readings with and without the concentrator in place. When the concentrator is not used, a mask is put in its place. The purpose of this mask is to expose only that area of the photocathode that is exposed by the concentrator, and hence obtain a concentration factor that arises from purely geometric effects, i.e., that does not depend upon the properties of the additional areas of photocathode that would be exposed to light in the absence of both the mask and the concentrator. Both the mask and the concentrator were firmly secured, and light was prevented from reaching the hidden area of the photocathode by extensive taping.

The Čerenkov source was developed by Boardman [91], and consists of a hollow sphere of UV-stabilised acrylic containing the radioisotope ^{90}Sr in a weak (0.1M) hydrochloric acid solution. The principal radiations produced are β^- particles;

$$^{90}\mathrm{Sr} \rightarrow {}^{90}\mathrm{Y} + e^- + \overline{\nu_e}\ , \tag{3.1}$$

which has a half-life of 28.6 ± 0.3 years, and an endpoint energy of 0.546 ± 0.001MeV, and

$$^{90}\mathrm{Y} \rightarrow {}^{90}\mathrm{Zr} + e^- + \overline{\nu_e}\ , \tag{3.2}$$

with a half-life of 64.07 ± 0.16 hours and an endpoint of 2.2792 ± 0.003MeV. The β particles produce Čerenkov radiation which passes out through the acrylic casing of the source, which has a wavelength cutoff of around 320nm. The light emanating from Boardman's source is isotropic and unpolarised when averaged over many decays. The half life of ^{90}Sr is very long when compared to the duration of the experiment; this fact means that there was no appreciable variation of the source strength during the period in which measurements were taken.

The concentration factor is defined as the ratio of the number of signal events with the concentrator and with the mask. It is a function of the angle of incidence of the photon beam. A perfect photomultiplier/concentrator system detects all photons that are incident upon it within the acceptance angle, and

for photon sources that produce more than one photon per decay event, this can lead to an underestimate of the concentration factor. This is because events of multiple correlated photons (such as those that occur in Čerenkov radiation) will be counted with a disproportionately high probability when the masked PMT is exposed. The design of Boardman's source is intended to minimise this effect by producing only a small number of photons per decay; one ^{90}Y decay in the source (the more energetic of the two β-decays in the source) produces an average of 32 photons. The effect is further reduced by the overall efficiency of the Hamamatsu R1408 for detecting photons (which is $\sim$ 15%, a convolution of a quantum efficiency of $\sim$ 28% and a collection efficiency of 55%). Assuming an ideal concentrator, the concentration factor is;

$$\text{C.F.} = \frac{\begin{pmatrix} \alpha P_c(1) & + & 2\alpha(1-\alpha)P_c(2) & + & 3\alpha(1-\alpha)^2 P_c(3) \\ & + & \alpha^2 P_c(2) & + & 3\alpha^2(1-\alpha)P_c(3) \\ & & & + & \alpha^3 P_c(3) \end{pmatrix}}{\begin{pmatrix} \alpha P_m(1) & + & 2\alpha(1-\alpha)P_m(2) \\ & + & \alpha^2 P_m(2) \end{pmatrix}} \tag{3.3}$$

where α is the PMT photon detection efficiency, and $P_c(n)$ is the probability of detecting an n-photon event with the concentrator in place, while $P_m(n)$ has the same meaning for the masked PMT. SNOMAN has been used to simulate Boardman's source and the frequency with which 1, 2, or 3 photons enter the solid angle occupied by masked and concentrator-bearing PMTs has been calculated. The results are; $P_c(1) = 0.0444$, $P_c(2) = 0.0050$, $P_c(3) = 0.0003$, $P_c(\geq 4)$ small, $P_m(1) = 0.0295$, $P_m(2) = 0.0001$, and $P_m(\geq 3)$ small. These values yield a concentration factor exactly in agreement with the theoretical limit for normal illumination; 1.824. This is entirely because of the low PMT photon detection efficiency, α; if it were 1, the C.F. would be underestimated at $\sim$ 1.679. To conclude; the photon intensity of Boardman's source and the PMT photon detection efficiency are sufficiently low that it is highly unlikely that more than one photon would be detected from a single β-decay. Consequently the concentration factor is correctly estimated to better than 1% from the simple ratio of the event rates with and without the concentrator in place.

3.4 Method

A measurement of the signal+background was made by exposing the PMT (with a mask or a concentrator in place) to Čerenkov light for a period of 5 seconds. The number of counts above the discriminator threshold accumulated during the period of exposure was recorded. A measurement of the background was taken either immediately before or immediately after a signal+background reading. The measurement was made by moving the source blocker infront of the source so as to prevent Čerenkov light from reaching the mirror. The exposure time was again 5s, and the number of counts above the discriminator threshold was recorded.

Sets of measurements were made with the concentrator in water and in air and with the mask in water and in air. Each set of measurements contains readings for 228 positions of the PMT rig defined by the four azimuthal orientations (colloquially: north, south, east, and west) with the polar angle ranging from $+70° \rightarrow -70°$ at 2.5° intervals. 5 measurements were made of the signal+background and the background at each orientation. The total number of measurements made was 9120.

Several problems were encountered when the first abortive set of measurements was taken. The PMT and its read-out electronics proved extremely sensitive to electrical disturbances from external sources (such as an electric arc-welder, for example). The PMT rig proved to be only nearly water tight, allowing water vapour to penetrate through the housing to the electronics after $\sim$ 4 hours. Various attempts were made to reduce the effects of both problems, but eventually it was decided to take the readings over a period of four nights of intensive measurement. The readings would be taken at night so as to reduce electronic noise from external sources, especially a nearby workshop which operated only during the day, and in which aluminium arc welding was taking place. They were also taken very rapidly in order to prevent the PMT rig from being penetrated by water (rendering the PMT useless). The main run proved sufficient to gather all the data. The results will be discussed in the next section.

3.5 Results and Comparison with the Monte Carlo Model

The results of each of the four data sets (with mask or concentrator and in water or air) were processed according to the formulæ;

$$\overline{y}(\theta,\phi) = \frac{1}{5}\sum_{i=1}^{5} y_i(\theta,\phi) \ , \tag{3.4}$$

and,

$$\sigma^2(\theta,\phi) = \frac{1}{20}\sum_{i=1}^{5}(y_i(\theta,\phi) - \overline{y}(\theta,\phi))^2 \ . \tag{3.5}$$

where $y_i(\theta,\phi)$ is the difference between the ith signal+background and the ith background reading made at an orientation of the PMT defined by θ, the polar angle, and ϕ, the azimuthal angle. The sum over i is the sum over the 5 readings at a single (θ,ϕ) orientation, and $\overline{y}(\theta,\phi)$ is the mean value of those readings. $\sigma^2(\theta,\phi)$ is the variance of associated with the quantity $\overline{y}(\theta,\phi)$.

The results (the $\overline{y}$ values and their errors) are shown in Figures 3.4 (air data), and 3.5 (water data). These plots clearly show that the concentrator rejects light incident at extreme angles. The apparently linear dependence of $C(\theta,\phi)$ on θ as $|\theta| \to 70°$, $|\theta| > 60°$ is due to the shadowing of the PMT photocathode by the concentrator. At these large angles, the concentrator rejects almost all of the incident light incident upon it, but some light falls directly onto the PMT. The signal is then proportional to the surface area of the photocathode presented to the light beam, which falls linearly with angle. Figures 3.4 and 3.5 suggest an approximate azimuthal symmetry in the data. This is emphasised in Figure 3.6, where the south and west data sets suffer the transformation $\theta \to -\theta$.

A concentration factor is obtained as follows;

$$C(\theta,\phi) = \frac{\overline{y}_c(\theta,\phi)}{\overline{y}_m(\theta,\phi)} \ , \tag{3.6}$$

where $C(\theta,\phi)$ is the concentration factor, and the subscripts c and m refer to the readings taken with the concentrator and mask respectively. The concentration factor data is shown in Figure 3.7. Figure 3.7 shows air and water concentration factors which are between 1.6 and 1.8 for $|\theta| <\sim 50°$, and which drop off rapidly for increasing $|\theta|$, $|\theta| >\sim 50°$.

Lay [63], [94] has prepared a detailed Monte Carlo model of a Hamamatsu PMT and a SNO concentrator. This model takes account of;

1. the geometry of the photomultiplier.
2. The geometry of the reflector.
3. The optical properties of the photomultiplier.
4. The optical properties of the reflector.

The PMT model assumes axial symmetry, and models the PMT as a combination of a sphere and an elliptical torus of circular cross-section, whilst the dynode stack is modelled as a cylinder in the lower region of the PMT (see Figure 3.8). The SNO concentrator takes the shape of a truncated Winston cone [92] [95]. This shape has no simple analytical form, and so Lay has chosen to approximate it using a section of an elliptical torus, an approximation which has very little effect on the validity of the PMT-concentrator simulation [63]. The modelling of the concentrators is complicated by the fact that their reflective surface is not a single piece, but instead is made up of 18 petals. This is explicit in Lay's model.

The optical properties of the photocathode were determined by Lay and are discussed in [94] and by Lay and Lyon in [96]. The absorptivity is shown to be linearly related to the quantum efficiency, and the relationship is deduced. The results are included in the Monte Carlo model. Of the remaining surfaces, the glass envelope is well described by Fresnel's Laws as is the reflective back hemisphere of aluminium. The optical properties of the dynode stack used in the PMT model were taken from [92]. Finally, the 18 petals in the concentrator were modelled using data provided by Waltham *et al.* [120], who examined the reflectivity of the dielectric coated aluminium (DCA, or Omega) for angles in the range $20° \to 75°$, and wavelengths between 305 and 800nm.

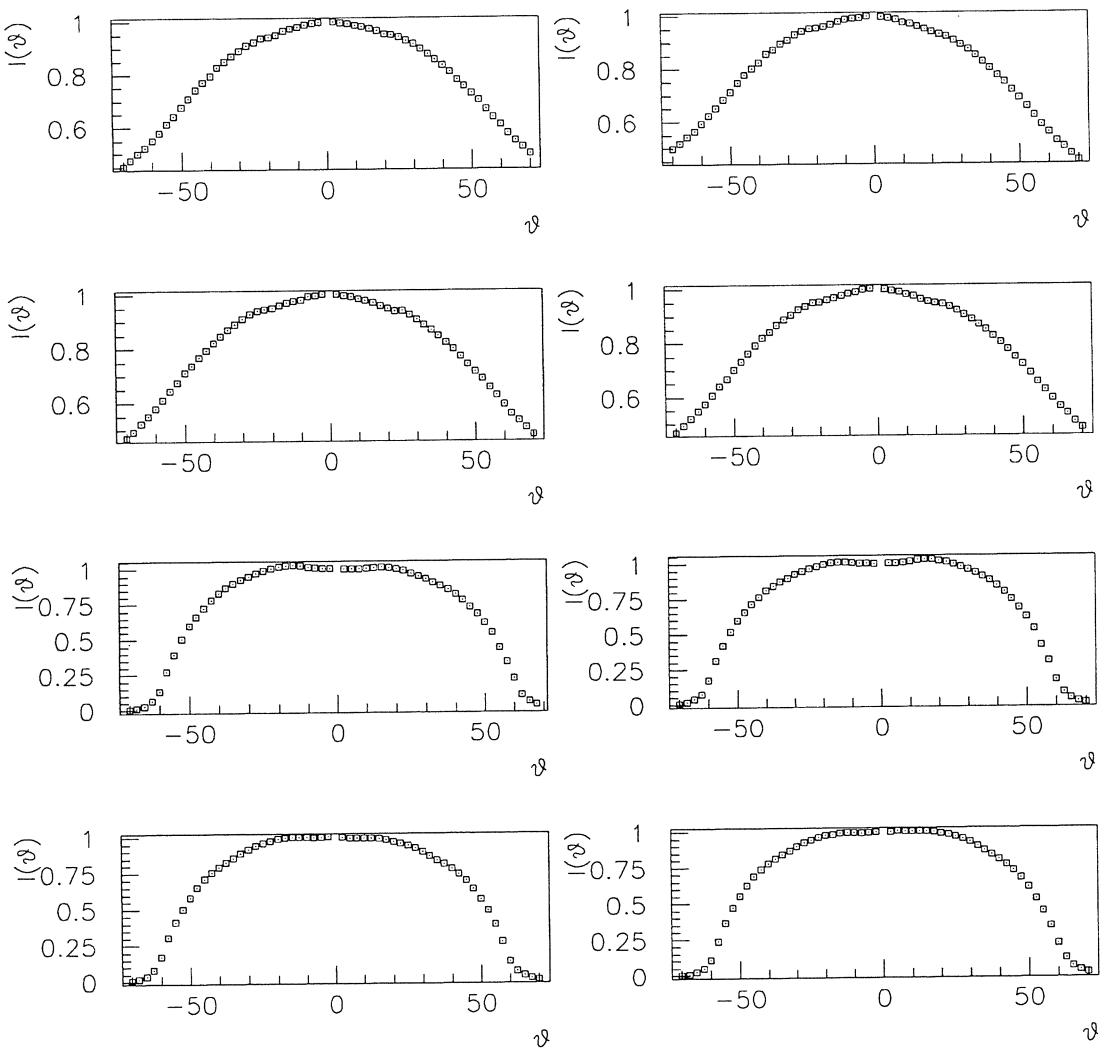

Figure 3.4: The results from the PMT measurements in air. Intensity is plotted against angle, normalised to 1 at 0 degrees. The orientations of the data sets are north, south, east, and west, repeated, as if reading from the top left. The top four results are taken with a mask in place, the remainder using SNO's concentrator.

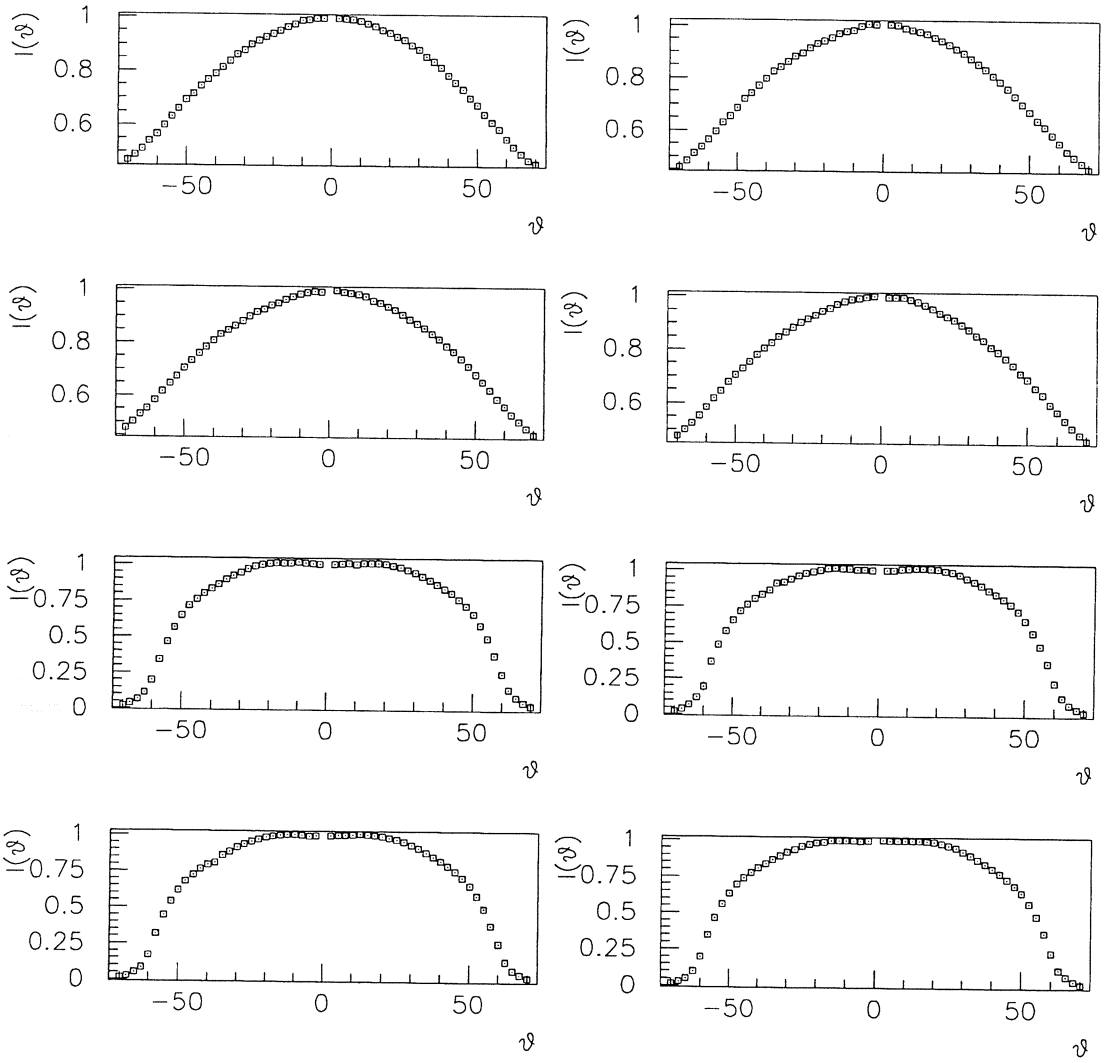

Figure 3.5: The results from the PMT measurements in water. Intensity is plotted against angle, normalised to 1 at 0 degrees. The orientations of the data sets are north, south, east, and west, repeated, as if reading from the top left. The top four results are taken with a mask in place, the remainder using SNO's concentrator.

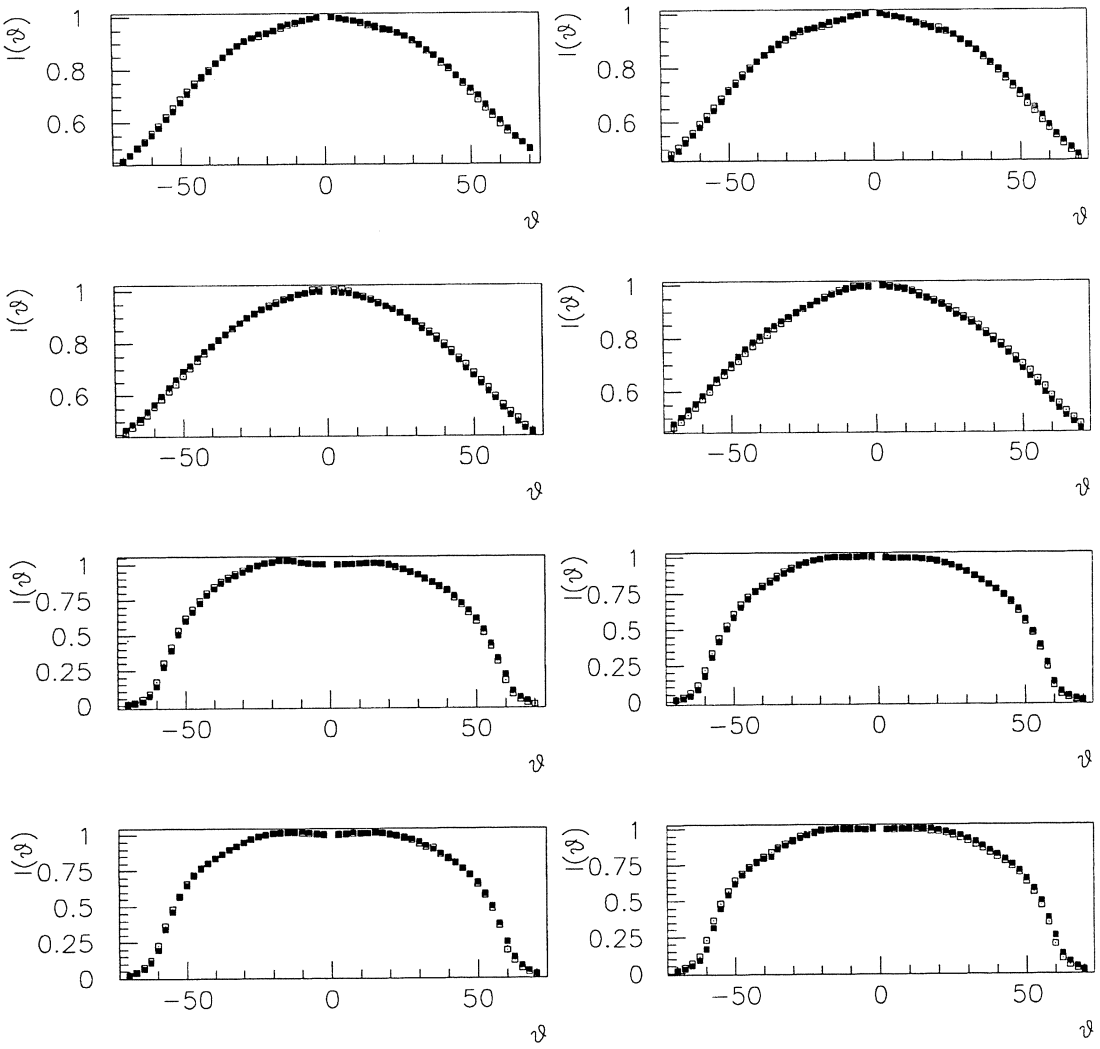

Figure 3.6: The graphs demonstrate the symmetry of the data under under reflection. Top four graphs show mask data, bottom four, the concentrator data sets. Left column shows the north data set with the south reflected and superimposed, right column shows the east data set with the west reflected. Rows show mask data and concentrator data alternately. The data are normalised just as before.

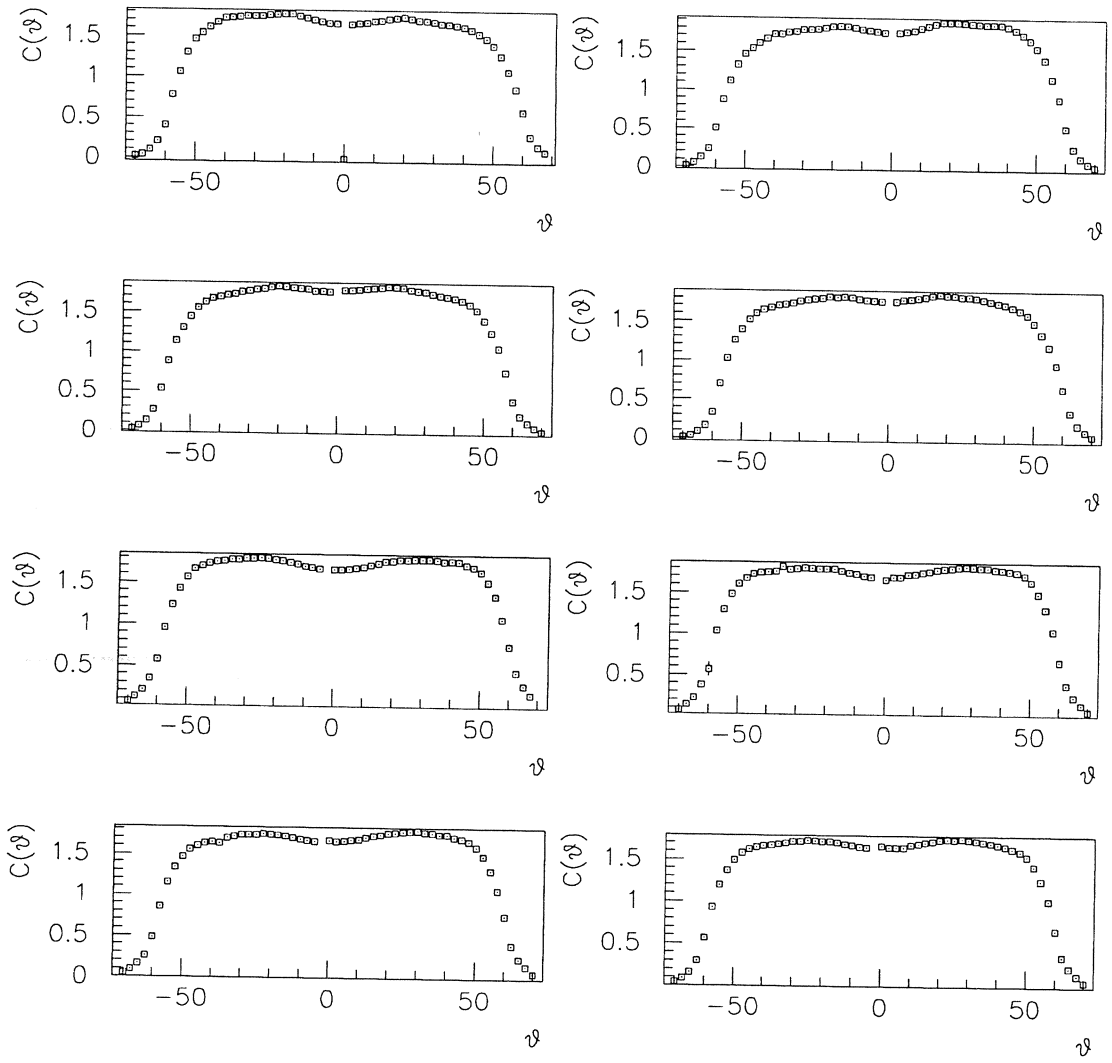

Figure 3.7: The concentration factors in air (top 4) and water (lower 4). When reading from the top, data sets are ordered north, south, east, west, north, south, east, and west.

Photomultiplier and Concentrator : Geometry

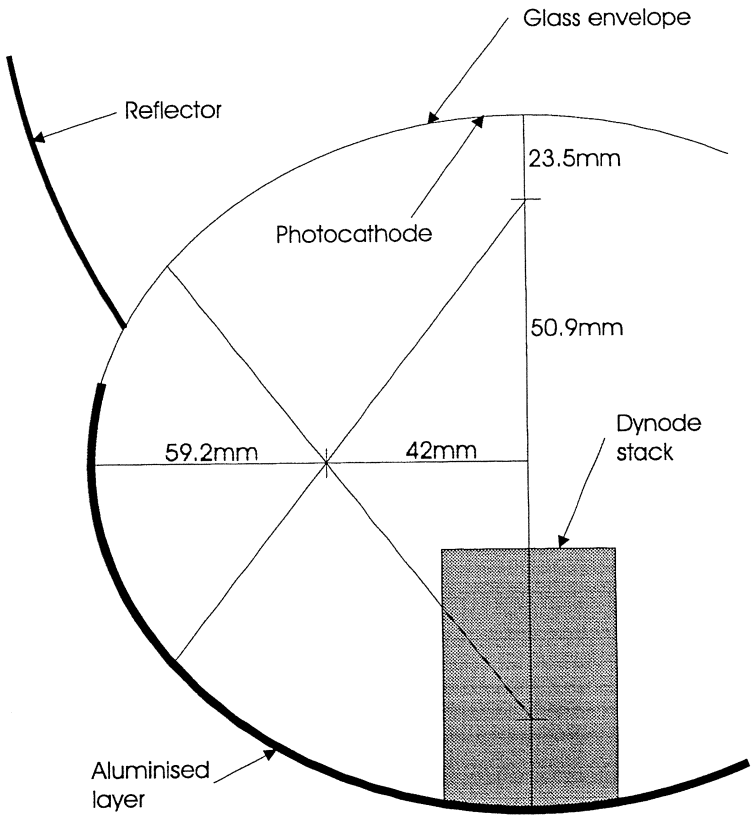

Figure 3.8: A schematic of the photomultiplier and concentrator design used in the preparation of Lay's computational model. Diagram reproduced with modifications from Lay [63].

Lay's modelling of the combined PMT and concentrator is very thorough. Although it was intended primarily for use in the SNOMAN program, it was easily adapted to provide a prediction for the performance of the PMT and concentrator arrangement in the bin. The bin, which was described in detail in Section 3.3, is modelled as a perfectly light-black container into which a spherical mirror is placed. The β-emitting source was assumed to be pointlike, although in reality it is a sphere of approximately 1cm in diameter. The source housing was modelled as a black cylinder 50mm in diameter, and the shadowing of the PMT front face by the source and housing was included in Lay's Monte Carlo model of the bin. The need to simulate the photon-spectrum of the Čerenkov source was avoided; Lay's simulation of the PMT and concentrator shows that their efficiency for the detection of single photons does not vary by more than 5% as a function of wavelength, independent of the angle of incidence. The comparison between data and model will assume the correctness of this result, and will by necessity compare only normalised quantities from the model with data.

It is this model whose results are compared with the data obtained by the author of this work. The predictions of the Monte Carlo of the bin experiment, together with an averaged data set (taken by combining the data from all four azimuthal orientations) are shown in Figures 3.9, 3.10, and 3.11.

It was realised that discrepancies might arise as a result of mispositioning the Čerenkov source. Lay modelled the effects of an error in the position of the source on the light collection efficiency of the PMT-concentrator arrangement, and the results are shown in Figures 3.12 and 3.13. Clearly, quite small displacements can alter the shape of the PMT-concentrator's response significantly. It was during this process that the realistic modelling of the spherical mirror was useful.

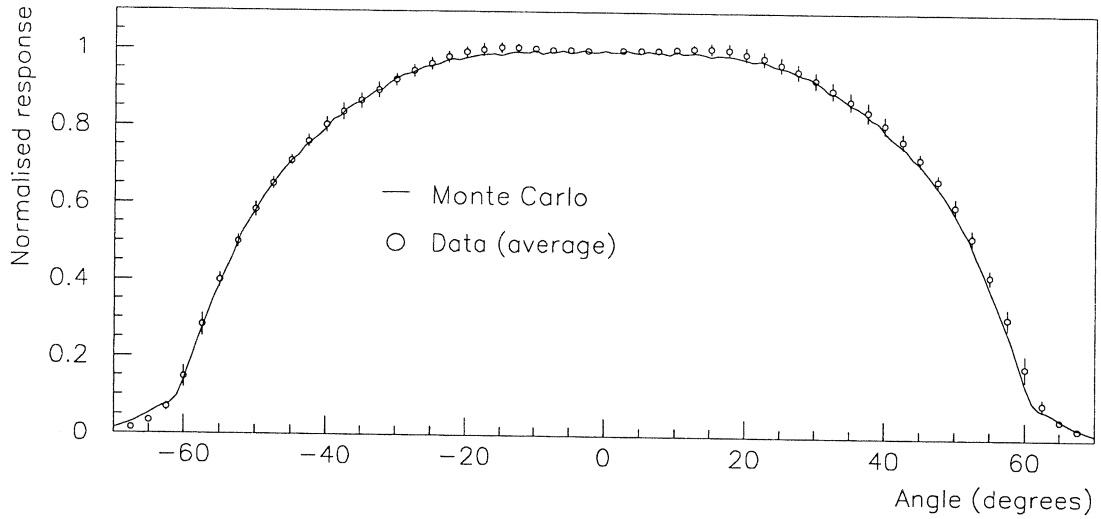

Figure 3.9: Lay's Monte Carlo model of SNO's concentrator and the R1408 photomultiplier in air agrees well with the experimental data collected.

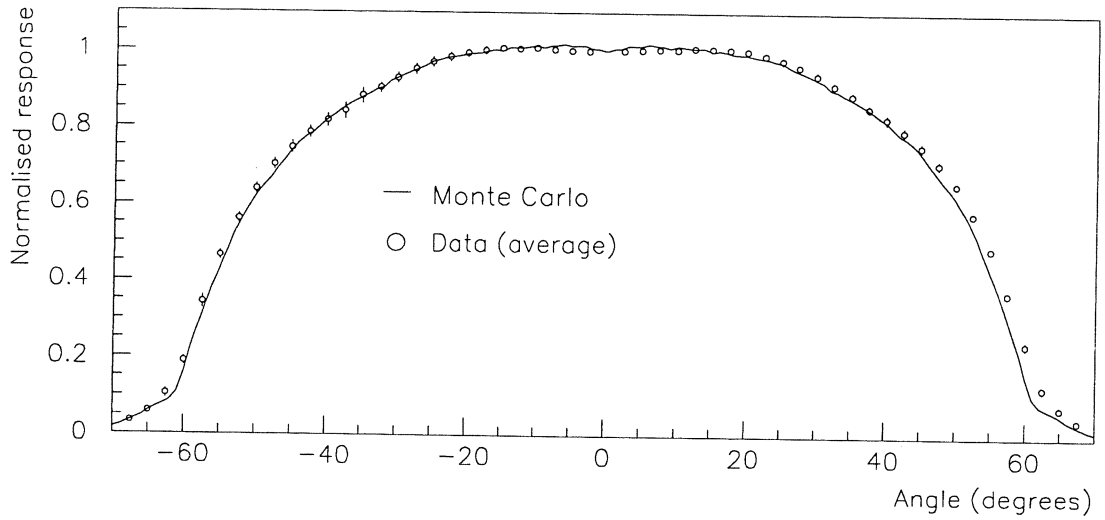

Figure 3.10: Lay's Monte Carlo model of SNO's concentrator and the R1408 photomultiplier in water agrees well with the experimental data collected.

A 2cm error in the positioning of the source is not considered likely, and therefore the plotted results indicate the extremal consequences of this error. It is believed to be this effect which is responsible for the small discrepancies between the Monte Carlo predictions and the data in the ranges $-55 < \theta < -30$ and $55 < \theta < 65$ in Figure 3.11. The Monte Carlo model used in preparing the results for that figure included a 5% increase in the absorptivity of the dielectric coated aluminium concentrator petals. A slight increase in light absorption is expected because the Monte Carlo neglects small effects such as the gap between neighbouring petals, and the spigots that retain them in position [95]. This reduces the light collection efficiency of the phototube by about 3%. It is clear from Figure 3.11 that the agreement between Lay's Monte Carlo model and the experimental data is very good.

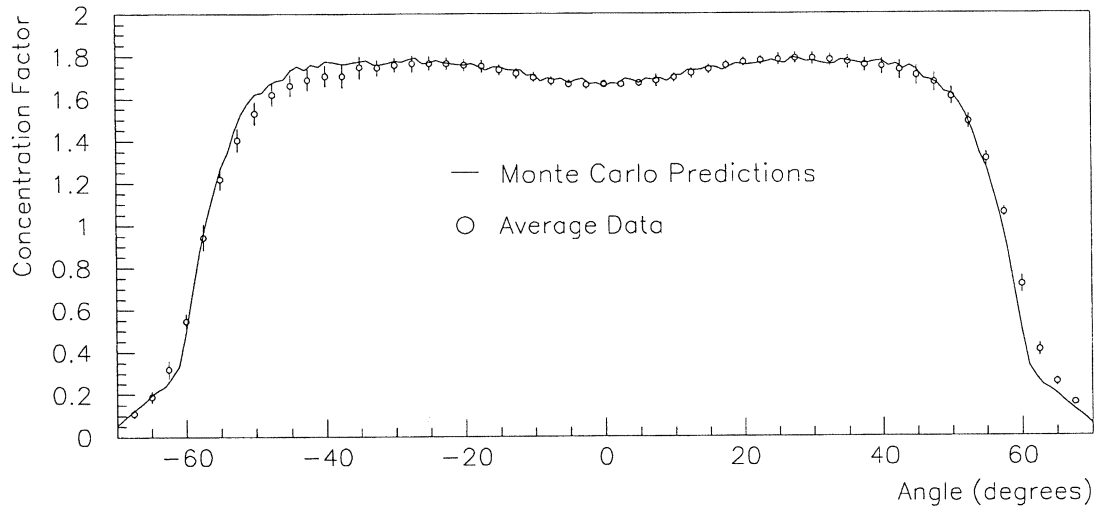

Figure 3.11: Lay's Monte Carlo prediction for the concentration factor in water agrees with the experimental data collected.

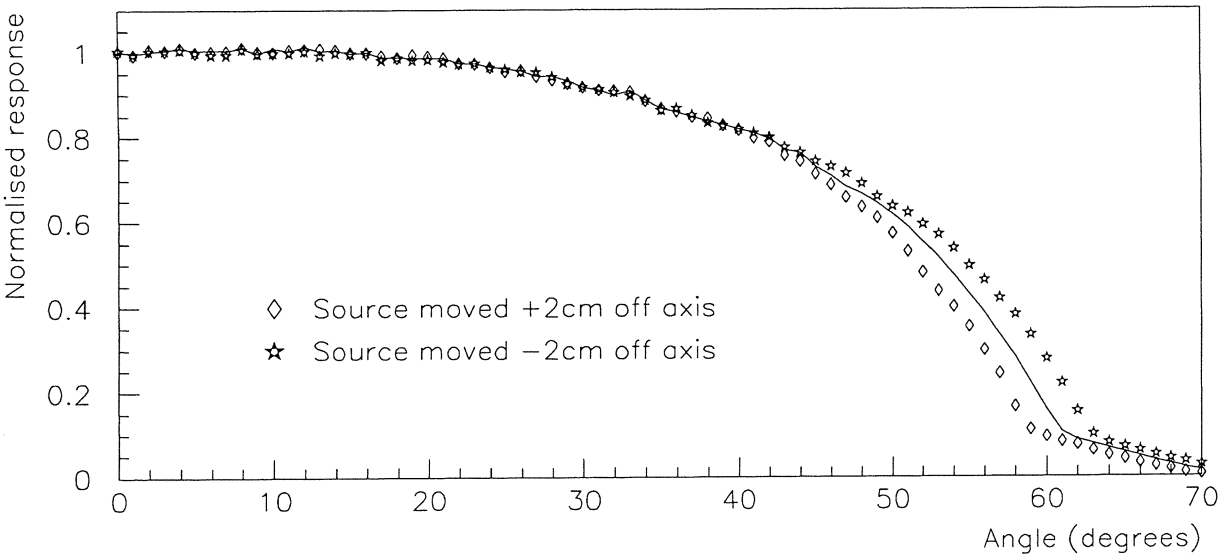

Figure 3.12: The effect of moving the source horizontally.

3.6 Conclusions

The angular response data gathered during this experiment serve to quantify the light gathering performance of the SNO PMTs as a function of angle. The strong similarity between all the air data sets, and separately between all the water data sets, suggests that an approximate azimuthal symmetry exists in the PMTs light collection efficiency. This is important to any model of the PMTs in SNO, meaning as it does that no significant error will be introduced either by assuming an azimuthal symmetry in the model, or by an ignorance of a PMTs orientation in the SNO detector. The reflection symmetry in the data indicates that the bin experiment is free of systematic variations in the illumination of the phototube-concentrator arrangement that might arise from the geometry of the bin itself. Overall, the data is of good quality, and most importantly, is very reproducible.

The results presented here have been used to verify Lay's Monte Carlo model [63] of the photomultipliers. Lay's model agrees well with the data at the 2% level, especially when systematic effects like an error in the Čerenkov source position are considered. The agreement between the experimental data and

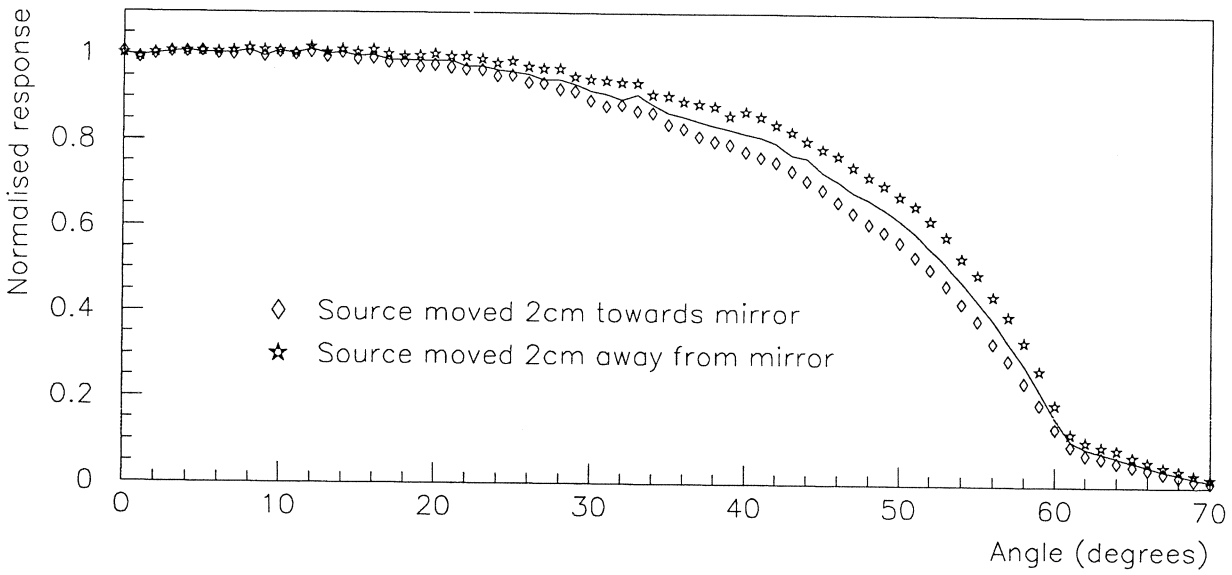

Figure 3.13: The effect of moving the source vertically.

Lay's model of the bin experiment gives some confidence that the behaviour of the PMTs will be well modelled in the SNO Monte Carlo. These results were first presented in a paper by Lay and Lyon [96].

Moorhead first measured the angular sensitivity and concentration factor for a prototype (24 petal) concentrator. Those measurements revealed a concentration factor for the performance plateau of $1.6 \rightarrow 1.7$ in water. The measurements presented here show that the production concentrators (18 petals) that will be placed in the SNO detector have a slightly better performance, as predicted. The plateau concentration factor is ~ 1.7. Moorhead's findings were slightly low because the petal area of the reflectors was slightly smaller. In all other respects, these measurements confirm Moorhead's findings. In particular, the two important design criteria, that the concentrators increase light collection inside the active volume of the detector, but decrease it elsewhere, and that the increase in light collection inside the active volume be roughly independent of angle, are met.

Chapter 4

Preparing Long Term Test Facilities for the SNO Experiment

4.1 Introduction and Purpose

Several components of the SNO detector are expected to suffer from water aided aging. It is known that pure water is highly corrosive [130]; water is an excellent solvent because of its high dielectric constant and very strong solvating power. Two examples of the effects of such corrosion have been;

1. production reflector petals have been subjected to accelerated aging tests. Initial results showed that the reflectivity of the dielectric coated aluminium falls upon aging by as much as 5% for wavelengths below 450nm [115]. More stringent test conditions and a less accelerated aging regime led to a mean loss of specular reflectance of only $1.2 \pm 2.3\%$ in a subsequent experiment [116]. It was realised that dissolved air in the deionised water increased the attack on some samples of dielectric coated aluminium. With the dissolved air removed, as it will be in SNO, and the water kept under nitrogen, the coated aluminium was much more robust, and survived immersion for 10 days at 95°C [117], which is approximately equivalent to 10 years at 8°C (see below).

2. Extensive testing of prototype rope for holding the acrylic vessel demonstrated that although aging did not occur in distilled water, a slight but significant loss of strength resulted from aging in de-ionised light water. The acrylic rope was replaced by VECTRAN, a material which is not susceptible to attack by ultra-pure light water.

The examples given here are illustrative and not exhaustive. The accelerated aging referred to above is brought about by increasing the temperature of the deionised water in which the samples were placed. By ageing samples at a variety of temperatures, it was found that reaction rates increase by a factor of 2.2 for each 10°C rise in temperature [117]. This is in accordance with the assumption that any physical or chemical ageing process would be governed by thermodynamic considerations [121]. Hence, it was assumed that a period of 10 days immersion at 95°C was equivalent to a time of the order of 10 years immersion at 8°C [95]. Only the possibility of a phase change in one of the materials renders this extrapolation to lower temperatures and longer times uncertain, but the results of [95] support the extrapolation.

The components of the SNO detector that are to be immersed in the SNO cavity have all been subjected to ultra-pure water survival tests. These tests can be criticised on two grounds:

1. the tests were not carried out using SNO quality water, which, while very pure, will have different residual contaminants to the water used in the tests; and,

2. the components were not subjected to survival tests on the same timescale as the SNO experiment.

As a result of the tests that have been carried out, certain critical components of the SNO detector are to be subject to observation throughout the lifetime of the experiment. It is not possible to immerse the tests in the SNO light water cavity for reasons of maintaining water cleanliness, ease of access and removal, and safety. A separate facility is needed whereby components of the SNO detector can be immersed for the duration of the experiment in conditions that are as similar as possible to those found in the SNO cavity. This chapter describes work done by the author in preparing such a facility (known

as the "test tank" facility). This facility is intended to be operational 6 months before the filling of the SNO light water cavity, so that any test component corrosion or failure will occur well in advance of a similar but potentially more serious event within the SNO cavity. Most test components will simply be immersed in the SNO ultra pure light water. The components will be extracted, blown dry with a gas (nitrogen or argon), packaged, and subject to testing elsewhere. Some components will be subject to mechanical stress. There will be three test tanks containing four tests:

1. samples of acrylic from the detector will be placed under stress;
2. a complete PSUP panel with PMTs and concentrators will be held under stress;
3. rope sections will be immersed; and,
4. reflector-concentrators will be immersed.

The rope sections will be held under a mild tension to keep the weave intact. A separate experiment will be constructed [118] to test the stress-related underwater ageing properties of the rope that supports the PSUP; the test includes one of the acrylic vessel panels with a rope groove that will support the whole acrylic vessel. This test cannot be accommodated in the test tank facility because of its large size and the considerable mechanical stresses involved.

In addition to the test tank facility, another apparatus has been designed in order to monitor the long term performance of the reflector-concentrators that are to be used in the SNO detector. This apparatus has been designed and built to overcome the deficiencies of the 'bin' (see Chapter 3) in performing very accurate comparative measurements. Doucas [114] has indicated that the empirical evidence suggests that petals which do suffer degradation in the accelerated ageing tests mentioned earlier do so in a relatively short period of time equivalent to $2 \rightarrow 3$ years in the SNO detector. As a consequence of this observation, it is intended that the concentrators that are submerged in the bin would be extracted and tested every $3 \rightarrow 4$ months in the first 3 years of detector operation, and every 6 months thereafter, surprises notwithstanding. This second apparatus will not be discussed any further in this thesis.

4.2 The Test Tank Facility

4.2.1 Design of the Test Tanks

The test tanks have been designed to meet several different requirements. Most of these requirements arise from the purpose of the test facility, that is, to mimic the conditions in the SNO cavity as closely as possible. The water in the SNO cavity is at approximately 10°C, and has been degassed and purified by ion exchange, filtering, and exposure to ultraviolet light (to kill biological contaminants) before entering the cavity [119, Section 2.2]. The similarity between the water in the SNO cavity and the test facility would be complete if three conditions could be met. These are:

1. the temperature in the test facility is the same as that in the SNO cavity;
2. the water purity in the test facility is the same as that in the SNO cavity; and,
3. the water flows at the same rate over the specimens in both the test facility and the SNO cavity.

In addition, the test tanks must minimise their effect on the light water recirculation loop, especially with regard to contamination of the water by radionuclides.

The temperature in the test facility will not be identical to that in the SNO cavity. This is because the water used in the test tanks will not be actively cooled (there is insufficient space in the mine for the equipment that would be required) and therefore its temperature will rise in response to heating by the environment. The water for the test facility is extracted from the main water circulation/cooling/purification loop and flows through about 30m of plastic piping which is surrounded by air whose bulk temperature is approximately 25°C. The low flow-rate and high surface to volume ratio mean that significant temperature changes could occur. The water then enters into one of the three test tanks. The tanks are 'turned over' in about 3 days. This rate is sufficiently slow to allow considerable heat to enter the tanks from the surrounding environment if they are not properly insulated.

Insulation of the pipes is a difficult issue in the Creigton mine - most insulation is either flammable (foam based), and may release poisonous fumes which in the event of a fire would endanger the lives of scientists and miners alike, or it contains particulate matter (fiberglass-like insulation) which, if it were to

become airborne, could contribute to radionuclide contamination in the SNO enclosure. Insulation also greatly increases the diameter of the pipework, for which there is relatively little space already. A suitable insulation material has been found, and it is a fire retardant foam manufactured by Instapak-Floral with a thermal conductivity of 0.3BTU hr^{-1} in ft^{-2} $°F^{-1}$), or 0.043W m^{-1} K^{-1} [108].

Obviously there are a number of difficulties associated with maintaining the temperature of the test tanks at an acceptably low level. These problems, and the closeness with which the conditions in the test facility do match those in the SNO cavity, will be discussed in a separate section.

The materials used in the construction of the test tank facility have been chosen in line with the recommendations of the SNO Water Group [119, Section 1.1.1]. The majority of the piping will be built on-site from SNO approved materials (polypropylene pipes and polyurethane valves), which have been selected as the best compromise between price and the requirement that contamination by leaching from the pipes into either light or heavy water be minimised. Contamination of polypropylene by radionuclides is generally lowest when fillers, colouring agents, and other additives are kept to a minimum. The test tanks have therefore been manufactured from unfilled polypropylene. Forbes Plastic Tanks and Environmental Technologies, from whom the test tanks were commissioned, were not able to manufacture the piping attached to the test tanks from unfilled polypropylene, and filled polypropylene was used in its place. In the case of the test tanks this is not felt to be a serious concern, since the pipe surface is less that a percent of the total surface of a test tank, and the water will be purified before being returned to the cavity. Contamination by radionuclides is a very small effect which will not have any effect on the chemical processes in the test tanks. The test tanks are part of the light water water recirculation loop, however, and hence such contamination must be minimised. Radon gas has been found to be entering the light water system through valves and 'O' rings. The diffusion rate for a 2" valve is 4.0 radon atoms per hour (Rn h^{-1}). This compares with a total acceptable rate of 45Rn h^{-1} [119, Section 2.6]. Once again, this is not a problem insofar as the water purity of the test tanks is concerned, but it would become a problem if the water was to be recirculated into the SNO light water cavity. Partly for this reason, the test tank facility has been positioned before the Process Degasser in the light water circulation loop (the Degasser reduces the Rn content of the light water by about a factor of 50 [119, Section 2.7.4]) and this means that the presence of valves and 'O' rings in the test tanks is not critical. The facility has none-the-less been designed to minimise the number of valves present in it. As a result of the facts presented here, the water purity in the test tank facility is expected to be essentially the same as the light water exiting the SNO cavity. The exit pipe from the cavity is positioned close to the PSUP region (see Chapter 2) and so the water arriving in the test tanks is essentially the same as that exiting the PSUP region.

The rate that water flows over the specimens in the test tanks can, of course, be matched to the rate at which the water flows past some point in the SNO cavity. Most of the components that are to be tested in the test tanks lie about 8.5 meters from the centre of the detector, and are part of the photomultiplier sphere or its support structure. The test tanks are being designed to mimic this region of the detector most closely. 200 litres of water will flow through this region every minute, and hence the mean flow velocity will be 3.7×10^{-4} cm s^{-1}. This means that the contents of the test tanks will be "turned over" in about 3.1 days.

4.2.2 Detailed Discussion of the Design of the Test Tank Facility

The test tank facility has been designed to prevent contaminants entering the water after it has left the SNO cavity. In particular, this has meant that the tanks must be sealed to prevent contact with the surrounding air. Sealing the tanks is not enough: either a covering gas must be provided to fill the volume of the tanks not filled by the water, or the tanks must be operated without any gas remaining in them. In the SNO cavity, nitrogen cover gas is provided above the D_2O, and a similar arrangement was considered for the test facility. This arrangement was rejected because of the additional pipework that would be necessary, and because of the difficulty in opening the tanks to examine and replace samples without venting N_2 gas, a serious safety issue when working in a confined space underground. Therefore the test facility will be entirely water-filled.

A schematic diagram of the test tanks is shown in Figure 4.1. Throughout the remainder of this section, particular features of the test tanks and surrounding apparatus will be given a number or a letter. These numbers and letters are marked on the relevant figures. Two detailed diagrams exist, one of a test tank and one of the return tank. Both will be referred to explicitly where appropriate. It is hoped that the reader will find the text easier to follow as a result of the marking of the figures.

The test tanks (Figure 4.2 and labelled 4 in Figure 4.1) have been designed to be opened and so they have been provided with a lid (labelled 7 in Figures 4.1 and 4.2). The lid contains a displacement volume

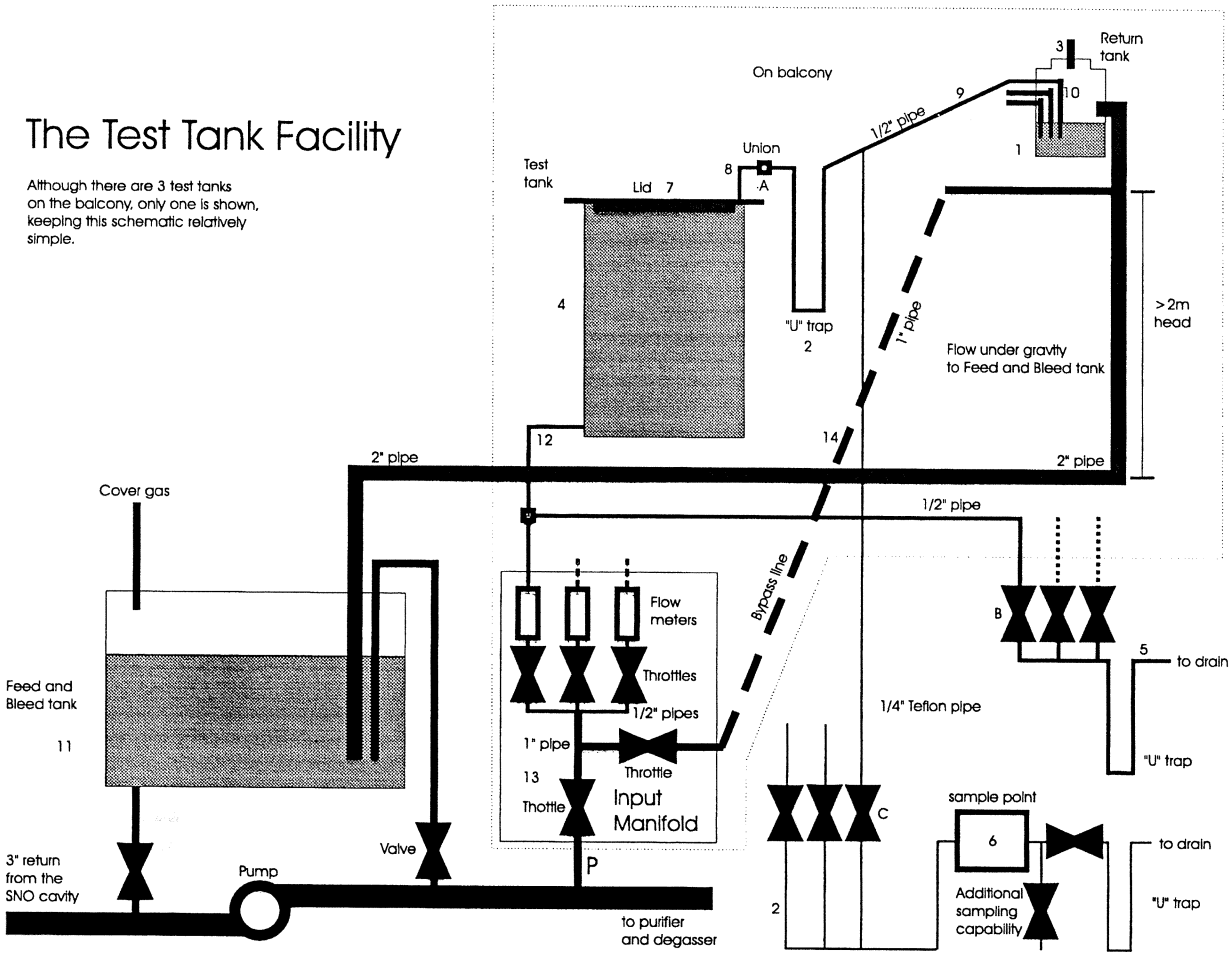

Figure 4.1: A schematic diagram of the test tank facility.

so that when a test tank is opened and the lid removed, the water falls away from the top edge of the tank. The lid-to-tank seal is accomplished by means of a large "O" ring with a PTFE jacket that clothes its inner edge. The PTFE jacket prevents the "O" ring from coming into direct contact with the water in the tanks. The feed pipe (12 in Figures 4.1 and 4.2) enters the tank at its base, and is terminated by a diffuser so that the cold water entering the tank mixes well. The tank exit pipe (8 in Figures 4.1 and 4.2) is flush with the lid so that no air can remain in the tank during normal operation.

The water exiting the test tanks is normally piped to a return tank (Figure 4.3 and labelled 1 in Figure 4.1), where a nitrogen cover gas is provided. The nitrogen in this tank is at few inches above atmospheric pressure, and it is prevented from escaping from the tank by water filled "U" bends (2) in all the pipes leading into it. The water outflow pipe from the return tank leads to the "Feed and Bleed" tank (11) which is used to control the water level in the SNO cavity, and which also has a nitrogen gas blanket. A cover gas (the feed pipe for which is labelled 3 in Figures 4.1 and 4.3) can be used in the return tank because is not intended to be opened.

The water exiting the test tanks (Figure 4.2 and labelled 4 in Figure 4.1) will flow into the return tank in the standard mode of operation, but it may instead be taken directly to drain (5) or to a sampling point (6). The drain and the sampling points are positioned about 10 feet below the test tank outlets, and the extremely slow flow of water through the tank outlet pipe (8 in Figures 4.1 and 4.2) will ensure that water will flow preferentially down to them rather than to the return tank whenever it is able. The sample point is isolated from the return tank and the test tanks by one or two water-filled "U" bends (2) that prevent air entering the system or nitrogen gas escaping it.

The pipes leading from the test tanks (4) to the return tank are inclined slightly to the vertical to ensure that they are full of water at all times (9). This dramatically reduces the surface area of the water that is in contact with the cover gas, and hence it reduces the amount of the N_2 cover gas that dissolves in the water. The outlet pipes from the test tanks enter the return tank horizontally and are joined to a vertical pipe that is open at both ends (10 in Figures 4.1 and 4.2). This pipe penetrates down into the reservoir of water in the return tank. This design has been used to ensure that no water can be sucked

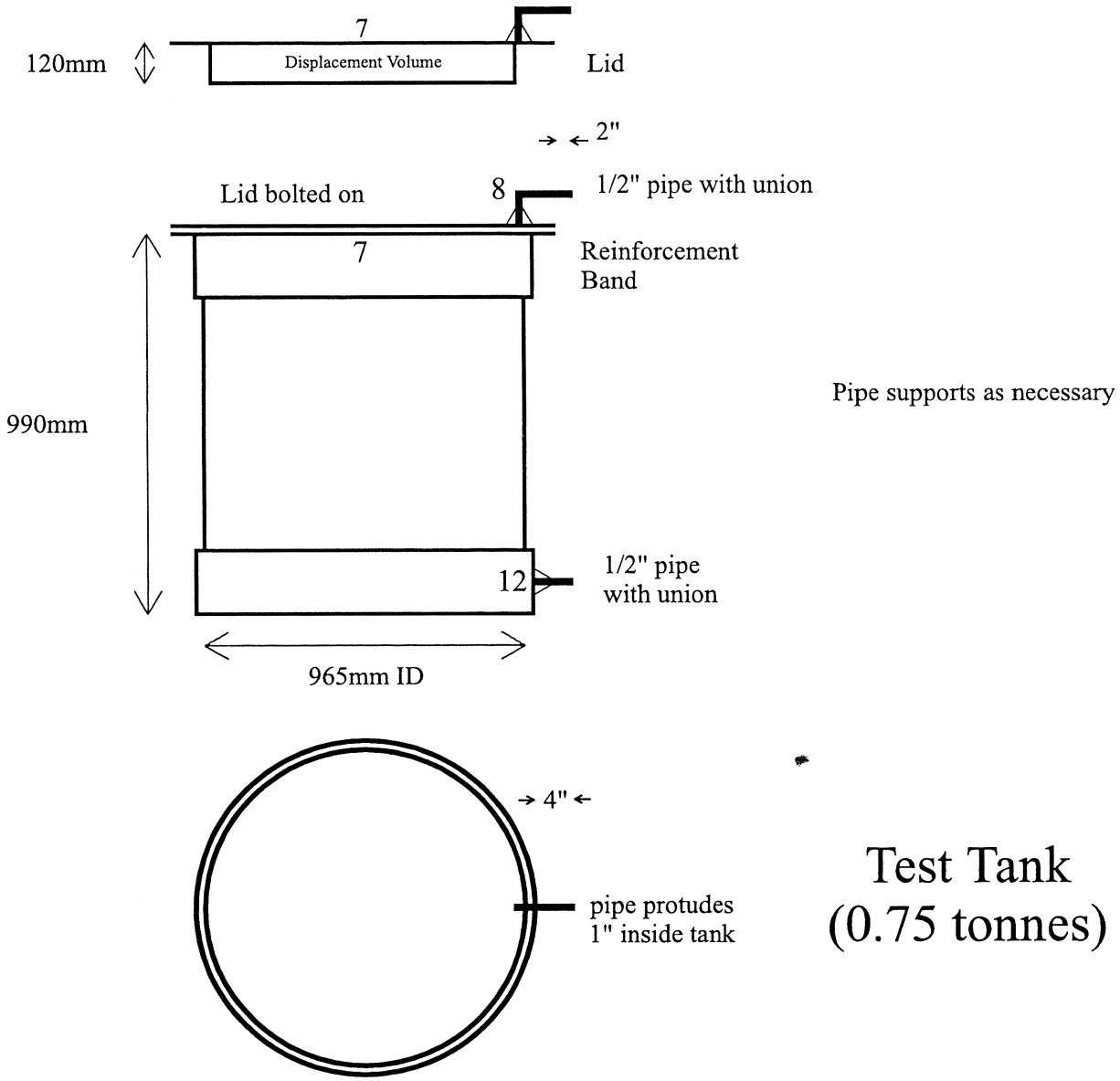

Figure 4.2: An example of a 3/4 tonne test tank.

back out of the return tank to the test tanks when they are emptied, and to prevent splashing in the return tank (due to its surface tension, the water will ride down the sides of the pipe into the return tank). This precaution has been taken to limit the amount of nitrogen dissolving in the water, and hence to avoid unnecessary loading of the water degasser used in SNO.

These flow options will allow the tanks to be opened to the air (dramatically reducing water quality as CO_2 dissolves rapidly in the water [117]) for the inspection of or removal of samples. The tank will then be closed, and water from it will then be taken to a drain through the sample point, where a conductivity or a pH meter will be used to assess the water quality until it has returned to a level such that it can be allowed to return to the "Feed and Bleed" tank (where water resistivity has a nominal value of $\sim 18M\Omega$ and a pH of 7 [119, Section 2.2]), and hence rejoin the main light water recirculation loop. In this way, serious loading of the light water purification loop can be avoided.

The need to keep the temperature of the water arriving at the test tanks as similar to that in the SNO light water cavity as possible without the use of a refrigerator means that water must flow as quickly as possible from the main 3" pipe carrying water from the SNO cavity to the input manifold of the test tank facility (13). The increased flow rate causes the volume of water arriving must be much larger than that passing through all 3 of the test tanks (see Section 4.2.3). The surplus water volume is piped through the bypass line to the test tank facility exit pipe. This pipe takes water from the bypass line and the return tank and returns it to the "Feed and Bleed" tank under gravity. The volume flow rate in a pipe

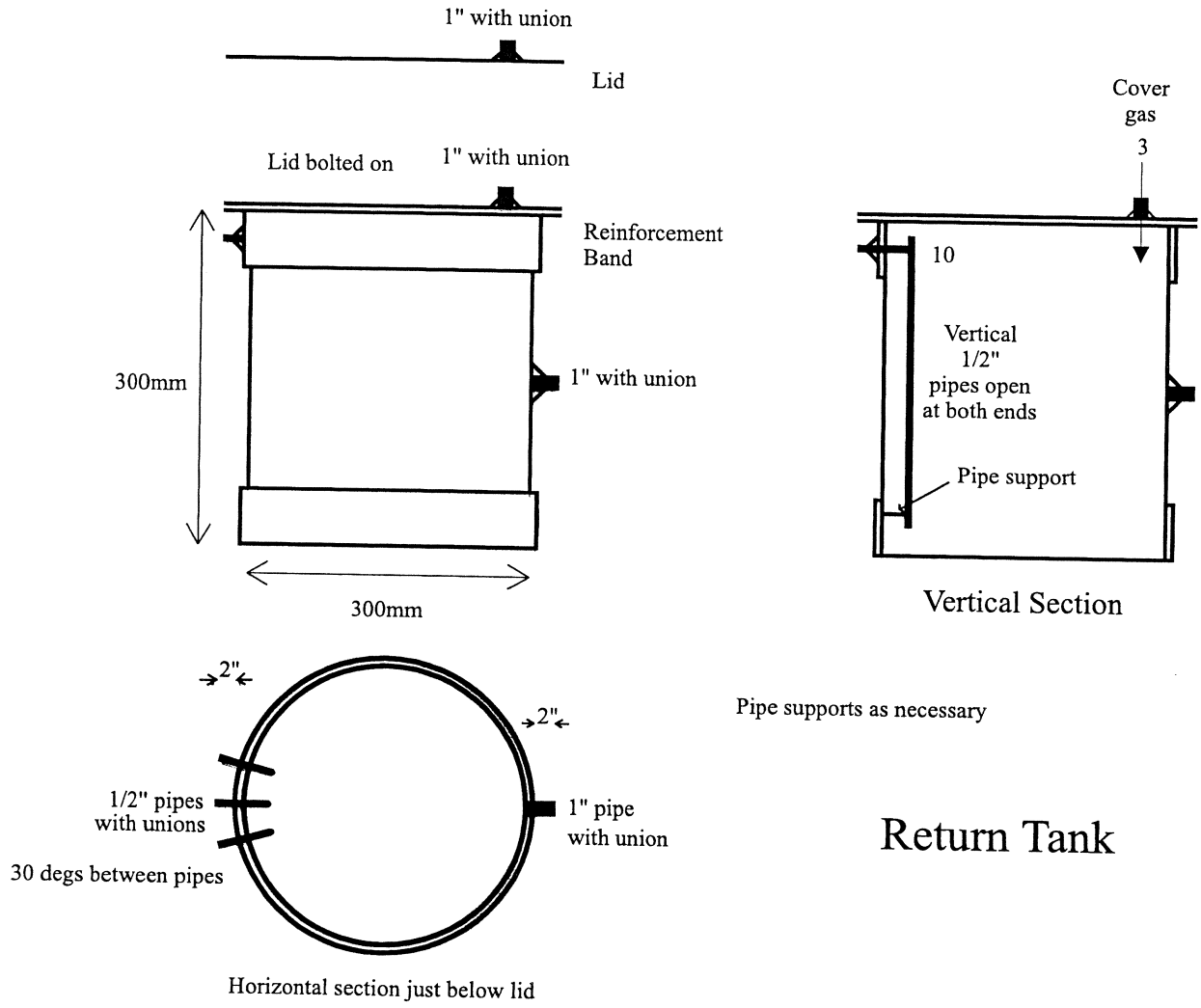

Figure 4.3: The return tank.

for a fixed pressure difference is [107];

$$Q = \frac{\pi R^4 \Delta p}{8 \mu L} \ , \tag{4.1}$$

where Q is the volume flow rate, R is the radius of the pipe, Δp is the pressure drop along a length L of the pipe, and μ is the viscosity of water. Q is a known quantity; from Section 4.2.3, to keep the water temperature low, the flow will be about 6 times that required to supply the test tanks (1.54cm s^{-1} in the 1" input manifold feed pipe). The formula $\Delta p = \rho g h$ relates the height of a column of water to the pressure developed at its base. From these relations, the height h required to drive the water through the exit pipe under gravity at the given rate is;

$$h = \frac{48 R_1^2 \overline{v} \mu L}{R_2^4 \rho g} = 1.12\text{m} \ . \tag{4.2}$$

The height given assumes that the exit pipe is 2" in diameter ($R_2 = 5.08$cm), and that the feed pipe to the input manifold is 1" in diameter ($R_1 = 2.54$cm). In order to allow for an increase in the flow rate required due to unforeseen circumstances, it is recommended that $h > 2$m. This can be achieved by raising the return tank as high as is possible.

The test tank operational procedure is simple:

1. Open flow control valve B, allowing water from the test tank to flow to drain.
2. Open union A and slowly drain the water from the test-to-return tank pipe (pipe 9), allowing the lid of the test tank to be removed. Air and nitrogen gas are prevented from mixing by the water filled "U" bend (2).

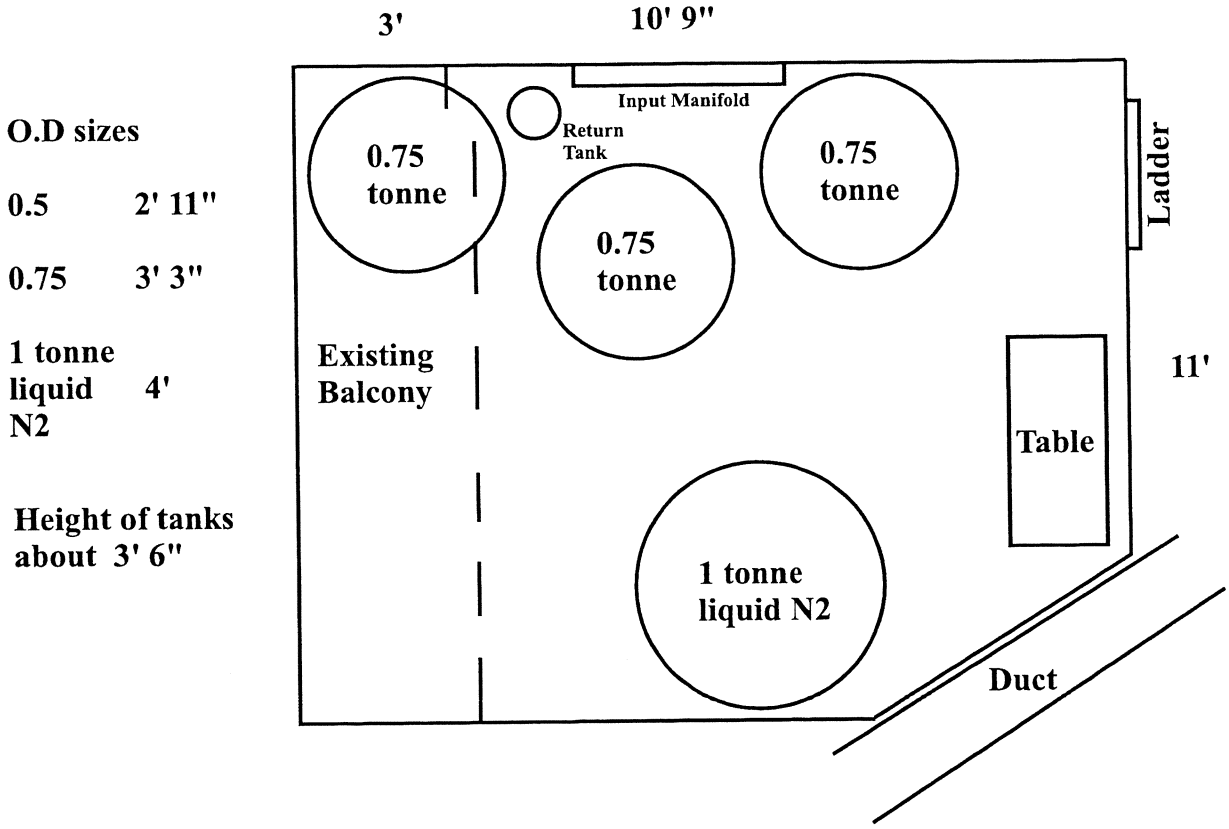

Figure 4.4: The relative location of the test tanks and the return tank.

3. Remove the lid of the tank (7), and insert, remove, or inspect an experiment.
4. Replace the lid of the tank.
5. Close union A.
6. Open valve C, allowing water to go to the sample point.
7. Close Valve B. Water will now flow to the sample point under gravity.
8. Monitor water quality in the tank at the sampling point until its purity is good enough to allow the water to be returned to the "Feed and Bleed" tank.
9. Close valve C. The tank is now in its normal mode of operation.

A balcony has been constructed to hold the test tanks and a nitrogen dewar. The nitrogen dewar is not part of the test tank facility, rather, it provides the nitrogen which is used as a cover gas throughout the SNO experiment. The balcony is shown in Figure 4.4. A photograph of a completed test tank has also been included (see Figure 4.5).

4.2.3 Thermal Conditions in the Testing Facility

It is desirable to have conditions within the test facility as similar as possible to those within the light water region of the SNO cavity itself. To this end, water will be drawn off the output pipe leading from the SNO cavity, through a 30m long horizontal pipe (labelled P in Figure 4.1) and directed into the test tanks. During this period the water, which exits the SNO cavity at a temperature of $\sim 10°C$, will undergo heating from the surrounding environment, where the mean temperature is about 25° centigrade. The water will then enter the test tanks where it will remain for a period of approximately three days, and again be heated.

Two questions arise concerning the temperature of the water as it flows slowly through the test tanks, and in the pipes leading up to the test facility. These are (overleaf):

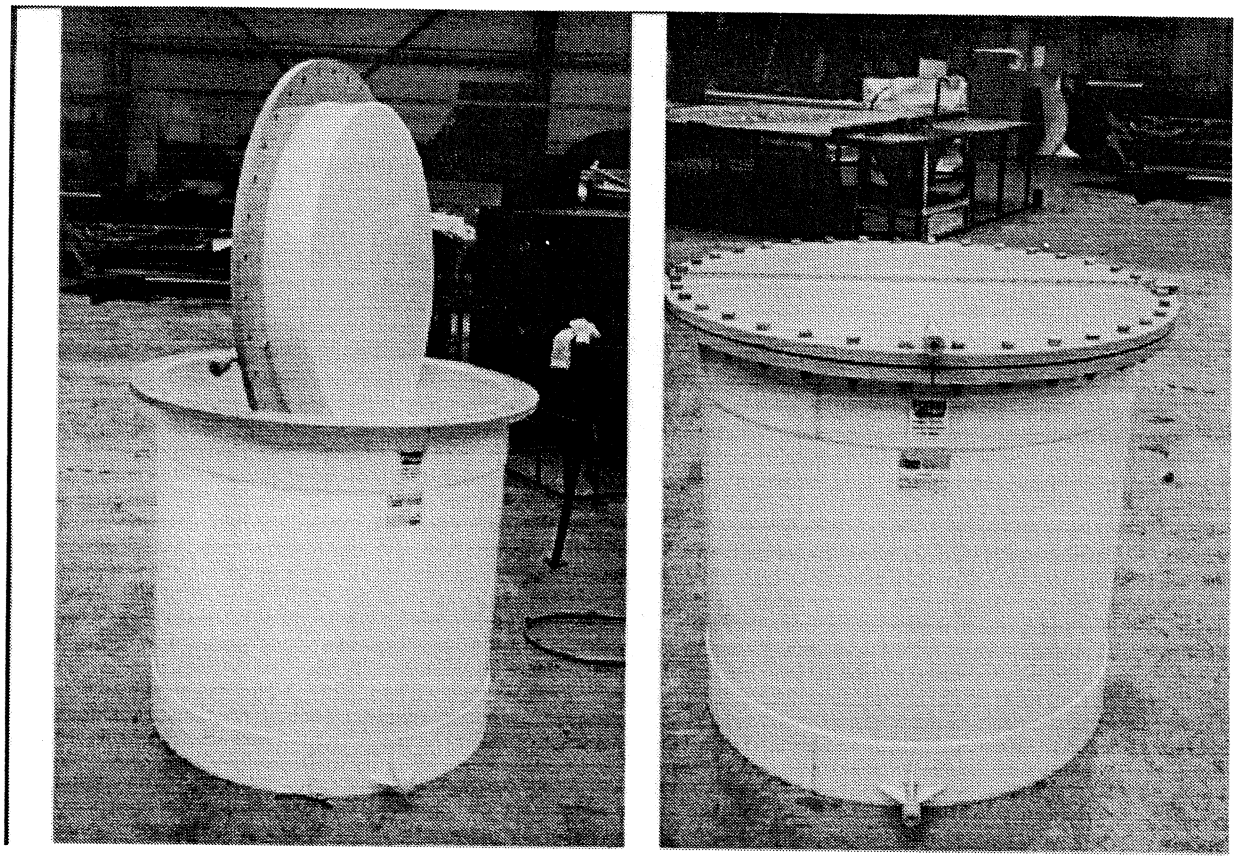

Figure 4.5: A photograph of a test tank, provided by Forbes.

1. What is the temperature of the water upon its arrival in the test tanks?

2. What is the equilibrium temperature of the test tanks themselves?

The first of these questions can be addressed by considering the heat gained in a pipe through which cold water flows very slowly. The water in the pipe is subject to heating by forced convection. The pipe itself, or more accurately, the insulation surrounding it, is subject to heating by free convection. This make the calculation of the heat lost from the pipe and the consequent temperature loss of the water in the pipe somewhat involved. The calculations are given in their entirety in Appendix B, where it is shown that it is reasonable to expect a temperature rise of the order of 1°C or less when 1cm of insulation is used and the water flows at $4 \rightarrow 6$ times the nominal rate.

The temperature rise in the test tanks is also calculated in Appendix B, as it also involves heating of the test tanks by free convection. The expected equilibrium temperature of the test tanks, when insulated with 5cm of Instapak-Floral foam, is 287°K. This is a temperature rise of 3°C for the water entering the tanks. This slight temperature rise cannot be avoided in view of the restricted water flow conditions required in tanks, and the purity requirements of the water found there, although it did lead to the consideration of a water jacket for the test tanks to further restrict the temperature rise. The cold water from the bypass line would have been used. Unfortunately the water jacket option proved to be too expensive. There is a possibility that this unavoidable rise in temperature (and hence reaction rate rise) will be matched by a slightly increased flow rate to produce a facility which mimics the conditions found in the PSUP region of the SNO detector but with an accelerated time constant.

4.3 Conclusion

The test tank facility will satisfy the design requirement of providing conditions similar to those within the SNO cavity. The four aims of the design, namely:

1. that the water purity in the test tanks be similar to that in the PSUP region of the SNO light water cavity,
2. that the water flow rate over the components under test be the same as the water flow rate in the PSUP region,
3. that the test tanks have little or no effect on the contamination of the light water system by radionuclides, and
4. that the water temperature also be similar,

will be met. There is sufficient redundancy in the design of the test tank facility to cope with a limited range of unexpected thermal conditions in the mine. The test facility, correctly operated, presents no threat to the purity of the SNO light water.

The test tanks have been commissioned and built, as has the balcony to support them in the INCO mine (where the SNO experiment in situated) in Canada. The facility will begin operation 6 months before the light water fill of the SNO cavity begins. This will give ample warning of any component failure.

Chapter 5

Modelling the Photodisintegration of the Deuteron in the SNOMAN Program

5.1 Introduction

Photodisintegration of the deuteron, $d + \gamma \rightarrow n + p$, is the principle background to the measurement of the neutral current rate in SNO. It will occur in the SNO detector in normal operation due to the β-γ decays of ^{208}Tl and ^{214}Bi, and during calibration when the 20MeV γ-ray source is in use. This chapter describes the work done by the author in modifying the SNOMAN (Sudbury Neutrino Observatory Monte Carlo and ANalysis) program to accommodate deuteron photodisintegration. This is a two step process; firstly the cross section for the process must be determined from the best available theory and data, and secondly it must be inserted into the SNOMAN code. In this presentation these steps will be described in reverse order.

Against the prevailing opinion of the time, the author determined that it was possible to introduce photodisintegration into SNOMAN without either making an approximation or modifying the FORTRAN code responsible for the calculation of the γ-ray physical interaction cross section, which was not provided by the authors of the SNOMAN program. This is important because it avoids the possibility of the introduction of an error into that code.

Photodisintegration is always less than 0.6% of the γ-ray interaction cross section. This is demonstrated in Figure 5.1, where the γ-ray interaction cross section (mostly Compton scattering and to a lesser extent pair production), the photodisintegration cross section, and the ratio of these two quantities are shown as a function of γ-ray energy. It might be thought that only a rough model of photodisintegration is required for the SNOMAN code, since it is such a small part of the total γ-ray cross section. However, there are objections to this approach. Firstly, while the fraction of γ-rays that photodisintegrate deuterons in the SNO detector is small, the number of such photodisintegrations is not (see Chapter 9). Secondly, the simple model of photodisintegration which is accurate near threshold is inaccurate at the 10% level for γ-rays with energies greater than 10MeV, a fact which has more significance for the high energy γ-ray calibration sources than it does for the normal operation of the SNO detector. In addition to the objections, there is one major advantage to be gained by a close comparison of the photodisintegration cross section with the experimental data; an error on the cross section can be determined.

Above 10MeV and below 20MeV there is a gap in the literature regarding deuteron photodisintegration. At higher energies there has been a great deal of theoretical and experimental work. The high energy experimental work has been plagued by systematic errors, and a few groups have summarised the data by obtaining phenomenological fits. Those fits extend down to 20MeV. Below 10MeV, a simple formal theory of the d(γ,n)p reaction gives an adequate description of the data. In this chapter, after a discussion of the computational aspects of deuteron photodisintegration, the relevant experimental data, the formal theory, and the best phenomenological fit will be presented. It will be shown that neither the theory nor the best phenomenological fit are adequate in the $10 \rightarrow 20$MeV region, and a new fit to the data will be carried out. An estimate of the error on the cross section will be made. Finally, a crude angular distribution will be deduced for SNOMAN.

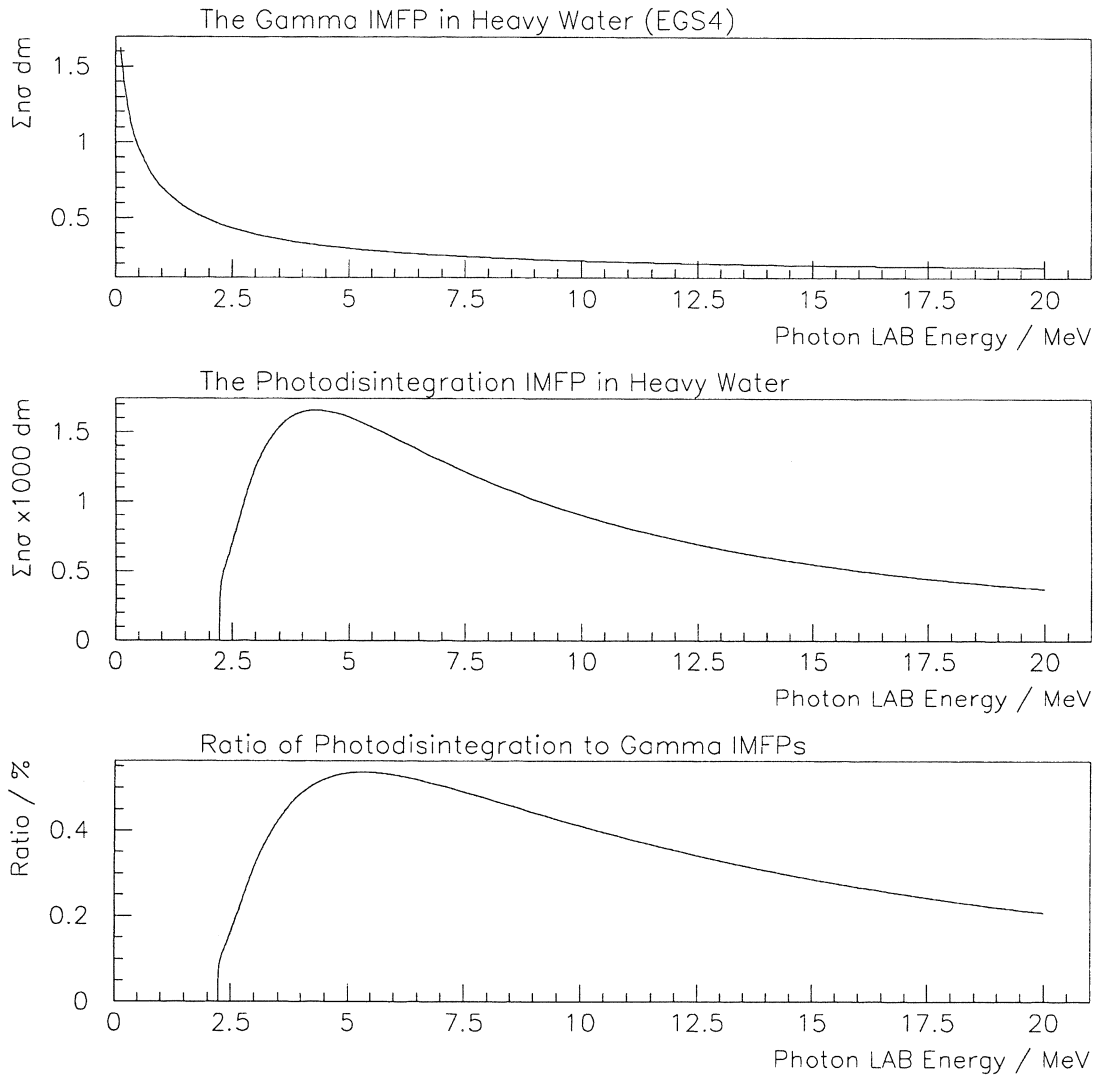

Figure 5.1: The photodisintegration inverse mean free path (IMFP) is never more than 0.6% of the standard γ interaction IMFP. The inverse mean free path, x, is defined as $1/\overline{x} = \sum n\sigma$, where the sum is over all the nuclides in the medium through which the γ-ray is passing, n is the number density of each nuclide, and σ is the interaction cross section.

5.2 Computational Aspects of the Photodisintegration Model

Within the SNOMAN program, the propagation of electrons, positrons, and γ-rays is undertaken by the EGS4 (Electron Gamma Shower) code. The authors of SNOMAN are not the authors of EGS4. The requirements that the EGS4 code must satisfy as a part of the SNOMAN program and the extent to which EGS4 meets those requirements have been evaluated by Lay [63]. A concise summary of the methods used by EGS4 in modelling the physical processes that occur during particle propagation has been given by Lay [63], and a full description is available directly from the EGS4 manual [65].

A central part of the EGS4 particle propagation code is the calculation of the mean step length between interactions. The mean free path is used to calculate the distance to the next interaction by sampling from an exponential distribution (see Appendix C). For a γ-ray, the calculation of the mean free path is particularly simple, because γ-rays do not suffer continuous energy loss like charged particles such as electrons. The γ-ray mean free path between discrete interactions is;

$$\frac{1}{\overline{x}} = \sum_i n_i \sum_j \sigma_{ij}(E_\gamma) \ , \tag{5.1}$$

where $\lambda = 1/\overline{x}$ is the interaction probability per unit length, $\overline{x}$ is the mean free path between interactions, n_i is the number density of the ith nuclide, σ_{ij} is the cross section for the jth interaction with the ith nuclide, and E_γ is the energy of the γ-ray being propagated. The summation over i in Equation 5.1 indicates summation over all the nuclear species in the medium through which the γ-ray is being propagated, while the summation over j is over all the interactions known to the EGS4 code between the ith nuclear species and the γ-ray of energy E_γ.

EGS4 models the photoelectric effect, Compton scattering, pair production, and coherent Rayleigh scattering for γ-ray propagation. It does not model deuteron photodisintegration. As a result of the EGS4 code ignoring the photodisintegration reaction, propagation of a γ-ray through D_2O is incorrectly carried out on two counts:

1. The mean interaction length is overestimated.
2. The photodisintegration interaction never occurs.

Both of these errors can be eliminated.

5.2.1 Modifying the EGS4 Code

The EGS4 code is provided with two external links to the routines HOWFAR and AUSGAB, which must be written by the user. HOWFAR is used by EGS4 to allow the user to specify the geometry of the detector. AUSGAB is used to provide the user's code with a scoring or recording mechanism. An important aspect of the use the two external link routines is that the EGS4 code need not be directly modified for use in modelling different experiments. This makes worldwide support of the EGS4 code much easier for its authors, and it provides its users with a limited guarantee of workmanship. This limited guarantee is not only reliant upon the efforts of the authors of EGS4 in testing the package, but upon the hours of CPU time expended by users of EGS4 around the world, and their subsequent bug reports. Any modification to the EGS4 program that alters the physics it is attempting to model risks introducing an error into the code, and thus reduces confidence in its ability to correctly model particle propagation. No modifications can be attempted without an extensive verification procedure taking place, a point which will be made more forcefully in Chapter 7. In modifying the SNOMAN program to take account of deuteron photodisintegration, it is therefore necessary that no change is made to the EGS4 code.

When it was first proposed that SNOMAN be modified to include deuteron photodisintegration, it was thought that either EGS4 would have to be modified, or that the inclusion of photodisintegration in SNOMAN would be approximate. This was thought to be true because without any code to account for the photodisintegration process in EGS4, neither EGS4 nor SNOMAN would be able calculate the γ-ray step length correctly. This is not the case. This author has shown that if EGS4 samples a step length, x_{EGS4}, based upon the mean free path of Equation 5.1 but without the inclusion of the photodisintegration cross section, and a second step length, x_{PD}, is sampled using the photodisintegration mean free path $1/n_d\sigma_{\mathrm{PD}}$, then choosing the interaction and propagation distance associated with the shorter of the two step lengths is analytically equivalent to calculating a single step length based upon the mean free path of Equation 5.1, but with photodisintegration included. The proof of this statement is contained in Appendix C. This is important because it means that photodisintegration can be taken into account correctly without any modification to the EGS4 code.

5.2.2 HOWFAR and AUSGAB

EGS4 calls HOWFAR specifying the current particle's position, direction and the type of media the particle is being propagated through, as well as the length of the step that the particle is about to take. HOWFAR must be able to determine if the particle will enter a different medium from the current one during the course of the impending step. If this is the case, HOWFAR must override the step length specified by EGS4 with the (shorter) distance to the next boundary along the particle's trajectory, and specify the medium the particle is about to enter. It is in this way that EGS4 takes account of the geometry of a problem. In extreme circumstances, such as a region of no importance to the Monte Carlo, HOWFAR can tell the EGS4 code to forget about a particle altogether by setting a discard flag.

After each step, AUSGAB (German, meaning output) is called with information that gives details about the particle's current state, which the user may have decided to record or ignore. AUSGAB is commonly used to record the particular details of a particle history that the user of EGS4 requires. AUSGAB has no means of discarding a particle, and hence is not useful for the purpose at hand.

The constraint imposed by the need not to modify the EGS4 program, the description of the HOWFAR routine, and the proof of Appendix C imply that a change to the HOWFAR routine can be made that will allow SNOMAN to correctly include the photodisintegration process in γ-ray propagation. To do so, FORTRAN code equivalent to the following pseudocode must be inserted into HOWFAR;

- If the particle being propagated is a γ-ray in D_2O and $E_\gamma > 2.2259$MeV, then;
    - Calculate the photodisintegration cross section ($\sigma_{PD}(E_\gamma)$).
    - Sample a photodisintegration step length (x_{PD}).
    - If ($x_{PD} < x_{EGS4}$) then;
        - Signal EGS4 to discard the γ-ray (set IDISC = 1).
        - Simulate a photodisintegration reaction a distance x_{PD} from the current position in the direction of travel of the γ-ray.
    - Endif
- Endif

where $x_{PD} = 1/n_d\sigma_{PD}$ and x_{EGS4} is the step length calculated in EGS4 and provided to the HOWFAR routine. The code, once inserted into HOWFAR, will be called before each step taken by a particle propagated in EGS4. This is exactly what is required. It should be noted that 2.2259MeV is the photodisintegration energy threshold in the laboratory frame.

The calculation of the photodisintegration cross section itself is based upon a model that will be discussed for the remainder of this chapter. An extended discussion of the step length probability distribution function and sampling methods with which a step length is generated can be found in Appendix C. It is worth emphasising that *the algorithm given above allows an exact simulation of the γ-ray mean free path*, at least in principle.

In addition to the logic presented above, a switch has been added to the SNOMAN code to allow the user to deactivate deuteron photodisintegration. It is anticipated that this physical impossibility may prove to be a useful computational device.

5.3 Discussion of the Formal Theory of Deuteron Photodisintegration at Low Energies

In Appendix D a simple theory of deuteron photodisintegration via the electric dipole interaction is given. In deriving the cross section, it is assumed that the incident γ-ray is of sufficiently low energy that the details of the nuclear wavefunction within the nucleus are unimportant because the γ-ray interacts mainly with the long range part of that wavefunction. As a result, the theory is expected to be valid only at low energies. In fact the divergence from the experimental cross section of the theoretical photodisintegration cross section, σ_{PD} ($= \sigma_{E1} + \sigma_{M1}$), occurs above $\sim$ 10MeV. The electric dipole cross section is;

$$\sigma_{E1} = \frac{8\pi}{3}\frac{e^2}{\alpha^2}\frac{(\gamma-1)^{3/2}}{\gamma^3(1-\alpha r_t)} \quad \text{(Appendix D)} , \tag{5.2}$$

where $\alpha = \sqrt{M\epsilon}$ and $\gamma = \omega/\epsilon$ and where e is the charge on the electron, M is the average nucleon mass, ϵ is the binding energy of the deuteron, ω is the incident photon energy, and r_t is the n-p triplet effective range. Note that the formula of Equation 5.2 is model independent, as it contains only experimental observables. This means that it is independent of any assumption made about the form of the potential used to derive it.

In addition to the electric dipole cross section, there is also a contribution from magnetic dipole effects. This contribution is small, but near the photodisintegration threshold its inclusion is critical. The derivation of the magnetic dipole cross section is more involved than that of the electric dipole cross section. The resulting expression, found in Bethe and Longmire [68], is

$$\begin{aligned}\sigma_{\mathrm{M1}} &= \frac{2\pi}{3}\frac{e^2}{M^2}(\mu_p-\mu_n)^2\frac{k\alpha}{k^2+\alpha^2} \\ &\quad\times\frac{(1-\alpha a_s+\frac{1}{4}a_s(r_s+r_t)\alpha^2-\frac{1}{4}a_s(r_s-r_t)k^2)^2}{(1+k^2\alpha^2)(1-\alpha r_t)}\ ,\end{aligned} \tag{5.3}$$

where the definitions of Equation 5.2 still apply, and in addition, μ_p and μ_n are the magnetic moments of the proton and the neutron respectively, and k is the final state nucleon relative momentum, $k = \sqrt{M(\omega-\epsilon)}$. a_s is the np singlet scattering length, r_s is the np singlet effective range, and r_t is again the np triplet effective range.

The last factor in Equation 5.3 corrects for finite size effects. Once again, this formula is model independent, containing only experimental observables. The only critical assumption made in the derivation of the expression for σ_{M1} is the absence of meson exchange contributions to the magnetic moment of the deuteron. In their absence, the magnetic moment operator in deuteron photodisintegration is the sum of the spin magnetic moments of the two free nucleons. This is thought to be the cause of a $\sim$ 10% discrepancy between the σ_{M1} given in Equation 5.3 and the experimental data. This point was made by Austern [72], and then again by Austern and Rost [73] and a detailed discussion presented by Noyes [74], where the discrepancy is estimated to be $9.5\% \pm 1.2\%$. Blatt and Weisskopf also present an analysis of deuteron photodisintegration [70]. There are no meson exchange contributions to the electric dipole operators [71][87].

There are no significant contributions to the photodisintegration cross section from higher electric or magnetic multipoles at the low energies (< 20MeV) considered here. For example, the electric quadrupole contribution to the d(γ,n)p cross section is $\sim 2\mu$b above threshold and below 20MeV, while the magnetic quadrupole contribution is less than 1μb in the same range [79]. This compares with a total d(γ,n)p cross section of greater than 500μb in the energy range 2.5MeV < E_γ < 20MeV (see Figure 5.5).

The errors on the cross sections of Equations 5.2 and 5.3 near threshold are calculated in Appendix D and are 0.2% and of the order of 0.1%, respectively. While the random error on σ_{M1} is not explicitly calculated at the threshold for photodisintegration, it is clear that its magnitude is small compared with that arising from the neglect of the exchange contributions to the σ_{M1} cross section, whose magnitude is $\pm \sim 1.2\%$. In other words, it has been established that near the threshold for photodisintegration the random error on the cross section $\sigma_{\mathrm{PD}} = \sigma_{\mathrm{E1}} + \sigma_{\mathrm{M1}}$ is negligible compared with the error arising from the correction to σ_{M1} for exchange effects. As the energy rises, the error on $\sigma_{\mathrm{PD}}(E_\gamma)$ becomes dominated by the random error on the electric dipole cross section, as the rate for the magnetic dipole transition becomes small compared with the rate for the electric dipole transition. This estimate of the error at the threshold for photodisintegration will prove useful later in this chapter.

5.4 Deuteron Photodisintegration at Intermediate Energies

It is the purpose of this section to provide evidence showing that the simplistic theory described earlier cannot be extended to cover the intermediate energy range between 10 and 20MeV. The best phenomenological fit, which is useful in describing data covering a broad energy range, from $\sim 20 \rightarrow 440$MeV, shall be shown to lack the precision desired here in its description of data at $\sim$ 20MeV.

5.4.1 Expression of Experimental Results

A brief discussion of the presentation of the phenomenological functions and the experimental data follows. The photodisintegration cross section has been the subject of a great deal of experimental and theoretical work. The general formalism can be presented using the standard procedures of relativistic quantum mechanics. Evaluation of the matrix element then proceeds in a model dependent way, details of which may be found in Arenhövel and Sanzone [69, Chapter 4]. However, it is possible to derive a model independent expression (again Arenhövel and Sanzone [69, Section 3.5]) for the partial differential cross section, showing that

$$\frac{d\sigma(E_\gamma,\theta)}{d\Omega} = \sum_{n=0}^{\infty} A_n P_n(\cos\theta)\ , \tag{5.4}$$

where A_n is the coefficient of the nth Legendre polynomial $P_n(\cos\theta)$. This expression is arrived at using a multipole decomposition of the transition amplitude, and applies to a photon beam incident on an unpolarised deuteron target. Equation 5.4 is particularly important because it allows the determination of the coefficients A_n of the Legendre polynomials $P_n(\cos\theta)$ independently of one another. This is because the Legendre polynomials form an orthogonal set of functions. The A_n may be determined from expressions of the form

$$A_n(E_\gamma) = \frac{2n+1}{2}\int_{-1}^{1} \frac{d\sigma(E_\gamma,\theta)}{d\Omega} P_n(\cos\theta)d(\cos\theta) \ . \tag{5.5}$$

This point about the independent determination of the Legendre coefficients is worth re-expressing; the values of the coefficients are independent of the truncation of the series that is used to represent the cross section of Equation 5.4. Another corollary of the expansion given in Equation 5.4 is the simple deduction

$$\sigma_{\rm PD}(E_\gamma) = 4\pi A_0(E_\gamma) \ , \tag{5.6}$$

which demonstrates the importance of the A_0 coefficient. All modern experiments and all review papers present their results in a form compatible with the Legendre polynomial expansion. However, many older experimental results are presented in the form of alternative angular decompositions, the most common of which is

$$\sigma_{\rm PD}(E_\gamma) = a + b(\sin\theta)^2 + c\cos\theta + d(\sin\theta)^2\cos\theta + e(\sin\theta)^4 \ . \tag{5.7}$$

The coefficients of this expansion are not independent of one another - their values can be altered by the use of an extended or truncated series. Older results of this type can be translated into the modern format using a number of simple relations, which follow;

$$A_0 = a + \frac{2}{3}b + \frac{56}{105}e \ , \tag{5.8}$$

$$A_1 = c + \frac{2}{5}d \ , \tag{5.9}$$

$$A_2 = -\frac{2}{3}b - \frac{16}{21}e \ , \tag{5.10}$$

$$A_3 = -\frac{2}{5}d \ , \tag{5.11}$$

$$A_4 = \frac{8}{35}e \ . \tag{5.12}$$

These relations have been used to allow the use of older results and their errors together with those presented in the modern format.

The explicit parameterisation of the photodisintegration cross section used to obtain phenomenological fits to experimental data is given in the form of the zero order Legendre polynomial coefficient:

$$A_0(E_\gamma) = C_1 e^{C_2 E_\gamma} + C_3 e^{C_4 E_\gamma} + \frac{C_5 + C_6 E_\gamma}{1 + C_8(E_\gamma - C_7)^2} \ . \tag{5.13}$$

The zero order coefficient is related to the total cross section by the expression in Equation 5.6.

5.4.2 Experimental Results

Several papers exist which collect the available experimental results and present them in the form of a phenomenological fitted function. The most comprehensive of these is the paper by Rossi *et al.* [78], which, because it is the most recent, has access to the latest data. A point stressed in [78] is the great difficulty of comparing results from different experiments because of the sizeable systematic errors that their results suffer from. By utilising results from several different experiments, each of which will suffer from different systematics, it is hoped that the overall effect of any individual experiment's systematic error will be greatly reduced. The experimental papers cited in the papers of De Pascale *et al.* [76], Thorlacius and Fearing [75], De Sanctis *et al.* [77] and Rossi *et al.* were used to provide data points below about 30MeV for a simple comparison with the theoretical and phenomenological cross sections. The results are displayed in Figures 5.2, 5.3 and 5.4.

It is immediately clear that neither the theoretical cross section nor the phenomenological cross section of Rossi *et al.* [78] is in especially good agreement with the experimental data in the $10 \rightarrow 25$MeV region.

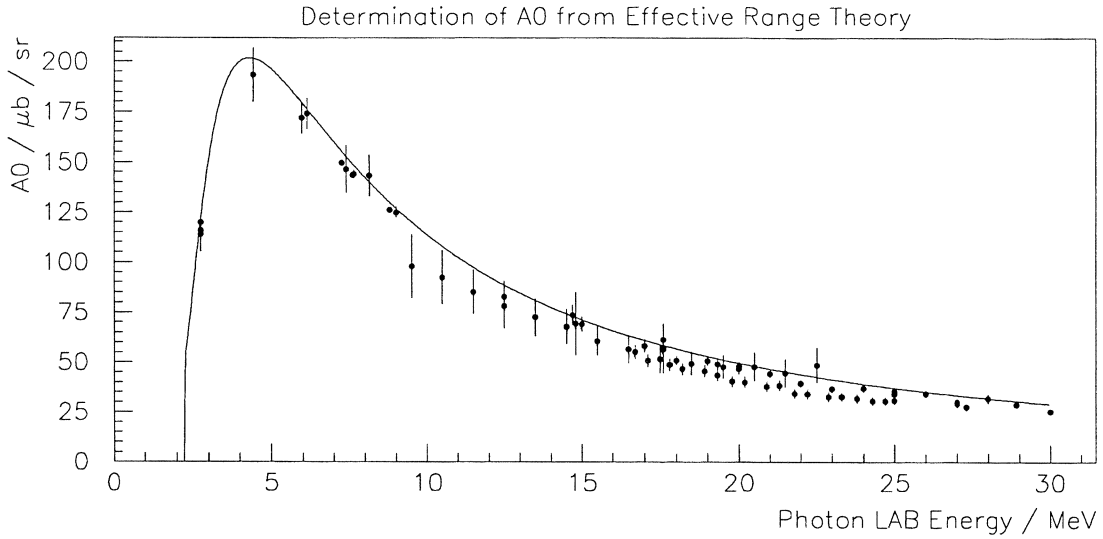

Figure 5.2: Effective range theory overestimates A0 in the 10 → 30MeV region. 1σ errors are given for the experimental data.

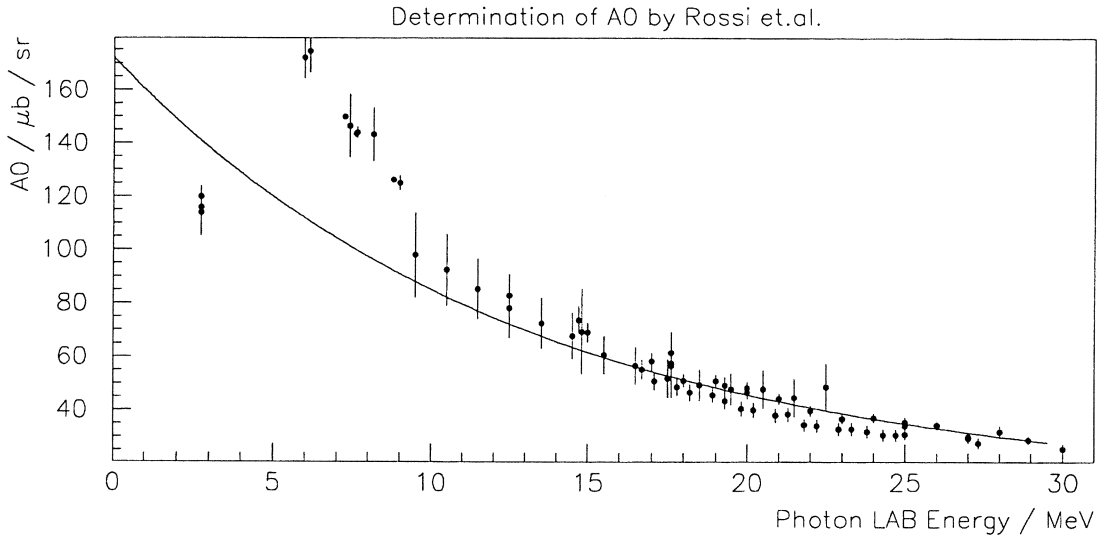

Figure 5.3: Rossi *et al.* overestimate A0 at 25MeV, and had no intention of accounting for threshold effects. 1σ errors are given for the experimental data.

It is not surprising that the low-energy theoretical cross section is wrong (and increasingly so) above about 10MeV; however, the comparison with experimental data indicates that the fit of Rossi *et al.* is also suspect in the 25MeV region. This is surprising because in Rossi *et al.* [78], the phenomenological fit is said to be valid between 20 and 440MeV. Despite this, it is felt necessary due to the disparity between experimental data and the theoretical and phenomenological results in the region of interest, to seek a better fit to the data, disregarding the work of Rossi *et al.* at the upper end of the 10 → 25MeV energy region.

Six experiments contribute data in the energy region from 20 to 30MeV, and because of this, it is clear that the trend for overestimating the experimental results by the phenomenological fit of Rossi *et al.* cannot be eliminated simply by supposing that just one of these experiments contains a large systematic error in its estimation of the photodisintegration cross section. A further compelling reason

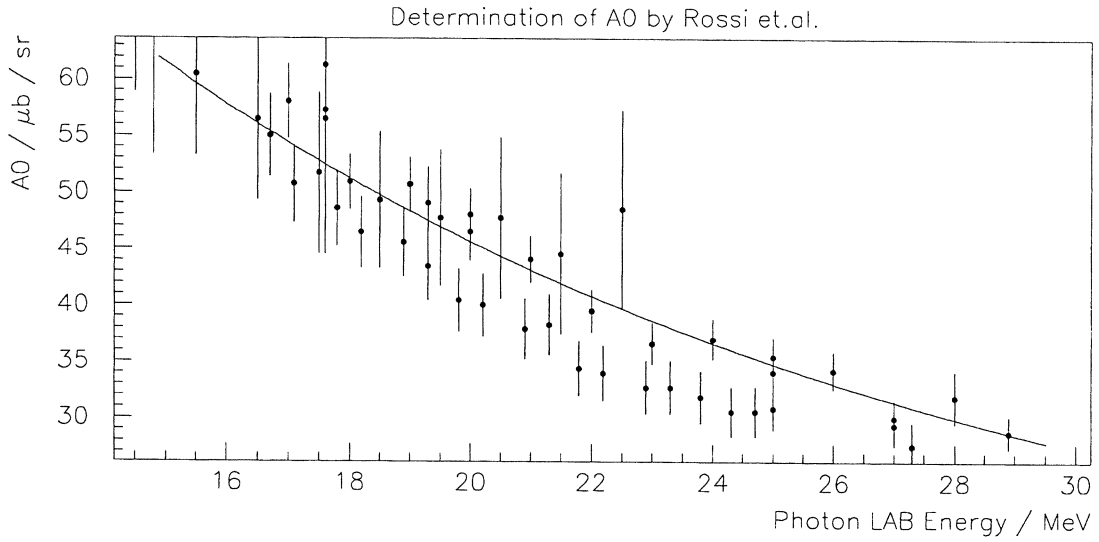

Figure 5.4: A detail of the fit of Rossi *et al.* showing its weakness in the 25MeV region. 1σ errors are given for the experimental data.

for distrusting the work of Rossi *et al.* near 25MeV is the nature of the fitting process: in making the phenomenological fit, data has been used covering a very large energy range ($20 \rightarrow 440$MeV), and much of it is at intermediate energies ($100 \rightarrow 225$MeV). The phenomenological function's dependence on its free parameters is not that required for a perfect fit to data in the low energy regions (below about 30MeV) where theoretical analysis indicates a very different line shape than that assumed for the fit. The combined effect of extending the phenomenological fit too far, and the relative paucity of data at the low energy edge results in the fit being 'pulled' away from data in this region. Such an argument applies to some degree to almost any part of the phenomenological fit, and Rossi *et al.* make the point that while their phenomenological fit may be useful in providing an overall shape for the cross section and in eliminating some of the effects of systematic error, at any single energy the best estimate of the overall cross section comes from experimental data points alone. Naturally, a fit should be used or disregarded based on the specific requirements of a particular application. In SNOMAN, special attention must be paid to low energies, and that is why the phenomenological fit of Rossi *et al.* has been found wanting. Note, however, that the fit of Rossi *et al.* does fit the data rather better at 30MeV than it does at 20MeV, and will be used to compare to the fit that follows at this higher energy, and to extend the photodisintegration model up to 440MeV.

5.5 Experimental Data and Phenomenological Fitting

It is intended that a phenomenological modification be made to the cross section provided in Section 5.3 to better model the photodisintegration cross section in the energy range from $10 \rightarrow 25$MeV. Earlier in this chapter, the expected weaknesses of the cross section given in Section 5.3 were discussed, and an estimate was obtained for the likely error associated with that cross section at very low energies. In the light of these results, the following functional forms were considered;

$$\sigma_C = \sigma_{PD}\left(1 + Ae^{Bx}\right) \text{ , and} \tag{5.14}$$

$$\sigma_C = \sigma_{PD}\left(1 + \sum_{n=1}^{m} a_n x^n\right) \text{ , and} \tag{5.15}$$

$$\sigma_C = \sigma_{PD}\sum_{n=0}^{m} a_n x^n \text{ ,} \tag{5.16}$$

where σ_C and σ_{PD} refer to the corrected and theoretical cross sections respectively, and $x = E_\gamma - E_0$, E_0 being threshold energy. All energies have been taken in the centre of momentum. The principal form

m	χ^2	ν	$P(\chi^2)$	Scale
2	76.4	70	28%	0.7%
3	76.3	69	25%	0.3%
4	64.2	68	61%	5%
5	63.9	67	58%	5.2%
6	60.6	66	66%	2.9%
7	60.1	65	65%	3.8%
8	59.8	64	62%	3.7%
9	59.1	63	61%	3.9%

Table 5.1: The results of fitting the functional modification $\sum_{n=0}^{m} a_n x^n$ to the experimental data.

of the proposed fitting functions of Equations 5.14 and 5.15 is $\sigma_{\mathrm{PD}}(1 + \cdots)$. This reflects the known accuracy of the simple theory for σ_{PD} at low energies, and increasing inaccuracy thereafter. The function of Equation 5.14 was thought to be able to provide just such behaviour. However, it may be dismissed immediately on the grounds that it provides a very poor fit to the data ($\chi^2 \simeq 3$ per degree of freedom). Such a poor fit results from the particular dependence of the fitting function on the x variable.

The second function, that of Equation 5.15, appeared to fit the data quite well as m was increased through the range $3 \rightarrow 7$. However, there was one serious objection to the resulting fitted function. Looking at Figure 5.2, there is only one data point in the region near 4.4MeV, near the peak of the photodisintegration cross section. While the data point is significantly below the theoretical curve, it has a sufficiently large error to render the data point not inconsistent with the simple theoretical cross section. The objection to the second proposed function is that as the number of parameters is increased from $3 \rightarrow 7$, which results in ever improving fits to the the experimental data, the corrected curve passes closer and closer to the single experimental point at 4.4MeV. Under normal circumstances, this is just what would be required of a fitted function. However, in this case, auxiliary information exists that requires the fitted function to approach the simple theoretical cross section as the interaction energy is reduced toward the photodisintegration threshold. The fitted behaviour of the function of Equation 5.15 is directly contrary to this requirement. As a result the second proposal for a fitted function, Equation 5.15, must also be rejected.

The failures of the functions presented above lead to the relaxation of the requirement that the fitting function take the general form $\sigma_{\mathrm{PD}}(1 + \cdots)$. The result is the function displayed in Equation 5.16. This proposal was not expected to satisfy the principal demand made of it, that of approaching the simple theoretical cross section as the energy of the incident photon is reduced. However, the earlier work presented in this chapter on the error associated with the simple theoretical cross section, σ_{PD}, allows for a small deviation from the expected cross section even at the lowest energies, of up to $\pm 1.2\%$. It is found that this third function of Equation 5.16 does in fact fit the data as well as the previous proposed function of Equation 5.15, without necessarily falling foul of the same objection, provided a difference between the fitted function and σ_{PD} is allowed in accordance with the evaluated error. Several attempts were made to fit Equation 5.16 to the experimental data points, each differing in the choice of the number of terms used in constructing the polynomial series. The results are set out in Table 5.1.

In the table, m indicates the index at which the multiplicative function $\sum_{n=0}^{m} a_n x^n$ is truncated. The quantity χ^2 takes its usual meaning, and ν is the number of degrees of freedom associated with the fitted function and is equal to the number of points less the number of free parameters in the fit (there are 72 data points). The scale quantity is the % difference between the fitted function and the simple theoretical cross section at the threshold for deuteron photodisintegration ($= 1 - a_0$). The quantity $P(\chi^2)$ is derived from both ν and χ^2. Its interpretation is as follows; it is the probability that a function which does genuinely describe the data would give a value of χ^2 that is as large or larger than that already obtained. On this basis, no particular truncation is either especially favoured or especially disfavoured. Once again, the auxiliary condition, that the fitted function approach the simple theoretical cross section as the incident photon energy is reduced to the photodisintegration threshold, is useful in selecting a particular multiplicative function. The application of this auxiliary condition to the problem at hand leads to the choice of the function with the smallest scale difference, all other factors being (roughly) equal. The final choice for the fitted cross section then becomes

$$\sigma_{\mathrm{C}} = \sigma_{\mathrm{PD}} \left(a_0 + a_1 x + a_2 x^2\right) \ . \tag{5.17}$$

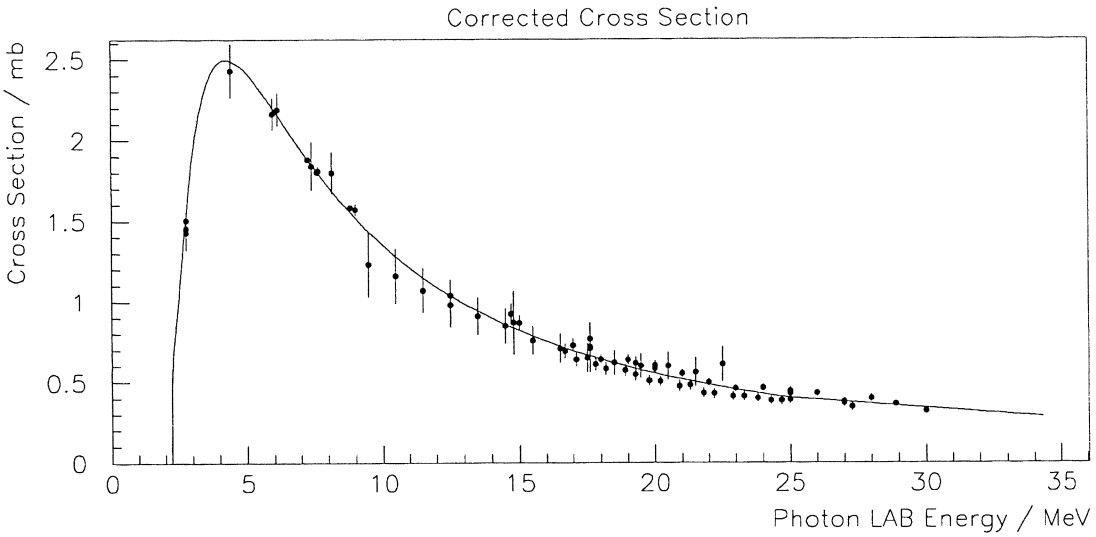

Figure 5.5: The fitted cross section for deuteron photodisintegration. Again, 1σ errors are given for the experimental data.

While this function is the least probable on the basis of the data given above in Table 5.1, it is by no means improbable, and its simplicity and small scale difference at the photodisintegration threshold, of 0.3%, are the crucial factors in its recommendation.

The final fit to the cross section for deuteron photodisintegration is displayed in Figure 5.5. This fit encapsulates the physics used in the derivation of the photodisintegration cross section from the simple theory leading to σ_{PD}. The physical assumptions made are expected to be entirely accurate at low energies, near the threshold, and here the multiplicative correction modifies the cross section by only 0.3%, well within error arising from the neglect of exchange effects, estimated at $\pm 1.2\%$. Away from the threshold, the assumptions made in the derivation decrease in validity, and the accuracy with which the cross section describes the experimental data suffers. It is here that the multiplicative polynomial has the freedom to correct the photodisintegration cross section in accordance with the data. The result is a function which models the available experimental data very well over the full energy range from $0 \rightarrow 25$MeV. This is a direct result of the theoretical input to the fitting procedure. Without such input, it is all too easy to obtain a physically far less justifiable fit to the data which is systematically wrong by up to 5% over the energy range already mentioned. Such a fit may even appear to have a more impressive statistical 'justification'.

The error on the corrected cross section shall be discussed shortly. The final fit includes a linear transition between the modified theoretical function and the phenomenological fit of Rossi *et al.* between 25 and 35MeV. Such a linear transition is possible because the fitted cross section approaches the phenomenological cross section of Rossi *et al.* above 20MeV. This was not sought during the fitting procedure, and serves to confirm the validity of the result.

All the fitting in this section was completed using algorithms presented in 'Numerical Recipes', [80]. Particularly heavy use was made of the single value decomposition method for a general linear least squares fit, applicable here as the fitted function is linear in its free parameters.

5.5.1 The Error on the Proposed Fit

The error associated with the fitted function has a statistical and a systematic component. The statistical component which dominates over most of the $0 \rightarrow 25$MeV energy range can be derived from the errors on the parameters a_n as follows

$$\begin{aligned} V\left(\frac{\sigma_{\mathrm{C}}}{\sigma_{\mathrm{PD}}}\right) &= V(a_0) + V(a_1)x^2 + V(a_2)x^4 \\ &\quad +2V(a_0,a_1)x + 2V(a_0,a_2)x^2 + 2V(a_2,a_3)x^3 \ , \end{aligned} \tag{5.18}$$

where $V(a_n)$ is the variance of the nth parameter, and $V(a_n, a_m)$ is the covariance between the nth and mth parameters. In addition to this, a Monte Carlo estimate of the statistical error associated with the fitting function was also prepared. To obtain the Monte Carlo estimate, it was assumed that the each data point was drawn from a Gaussian distribution whose mean was represented by that data point and whose standard deviation was consistent with the error on that point. Several thousand data sets were generated at random using these assumptions. A best fit function was then generated for each data set, in the same way as the best fit function was calculated for the actual data set. The error was estimated at representative values of the variable x, defined above, by finding the upper and lower limits within which 68% (representing one standard deviation) of all the fitted functions lay at that value of x.

The Monte Carlo estimation of error on the fitted curve was originally employed because in fitting the function of Equation 5.15 with $m = 6$, it was noted that the χ^2 function was not parabolic in its parameter space, as it would be if the data points were drawn from a Gaussian distribution. This rendered the variances and covariances on the parameters of the fit unreliable, and the Monte Carlo method was proposed as a mechanism whereby direct calculation of the variances and covariances of the parameters could be avoided whilst still resulting in an estimate of the error on the overall fit. The final fitted function of Equation 5.17 does not appear to have sufficient sensitivity to suffer from the same problems as that of Equation 5.15, $m = 6$, and hence the Monte Carlo method of error estimation merely serves as a further check on the validity of the error estimate derived from Equation 5.18.

In fact, the two methods of error estimation agree extremely well, both in determining the overall shape and the absolute magnitude of the statistical error. Effectively, they serve to confirm one another. The statistical error on the final fit to the cross section for deuteron photodisintegration is displayed in Figure 5.6. It is typically $\sim 1\%$, up to about 25MeV, increasing to 3.5% at 35MeV. The increase in the error associated with the multiplicative polynomial at the upper end of the fitted energy region (30MeV) results from the greater uncertainty in the magnitude of the higher terms ($\propto E$, E^2) arising from the uncertainty in the values of their coefficients. For comparison with the data presented in Figure 5.6, the error on the fit of Rossi *et al.* between 20 and 30MeV is approximately 0.2μb/sr, or $\sim 0.5\%$. The data provided in Figure 5.4 shows these errors to be slightly optimistic, and once again the reason for the small magnitude of the errors lies in the use of the particular functional form adopted by Rossi *et al.* . The fact that at low energies it has not been provided with sufficient freedom to account for the behaviour of the photodisintegration cross section has already been discussed. By the same token the fit must fail to account for the error on that cross section, except possibly by chance. Once again it should be noted that the fit of Rossi *et al.* is much better at 30MeV than it is at 20MeV.

The systematic error on the new fit dominates the statistical error in the range $18 \rightarrow 25$MeV. This error exists because it is clear that in that region there are two large data sets whose results differ only in normalisation, and because the systematic error on the data points of those data sets has been underestimated. The best estimate of the systematic error on the fit in the region where these data sets lie is the average percentage difference between the data sets. The systematic error is estimated to be $\sim 10\%$. In considering this error, it is important to remember that is cannot be treated as a 1σ Gaussian error.

5.6 The Angular Distribution of the Deuteron Photodisintegration Interaction

The simple theory of deuteron photodisintegration described earlier makes a definite prediction regarding the angular distribution of the products of deuteron photodisintegration, which is

$$\frac{d\sigma_{\mathrm{PD}}}{d\Omega} = a + b(\sin\theta)^2 \ , \tag{5.19}$$

where σ_{PD}, a, and b are functions of the incident photon energy E_γ, and where a and b are related to the photoelectric and photomagnetic cross sections by the equations

$$\sigma_{\mathrm{PD}} = 4\pi a + \frac{8\pi}{3} b \tag{5.20}$$

$$= \sigma_{\mathrm{M1}} + \sigma_{\mathrm{E1}} \ . \tag{5.21}$$

and to the Legendre polynomial coefficients A_0 and A_2 by

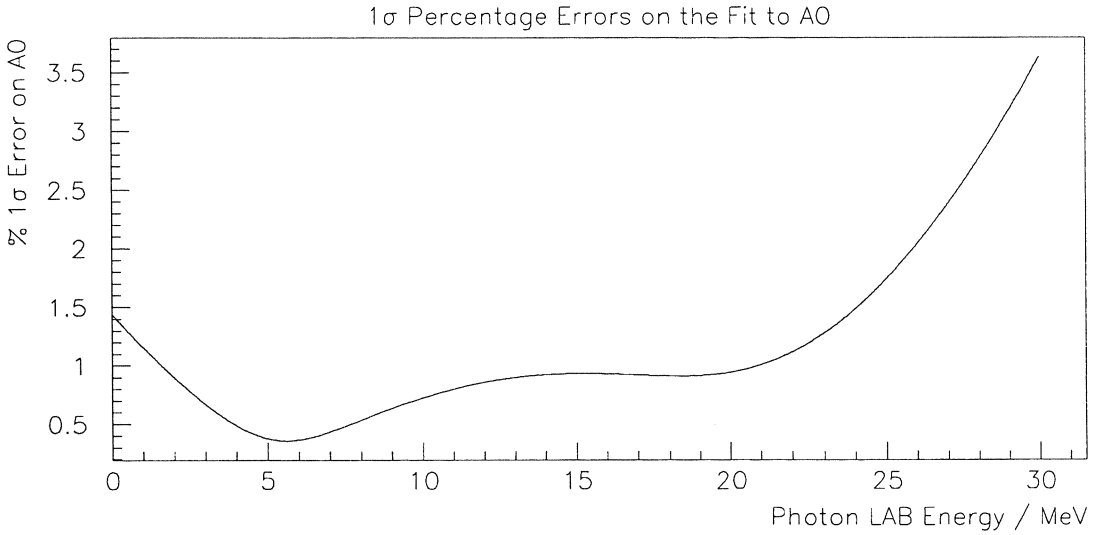

Figure 5.6: The estimated error on the fit to the cross section. Below 25MeV it is always less than 2%. Above 25MeV, the fit of Rossi *et al.* begins to take over, and the error displayed in this figure becomes irrelevant.

$$A_0 = a + \frac{2}{3}b \,, \tag{5.22}$$

$$A_2 = -\frac{2}{3}b \,. \tag{5.23}$$

While the simple theory that was described earlier gives quite a good description of the deuteron photodisintegration cross section at low energies, it does not provide the same accuracy in its prescription for the angular distribution, or differential cross section. Note that the total cross section is dependent only on A_0 as shown in Equation 5.6, and that the angular distribution of the emitted neutron with respect to the incident γ-ray is not important in SNO, where it will be washed out by the many nearly isotropic scatterings a neutron will experience before capture. The angular distribution is included here and in the SNOMAN Monte Carlo simulation for completeness.

If the formula in Equation 5.19 were correct, a very accurate description of the experimental data could be achieved using a Legendre series of the form of Equation 5.4 where only A_0 and A_2 differed significantly from zero. This is not the case. However, the coefficients A_0 and A_2 are the principal components involved in the expansion, as they are the largest by a factor of about 10. It follows that they are also the easiest to deduce from experimental data, and therefore more data is available, to a higher accuracy, with which to study the energy dependence of these components, than is available for the study of the coefficients A_1, A_3, and A_4. It is the accuracy of the experimental results associated with the smaller coefficients that restricts the accuracy to which the angular distribution of the products of the photodisintegration interaction may be determined. The data is presented in Figure 5.7.

From the data presented, it is clear that an overall accuracy of a few μb/sr is all that can be achieved, and that it is pointless to expend a great deal of effort in producing anything more than an approximate angular distribution. This is particularly true near the threshold energy, where there is no experimental data available at all for the coefficients A_1, A_3, and A_4. What then, is the magnitude of these coefficients near threshold? The answer to this question is that it is generally accepted that the expansion of Equation 5.19 does give a reasonable description of the experimental data, and therefore any additional terms must be small. Consequently it is only considered necessary to determine the principal components of the angular distribution. This will result in an error in the differential cross section whose magnitude is $\sim 10 \rightarrow 15\mu$b/sr. This should be compared to a typical magnitude of the principal components A_0 and A_2 of approximately $100 \rightarrow 200\mu$b/sr at energies between 2 and 10MeV. The coefficient A_0 was the subject of the earlier part of this chapter. The procedure for fitting A_2 is identical to that for fitting A_0, and shall not be repeated here. The only significant point to be made about the fit to A_2 is that it was very much poorer than that for A_0 (giving $\chi^2 \sim 3$ per point). This was not because any individual data

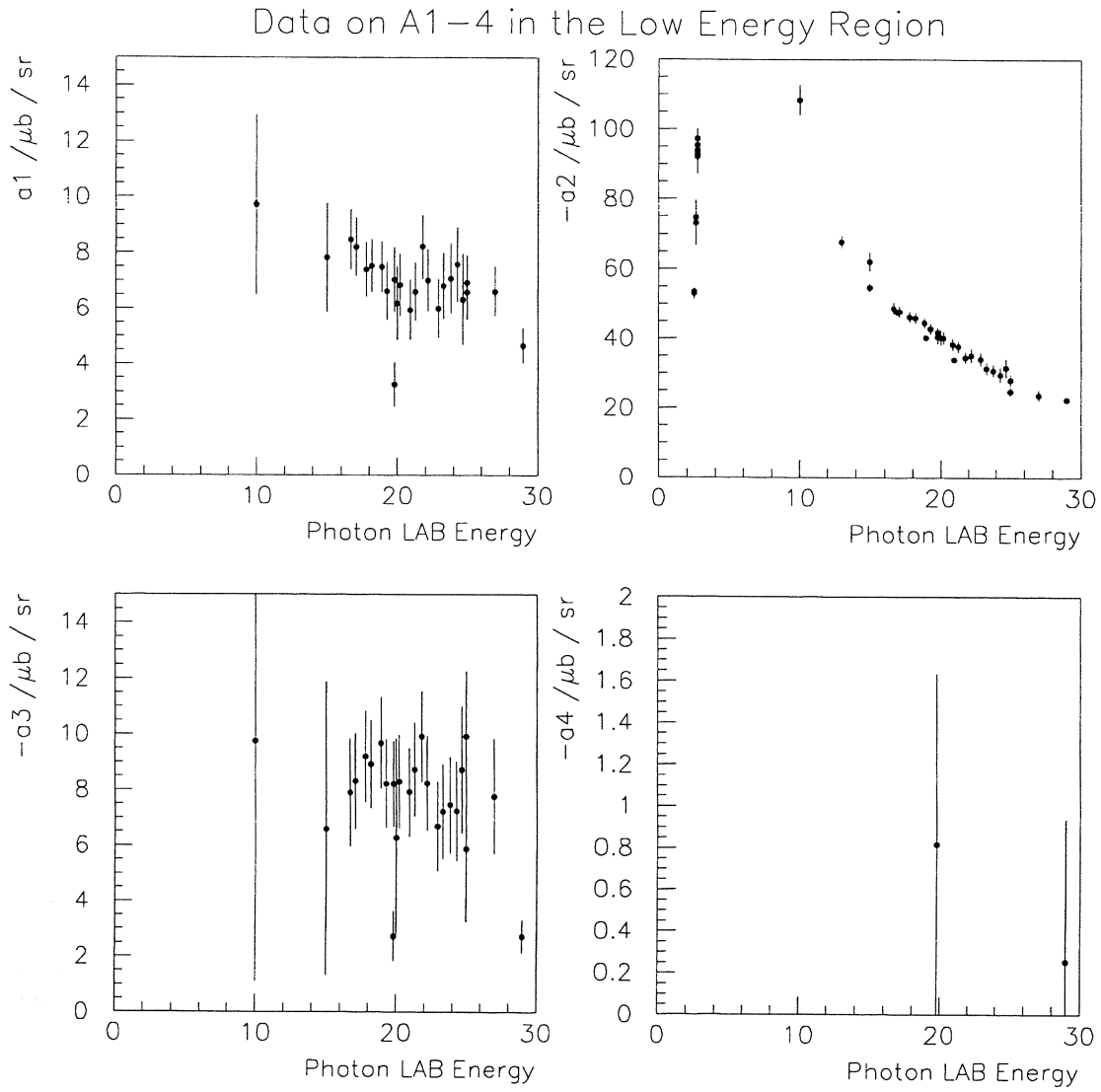

Figure 5.7: There is no data for A_1 near the threshold energy, and what there is is somewhat indiscriminate. A_2 has the same approximate shape as the overall cross section, but its magnitude is reduced by about 2/3. Both A_3 and A_4 suffer from large errors. 1σ errors are given for all the experimental data.

point could not be fitted, rather, all the points contribute to the poor fit. This was because the errors on each point are small relative to the difference in magnitude between neighbouring pairs of points. This results in the fitted smooth curve passing far from either point in such a pair, where far from a point here means outside the 1σ error margin of that point. This is because the errors on the coefficient A_2 have been generally underestimated. This is not surprising when the history of measurement of the deuteron photodisintegration interaction is considered - Rossi *et al.* refer to a factor of 2 discrepancy between experimental results at higher energies (approximately 100 $\rightarrow$ 200MeV) that remained unresolved until as late as 1985. Note that the fact that the fit to A_2 was poor is of little significance when the magnitude of the difference between the fitted function and data is considered - that magnitude is small compared to the magnitude of the coefficients A_1, A_3 and A_4, which have been ignored.

The fit to A_2 is presented in Figure 5.8. Once again, the figure shows a smooth transition at about 18MeV between the modified theoretical function and the phenomenological function of Rossi *et al.* . The linear transition occurs between $\sim$ 17 and 19MeV because the fit of Rossi *et al.* is entirely satisfactory at higher energies, and the magnitudes of the two functions describing the cross section agree very well at this point. No error on the angular distribution of the final state products is formally presented, but a

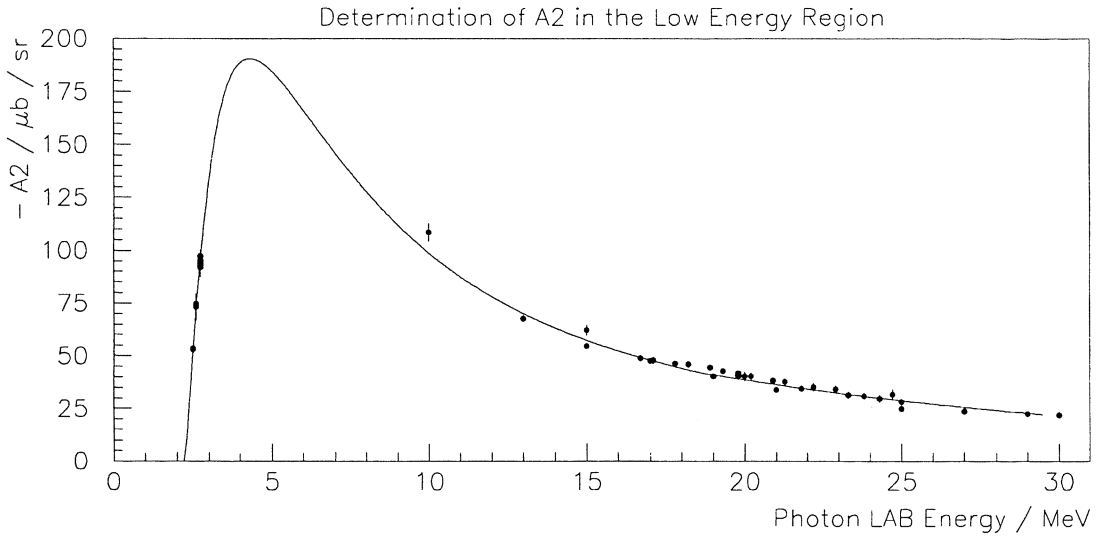

Figure 5.8: A_2 is one of the two principal components determining the angular distribution of the reaction products of photodisintegration at low energies. The other is A_0.

good estimate is about 15μb/sr at the peak cross section ($\sim$ 4.4MeV). This rough estimate of the error on A_2 is all that is necessary since a rough determination of the angular distribution is all that is possible, and because A_2 does not contribute to the total interaction cross section.

5.7 Conclusions

It is important to model the deuteron photodisintegration interaction in the SNOMAN program because photodisintegration is the principle background to neutral current events. The change to the γ-ray interaction cross section can be made to SNOMAN without modifying the EGS4 code which calculates that cross section, and without introducing any approximations.

The photodisintegration model used relies on both theoretically and experimentally derived cross cross sections (phenomenological cross sections), neither of which fit the data at intermediate energies between 10 and 25MeV particularly well. It is possible to fit the available experimental data rather better between 0 and 25MeV by modifying the theoretical cross section by a multiplicative correction. The form of the multiplicative function has been chosen so that it is in accordance with the physical assumptions underlying the simple theoretical cross section of Appendix D. The error on the fitted cross section is dominated by statistical uncertainties of the order of 1% below 18MeV and by a systematic error of the order of 10% between 18MeV and 25MeV. The fit and its error are the principal results of this chapter.

To complete the low energy photodisintegration model, the angular distribution of the reaction products has been provided. Due to the paucity of data near the interaction threshold only an approximate distribution is justified below about 25MeV. The angular distribution is not critical to simulations of the SNO detector.

Finally, a smooth transition is made between the low energy model of photodisintegration derived here and the best available phenomenological fit, that of Rossi *et al.* [78], which describes both the interaction cross section and the angular distribution of the products up to 440MeV.

Chapter 6

Neutron Interactions In The SNO Detector

6.1 Introduction

The purpose of this chapter is to describe all the basic neutron physics that will occur within the SNO detector. This physics sets the requirements for the neutron transport code that will be used in the Monte Carlo analysis of the performance of the experiment in subsequent chapters.

Neutrons in the SNO experiment have a maximum energy of 17.33MeV (the maximum energy of neutrons emitted from hep neutrino neutral current interactions), however the flux of hep neutrinos is exceedingly small, and ^{8}B neutrinos are the majority of neutrinos detected in SNO. The spectrum of neutrons emitted from the NC interaction falls away rapidly above threshold, and has a mean of $\sim$ 200keV. The NC neutron spectrum is shown in Figure 6.1. In practice, the highest energy neutron source within the SNO detector is the ^{252}Cf calibration source, which commonly emits neutrons with energies of 1MeV, and whose spectrum extends to $\sim$ 5MeV. All discussion of neutron interactions will be confined to energies in the range $0 \rightarrow 20$MeV, with the understanding that interactions that have thresholds much above 1MeV will be rare in the SNO detector.

Readers who are already familiar with the variety and magnitude of neutron-nucleus interactions at thermal and few MeV energies are invited to proceed directly to the next chapter. The situation as regards thermal neutron transport through the SNO detector is summarised in Tables 6.1/6.2.

6.2 Neutron Interactions Below 20MeV

Neutrons are involved in two general classes of interaction. These are 1; discrete nuclear reactions and 2; the interaction between the magnetic moment of the neutron and those of the electrons of the target atom. A third class, involving the interaction between the magnetic moment of the neutron and the magnetic fields of electrons and nuclei can be neglected in comparison to the contributions from the first two effects [98]. The media in SNO are non-magnetic media, and as a result the only interactions that need to be considered are discrete interactions with nuclei. The principle nuclear interactions in SNO, for neutrons with energies below 20MeV, are:

1. elastic scattering (elastic in the centre of momentum);
2. (n,γ) capture;
3. (n,p), (n,d), (n,t), (n,^{3}He) and (n,α) capture;
4. inelastic scattering of the form X(n,n')X*, leaving the struck nucleus in an excited state, later to decay by γ-ray emission; and,
5. the (n,2n) reaction, in particular d(n,2n)p.

The (n,γ) reaction has been listed separately from the other capture mechanisms because it is the only significant reaction that can produce a signature above a 60 NHIT threshold in the SNO detector (the (n,n'γ) reactions are infrequent, and their energies are generally too low to breach a 60 NHIT threshold).

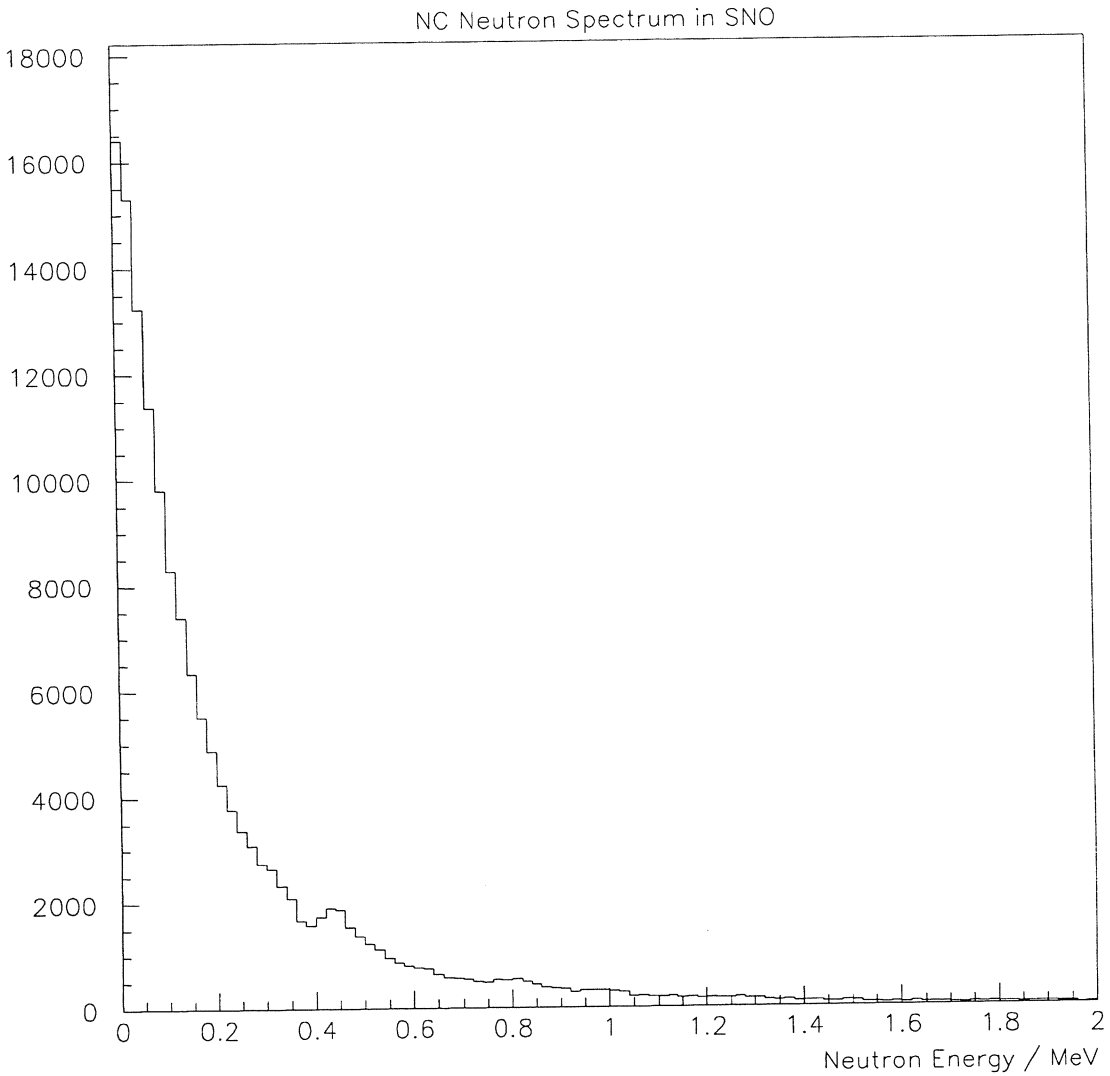

Figure 6.1: The NC spectrum in the SNO detector, as simulated by SNOMAN. The mean energy is approx. 200keV.

6.3 Neutron Physics

The interactions of neutrons with nuclei are either via compound or direct nuclear reactions. In a direct reaction, the energy and momentum of the incident particle are shared with a small number of particles which then escape the nucleus. Direct nuclear interactions are characterised by a number of distinct features;

1. the incident particle has a high energy;
2. the energy of the incident particle is shared among a few outgoing particles; and,
3. the angular distributions of the products of the reaction are forward peaked.

A compound nuclear interaction occurs when a nuclear transition $A + a \rightarrow B + b$ occurs through an intermediate state C;

$$A + a \rightarrow C \rightarrow B + b \ , \tag{6.1}$$

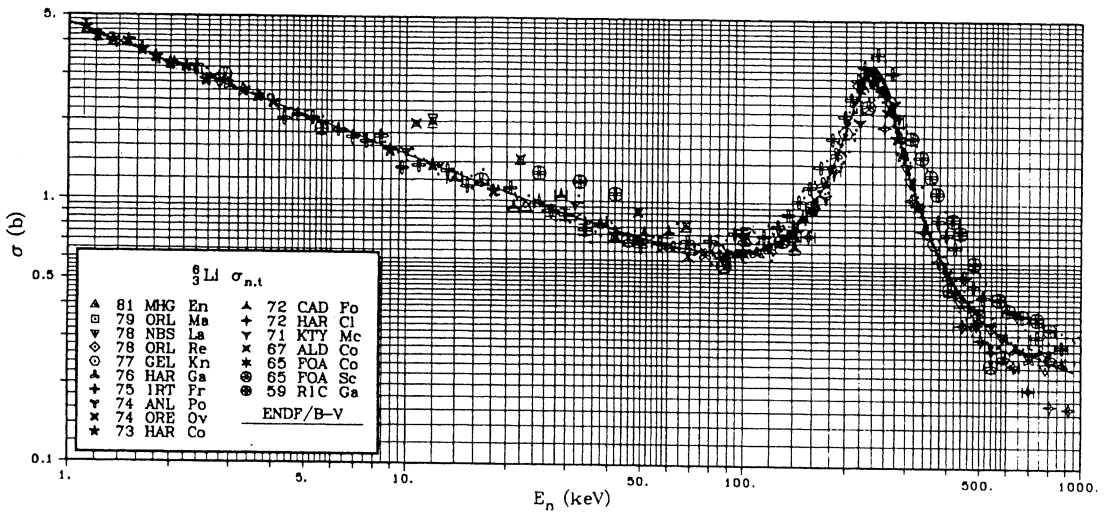

Figure 6.2: The ^{6}Li(n,α)t reaction cross section is a good example of a Breit-Wigner resonance [141].

where A, C and B are the initial, intermediate and final nuclei respectively, a is the incident particle and b is the emitted particle. Compound nucleus reactions have the following characteristic features;

1. the momentum and energy of the incident particle are shared among all the nucleons in the target;
2. the relative probability for the decay of an intermediate nucleus into a specific set of final products is independent of the means of formation of the compound nucleus; and,
3. the angular distribution of the products of the reaction is symmetric in the centre of mass.

The time scales for direct and compound reactions (10^{-22}s and $10^{-16} \rightarrow 10^{-18}$s respectively) are both negligible in the SNO detector and therefore a neutron-nucleus interaction may be simulated in a Monte Carlo code as a point event in time and space. For an isolated resonance of width Γ, the cross section for the formation and decay of a compound nuclear state is well described by the Breit-Wigner formula [141];

$$\sigma = \pi\lambda_0^2 g \left(\frac{E_0}{E}\right)^{\frac{1}{2}} \frac{\Gamma_{\text{i.s.}}\Gamma_{\text{f.s.}}}{(E-E_0)^2 + (\Gamma/2)^2}\ , \tag{6.2}$$

where $\Gamma_{\text{i.s.}}$ is the partial width for the initial state, $\Gamma_{\text{f.s.}}$ is the partial width for decay into the final state, λ_0 is the reduced wavelength in the centre of momentum at the resonance energy E_0, g is the spin multiplicity factor which for neutrons ($s = \frac{1}{2}$) is equal to $g = (2J+1)/(2s+1)(2I+1) = (2J+1)/2(2I+1)$, and E is the energy of the incident particle in the centre of momentum. When the compound nuclear interaction is of the form $A + a \rightarrow A + a$, the shape of the resonance is not that given in 6.2 because of the interference of potential scattering with the compound process.

Well away from a resonance, the Breit-Wigner formula has a $1/\sqrt{E} \equiv 1/v$ dependence on the energy of the incident particle. This energy dependence characterises the capture cross section for thermal neutron reactions with light nuclei. Figure 6.2 shows the Breit-Wigner resonance for the ^{6}Li(n,t)^{4}He reaction. The $1/v$ dependence of the cross section below resonance is clear.

6.4 Common Neutron Interactions in the SNO Detector

Only three media in SNO are significant for the purposes of neutron transport. This is because the 2.5m of H_2O inside the PSUP and the 2m outside it will effectively absorb neutrons from the PSUP or cavity rock. The inner three media are light water, the acrylic vessel, and the heavy water. A short description of neutron transport through each of these media will be given. In what follows, where a cross section is given for a thermal neutron, it is the cross section for neutrons at $\frac{1}{40}$th of an eV. Thermal neutron transport is transport at or about this energy. High energy refers to neutrons with greater than 1MeV in energy. In SNO, transport below 1MeV and above thermal energies is dominated by elastic scattering. Tables 6.1, 6.2, 6.3, 6.4, and 6.5 present detailed summaries of the dominant thermal and non-thermal interactions, some of which are not included in the discussions.

Nucleus	$\sigma_{n,n}$ (b)	$\sigma_{n,\gamma}$ (mb)	X, $\sigma_{n,X}$ (mb)	Loc	A (%)	$n\sigma_{n,n}$ (cm^{-1})	$n\sigma_{n,\gamma}$ ($10^{-5}cm^{-1}$)	$n\sigma_{n,X}$ ($10^{-5}cm^{-1}$)
^{1}H	20.49	333		LW	100	1.37	2220	
				AV	100	0.948	1540	
				HW	0.09	0.001	1.96	
^{2}H	3.39	0.508		HW	99.91	0.226	3.38	
^{3}He	3.39	0.519	p, 5333b	CG	100	small	small	12328
^{6}Li	0.75	38.5	α, 940b	S2	95	small	small	261
^{7}Li	0.97	45.4		S2	5	small	small	
^{12}C	4.75	3.53		AV	98.9	0.136	small	
				CG	98.9	small	small	
^{13}C	4.19	1.37		AV	1.10	0.001	small	
				CG	1.10	small	small	
^{14}N	10.05	75.0		S2	99.63	small	small	
^{15}N	4.59	0.024		S2	0.37	small	small	
^{16}O	3.76	0.190		LW	99.762	0.125	small	
				AV	99.762	0.044	small	
				HW	99.345	0.124	0.63	
^{17}O	3.61	0.538	α, 235	LW	0.038	small	small	small
				AV	0.038	small	small	small
				HW	0.055	small	small	0.43
^{18}O	3.83	0.160		LW	0.200	small	small	
				AV	0.200	small	small	
				HW	0.600	small	small	
^{19}F	3.641	9.8		CG	100	small	small	
^{24}Mg	3.74	51		S1	78.99	small	small	
^{25}Mg		190		S1	10.00	small	small	
^{26}Mg	2.83	38		S1	11.01	small	small	
^{35}Cl	20.6	43.6b	p, 489	S1	75.77	small	94.8	1.0
^{37}Cl	1.15	433		S1	24.23	small	0.3	
^{58}Ni	25.3	4.6b		NCD	68.27	1.59	0.289	
^{60}Ni	0.98	2.9b		NCD	26.10	0.02	0.069	
^{61}Ni	9.0	2.5b		NCD	1.13	0.01	0.003	
^{62}Ni	9.1	14.5b		NCD	3.59	0.03	0.047	
^{64}Ni	0.0014	1.52b		NCD	0.91	small	0.001	

Table 6.1: Thermal microscopic and macroscopic cross sections for nuclei in the inner three media of the detector by nucleus [135]. The location is indicated by an abbreviation; LW = Light Water, AC = Acrylic Vessel, HW = Heavy Water, NCD = Neutral Current Detector, and CG = Counter Gas. S1 indicates that the nuclide is in a solution of 0.2% $MgCl_2$ salt in the heavy water, whilst S2 indicates that it is in a solution of 0.03% $LiNO_3$ in the heavy water and in this case the presence of additional oxygen in the water has been neglected. 'small' indicates that a macroscopic cross section is at least 1000 times smaller than the largest macroscopic cross section in the same medium (scattering and absorption cross sections are considered separately). The column entitled 'A' gives the isotopic abundance by mass of each nuclear species in each medium. The isotopic enrichment of ^{18}O (a factor of 3, from 0.2% $\rightarrow$ 0.6%) in heavy water has been assumed to be approximately double that of ^{17}O (a factor of $\sim$ 1.5, from 0.038% $\rightarrow$ 0.055%).

Loc	Nucleus (b)	$\sigma_{n,n}$ (mb)	$\sigma_{n,\gamma}$ (mb)	X, $\sigma_{n,X}$	A (%)	$n\sigma_{n,n}$ (cm^{-1})	$n\sigma_{n,\gamma}$ ($10^{-5}cm^{-1}$)	$n\sigma_{n,X}$ ($10^{-5}cm^{-1}$)
LW	^{1}H	20.49	333		100	1.37	2220	
	^{16}O	3.76	0.190		99.762	0.125	small	
	^{17}O	3.61	0.538	α, 235	0.038	small	small	small
	^{18}O	3.83	0.160		0.200	small	small	
AV	^{1}H	20.49	333		100	0.948	1540	
	^{12}C	4.75	3.53		98.9	0.136	small	
	^{13}C	4.19	1.37		1.10	0.001	small	
	^{16}O	3.76	0.190		99.762	0.044	small	
	^{17}O	3.61	0.538	α, 235	0.038	small	small	small
	^{18}O	3.83	0.160		0.200	small	small	
HW	^{1}H	20.49	333		0.09	0.001	1.96	
	^{2}H	3.39	0.508		99.91	0.226	3.38	
	^{16}O	3.76	0.190		99.345	0.124	0.63	
	^{17}O	3.61	0.538	α, 235	0.055	small	small	0.43
	^{18}O	3.83	0.160		0.600	small	small	
S1	^{24}Mg	3.74	51		78.99	small	small	
	^{25}Mg		190		10.00	small	small	
	^{26}Mg	2.83	38		11.01	small	small	
	^{35}Cl	20.6	43.6b	p, 489	75.77	small	94.8	1.0
	^{37}Cl	1.15	433		24.23	small	0.3	
S2	^{6}Li	0.75	38.5	α, 940b	95	small	small	261
	^{7}Li	0.97	45.4		5	small	small	
	^{14}N	10.05	75.0		99.63	small	small	
	^{15}N	4.59	0.024		0.37	small	small	
CG	^{3}He	3.39	0.519	p, 5333b	100	small	small	12328
	^{12}C	4.75	3.53		98.9	small	small	
	^{13}C	4.19	1.37		1.10	small	small	
	^{19}F	3.641	9.8		100	small	small	
NCD	^{58}Ni	25.3	4.6b		68.27	1.59	0.289	
	^{60}Ni	0.98	2.9b		26.10	0.02	0.069	
	^{61}Ni	9.0	2.5b		1.13	0.01	0.003	
	^{62}Ni	9.1	14.5b		3.59	0.03	0.047	
	^{64}Ni	0.0014	1.52b		0.91	small	0.001	

Table 6.2: Thermal microscopic and macroscopic cross sections for nuclei in the inner three media of the detector by location [135]. The location is indicated by an abbreviation; LW = Light Water, AC = Acrylic Vessel, HW = Heavy Water, NCD = Neutral Current Detector, and CG = Counter Gas. S1 indicates that the nuclide is in a solution of 0.2% $MgCl_2$ salt in the heavy water, whilst S2 indicates that it is in a solution of 0.03% $LiNO_3$ in the heavy water and in this case the presence of additional oxygen in the water has been neglected. 'small' indicates that a macroscopic cross section is at least 1000 times smaller than the largest macroscopic cross section in the same medium (scattering and absorption cross sections are considered separately). The column entitled 'A' gives the isotopic abundance by mass of each nuclear species in each medium. The isotopic enrichment of ^{18}O (a factor of 3, from 0.2% $\rightarrow$ 0.6%) in heavy water has been assumed to be approximately double that of ^{17}O (a factor of $\sim$ 1.5, from 0.038% $\rightarrow$ 0.055%).

Loc	Isotope	Density (cm^3)	R	Q (MeV)	XS	E (MeV)	Macro XS (cm^{-1})	Comment
LW	^{1}H	6.69×10^{22}	All		4.25b	1	0.28	$\sim$ 1b at 10MeV
	O	3.34×10^{22}	All		$\sim$ 1.5b	2 $\rightarrow$ 10	0.050	
	^{16}O	3.34×10^{22}	(n,n')		0.2 $\rightarrow$ 0.6b	10 $\rightarrow$ 14	0.020	Rough guide
			(n,2n)	-17	25mb	33	8.34×10^{-4}	Rises slowly
			(n,p)	-9.64	85mb	11	2.84×10^{-3}	Rises rapidly, falls off slowly
			(n,d)	-9.90	15mb	14.1	5.05×10^{-4}	
			(n,α)	-3.2	60mb	4 $\rightarrow$ 18	2.00×10^{-3}	Many resonances
	^{17}O	1.27×10^{19}	(n,p)		$<$ 10mb	$\sim$ 14	$< 1.27 \times 10^{-7}$	
	^{18}O	6.69×10^{19}	(n,p)		$<$ 10mb	$\sim$ 14	$< 6.69 \times 10^{-7}$	
			(n,α)	-5.01	$<$ 10mb	$\sim$ 14	$< 6.69 \times 10^{-7}$	
			(n,γ)		$<$ 10mb	$\sim$ 14	$< 6.69 \times 10^{-7}$	
AV	^{1}H	5.49×10^{22}	All		4.25b	1	0.233	$\sim$ 1b at 10MeV
	C	3.43×10^{22}	All		2.6b	1	0.0892	$\sim$ 1.3b at 10MeV
			(n,2n)	-4.95	6mb	14.1	2.06×10^{-4}	
			(n,α)	-5.70	$\sim$ 330mb	9.2	1.13×10^{-2}	$\sim$ 270mb at 8MeV, 69mb at 14.1MeV
			(n,n3α)	-7.27	$\sim$ 210mb	11.5 $\rightarrow$ 16	7.21×10^{-3}	
			(n,p)	-12.6	10s of mb	$<$ 20	$\vartheta(3.43 \times 10^{-4})$	
			(n,d)	-13.8	10s of mb	$<$ 20	$\vartheta(3.43 \times 10^{-4})$	
	O	1.37×10^{22}	All		$\sim$ 1.5b	2 $\rightarrow$ 10	0.0205	
	^{16}O	1.37×10^{22}	(n,n')		0.2 $\rightarrow$ 0.6b	10 $\rightarrow$ 14	8.22×10^{-3}	Rough guide
			(n,2n)	-17	25mb	33	3.42×10^{-4}	Rises slowly
			(n,p)	-9.64	85mb	11	1.16×10^{-3}	Rises rapidly, falls off slowly
			(n,d)	-9.90	15mb	14.1	2.05×10^{-4}	
			(n,α)	-3.2	60mb	4 $\rightarrow$ 18	8.22×10^{-4}	Many resonances
	^{17}O	5.22×10^{18}	(n,p)		$<$ 10mb	$\sim$ 14	$< 5.22 \times 10^{-8}$	
	^{18}O	2.75×10^{19}	(n,p)		$<$ 10mb	$\sim$ 14	$< 2.75 \times 10^{-7}$	
			(n,α)	-5.01	$<$ 10mb	$\sim$ 14	$< 2.75 \times 10^{-7}$	
			(n,γ)		$<$ 10mb	$\sim$ 14	$< 2.75 \times 10^{-7}$	
HW	^{1}H	5.89×10^{19}	All		4.25b	1	2.50×10^{-4}	$\sim$ 1b at 10MeV
	^{2}H	6.62×10^{22}	All		2.9b	1	0.192	1.05b at 10MeV
			(n,2n)	-2.23	200mb	16	1.32×10^{-2}	50mb at 5.5MeV
	O	3.31×10^{22}	All		$\sim$ 1.5b	2 $\rightarrow$ 10	0.050	
	^{16}O	3.29×10^{22}	(n,n')		0.2 $\rightarrow$ 0.6b	10 $\rightarrow$ 14	0.020	Rough guide
			(n,2n)	-17	25mb	33	8.22×10^{-4}	Rises slowly
			(n,p)	-9.64	85mb	11	2.80×10^{-3}	Rises rapidly, falls off slowly
			(n,d)	-9.90	15mb	14.1	4.93×10^{-4}	
			(n,α)	-3.2	60mb*	4 $\rightarrow$ 18	1.97×10^{-3}	Many resonances
	^{17}O	1.82×10^{19}	(n,p)		$<$ 10mb	$\sim$ 14	$< 1.82 \times 10^{-7}$	
	^{18}O	1.99×10^{20}	(n,p)		$<$ 10mb	$\sim$ 14	$< 1.99 \times 10^{-6}$	
			(n,α)	-5.01	$<$ 10mb	$\sim$ 14	$< 1.99 \times 10^{-6}$	
			(n,γ)		$<$ 10mb	$\sim$ 14	$< 1.99 \times 10^{-6}$	

Table 6.3: Non-thermal microscopic and macroscopic cross sections for nuclei in the inner three media of the detector by location [132]$\rightarrow$[139]. The location is indicated by an abbreviation; LW = Light Water, AC = Acrylic Vessel, HW = Heavy Water. The density is given in units of number per unit volume. R stands for reaction, Q stands for Q-value, XS stands for cross section, E is the energy, and Macro XS stands for macroscopic cross section ($= n\sigma$, where n is the number density and σ the reaction cross section). The isotopic enrichment of ^{18}O in heavy water has been assumed to be approximately double that of ^{17}O.

6.4.1 Light Water

Neutron transport through the light water is dominated by the ^{1}H(n,n)^{1}H scattering cross section, which is (20.491±0.014)b for bare hydrogen at thermal energies [135] and about a factor of 3 higher for hydrogen contained in the water molecule. ^{1}H(n,n)^{1}H overwhelms the (n,n) thermal scattering cross sections of ^{16}O, ^{17}O and ^{18}O. Thermal neutron capture processes are also dominated by the hydrogen in the light water; although the ^{17}O(n,α)^{14}C capture cross section is of the same order of magnitude as the ^{1}H(n,γ)^{2}H cross section, at (0.235 ± 0.010)b compared with (0.3326 ± 0.0007)b [135], the number of hydrogen nuclei is ~ 5300 times the number of ^{17}O nuclei. Additional capture processes are negligible.

At 10MeV the total cross section for all n+^{1}H processes is 2b, comparable to that for all n+O processes (~ 1.5b). What capture there is will be dominated below 10MeV by the (n,α) reaction on ^{16}O, and above it by (n,α) and (n,p) capture, also on ^{16}O. More significant than the capture reactions in oxygen are the inelastic scattering reactions, which take the form X(n,n')X*, and contribute to neutron energy loss. The cross section for inelastic scattering on oxygen varies between 0.2 → 0.6b from 10 to 14MeV [136], and therefore about $\frac{2}{5}$ths of all scattering reactions on oxygen at 10MeV are expected to be inelastic. The importance of this process in SNO is limited by the very small number of neutrons which have energies above 6MeV (the threshold for inelastic scattering on ^{16}O). Table 6.3 contains a summary of the common neutron interactions in light water at non-thermal energies.

6.4.2 The Acrylic Vessel

The acrylic vessel contains hydrogen, carbon and oxygen in the form of polymethylmethacrylate ($H_8C_5O_2$). The reactions of neutrons with hydrogen and oxygen have already been described. Thermal transport through the acrylic is dominated by hydrogen because of its large scattering cross section compared with those of both oxygen and carbon. Both the stable isotopes of carbon have small thermal (n,γ) capture cross sections which are also negligible compared to that of hydrogen.

Below 20MeV, ^{12}C has an (n,α) capture interaction, and the extraordinary (n,n3α) carbon disintegration reaction. The (n,α) interaction has peak cross sections of ~ 270mb at 8MeV and ~ 330mb at 9.2MeV [136]. The cross section falls slowly to 69mb at 14.1MeV [136]. The (n,n3α) interaction cross section averages roughly 210mb in the energy range 11.5 → 16MeV [136]. These interactions compete with those in oxygen to capture high energy neutrons. Other reaction cross sections are much smaller. Table 6.3 contains a summary of the common neutron interactions in the acrylic vessel at non-thermal energies.

6.4.3 Heavy Water

In SNO, D_2O accounts for 99.92% of the mass of the heavy water, H_2O accounting for the remainder. It is also known that ^{17}O represents 0.055% of the total mass of oxygen in heavy water, up from 0.038% in natural water [140]. The isotopic content of ^{18}O will also be enhanced over that of natural water, where it is 0.2%. It is expected to be ~ 0.6%.

In the heavy water, elastic scattering from deuterium and oxygen are the dominant thermal processes. The ^{2}H(n,n)^{2}H cross section is (3.390 ± 0.012)b [135], much less than the ^{1}H(n,n)^{1}H cross section given above, but in SNO quality D_2O deuterium is three orders of magnitude more abundant than hydrogen. Thermal capture processes are more evenly distributed between ^{1}H, ^{2}H, and ^{17}O, because the numerical superiority of deuterium over both hydrogen and ^{17}O makes up for its rather small thermal capture cross section of (0.508 ± 0.015)mb [135].

At high energies in D_2O the most significant cross sections are those for elastic scattering, inelastic scattering from oxygen (the magnitude of the other oxygen cross sections is small) and additionally the ^{2}H(n,2n)^{1}H reaction. This last reaction has a cross section of 50mb at 5.5MeV, which rises to 200mb at around 16MeV [136]. These cross sections are such that of order 10% of all reactions at and about 10MeV in heavy water are expected to be deuteron breakup reactions. The fraction of such reactions decreases with decreasing energy down to the reaction threshold (the Q value is −2.225MeV). The total cross section in heavy water falls with increasing neutron energy; at 10MeV the total cross section for D_2O is 3.25b (σ_T(deuterium) = 1b) [123]. Table 6.3 contains a summary of the common neutron interactions in SNO quality heavy water at non-thermal energies.

6.4.4 Summary of Transport in the Bare Detector

The reaction cross sections in light water and the small mass of hydrogen mean that high energy neutrons will suffer rapid energy loss through inelastic scattering with oxygen and elastic scattering with hydrogen.

Loc	Isotope	Density (cm^3)	R	Q (MeV)	XS	E (MeV)	Macro XS (cm^{-1})	Comment
S1	Mg	1.24×10^{19}	All		1.6b	10	1.98×10^{-5}	
			(n,np)	−12.0	ϑ(10)mb	< 20	$\vartheta(1.24 \times 10^{-7})$	
			(n,nα)	−9.31	ϑ(1)mb	< 20	$\vartheta(1.24 \times 10^{-8})$	
	^{24}Mg	9.77×10^{18}	(n,p)	−4.37	ϑ(150)mb	8 → 20	$\vartheta(1.47 \times 10^{-6})$	
			(n,2n)		24.5mb	18	2.39×10^{-7}	
	^{25}Mg	1.24×10^{18}	(n,p)	−8.53	ϑ(40)mb	13 → 16	$\vartheta(4.95 \times 10^{-8})$	
	^{26}Mg	1.36×10^{18}	(n,α)	0.480	ϑ(70)mb	13 → 17	$\vartheta(9.53 \times 10^{-8})$	
	Cl	2.47×10^{19}	All		∼ 2b	10 → 20	$\sim 4.94 \times 10^{-5}$	
	^{35}Cl	1.87×10^{19}	(n,2n)		47mb	19.2	8.81×10^{-7}	5mb at 14MeV
			(n,p)	0.615	160mb	0.4keV	3.00×10^{-6}	Peak
			(n,α)	0.938	200mb	8	3.75×10^{-6}	Peak
	^{37}Cl	5.99×10^{18}	(n,p)	−4.08	ϑ(10)mb		$\vartheta(5.99 \times 10^{-8})$	
			(n,α)	−1.56	100mb	13 → 16	5.99×10^{-7}	
S2	Li	2.65×10^{18}	All		1.55b	10	4.1×10^{-6}	
	^{6}Li	2.52×10^{18}	(n,p)	−2.73	36mb	4.1	9.08×10^{-8}	
			(n,nd)		0.625b	5.2	1.58×10^{-6}	Broad peak
			(n,t)	4.78	4.4b	240keV	1.11×10^{-5}	0.512b at 14.95MeV
			(n,2np)	−5.67	∼ 80mb	15	2.01×10^{-7}	
	^{7}Li	1.33×10^{17}	(n,2n)		50mb	14.5	6.64×10^{-9}	Broad (4.5MeV $\frac{1}{2}$ width)
			(n,nt)		475mb	5.8	6.31×10^{-8}	250mb at 17MeV
			(n,α)		0.336b	14.95	4.46×10^{-8}	
			(n,d)	−7.75	14mb	14.8	1.86×10^{-9}	
	N	2.66×10^{18}	All		1.3b	10	3.5×10^{-6}	
			(n,2n)	−10.6	< 30mb		$< 7.97 \times 10^{-8}$	
			(n,p)	0.626	< 30mb		$< 7.97 \times 10^{-8}$	
			(n,t)	−4.02	< 30mb		$< 7.97 \times 10^{-8}$	
			(n,α)	−0.16	∼ 400mb	4	1.06×10^{-6}	Peak, $\overline{(\sigma)}$ = 100mb, 4 → 15MeV

Table 6.4: Non-thermal microscopic and macroscopic cross sections for nuclei in the inner three media of the detector by location [132]→[139]. The location is indicated by an abbreviation; S1 indicates that the nuclide is in a solution of 0.2% $MgCl_2$ salt in the heavy water, whilst S2 indicates that it is in a solution of 0.03% $LiNO_3$ in the heavy water and in this case the presence of additional oxygen in the water has been neglected. The density is given in units of number per unit volume. R stands for reaction, Q stands for Q-value, XS stands for cross section, E is the energy, and Macro XS stands for macroscopic cross section ($= n\sigma$, where n is the number density and σ the reaction cross section).

Once a neutron has reached thermal energies it will scatter predominantly from the H in H_2O molecules before capturing on hydrogen.

In the acrylic vessel, high energy neutrons react inelastically with oxygen and carbon and elastically with hydrogen. At thermal energies, hydrogen completely dominates the neutron transport.

In the heavy water high energy neutrons will scatter elastically and inelastically from oxygen and deuterium, and the d(n,2n)p reaction is important. Thermal neutrons scatter repeatedly from the D_2O molecule before capture onto hydrogen, deuterium, or ^{17}O.

6.5 Additives in the Heavy Water

Salt ($MgCl_2$), the neutral current detectors (NCDs), and possibly also poison ($LiNO_3$) will be added to the heavy water in the SNO detector, as described in Chapter 2. The subject of this section are the consequences of these options for neutron transport.

6.5.1 The Salt and Poison Options

The addition of 2 tonnes of $MgCl_2$ to the heavy water in SNO will have no significant effect on the transport of high energy neutrons (compare Tables 6.3 and 6.4). This is because the number of magnesium and chlorine nuclei present in the water is small compared to the number of deuterium and oxygen nuclei. At thermal energies the situation is quite different, because of the $^{35}Cl(n,\gamma)^{36}Cl$ cross section, which is 43.6 ± 0.4b [135], and which is responsible for 82.5% of all thermal neutron capture in a 0.2% heavy water salt solution. Scattering at thermal energies remains dominated by the D_2O molecule.

The addition of 300kgs of $LiNO_3$ to the detector has the same general effect on the transport of neutrons as the addition of salt in that the transport of high energy neutrons is unaffected, and thermal

Loc	Isotope	Density (cm^3)	R	Q (MeV)	XS	E (MeV)	Macro XS (cm^{-1})	Comment
CG	^{3}He	5.55×10^{19}	All		1.5b	10	8.32×10^{-5}	
			(n,p)	0.746	210mb	8.07	1.16×10^{-5}	0.61b at 0.95MeV, 0.14b at 14.4MeV
			(n,d)	−2.37	76mb	14	4.22×10^{-6}	
	C	1.37×10^{19}	All		2.6b	1	3.56×10^{-5}	∼ 1.3b at 10MeV
			(n,2n)	−4.95	6mb	14.1	8.22×10^{-8}	
			(n,α)	−5.70	∼ 330mb	9.2	4.52×10^{-6}	∼ 270mb at 8MeV, 69mb at 14.1MeV
			(n,n3α)	−7.27	∼ 210mb	11.5 → 16	2.87×10^{-6}	
			(n,p)	−12.6	10s of mb	< 20	$\vartheta(1.37 \times 10^{-7})$	
			(n,d)	−13.8	10s of mb	< 20	$\vartheta(1.37 \times 10^{-7})$	
	^{19}F	5.55×10^{19}	All		1.6b	10	8.88×10^{-5}	
NCD	Ni	9.12×10^{22}	All		3 → 4b	5 → 10	∼ 0.319	
	^{58}Ni	6.23×10^{22}	(n,2n)		67mb	20	4.18×10^{-3}	2mb at 12.8MeV
			(n,p)		600mb	10	3.74×10^{-2}	1mb at 1MeV and 150mb at 20MeV
			(n,np)		828mb	17	5.16×10^{-2}	1mb at 10MeV and 244mb at 12MeV
			(n,d)		30mb	15	1.87×10^{-3}	
			(n,nα)		< 10mb	16 → 20	$< 6.23 \times 10^{-4}$	
			(n,α)		122.5mb	10.5	7.63×10^{-3}	
	^{60}Ni	2.38×10^{22}	(n,2n)		490mb	16	1.17×10^{-2}	19mb at 12MeV and 160mb at 13MeV
			(n,np)		> 100mb	> 14	$> 2.38 \times 10^{-3}$	
			(n,nα)	−6.29	< 100mb	< 20	$< 2.38 \times 10^{-3}$	
			(n,d)		< 30mb	< 20	$< 7.15 \times 10^{-4}$	
	^{61}Ni	1.03×10^{21}	(n,2n)		ϑ(100)mb	> 9.2	$\vartheta(1.03 \times 10^{-4})$	
			(n,np)		ϑ(100)mb	> 14.5	$\vartheta(1.03 \times 10^{-4})$	
			(n,p)	−0.540	ϑ(10)mb		$\vartheta(1.03 \times 10^{-5})$	
			(n,α)	−3.57	ϑ(10)mb		$\vartheta(1.03 \times 10^{-5})$	
	^{62}Ni	3.27×10^{21}	(n,2n)		ϑ(1)mb	< 20	$\vartheta(3.28 \times 10^{-6})$	
			(n,nα)		ϑ(1)mb	< 20	$\vartheta(3.28 \times 10^{-6})$	
			(n,p)		ϑ(1)m	< 20	$\vartheta(3.28 \times 10^{-6})$	
			(n,d)		ϑ(1)m	< 20	$\vartheta(3.28 \times 10^{-6})$	
			(n,α)	−0.437	ϑ(10)mb	> 12.5	$\vartheta(3.28 \times 10^{-5})$	
			(n,np)	−11.1	ϑ(10)mb		$\vartheta(3.28 \times 10^{-5})$	
	^{64}Ni	8.31×10^{20}	(n,2n)		ϑ(1)mb	< 20	$\vartheta(8.31 \times 10^{-7})$	
			(n,nα)		ϑ(1)mb	< 20	$\vartheta(8.31 \times 10^{-7})$	
			(n,p)		ϑ(1)mb	< 20	$\vartheta(8.31 \times 10^{-7})$	
			(n,d)		ϑ(1)mb	< 20	$\vartheta(8.31 \times 10^{-7})$	
			(n,α)	−2.44	ϑ(10)mb	> 16	$\vartheta(8.31 \times 10^{-6})$	

Table 6.5: Non-thermal microscopic and macroscopic cross sections for nuclei in the inner three media of the detector by location [132]→[139]. The location is indicated by an abbreviation; NCD = Neutral Current Detector, and CG = Counter Gas.The density is given in units of number per unit volume. R stands for reaction, Q stands for Q-value, XS stands for cross section, E is the energy, and Macro XS stands for macroscopic cross section ($= n\sigma$, where n is the number density and σ the reaction cross section).

neutron scattering is dominated by D_2O. Thermal neutron capture, however, is predominantly via the ^{6}Li(n,α)^{3}H reaction, whose cross section is 940 ± 4b.

6.5.2 Interactions in the NCDs

The gas in the NCD proportional counters will be an equal mixture of ^{3}He and CF_4. Neutron transport is dominated at thermal energies by ^{3}He, with its (n,p) reaction, whose cross section is 5333 ± 7b [135]. The (n,p) cross section falls only slowly to 0.61b at 0.95MeV and to 0.21b at 8.07MeV [139], and hence competes with the (n,α) and (n,n3α) reactions in ^{12}C at MeV energies. Other interactions are negligible. The NCD counter is manufactured from pure nickel. See the summary Tables 6.1, 6.2, and 6.5 for information on n-transport through Nickel.

6.6 Effect of Neglect of Certain Nuclei

Certain isotopes which have low abundances (< 1%) can be neglected in any assessment of the neutron physics that takes place in the SNO detector. This is provided that they have scattering cross sections of

similar or smaller magnitudes to more abundant isotopes of the same element. All the isotopes present in the SNO detector will be included in the neutron transport calculations except ^{13}C, ^{17}O, and ^{18}O. The effects of these 3 low abundance nuclei on neutron transport in SNO can be neglected.

The nuclei ^{13}C, ^{17}O, and ^{18}O do not contribute significantly to high energy neutron scattering because although their cross sections are similar in magnitude to the other isotopes of the same atomic species in the media in which they are present, their abundances are very low (see Tables 6.3 and 6.2).

The nucleus ^{18}O has a scattering and capture cross sections comparable to that of ^{16}O, but a much smaller abundance ($\sim$ 0.6% compared with $\sim$ 99.3% in D_2O). The neglect of ^{18}O will introduce three errors;

1. an error in the thermal neutron scattering cross section; and,
2. an error in the thermal neutron capture cross section; and,
3. an error because the energy-angle distribution function specific to scattering from ^{18}O will be ignored.

The thermal neutron scattering cross section of ^{18}O (3.83b) is similar to that of ^{16}O (3.76b). The thermal capture cross section is also similar (0.160mb as opposed to 0.190mb). If ^{18}O were to be neglected, it would result in an error of approximately 0.6% to the total oxygen scattering and absorption cross sections in the D_2O. If instead ^{16}O were to be substituted for ^{18}O, the error in the cross section would be much smaller. The remaining error, the neglect of the energy-angle distributions specific to ^{18}O, is unimportant in SNO because even if it were to be included it would be infrequently sampled and hence have little impact on the random nature of thermal neutron transport. The effect of the neglect of ^{18}O is smaller in the H_2O than in the D_2O, because the abundance of ^{18}O is lower there, and because oxygen contributes a much smaller fraction of the total cross section at thermal energies.

The ^{13}C cross section can be neglected for reasons similar to those given for ^{18}O (see Table 6.1). Like ^{18}O, the scattering interactions of ^{17}O can be neglected. However, the (n,α) capture cross section must be explicitly included for heavy water, because its cross section is $\sim$ 7% of the total absorption cross section at $\frac{1}{40}$eV. In the Monte Carlo calculations, ^{13}C is replaced by ^{12}C, and ^{17}O and ^{18}O by ^{16}O, except for the $^{17}O(n,\alpha)^{14}C$ reaction, which is explicitly included.

6.7 Hydrogen in the Heavy Water

D_2O is the most common constituent molecule in heavy water. The other molecules present in SNO quality heavy water are the light water molecule, H_2O, and the molecule HDO, which forms as a result of isotopic mixing. The isotopic mass purity of heavy water is

$$p_h = \frac{m_h}{m_h + m_l} , \tag{6.3}$$

where p_h is the fraction of the mass of the heavy water that is D_2O, m_h is the mass of heavy water, and m_l is the mass of the light water. p_h is calculated by assuming that all of the hydrogen in the heavy water is present in the molecule H_2O, and all of the deuterium is present in D_2O. In SNO, $p_h = 0.9992$, and hence, due to the great numerical superiority of deuterium over hydrogen, the process $HDO + H \rightarrow H_2O + D$ has a very much lower rate than $H_2O + D \rightarrow HDO + H$. Therefore almost all the hydrogen in the SNO heavy water is present as part of the HDO molecule.

6.7.1 Interaction Cross Sections

The fact that nearly all the hydrogen in the heavy water is present as part of the HDO molecule presents some difficulties for the accurate simulation of neutron transport in SNO heavy water. This is because although the n-transport Monte Carlo selected for use in SNOMAN in Chapter 7 does have a sophisticated thermal transport capability, no data tables are provided for the simulation of thermal neutron transport involving the HDO molecule. Therefore in SNOMAN the presence of HDO will be ignored, and what hydrogen there is in the heavy water will be simulated as belonging to an H_2O molecule. This means that thermal data tables appropriate to the light and heavy water molecules will be used in SNOMAN in that small fraction of collisions that should be simulated as involving the HDO molecule.

There are three sources of error that the use of H-in-H_2O and D-in-D_2O thermal tables will introduce to the simulation of scattering from the HDO molecule. These are (overleaf);

1. the reduced mass;

2. rotational effects; and,

3. vibrational effects.

The use of an incorrect reduced mass causes the elastic scattering cross section to be in error by up to $\sim 10\%$ (see Equation E.2). This error is mitigated by the small number of HDO molecules in the heavy water ($\sim 0.17\%$ by number). Vibrational states are not excited as a result of inelastic neutron scattering at thermal energies. This is because there is insufficient energy available in the collision to excite a vibrational mode. Any error in the simulation of the effect of vibrational modes upon neutron transport will be ignored as a result. More serious is the error caused by the identical nature of the nuclei in the H_2O and D_2O molecules. Hydrogen nuclei (protons) are fermions, and their wavefunction in the H_2O molecule must be antisymmetric under exchange. This means that it must take the form $\psi_a = \chi_a\phi_s$ or $\psi_a = \chi_s\phi_a$, where ψ is the overall wavefunction, χ and ϕ are the spin and space wavefunctions respectively, and the subscript a implies that the wavefunction is antisymmetric under particle exchange, whilst s has the opposite sense. In both the cases given, the spatial wavefunction has a definite symmetry under the exchange of the hydrogen nuclei. A similar argument can be made for D in D_2O (deuterons are bosons, and must have wavefunctions that are symmetric under particle exchange), to reach the same conclusion, i.e. that the spatial wavefunction must have a definite symmetry under the exchange of the deuterium nuclei. No such restriction exists in the HDO molecule, where there are no identical nuclei present. A crude overestimate of the magnitude of the effect on the macroscopic cross section at thermal energy can be made if it is assumed that the entire $H_2O/D_2O/HDO$ cross section not arising from direct nuclear interactions is a result of the inelastic scattering of the target molecule into rotational states, and that the HDO cross section for this process is approximately double that of H_2O due to the lack of any restriction to final states of particular symmetry. This is of course an overestimate, since the scattering cross section for hydrogen is very much larger than that from deuterium and hence, in the absence of any symmetry considerations, it would be reasonable to expect the rotational cross section for H_2O to be in excess of that for HDO. Define;

$$\sigma^h = \sigma_i^h + \sigma_r^h \ , \tag{6.4}$$

$$\sigma_i^h = 2\sigma(D) + \sigma(O) \ , \tag{6.5}$$

where σ^h is the total thermal neutron cross section for the D_2O molecule, σ_i^h is the cross section without the inclusion of the rotational states of D_2O, and σ_r^h is the cross section for thermal inelastic scattering of the heavy water molecule into rotational final states. σ(D) and σ(O) are the total cross sections for neutrons interacting with free deuterium and oxygen nuclei. Equivalent quantities are defined for the H_2O and HDO molecules. σ^h, σ^l (the light water cross section), σ(H),σ(D), and σ(O) are known, whilst the 'rotational' cross sections are defined by the following example; $\sigma_r^h = \sigma^h - \sigma_i^h$. This calculation overestimates the contribution of the rotational states to the total cross-section because the increase in the cross-sections for elastic scattering from the H and D nuclei due to the increased effective reduced mass from molecular binding (Equation E.2) is neglected. This will make the estimate of the error in the computer simulation appear larger than it is. The true cross section for scattering from HDO is;

$$\sigma = (1-2f)\sigma^h + 2f\sigma^m \ , \tag{6.6}$$

$$= (1-2f)(\sigma_i^h + \sigma_r^h) + 2f(\sigma_i^m + \sigma_r^m) \ , \tag{6.7}$$

$$\simeq (1-2f)(\sigma_i^h + \sigma_r^h) + 2f\sigma_i^m + 4f\sigma_r^l \ , \tag{6.8}$$

assuming as stated that $\sigma_r^m = 2\sigma_r^l$, and where $\sigma_i^m = \sigma$(H) + σ(D) + σ(O) and $f = 0.0008888$ is the numerical fraction of H_2O molecules in the SNO heavy water, derived from Equation 6.3. The factor $2f$ arises because the definition of purity refers to the mass presence of H_2O rather than HDO. The crude estimates of the interaction and rotational cross sections are denoted by the subscripts i and r, and cross sections for D_2O, H_2O, and HDO are denoted by the superscripts h, l, and m. The cross section simulated in SNOMAN is;

$$\sigma' = (1-f)(\sigma_i^h + \sigma_r^h) + f(\sigma_i^l + \sigma_r^l) \ . \tag{6.9}$$

The fractional error is

$$\text{error} = \frac{\sigma' - \sigma}{\sigma'} , \tag{6.10}$$

$$= \frac{f(\sigma_i^h + \sigma_r^h) + \sigma_i^l - 2f\sigma_i^m - 3f\sigma_r^l}{(1-f)(\sigma_i^h + \sigma_r^h) + f(\sigma_i^l + \sigma_r^l)} , \tag{6.11}$$

$$\simeq -0.01 . \tag{6.12}$$

There is a maximum error of 1% in the simulated total cross section for SNO quality heavy water. This is an over estimate of the true error because of the neglect of the effects of the reduced mass on the elastic scattering cross sections, and because the rotational cross section for HDO has been taken as twice that of H_2O. Despite these overestimates, this error is small when compared to the estimated $\sim 3\%$ accuracy of MCNP (the estimate is discussed in Chapter 8). Hence, no further discussion of this error will take place.

6.7.2 Capture Cross Sections

In the preceding section, the effect of symmetries upon the scattering cross section was examined and found to be insignificant. In this section, it will be shown that the modelling of the HDO molecule as D_2O and H_2O molecules has no effect upon the capture cross sections. Consider the capture interaction for the hydrogen nucleus;

$$\mathrm{n} + \mathrm{H} \rightarrow \mathrm{D} + \gamma + 2.23\mathrm{MeV} . \tag{6.13}$$

The recoil energy of the deuterium nucleus in the final state is $\sim$ 5keV. This is far higher than the binding energy of the hydrogen atom to the water molecule, and therefore the deuterium nucleus resulting from n-capture on hydrogen in water is free in the final state, and hence suffers no symmetry constraints. This also true of the tritium nucleus that results from n-capture on deuterium in heavy water or the HDO molecule. In the initial state, the wavefunction for the hydrogen nuclei must have the appropriate antisymmetry property, and must be normalised to 2, for the two hydrogen nuclei. Taking the operator $\check{\mathrm{C}}$ as the capture operator, the squared matrix element for capture is;

$$M_{if}^2 = \left|\langle \psi_n \psi_{HOH} | \check{\mathrm{C}} | \psi_D \psi_{OH} \psi_\gamma \rangle\right|^2 . \tag{6.14}$$

Now consider one possible example of the wavefunction of the water molecule, where the decomposition of ψ_{HOH} into a symmetric spatial part and an antisymmetric spin part takes place;

$$M_{if}^2 = \Big|\langle \psi_n \frac{1}{\sqrt{2}} (\chi_{H,1}^1 \chi_{H,2}^2 - \chi_{H,2}^1 \chi_{H,1}^2) \chi_O \phi_{H,1} \phi_O \phi_{H,2} | \check{\mathrm{C}} | \psi_D \left(\chi_{H,2}^2 \phi_{H,2} \chi_O \phi_O \right.$$
$$\left. + \chi_{H,1}^1 \phi_{H,1} \chi_O \phi_O - \chi_{H,1}^2 \phi_{H,1} \chi_O \phi_O - \chi_{H,2}^1 \phi_{H,2} \chi_O \phi_O \right) \psi_\gamma \rangle \Big|^2 , \tag{6.15}$$

$$= 2 \left|\langle \psi_n \chi_{H,1} \chi_{H,2} \chi_O \phi_{H,1} \phi_O \phi_{H,2} | \check{\mathrm{C}} | \psi_{D,1} \chi_{H,2} \phi_{H,2} \chi_O \phi_O \psi\gamma \rangle\right|^2 , \tag{6.16}$$

where χ is always a spin wavefunction, ϕ a spatial wavefunction, and ψ a total wavefunction. Equation 6.15 assumes that the capture operator does not affect the spins of either the H or the O spectator nuclei, and hence that there are only 4 possible final states corresponding to neutron capture onto hydrogen in any of the four hydrogen wavefunctions in the initial state. In deriving Equation 6.16 from Equation 6.15 it has been assumed that the four possible final states are incoherent with one another. Equation 6.16 demonstrates that the numerical effects of any symmetry in the initial state are counterbalanced by the normalisation of that initial state, and hence that the capture cross section on bound nuclei is equal to that in free nuclei. A similar argument can be made for deuterium in heavy water and for both the H and D nuclei in the molecule HDO. A comparison of the four final expressions for the capture cross sections then reveals that the simulation of the capture cross section on HDO using those for light and heavy water does result in the cross section being calculated correctly.

In summary, the simulation of the capture process on HDO is carried out correctly in the SNOMAN program by modelling the HDO molecule using light and heavy water molecule simulation data. This is made possible because the symmetry effects present in the H_2O and D_2O molecules but not in the HDO molecule do not affect the calculation of the matrix element, and because the nucleus created as the result of capture (either deuterium or tritium) is free in the final state.

Concentration of $MgCl_2$	Reported Density (g/cm^3)	Calculated Density (g/cm^3)	Error
0.0%	0.9997	0.9997	0
0.5%	1.0022	1.0047	0.25%
1.0%	1.0062	1.0097	0.35%
2.0%	1.0144	1.0197	0.52%
3.0%	1.0226	1.0297	0.69%

Table 6.6: The reported and calculated density of light water salt solutions. Reported density taken from [142]. For an explanation of the calculated density, see text.

6.7.3 Salted Heavy Water

The heavy water in the SNO experiment will at some stage contain $MgCl_2$, probably at a concentration of 0.2%. This will change the neutron absorption and scattering lengths. The calculation of these quantities in salted heavy water is dependent upon the molecular densities of H, D, O, Mg and Cl there. In the absence of data on the density of heavy water $MgCl_2$ salt solutions, a simple model has been devised. The model assumes that there are no long range forces due to the presence of the salt ions in the D_2O, and that the Mg^{2+} and Cl^- ions occupy no net volume, and hence that the change in the density of the salted heavy water can be attributed to the mass of the $MgCl_2$ alone. Hence, a 2% salt solution should have a density that is 1% greater than a 1% salt solution. Table 6.6 shows that this model accounts for the density of a salt and light water solution of $MgCl_2$ at the 0.25% level or better for salt concentrations of 0.5% and below. This level of accuracy is acceptable for use in SNOMAN in the absence of data on heavy water salt solutions, and hence it has been assumed that the density of heavy water salt solutions can be calculated in the same way. It is envisaged that this model will be replaced by experimental data when it becomes available.

6.8 Conclusion

The physics of neutrons in the SNO detector is dominated by thermal transport. In the light water and acrylic vessel, hydrogen is the dominant nucleus, in the heavy water, deuterium dominates scattering (although oxygen makes a significant contribution) and hydrogen, deuterium, and oxygen all contribute to neutron capture. The chlorine and lithium additives that may be used in the D_2O have little effect on the scattering cross section, but they dominate neutron capture.

The nucleus ^{12}C can be substituted for ^{13}C. The error introduced into the carbon scattering and capture cross sections is less than 1%. Likewise ^{16}O can be substituted for ^{18}O. The error introduced into the oxygen scattering and capture cross section is less than 0.2%. In addition ^{16}O can also be substituted for ^{17}O provided the $^{17}O(n,\alpha)^{14}C$ reaction is explicitly catered for.

The effects of the dissociation of the H_2O molecule in heavy water can be ignored. This results in an error of less than 1% in the macroscopic scattering cross section of water, and no error is made in the capture cross section. At the low concentrations that salt is present in the heavy water, the density of the resulting salt solution can be simulated in a purely additive manner. The error introduced is 0.1% when 2 tonnes of salt are added to 1 kilotonne of D_2O.

Chapter 7

The Simulation of Neutron Transport Physics

7.1 Introduction and Purpose

In the last chapter, Chapter 6, the subject of neutron transport physics in the SNO detector was examined. In this chapter, the simulation of that process will be discussed. This will entail;

1. an introduction to the SNOMAN program which is used to simulate the SNO detector as a whole;
2. an explanation of how physical results can be obtained from a neutron transport code;
3. the selection, subject to certain criteria, of an appropriate neutron transport program for use in SNOMAN; and,
4. a discussion of the difficulties in modifying the code to work with the SNOMAN program.

The coverage of each topic will be brief.

7.2 The SNOMAN Program

SNOMAN (Sudbury Neutrino Observatory Monte Carlo and ANalysis) is the program that has been written to simulate the SNO detector. In addition to neutron transport, to be capable of representing the SNO detector, the SNOMAN program contains a comprehensive physical model of the structure of the detector and the physical processes that occur within it. The SNOMAN program contains the following physics-related elements that are critical to the simulation of the detector:

1. a comprehensive geometric model, together with its material properties, of the structure of the SNO detector;
2. neutron, γ, photon and electron sources;
3. γ and $e^{\pm}$ transport;
4. Čerenkov light production and transport;
5. Čerenkov light detection by the photomultipliers;
6. the SNO detector trigger and output mechanisms.

The SNOMAN program also has the capability to read and analyse data that is written to tape by the data acquisition electronics that 'observe' the detector. It also has a complex error recovery and process report mechanisms. None of the details surrounding these latter functions will be explored here.

7.2.1 Geometry in the SNOMAN Program

No model of the detector would be complete without an accurate model of the detector's physical geometry. The geometry code serves to define the boundaries of the media of the detector in the SNOMAN program. A great deal of work by a number of individuals has been done in simulating the SNO detector's geometry in SNOMAN. For more detail, the reader is invited to survey work by West *et al.* [89], Brice [122] and Lay [63].

The principle features of the SNOMAN geometry are the inclusion of the acrylic vessel, tile by tile, the acrylic vessel neck, each individual photomultiplier position and orientation, and the PMTs and light-concentrators themselves. All the particles whose transport is modelled by SNOMAN can be propagated through all the media.

7.2.2 Particle Production: Sources in SNOMAN

SNOMAN is capable of generating an enormous variety of source distributions. SNOMAN can simulate a number of different physical particle production mechanisms. These include the charged current interaction, the neutral current interaction, and neutrino electron scattering, which constitute the principal signals in the SNO detector. The SNOMAN generator can also simulate the β decays, β-γ decays, and α-γ decays that occur when contaminating nuclides are present in the SNO detector.

The source distributions can be used to generate events from a point, along a line, from within a spherical shell, from a region, a number of regions, or a number of regions with different weights, or at a distance from a previous source event (that distance varying exponentially). The distribution of event directions may be isotropic, or in a beam, or in a cone, or the proper distribution for events arising from the neutrino interactions within the detector. Various direction distributions that arise as a result of calibration source geometries may also be generated. The energies of the events may be drawn from a Čerenkov energy spectrum, or from a charged current or electron scattering distribution, with or without the expected MSW distortion. The energies may be distributed according to a neutral current spectrum, or a Maxwell-Boltzmann thermal spectrum, or they may be fixed. They may also be drawn from β and β-γ decay spectra. The time associated with the start of an event may be fixed, or be distributed uniformly between two times, or their distribution may be exponential in character when taken from a fixed time, or from the time another particle was generated. It may be Gaussian, with cutoffs, or it may be in accordance with the event distribution for solar neutrino events within the detector.

There is no shortage of possible event distributions which the SNOMAN program is capable of simulating. Further detail can be found in [89].

7.2.3 Gamma and $e^{\pm}$ Transport, and Čerenkov Photon Transport and Detection, and Detector Triggering

SNOMAN is equipped to propagate $e^{\pm}$ and γ particles. It does so using the routines provided by the EGS4 (Electron Gamma Shower) code system. The electron/positron transport simulation includes the following effects:

1. Bhabba (e^+e^-) and Møller (e^-e^-) scattering;
2. Bremsstrahlung production;
3. continuous energy loss for charged particles;
4. multiple scattering of electrons using Molière theory;
5. positron annihilation.

whilst the γ transport simulation includes:

1. Compton scattering;
2. pair production;
3. the photoelectric effect (only the primary generated electron is considered).

The creation and propagation of Čerenkov particles is handled separately - absorption, boundary interactions, and Rayleigh scattering are included [63, Chapter 4]. Bowler [126] has shown that the single and multiple scattering suffered by electrons in water has no significant effect on Čerenkov light output. In addition, Lay and Bowler [127] have shown that the average angular distribution of electrons resulting from their multiple scattering as described by EGS4 agrees closely with the result of the formalism of Goudsmit and Saunderson. This is significant because the angular distribution of Čerenkov photons is a direct result of that of electrons.

Lay [63] has modelled the Hamamatsu R1408 photomultiplier and concentrator arrangement (see Chapter 3 for more detail) and this is included in the SNOMAN simulation. The SNOMAN program does not currently take account of individual PMT quantum efficiencies (which is intended here to be interpreted in the loose sense of Chapter 2) or the data acquisition electronics (DAQ) calibration. It currently simulates the average properties of a phototube, and work on a full PMT and DAQ calibration simulation is in progress. The mechanism of the SNO trigger is simulated; SNOMAN searches a time window of 100ns for a number of hits in excess of a hardware threshold and declares a global trigger in the same manner as will the detector hardware during the operation of the detector.

7.3 Obtaining Physical Results from a Computer Code

7.3.1 Neutrons and the Monte Carlo Mechanism

This section will explain how it is that physical results pertaining to the transport of neutrons can be obtained from a computer program. The neutron is a heavy uncharged hadron with a magnetic moment. When passing through non-magnetic media, the forces that act upon the neutron are of nuclear origin. These forces are of extremely short range when compared to a typical inter atomic spacing (10^{-15}m compared with 10^{-10}m), and nuclear radii are themselves small when compared to atomic radii (a ratio of 10^{-4} is not untypical): it follows that [97]:

1. the motion of neutrons can be described it terms of its collisions with atomic nuclei;
2. these collisions are well defined events in space and time, with definite outcomes;
3. between collisions, the velocity of the neutron is a constant;
4. in general mutual collisions between neutrons can be ignored;
5. for a neutron travelling at a given speed through a given medium, the probability of interaction per unit path length is a constant;
6. the neutron(s) emerging from a collision do so at the point where the collision took place.

Thus the neutron moves directly from one nuclear collision to another. The computational analogue of the neutron's life is conceptually straightforward, the following cycle is repeated until the neutron is captured:

1. calculate the neutron's mean free path (λ) in the medium;
2. randomly sample the neutron's step length (S) to the next interaction;
3. find the distance to the next media boundary (D), in the direction of the neutron's motion;
4. if S<D then propagate the neutron a distance S, and simulate a neutron interaction. If (D<S) then propagate the neutron a distance D to the medium's boundary, and look up the n-transport related properties of the next medium.

It is only the difficulty in preparing comprehensive data sets with which to calculate neutron cross sections and simulate neutron collisions with the nuclei in a medium that make the preparation of an analogue neutron transport code a non-trivial task. What is meant by 'analogue' in this context will be explained in a moment. Simulation of a neutron history is the simulation of the physical processes of a neutron's 'birth', transport, and 'death'. Exactly what constitutes the 'birth' and 'death' for a simulated neutron depends upon the circumstances of the simulation. In the SNO experiment, every neutron is potentially capable of being captured in the heavy water and triggering the detector. In the SNOMAN program therefore, the 'birth' of a neutron is any process that introduces a free neutron into the detector, and the 'death' of a neutron occurs only when a neutron is captured by an (n,γ), (n,α), (n,p), or some

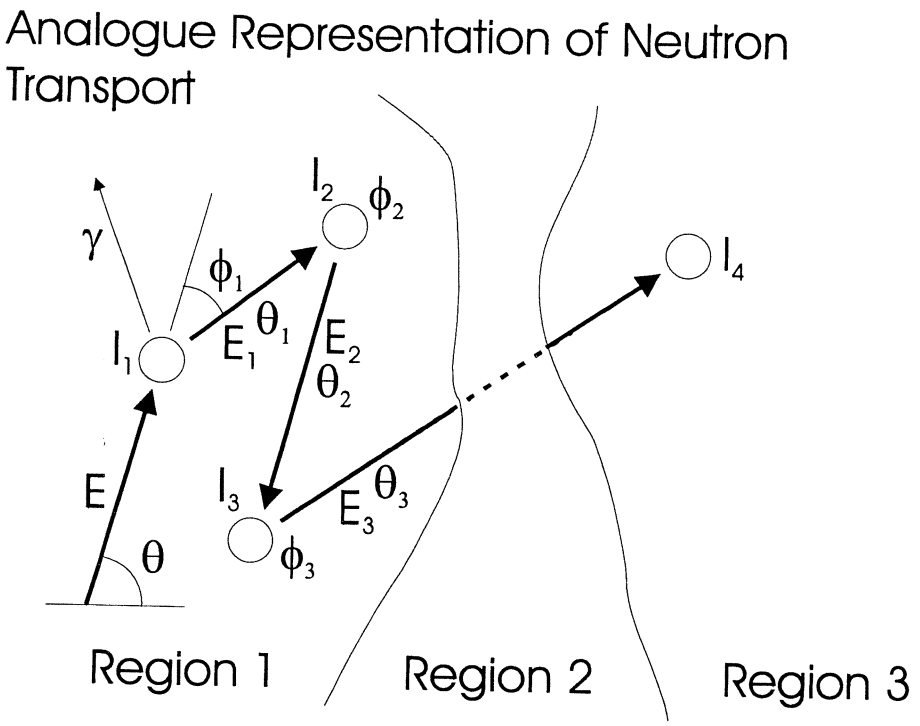

Figure 7.1: The computed history is the analogue of one possible physical neutron history.

other similar zero-neutron-out process. A computer code that carries out neutron transport calculations by iterating through the computational analogues of many neutron histories is known as an 'analogue' code. The SNOMAN code is an analogue code in all respects. This reflects the fact that the number of signal events expected in the SNO detector in a year is numbered in the thousands (see Chapter 2), and hence several years of detector running can be simulated in detail with the CPU time available in a few calendar days. Physical results are obtained from such codes by the analysis of the neutron histories for experimentally relevant criteria. In the SNO experiment, neutrons may be observed if they 1; (n,γ) capture at thermal energies onto a small selection of nuclei (D and Cl in particular), provided the capture event exceeds some threshold value for the number of phototubes reporting hits, or 2; (n,p) capture in the NCDs. The SNOMAN code reflects this process; each neutron history, coupled with its consequential γ and Čerenkov photon transport, is analysed. Any simulated phototube or NCD hits are then reported just as they would be in the SNO experiment. In addition to direct simulation of the SNO experiment, the SNOMAN code is also capable of reporting simulated results that could not be learned directly from the detector.

Unfortunately for the addition of a neutron transport capability to the SNOMAN program, the analogue mechanism is not appropriate for Monte Carlo codes simulating neutron-rich environments, including nuclear reactors. This is because the number of neutron histories that would need to be simulated is prohibitive in terms of the CPU usage required. Neutron transport Monte Carlo codes used in reactor design and simulation are the most comprehensive and accurate n-transport codes available - and all of them make use of so-called non-analogue methods. The distinction between analogue and non-analogue codes will be discussed in the next section.

7.3.2 Analogue versus Non-Analogue

An analogue code is one in which each neutron history is the computational analogue of one possible neutron history. An analogue code attempts to simulate each stage of the physics of neutron transport as closely as possible. Figure 7.1 contains a 2-dimensional representation of a possible neutron history. Each stage of the history can be understood in terms of the rules given earlier in Section 7.3.1. The landmark events in the history are:

1. the neutron, approaching along a bearing θ with an initial energy E, suffers an inelastic scattering reaction, I_1. As a result of the interaction I_1, the neutron is scattered through an angle ϕ_1, and emerges on a bearing θ_1 with energy E_1. A γ-ray is emitted from the struck nucleus.

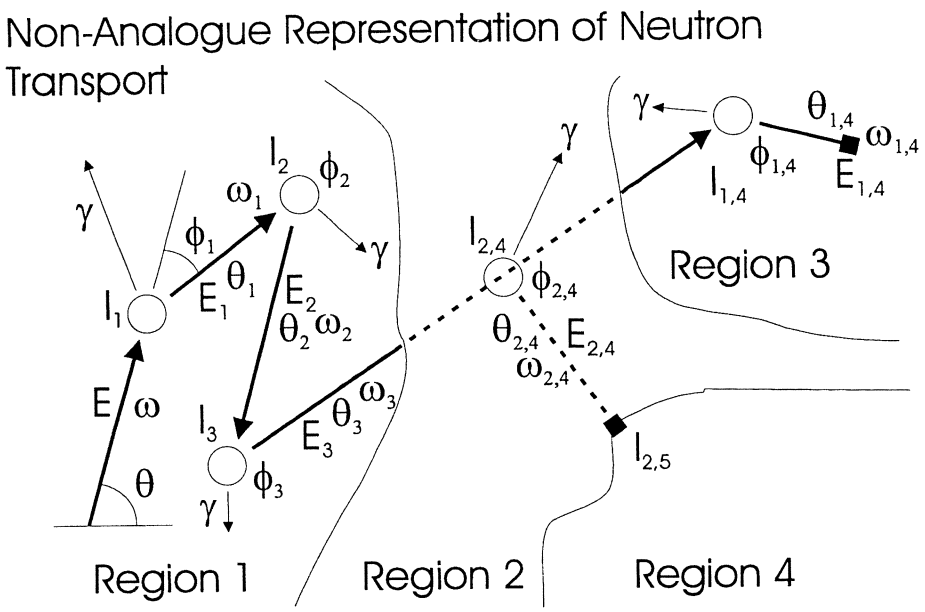

Figure 7.2: The computed history is a weighted sum of a number of possible neutron histories.

2. The neutron is scattered elastically at I_2 through an angle ϕ_2, and subsequently has a bearing θ_2 and energy E_2.

3. The neutron is scattered elastically at I_3 through an angle ϕ_3, and subsequently has a bearing θ_3 and energy E_3.

4. The neutron passes through a media boundary (region 1 $\rightarrow$ 2). The dashed line indicates that an extensive section of the history has been omitted for brevity. The neutron enters region 3.

5. The neutron is captured by an (n,γ) interaction at I_4.

Any analogue code suffers from one major drawback. It is that if only a very small percentage of all simulated events are important, then collecting data about those important events can be very time consuming, necessitating as it does the simulation of large numbers of unimportant events. To take an example from the history described above, if the analogue Monte Carlo is being run to determine the distribution of capture events, then each neutron history yields only 1 such event, and many events need to be run to build up a meaningful distribution. The advantage to the analogue method is that the statistics applicable to it are extremely simple, and the interpretation of data is unambiguous.

To overcome the major drawback of the analogue method, non-analogue methods have been devised. A non-analogue code increases the number of histories in important regions of the neutron phase space whilst reducing their weight, or it may decrease the number of histories in unimportant regions of the phase space whilst increasing their weight, or both. Increasing the number of histories decreases the statistical error on quantities derived from those histories. Changing the weights associated with each history allows meaningful probabilities to be extracted from the Monte Carlo results. For example, suppose a user of the SNOMAN program was interested in what happens to the neutrons released into the SNO detector following the photodisintegration of the deuteron by ^{208}Tl contaminating the acrylic vessel. On average, 1 photodisintegration occurs for every $\sim$ 1358 ^{208}Tl decays in the acrylic vessel. To collect 100 such events using the analogue version of SNOMAN would require a total of $\sim$ 135800 simulated events. If SNOMAN had been written as a non-analogue code (which is not the case), the user might choose to emit not 1 but 10 neutrons from a photodisintegration event, each with 1/10th the weight of the incoming photon (which must be 1 if no other non-analogue game is being played). The advantage of this non-analogue game is very clear; the average number of neutron histories simulated per ^{208}Tl decay event has been increased. The disadvantage is just the opposite; fewer (γ,n) events occur for each neutron, and therefore if the nature of the neutron history after the photodisintegration event is heavily dependent on the position of the (γ,n) event in the detector, then running fewer such events may result in the introduction of a significant bias into the results obtained from the Monte Carlo. To

summarise; non-analogue games increase the rate at which data can be acquired by a Monte Carlo at the risk of introducing a bias into the results. Data interpretation may also become complicated if a large number of non-analogue games are being played at the same time.

To simulate physical neutron transport as accurately as an analogue code, a non-analogue code must contain the same information about the neutron transport process, including the scattering and capture of neutrons. Figure 7.2 contains a 2-dimensional representation of a possible non-analogue neutron history. The history contains a number of examples of the type of non-analogue techniques that can be used. The examples given are not exhaustive, and have no special significance. The figure shows the underpinning of the non-analogue method by the analogue method. The salient differences between the analogue and non-analogue methods demonstrated in Figure 7.2 are:

1. each stage of the neutron history is accompanied by a weight, ω_i. The weight may be used in a variety of ways, one example of which is implicit capture. Implicit capture is used to build up a comprehensive picture of the capture distribution of neutrons in a relatively small number of histories. In implicit capture, each neutron-nucleus interaction has 2 outcomes; scattering and capture. The scattered neutron has its weight reduced by the probability for scattering, such that the new weight, $\omega_{s,i}$, is related to the old, ω_{i-1}, by the formula $\omega_{s,i} = \omega_{i-1} * \sigma_s/\sigma_t$. The capture event has the weight $\omega_{c,i} = \omega_{i-1} * \sigma_c/\sigma_t$. Probability is conserved, since $\omega_{s,i} + \omega_{c,i} = \omega_{i-1} * (\sigma_s + \sigma_c)/\sigma_t = \omega_{i-1}$.

2. Each neutron interaction is accompanied, whether the interaction calls for it or not, by a weighted γ-ray emission. The actual emission is independent of the interaction that takes place, and has a weight $\omega_{\gamma,i} = \omega_{i-1} * \sigma_\gamma/\sigma_t$, where ω_{i-1} is the weight of the incoming neutron, and σ_γ/σ_t is the probability that γ-rays will be emitted. Once again, this enables γ-ray distributions to be built up rapidly.

3. The transition between regions 1 and 2 involves splitting. That is to say that where a single neutron of weight ω_{i-1} was propagated just inside Region 1, two neutrons of equal weight $\omega_{1,i} = \omega_{2,i} = \omega_{i-1}/2$ are propagated through Region 2. These neutrons are initially the same in all respects, but once the splitting has taken place, the two histories develop independently of one another.

4. The transition between regions 2 and 4 involves the termination of one of the neutron paths. This termination might take place because the weight of the neutron was below some cut-off, or because a non-analogue method known as Russian roulette was being employed (in Russian roulette, a fraction f of all the neutrons are terminated at random, and those that remain have their weight increased by a factor $1/f$), or because the region is a region of no importance. All these methods are used in order to avoid allocating excessive computer time to low priority regions of the neutron phase space.

5. Finally, the interaction in Region 3 results in a neutron whose weight is now so low as to fall below some cut-off. The neutron path is terminated without further ado. Note that in non-analogue simulations where implicit capture is used, elimination by weight cut-off or some other non-physical termination is the only mechanism by which neutron histories finally end.

Non-analogue methods are best suited to the simulation of neutron rich situations, where individual events are not expected to be observed. Analogue simulations are most suited to situation in which each neutron event has a reasonable chance of contributing to an observation. Analogue methods are suitable for use with the SNOMAN program.

7.4 Choice of Neutron Transport Code

SNOMAN is an analogue program. It is also intended for use by a large collaboration, and any interested party must be capable of verifying that SNOMAN works as it is intended to. SNOMAN is intended for simulation and/or analysis of every significant event within the SNO detector. These general requirements lead to specific demands that the neutron transport code must meet (a similar set were first given by Lay [63, Chapter 4] in another circumstance; they still apply):

1. the neutron transport code must be well documented, both in its original form, and in its implementation in SNOMAN;

2. the neutron code must be capable of simulating all the neutron physics that may occur in the SNO detector (see Chapter 6);

3. the neutron code must be correct on an event by event basis, not merely on average;

4. the neutron code must be an analogue code to be used in SNOMAN;

5. the neutron code must have been widely tested and accepted.

This last requirement arises because there is no possibility that so large a subject as neutron transport can be fully tested, i.e. real experiments compared with simulations, by the authors of SNOMAN. Therefore, a neutron transport code can only be selected if it has already undergone extensive testing. This does not mean that the implementation of the neutron transport code in SNOMAN will not be tested against calibration sources that emit neutrons, but rather that these tests will only involve neutron capture distributions.

7.4.1 Introduction of MCNP

Of all the neutron transport codes available, one stands out as the most useful to SNOMAN. It is MCNP (Monte Carlo N Particle) [88], a well known transport code developed at Los Alamos National Laboratory, which describes itself as follows;

"MCNP is a general-purpose Monte Carlo N-Particle (MCNP) code that can be used for neutron, photon, electron, or coupled neutron/photon/electron transport ... Pointwise cross-section data are used. For Neutrons, all reactions given in a particular cross section evaluation (such as ENDF/B-VI) are accounted for. Thermal neutrons are described by both the free gas and S(α,β) models."

MCNP will not be used for anything other than neutron transport. MCNP is not only unsuited to $e^{\pm}$ and γ-ray transport in SNOMAN due to its non-analogue nature, but it has also been superseded by the EGS4 (Electron Gamma Shower) code system [63, Chapter 4], [65].

MCNP is particularly attractive because of the widespread verification and usage it has received at many research establishments around the world (particularly those involved with weapons and reactor design), and because of its extremely sophisticated handling of thermal neutron transport generally and the molecular effects in H_2O and D_2O in particular, without which no accurate simulation of neutron transport in the SNO detector could be carried out. Appendix E describes how MCNP handles neutron transport. It also contains information relating to the choice of data tables for the use of MCNP with SNOMAN, and the sampling processes used by MCNP.

MCNP is primarily intended as a non-analogue Monte Carlo which is capable of being run in an analogue mode. To achieve this, MCNP has a set of physics-related routines that form the analogue core of its simulated transport method. As a result MCNP is capable of simulating a history similar to that detailed in Figure 7.1 and the associated discussion in all but one respect. It does not correlate the γ-ray emission of any nucleus involved in the simulated neutron history with the interaction of the neutron with that nucleus. This makes no sense in an analogue code, but is one of the freedoms allowed to a non-analogue code. MCNP does however correctly indicate which γ-emitting interaction should follow inelastic scattering, and when (n,γ) capture occurs. This information can be used by additional routines in SNOMAN to simulate the emission of the appropriate γ-rays. Brice [122] has prepared routines that simulate the γ-ray emission after (n,γ) capture upon the isotopes ^{1}H, ^{2}H, ^{35}Cl, and the 5 stable isotopes of nickel. γ-rays from inelastic scattering are not yet simulated in SNOMAN. This is not a significant problem (see Chapter 6).

7.5 The Addition of MCNP to SNOMAN

The addition of MCNP's neutron transport capabilities to SNOMAN presented a significant challenge for the author of this thesis. This is because the two programs have a number of very significant differences, despite the fact that they are both written in the same computer language (FORTRAN77). The major differences between the two programs are;

1. that the two programs operate different memory models; and,

2. that MCNP and SNOMAN use different code to calculate cross sections and select interactions; and,

3. that MCNP contains a large quantity of code that is not required in the SNOMAN neutron transport routines.

These differences meant that almost every line of code used in MCNP had to be altered for use in SNOMAN, and that large parts of the MCNP code were rewritten from scratch. A brief description of the differences follows.

7.5.1 Different Memory Models

SNOMAN and MCNP both contain mechanisms whereby they can overcome FORTRAN77s most limiting shortcoming - FORTRAN77 does not contain any mechanism for dynamic allocation of memory. Most modern computer languages have built into them the ability to respond to a request for memory at any point in the program. This capability allows a program to respond to memory demands that are unknown when the program is compiled. Without this capability neither SNOMAN nor MCNP could function without repeated compilation, which is costly in terms of time and disk space for both of these programs. This is because both programs load in data from files which are selected at run time by the user.

MCNP overcomes the lack of dynamic memory allocation in FORTRAN77 by including an extremely large array in the program code, which is then compiled. The array is used as a storage space for the whole of the MCNP program, and consequently MCNP maintains a very large number of pointers that inform it where particular pieces of information can be found in the array. Should the array prove to be too small, its size can only be changed by recompiling the MCNP program.

SNOMAN makes use of the ZEBRA [144] program to manage dynamic memory allocation and the associated information pointers for it. ZEBRA was chosen for the task because;

1. its memory allocation and referencing procedures are relatively simple, allowing ZEBRA non-experts to use them once it was installed in SNOMAN; and,
2. it is maintained by CERN; and,
3. it is available for several different computer hardware platforms; and,
4. it provides platform independent binary file formats for input and output; and,
5. it provides a limited fault reporting and recovery procedure.

The selection of ZEBRA for use in SNOMAN occurred some time before the neutron transport code was added, and forms a core part of the code. Unfortunately, SNOMAN's use of ZEBRA to allocate and access memory during program execution make it very different from MCNP.

The differences in memory allocation between SNOMAN and MCNP mean that every piece of information that must be obtained from an MCNP data table by SNOMAN is obtained from it using different FORTRAN77 code than is used in the MCNP program. The result is that every line of MCNP that was used in SNOMAN that accessed a nuclear data table had to be modified. In addition, SNOMAN's use of ZEBRA to read in data meant that all the MCNP data files had to be converted to a format compatible with ZEBRA.

7.5.2 Different Calculation of Cross Sections and Other Matters

The SNOMAN neutron transport code obtains information about the current medium through which a neutron is being propagated in a way that is very different from MCNP. In addition, as was explained in the previous section, SNOMAN accesses nuclear data tables in a different way. Therefore it was decided to rewrite (rather than translate) the routines used in MCNP for the calculation of interaction cross sections for the SNOMAN program. This was felt to be quicker than making extensive modifications to the routines already provided in MCNP. It was also felt that the nature of the task, that of calculating cross sections by linear interpolation between tabulated points on a graph of $\sigma(E)$, was sufficiently simple that it could be reproduced in SNOMAN without error. Code was also written to select an interaction based upon the cross sections calculated by SNOMAN. This code was closely modelled on the equivalent code in MCNP.

The routines in MCNP that change between the laboratory, target-at-rest, and centre-of-momentum frames, and that control the resolution of an interaction were rewritten for SNOMAN. The routines in MCNP that select E_{out} and $\theta_{\text{scattering}}$ from data provided in the MCNP nuclear data tables were translated for use in SNOMAN.

7.5.3 Different Program Structures and Capabilities

MCNP contains code in its neutron physics routines specific to its non-analogue nature that has no place in the SNOMAN program. This code is usually concerned with either the tallying process whereby the program records neutron fluxes or energy depositions, or the elimination of particles through non-analogue games, or both. This code must be recognised and removed from MCNP physics-related routines before they can be used in the SNOMAN program. In addition, MCNP and SNOMAN have different error reporting and error recovery mechanisms. Every piece of code in the MCNP physics routines that reports and error must be understood, and either discarded or replaced by appropriate code in SNOMAN.

MCNP is an extremely large program. The majority or the code contained within it is related to interpreting the problem geometry specified by the user to the program, to the non-analogue games that MCNP can be used to calculate, and to the tallying process and related statistics. These portions of MCNP are not used in SNOMAN because it provides its own geometry, because it is not a non-analogue code, and because it does not record tallies or do any statistical bookkeeping.

7.5.4 Summary of Status of MCNP in SNOMAN

The large number of changes made to sections of MCNP before they were used in SNOMAN meant that MCNP had to be understood in enough detail to understand exactly how it transports individual neutrons, and to distinguish necessary and unnecessary pieces of code. To give an idea of the magnitude of this task, it suffices to say that MCNP has been under development since 1965, and contains ~ 40000 lines of FORTRAN77 code, most of which has not proved useful in SNOMAN.

The neutron code written for SNOMAN by the author of this thesis represents 8415 lines of code and comments, about half of which is FORTRAN77 code. Each SNOMAN neutron transport routine had to be either written from scratch, or based upon an equivalent routine in MCNP, or transposed from MCNP, or translated from code contained within MCNP. The great majority of code from MCNP had to be translated rather than simply transposed.

The vast number of changes made raised the possibility that SNOMAN no longer reproduces the results of MCNP. During the process of adapting MCNP for use with SNOMAN, a comprehensive set of verification programs were prepared to test SNOMAN against MCNP. The comparison was sufficiently complex that it was initially used to provide clues as to the whereabouts of 'bugs' in the SNOMAN n-transport code. When the verification routines were no longer capable of finding differences between SNOMAN and MCNP, they were greatly extended, and new verification techniques were introduced. All the n-transport verification techniques are the subject of the next chapter, Chapter 8, where it is shown that SNOMAN does reproduce the results of MCNP. The parallel development of the SNOMAN n-transport code and the verification process and the subsequent extension of that process took approximately 12 months.

7.6 Conclusion

In this chapter, the gross capabilities of the SNOMAN program that is used to simulate the SNO detector have been discussed. The use of computer codes to obtain physical results, and the difference between the analogue and non-analogue methods of computational neutron transport have been examined.

The selection criteria that a code must satisfy in order to be used in SNOMAN to simulate neutron transport have been outlined. The choice of the MCNP program to simulate neutron transport in SNOMAN has been explained, and the difficulties encountered in adding the n-transport capability of MCNP to SNOMAN described. The use of MCNP in SNOMAN is felt to be worthwhile despite the difficulties encountered because the SNOMAN program, with the addition of the MCNP code, is capable of simulating all the important physics of neutron transport in the SNO detector. In the next chapter, the accuracy of the n-transport code will be examined.

Chapter 8

Verification of the Neutron Transport Code

8.1 Introduction

SNOMAN contains the the neutron transport code in MCNP, as described in Chapter 7. This chapter is intended to address two questions, namely:

1. does SNOMAN faithfully reproduce the physical results of MCNP?
2. How accurate a model of experimental physics is MCNP (and hence SNOMAN)?

The first question was raised in Chapter 7 in response to the large number of changes made to the MCNP code transferred into SNOMAN, but there is a larger issue to hand. The verification of the SNOMAN n-transport code that is presented in this chapter is part of a much larger effort to provide evidence that the SNOMAN code does in fact do what it is intended to do. The use of formal verification procedures as well as the comparison of Monte Carlo with calibration data to demonstrate the verity of results produced by a Monte Carlo code is in line with the increasingly important part that Monte Carlo codes play in the interpretation of experimental data. The formal verification of SNOMAN was undertaken following demands by the SNO collaboration, and follow on from similar demands that the neutron transport code be demonstrated to work. These demands were initially made because of the importance of the neutron transport simulation to the analysis of the SNO experiment.

There are two general types of verification that can take place; a direct comparison between Monte Carlo and physical results, and tests to determine the sensitivity of analyses that are completed with the help of a Monte Carlo to systematic errors in that Monte Carlo. To test the sensitivity of an analysis that uses SNOMAN to systematic errors a parameter within SNOMAN would be artificially altered and the analysis repeated. A comparison of the results of the two analyses can then take place. Analyses that use SNOMAN are being tested in this way, but no such test will be presented here. In this chapter, the SNOMAN n-transport code is compared directly or indirectly to a number of physical results.

8.2 Purpose

In this chapter, the verification of the neutron transport code will be described in detail. This verification will proceed in four stages:

1. Discussion of experimental verifications of MCNP.
2. Proof that the neutron transport code in SNOMAN meets its design criteria (to reproduce n-transport results from MCNP).
3. Values from SNOMAN will be obtained for a representative set of physical quantities.
4. A comparison of the SNOMAN code with the diffusion equation.

Finally, an attempt will be made to estimate the theoretical error associated with results produced using the neutron transport code.

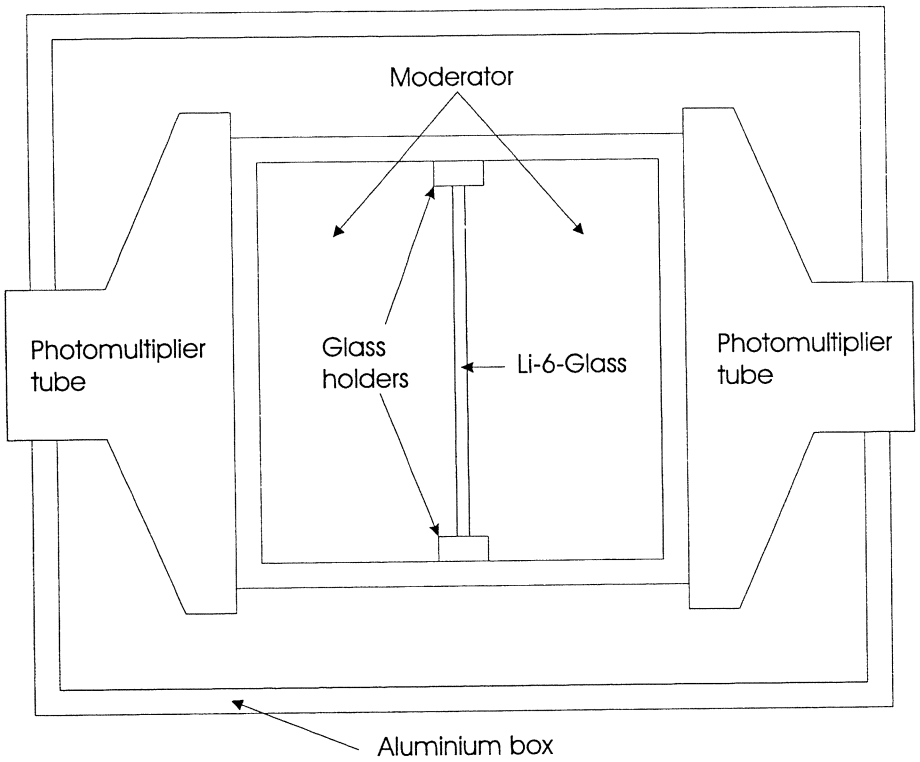

Figure 8.1: The neutron detector of Wang *et al.* . The beam from the neutron source travels perpendicular to the plane of the page and downward.

8.3 Experimental Verification of MCNP

First, it should be noted that MCNP is supplied with 20 test input and output data sets that, when successfully completed, assure the user of the code that he or she is in possession of the correct version of MCNP and its principal data tables, and that no errors are present. These tests have been completed on that version of MCNP used to prepare and to test SNOMAN. All users of MCNP have access to this benchmark code.

Despite the widespread use of MCNP, very little material is available in the literature that makes direct comparisons between the results of MCNP and experiment. What there is does not always pertain to the aspects of MCNP that will be used by the SNOMAN program. For example, a benchmark of the photon transport capabilities of MCNP has been carried out [105], but in SNOMAN, EGS4 [65] has been preferred over MCNP for photon transport. The dosimetry capabilities of MCNP have also been tested [106], but once again these capabilities will not be used in SNOMAN.

An experiment to test MCNP in a regime similar to that which will be found in the SNO detector has been done by Wang *et al.* [104]. The experiment determined the efficiency of a ^{6}Li-glass moderating neutron detector with both mineral oil and Lucite acting as the moderator. The experimental setup of the detector is shown in the schematic diagram in Figure 8.1. The detector makes use of the thermal capture of neutrons on ^{6}Li;

$$n + {}^6\mathrm{Li} \rightarrow t + \alpha + 4.76\mathrm{MeV} \tag{8.1}$$

which occurs within the glass scintillator. Neutrons were emitted from a fissionable ^{252}Cf source, releasing an average of 2.75 neutrons per fission. This choice of source is fortuitous, since the ^{252}Cf source will be used within SNO itself. Wang *et al.* also used a Van de Graaff accelerator to produce 1.2MeV neutrons from the t(p,n) reaction, but they conclude that the data for the 1.2MeV neutrons is unreliable, due to the instability of the proton beam in the Van de Graaff accelerator. Henceforth, this discussion will concentrate upon the ^{252}Cf source.

Wang *et al.* run their experiment with and without the ^{252}Cf source in order to subtract backgrounds and calculate the experimental ratio of the detector counting rates with the two moderators, $R_E = E_{\mathrm{Lucite}}/E_{\mathrm{Oil}}$. They repeat these calculations using the MCNP program which results in a value for the

Moderator	Experimental Rate	Calculated Efficiency
Lucite	352820 ± 1140	$0.0798 \pm 0.3\%$
Mineral Oil	450870 ± 1120	$0.1017 \pm 0.3\%$

Table 8.1: The results of Wang *et al.* . See text for further explanation.

same ratio, R_{MCNP}. Their raw results are given in Table 8.1, in which the unnormalised experimental rates for neutron capture in the glass scintillator is shown beside the MCNP estimates of the glass scintillator n-capture efficiency.

Wang *et al.* define the relative error in the MCNP result as;

$$\text{Relative Error} = \frac{R_E - R_{\mathrm{MCNP}}}{R_{\mathrm{MCNP}}} , \tag{8.2}$$

and they conclude that the relative error in the ratio of the efficiencies calculated by MCNP is $(0.3 \pm 0.6)\%$. A relative difference of the efficiencies of mineral oil and Lucite can also be defined;

$$\text{Relative Difference} = \frac{E_{\mathrm{Oil}} - E_{\mathrm{Lucite}}}{E_{\mathrm{Lucite}}} . \tag{8.3}$$

The experimental relative difference in efficiencies is 0.278 ± 0.005, whilst MCNP's prediction of this value is 0.274 ± 0.005. The relative error on the relative difference is $1.5 \pm 3\%$. Since the relative difference in the absolute efficiencies can be determined at the 3% level, it can be inferred that the absolute efficiencies are themselves accurate at this level.

Wang *et al.* [104] have experimentally verified MCNP in just the regime we require; the neutron transport in their experiment is dominated by moderation events involving carbon and hydrogen. They conclude from their results that MCNP is most accurate when a ratio of efficiencies is calculated (the error is significantly less than 1%), but that when it is used to determine an absolute efficiency, it is still adequate (at the 3% level). Wang *et al.* used MCNP version 3 - the version used in SNOMAN, version 4a, was not available to them. This is not thought to compromise the validity of their results in the context of SNOMAN, since the transport physics contained within the two versions is the same.

8.4 Testing the Neutron Transport Code With Respect to its Design Criteria

8.4.1 The Design Criteria

The principal design criteria for the neutron transport code is that it match exactly the results produced by its parent code MCNP. Once this has been established, all the benefits of the thorough testing and widespread use of MCNP could be said to apply to the neutron transport in SNOMAN. That is one of the greatest benefits to be had from the use in SNOMAN of the neutron transport code used in MCNP.

8.4.2 Introduction to Testing

The computational analogue of a neutron history proceeds in discrete stages, as discussed in Sections 7.3.1 and E.1. As a result at each stage of the neutron's history, independent of any other, the immediate future of the neutron is decided on the basis of a number of physical parameters. These are:

1. The mean free path of the neutron in its current medium.
2. The relative partial cross sections for all possible reactions.
3. The energy-angle spectrum of each possible reaction.

All these quantities are assumed to be taken in the laboratory (LAB) frame. Provided that MCNP and SNOMAN can be demonstrated to produce similar distributions for each of these quantities then MCNP and SNOMAN can be regarded as predicting the same physical results. There is one caveat; it is that SNOMAN and MCNP must both have the property that each stage in a neutron's history is independent of those that have preceded it, at least with regard to the quantities listed above. This point will be addressed later.

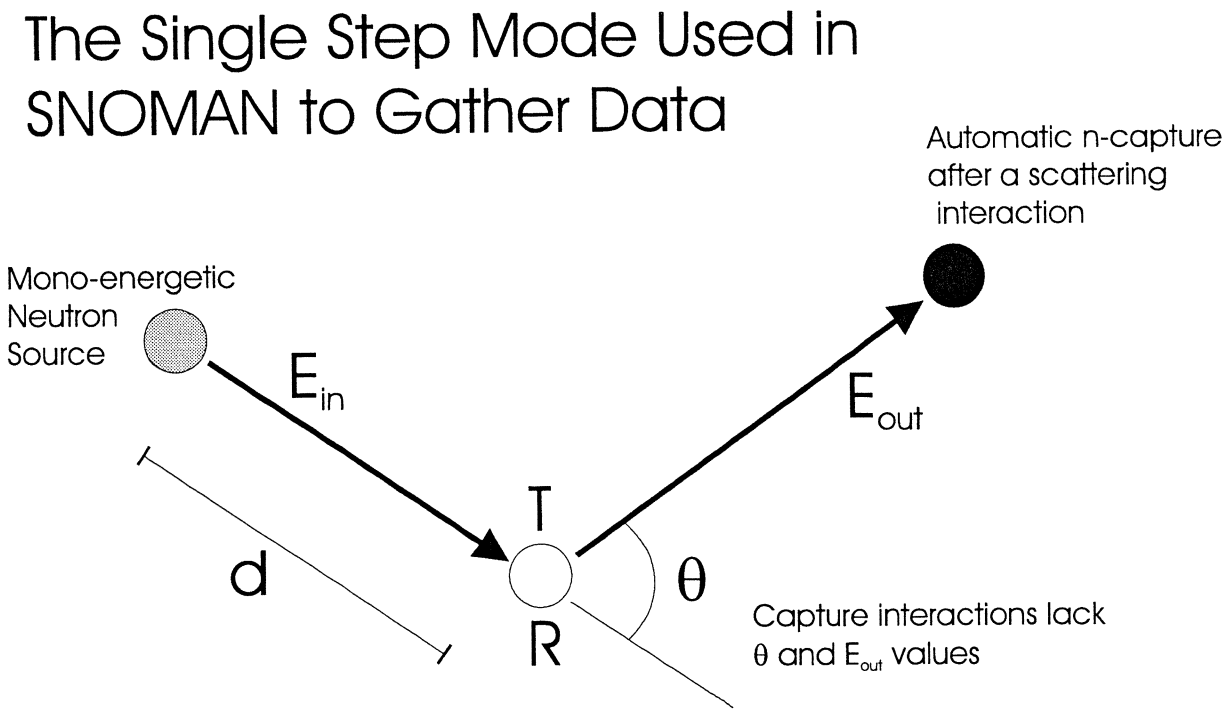

Figure 8.2: SNOMAN was operated in its single interaction mode. Similar data was extracted from MCNP.

MCNP was modified to allow details of individual stages of the neutron's history to be extracted from the program. These modifications did not change any aspect of MCNP's neutron transport properties, rather, they added a previously non-existent output capability to the program. In addition, a new random number generator was added to MCNP to facilitate the rigorous testing that was to take place. This is the random number generator of Marsaglia, Zaman, and Tsang as described by James [102], and used in SNOMAN. The most attractive properties of this generator are the guaranteed independence of the random number sequences resulting from different initial seeds, and the long period of the sequences themselves.

The quantities that were compared were not those listed above. For reasons of simplicity, the following outputs were extracted from MCNP and SNOMAN for the initial stage of each history (the ith such history):

1. the step length, d_i,
2. the identity of the target nucleus, T_i,
3. the interaction type, R_i,
4. the emitted neutron's energy, E_i, and
5. the cosine of the angle between the initial neutron and the emitted neutron, $\cos\theta_i$,

and it is the distributions of these five quantities that were compared. This list differs from that given earlier because the energy and angle distributions from MCNP and SNOMAN are compared independently, and the correlated energy-angle distributions from MCNP and SNOMAN are not compared at all. To ensure that the correct energy angle correlations were being reproduced, a small number of distributions such as that seen later in this chapter were obtained and examined for gross systematic errors in the energy-angle correlations. These examinations were not quantitative. Figure 8.2 gives a pictorial representation of the results that were gathered from the MCNP and SNOMAN programs. Otherwise the list given above does allow a direct comparison of the mean free paths and the partial interaction cross sections from MCNP and SNOMAN.

Neutrons were generated isotropically and at a fixed energy in a practically infinite medium. The six media used were pure hydrogen, deuterium, carbon, and oxygen, SNO quality heavy water, and acrylic (these last two materials are a composite of some of the others). The energies at which this test was

carried out were 10MeV, 1MeV, 100keV, 10keV, 1keV, 100eV, 10eV, 1eV, 10^{-1}eV, 10^{-2}eV, 10^{-3}eV, and 10^{-4}eV. On average 10000 neutrons were started as part of each test. Each test was repeated five times. The total number of possible comparisons between data sets from MCNP and data sets from SNOMAN is 1800, but in actual fact due to the simplicity of some of these tests, only 1395 contribute non-trivial results.

8.4.3 The Statistical Comparisons

For each quantity, at each energy, and in each medium, a distribution from MCNP and a corresponding distribution from SNOMAN was prepared. The angle, energy, and step length distributions output from the two programs were then compared using the well known Kolmogorov-Smirnov (KS) test [103, Ch.14]. The advantages accrued in using this test are:

1. That it is a bin-free test mechanism.

2. That the results of the test are not affected by a transformation of the axis upon which the data lie.

This test was adopted because the principal alternative, the χ^2 test for the comparison of two binned distributions, is sensitive to the binning to which the distributions needed to be subjected before the test could be carried out. It was decided to avoid using a statistical test that required binning except where the data was itself drawn from a binned distribution.

The Kolmogorov-Smirnov test is applicable to continuous distributions that are a function of a single independent variable, and hence to the situation at hand. The test uses the maximum value of the absolute difference between the cumulative distribution functions of the data sets that are being compared as the measure of their "overall" difference. Unfortunately, the Kolmogorov-Smirnov test is applicable only to distributions where a cumulative distribution defined from;

$$S_n(x) = \begin{cases} 0 & x < x_1 \\ \frac{i}{n} & x_i \leq x < x_{i+1} \\ 1 & x > x_n \end{cases} , \tag{8.4}$$

exists, where the x_i are ordered in increasing magnitude, there being n observations in the sample. This explicitly excludes distributions where $x_i = x_j$, $i \neq j$, and therefore the KS test is not applicable to binned distributions. This is contrary to expectation if one considers a binned distribution as one possible limit of a continuous distribution.

MCNP (and hence SNOMAN) reproduces the behaviour of neutrons at thermal energies using an S(α,β) scattering formalism for select nuclei (see Appendix E). One consequence of this formalism is that for a fixed incident energy E_i, the output neutron's energy is selected from a small number (typically four or eight) of equi-probable final state energies ($E_{i,j}$). The part of the final state energy-angle spectrum that arises from the use of the S(α,β) formalism is known as "discrete", and it is equivalent to a binned distribution. The Kolmogorov-Smirnov test was applied only to the continuous part of the energy and angle spectra. The χ^2 test for the equivalence of two binned distributions was applied to the discrete part of these spectra. The distribution of reaction and target types falls naturally into discrete bins, and hence the χ^2 test was also used in these instances.

Approach to Gaussian Statistics in the χ^2 Tests

The χ^2 test for the equivalence of two distributions was applied to all the distributions that lent themselves to a binning procedure. This included the discrete parts of the energy and angle spectra at thermal energies, and the reaction and target data at all energies. SNOMAN and MCNP could have been operated to produce data for a fixed number of events, however this would have meant that the statistics applicable to the resultant bin content were those of a multinomial distribution, rather than those of a Gaussian distribution. SNOMAN and MCNP were instead operated in a regime were the total number of events in a data set was allowed to vary according to Poisson statistics. It is shown in Frodesen *et al.* [103, Section 4.4.3] that when binomial statistics apply to events within a data set, and the total number of events in that data set are allowed to vary according to Poisson statistics, then the underlying distribution of events in a bin is also Poisson. The proof is sufficiently central to the tests that have been conducted to be given for the multinomial case in Appendix F. In order to achieve nearly Gaussian statistics in each and every bin, bins of small content were summed so that no bin contained less that 30 events.

Identifying Bins in the Discrete Spectra

Before a χ^2 test can be applied to the discrete (artificial) part of the energy or angle spectra, it is necessary to bin the data. Because the spectra are discrete, only a small number of values should arise in the data. These values should be the same in SNOMAN and in MCNP. This is not the case. MCNP uses "FORTRAN DOUBLE PRECISION" precision throughout, whilst SNOMAN uses "FORTRAN REAL" precision in reading and writing values that form part of a neutron's history, such as a set of direction cosines, and "FORTRAN DOUBLE PRECISION" precision for all intermediate calculations of that history. This leads to differences in the values input and output by SNOMAN and MCNP. Differences in the output were most significant for the output value of $\cos\theta$, which is calculated using the direction cosines from before and after an interaction;

$$\cos\theta = u_x v_x + u_y v_y + u_z v_z \ . \tag{8.5}$$

Differences in the input arise when SNOMAN represents an initial energy of $1.0000000000 \times 10^{-8}$ as $E_{\text{SNOMAN}} = 0.999999999 \times 10^{-8}$, whilst MCNP represents it correctly. For energies where an S(α,β) table will not be used (> 4.46eV), this difference is of no importance. This is reflected in the results of the KS tests that are carried out for high energies. However, at low energies, the difference becomes significant because of artificial energy boundaries in the S(α,β) tables. For a complete explanation of the S(α,β) tables, the reader is referred to Appendix E. For now, it is sufficient to note that for incident energies in SNOMAN and MCNP that straddle the boundary, i.e. when;

$$E_{\text{SNOMAN}} < E_{\text{BOUNDARY}} \leq E_{\text{MCNP}} \ , \tag{8.6}$$

the SNOMAN program will select final state energies from the set $E_{i,1}, E_{i,2}, \ldots, E_{i,N}$, whilst the MCNP program will select from a different set $E_{i+1,1}, E_{i+1,2}, \ldots, E_{i+1,N}$. Hence the results of the two programs will no longer be drawn from the same set of values, and will be quantitatively different.

The input and output problems were overcome in a similar manner. A precision degrading filter was added to MCNP, filtering the data that was input into it to ensure that the precision of the input was lowered to that of SNOMAN. The lowered the numerical precision from 1 part in 10^{10} to 1 part in 10^5, both of which are adequate for the simulation of analogue neutron transport. This was done with FORTRAN code of the following form;

```
DOUBLE PRECISION V
REAL Q
Q = REAL(V)
V = DBLE(Q)
```

where V is the variable that is being input into MCNP, and Q is the filter variable. The numerical precision maintained in V ($\sim$ 10 digits) is about double the number of digits in Q ($\sim$ 5 digits). A similar filter was applied to MCNP's direction cosines before they were used to calculate and output $\cos\theta$, and to the output of the final state energy. As a result of these changes, MCNP was operated in a manner similar to that of SNOMAN, its inputs and outputs being degraded in precision with respect to its intermediate calculations.

After degrading the precision of MCNP to match that of SNOMAN, the output of the two programs could be directly compared. The data was binned in preparation for the χ^2 test such that $(B_{i+1,1} - B_{i,N})/B_{i,N} > 10^{-5}$, where $B_{i,j}$ is the jth data element in the ith bin, and $B_{i,j} \leq B_{i,j+1}$, and $B_{i,j} < B_{m,n}$, $m > i$. This prescription for the binning of data allows for the limited numerical precision of a computer; for example, the cosine of the angle between two sets of direction cosines such as those in Equation 8.5 may be different after the rotation of both sets of cosines, such that $\cos\theta \rightarrow \cos\theta' = \cos\theta + \delta$. This is purely a computational effect.

It should be noted that the modification of MCNP that has been detailed was undertaken in an effort to pinpoint the differences between MCNP and MCNP as implemented in SNOMAN. Any future tests comparing SNOMAN and MCNP could avoid many of the problems that have been described here by generating neutrons at energies that are not close to artificial energy boundaries in the tables that are used to simulate neutron physics, or preferably by generating neutrons not at a fixed energy (monoenergetic particles) but with a Gaussian energy distribution whose small width would avoid the unphysical problem of machine precision. Finally, note that the problems of numerical precision which were encountered when MCNP and SNOMAN were compared as described here do not produce physically significant differences in their outputs. This is because MCNP and SNOMAN agree in all respects at the level of 1 part in 10^5.

Test Results

The results of both the KS test and the χ^2 test are expressed in terms of a probability, p. Assuming the two distributions being tested are drawn from the same parent distribution, then p is the probability that two new distributions drawn from that parent distribution are as different or more different than the two samples that have been compared.

The range of acceptable values for this statistic varies with the context of the test, but in general, a value that is too large or too small is suspicious. Where the statistic is too small, it is likely that the two test distributions have not been randomly selected from the same parent distribution. Where it is too large, the agreement between the two distributions may be better than would be produced by chance alone. If 100 such tests were to be carried out on sample pairs that were drawn from the same parent distribution, it would not be unexpected if 1 of the tests resulted in a probability p such that $p < 0.01$, and if 1 resulted in $p > 0.99$, but it would be unexpected if one of the 100 tests resulted in a value of p such that $p \ll 0.01$, for example, $p = 1 \times 10^{-10}$. In fact, the values of the outcomes of the KS and χ^2 tests that compare MCNP to SNOMAN should be uniformly distributed between 0 and 1.

Relationship Between Energy and Angle in Elastic Scattering

The Kolmogorov-Smirnov test is unaffected by a transformation of axis, a fact that has an impact on the test procedure. For elastic scattering at energies where the thermal energy of the target nucleus can be neglected in comparison to the kinetic energy of the incident neutron, the scattering in the laboratory (LAB) frame is related to that in the centre-of-momentum (COM) frame using only COM variables and the neutron's LAB energy. The COM final state energy is related to the sampled COM angle and the incident COM energy by the kinematic formula;

$$E_{\text{out}} = E_{\text{in}} \frac{1 + A^2 + 2A\mu_{\text{COM}}}{(1 + A)^2} \tag{8.7}$$

where A is the mass of the collision nuclide in units of the neutron mass, and μ_{COM} is the cosine of the centre-of-mass scattering angle. It is clear that when E_{in} is a constant, the distribution of values of E_{out} in the COM frame and the LAB frame is related to that of μ_{COM} (COM or LAB) by simple transformations of axis.

The one-to-one correspondence between scattered energy and angle does not hold in the LAB frame when the incident neutron has an energy comparable to that of the target. It does not hold because two scatterings that are identical in the COM frame will be very different in the LAB frame after the motion of their respective target nuclei have been taken into account.

To recap; at high energy, the LAB scattered energy and angle are related by a simple transformation of axis. At low energies for collisions with light nuclei, this is no longer true, and energy and angle become effectively independent. Later, the distribution of the probabilities arising from nearly all the comparisons between MCNP and SNOMAN will be subject to a KS test. In order to simplify the selection of data in this test, data from the continuous angle comparisons was used, but data from the continuous energy comparisons was not included. This ensured that only one of a pair of correlated results from the continuous energy and angle comparisons were included in the test, at the expense of discarding a few low energy results that were not correlated with their corresponding angular results.

8.4.4 The Results of the Statistical Comparisons

After the comprehensive set of results enumerated in Section 8.4.2 had been collected from the MCNP and SNOMAN programs by the process described in Appendix G, there were:

1. 310 paired continuous angle distributions (CA_i, $1 < i \leq 310$),
2. 100 paired discrete angle distributions (DA_i, $1 < i \leq 100$),
3. 310 paired continuous energy distributions (CE_i, $1 < i \leq 310$),
4. 100 paired discrete energy distributions (DE_i, $1 < i \leq 100$),
5. 360 paired step length distributions (SL_i, $1 < i \leq 360$),
6. 95 paired reaction distributions (R_i, $1 < i \leq 95$), and
7. 120 paired target distributions (T_i, $1 < i \leq 120$).

where the phrase 'angle distribution' refers to the distribution of the cosine of the angle of scattering.

Each pair of the continuous angle, continuous energy, and step length distributions were subjected to the Kolmogorov-Smirnov test for the comparison of two continuous distributions. Each pair of the discrete angle, the discrete energy, the reaction, and the target distributions were subjected to a χ^2 test for the comparison of two binned distributions. The results of these tests are a probability p, which in each case are labelled as indicated in the parenthesis accompanying the list given above. The results of all the comparisons between MCNP and SNOMAN that involved distributions of the same variable will be known as a group. For example, the all the SL_i form one group, all the DE_i form another.

In the first instance, an anomalous value for a test result indicates that in at least one circumstance, SNOMAN and MCNP produce distributions that are likely not to have been drawn from the same parent distribution. This implies that SNOMAN and MCNP are not the same. An 'anomalous value' is a value that is unexpected given the number of tests performed, or one where $p \ll 1/n$, or $1 - p \ll 1/n$, where p is the poor result and n is the number of tests. A more subtle difference between the two codes might make all the SNOMAN distributions less similar to the MCNP distributions than chance would do alone; this would mean that a particular group of results (the CA_i, for example) were not uniformly distributed between 0 and 1, as they should be. A subtle effect such as this can be uncovered by using the Kolmogorov-Smirnov test again to check the null hypothesis that the results of a group of comparative tests (the CA_i) should be uniformly distributed between 0 and 1.

Historically, before the comprehensive test program described here was undertaken, a more limited version was carried out. The early limited test program was used to track down, identify, and fix coding errors in the SNOMAN program that caused it to differ from MCNP. The statistical tests described here proved to be a powerful method for uncovering differences between MCNP and SNOMAN, and the wide range of target materials and energy ranges over which the tests were performed proved useful in identifying the general location of the errors in SNOMAN. The test program described in this chapter was then drawn up and completed.

The relationship between the energy and angle of a neutron scattered at 10MeV from a water molecule, from both MCNP and SNOMAN, is shown in Figures 8.3 and 8.4. The separate energy and angle distributions which were actually used in the statistical comparisons are also shown as an example of the data sets that were compared (Figure 8.5). Notice that the data presented cannot be used to distinguish between the SNOMAN program and the MCNP program either visually or statistically.

The individual results of all the MCNP-SNOMAN comparisons will not be given. Rather, the cumulative distribution functions of the results from groups of Kolmogorov-Smirnov or χ^2 tests are displayed (the cumulative distribution function of the CA_i, for instance). The probabilities that are the results of any one group of comparisons should be uniformly distributed between 0 and 1. Consequently, the cumulative distribution function of the probabilities from any group should take the form $\mathrm{C.D.F}(x) \propto x$. This is true not only of each group of comparisons separately, but of an amalgamated distribution which is formed by combining all the results that are available except those of the continuous energy group (see Section 8.4.3).

The cumulative distributions from each group and for the amalgamated data are displayed in Figures 8.6 and 8.7, where it can be seen that they all take the form $\mathrm{C.D.F}(x) \propto x$, as expected. Each cumulative distribution function was compared with the null hypothesis, that $\mathrm{C.D.F}(x) \propto x$, using the KS test. The quantitative results are given in Table 8.2. They are in favour of the null hypothesis. In addition no one comparison resulted in a probability p where $p \ll 1/n$ or $1 - p \ll 1/n$. Note also that the comparative examination of a small number of correlated energy-angle distributions from MCNP and SNOMAN, such as that seen Figures 8.3 and 8.4, revealed no visible differences between the two programs.

1395 comparisons between distributions produced by MCNP and SNOMAN have been carried out. None of the values obtained as a result of these tests are anomalous. The distribution of the results from each group of comparisons has also been examined, to test the hypothesis that they should be uniform between 0 and 1. All 6 independent results are acceptable. A test of an amalgamated distribution was also performed under the same hypothesis. The result is also acceptable. In short, after extensive comparisons involving 2.64 million data elements, no difference between the output of MCNP and the output of SNOMAN has been observed. The range of incident neutron energies over which comparisons were carried out, the variety of transport media, and the number of variables tested imply that all the SNOMAN neutron transport code has been subject to statistical examination. Therefore the SNOMAN neutron code should reproduce the results of MCNP even at energies and with target nuclei which were not explicitly included in the tests presented here.

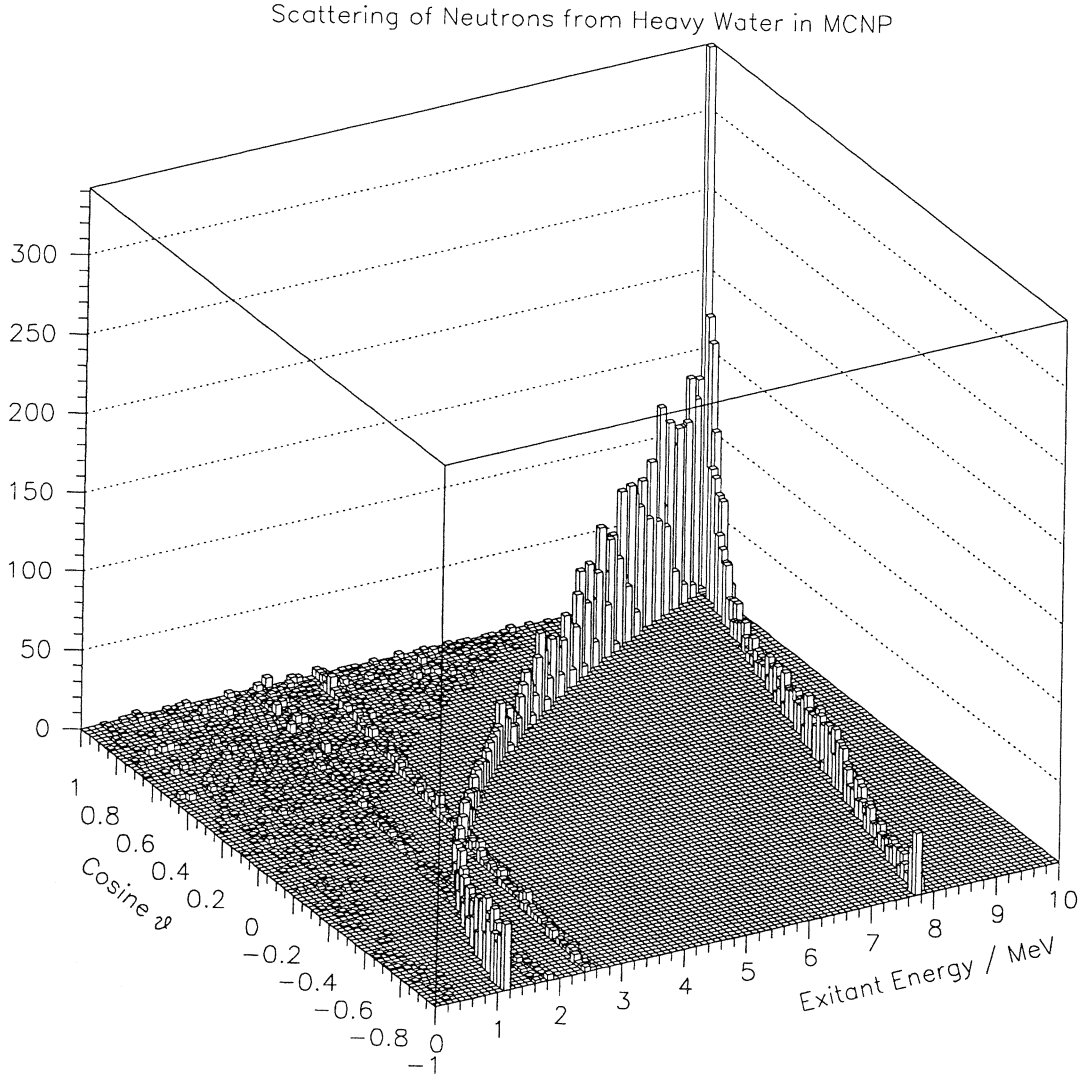

Figure 8.3: The energy-angle distribution from MCNP for 10MeV neutrons scattering from SNO quality heavy water.

8.4.5 Elimination of Systematic Objections to the Single-Step Data Collection

The statistical tests carried out so far have demonstrated that the first interaction (or 'step') in a neutron history simulated in the SNOMAN program is the same as the first interaction simulated in the MCNP program. Only the first interactions have been compared (see Section 8.4.2). The demonstration that SNOMAN meets its design criteria, that of reproducing the results of MCNP, can be criticised for not having proved that SNOMAN continues to produce the correct results after the first interaction. This section will show that SNOMAN does continue to reproduce the correct interaction distributions.

An isotropic point source of 1keV neutrons at the centre of the SNO detector was simulated using the SNOMAN program. The transport medium was SNO quality heavy water (D_2O contaminated by 0.08% H_2O by mass and a ^{17}O isotopic content of 0.055% by mass). Data was collected from each and every neutron interaction where the energy of the incident neutron was confined in the range (0.0249eV $\leq E_n <$ 0.0251eV), corresponding to neutrons at or about 1/40th of an eV. SNOMAN had therefore simulated the thermalisation of the neutrons before any data collection occurred. The data collected was the same as that of Section 8.4.2. This means that the target, reaction, step length, the neutron's scattered energy, and cosine of the scattering angle were recorded. The low energy used for data collection meant

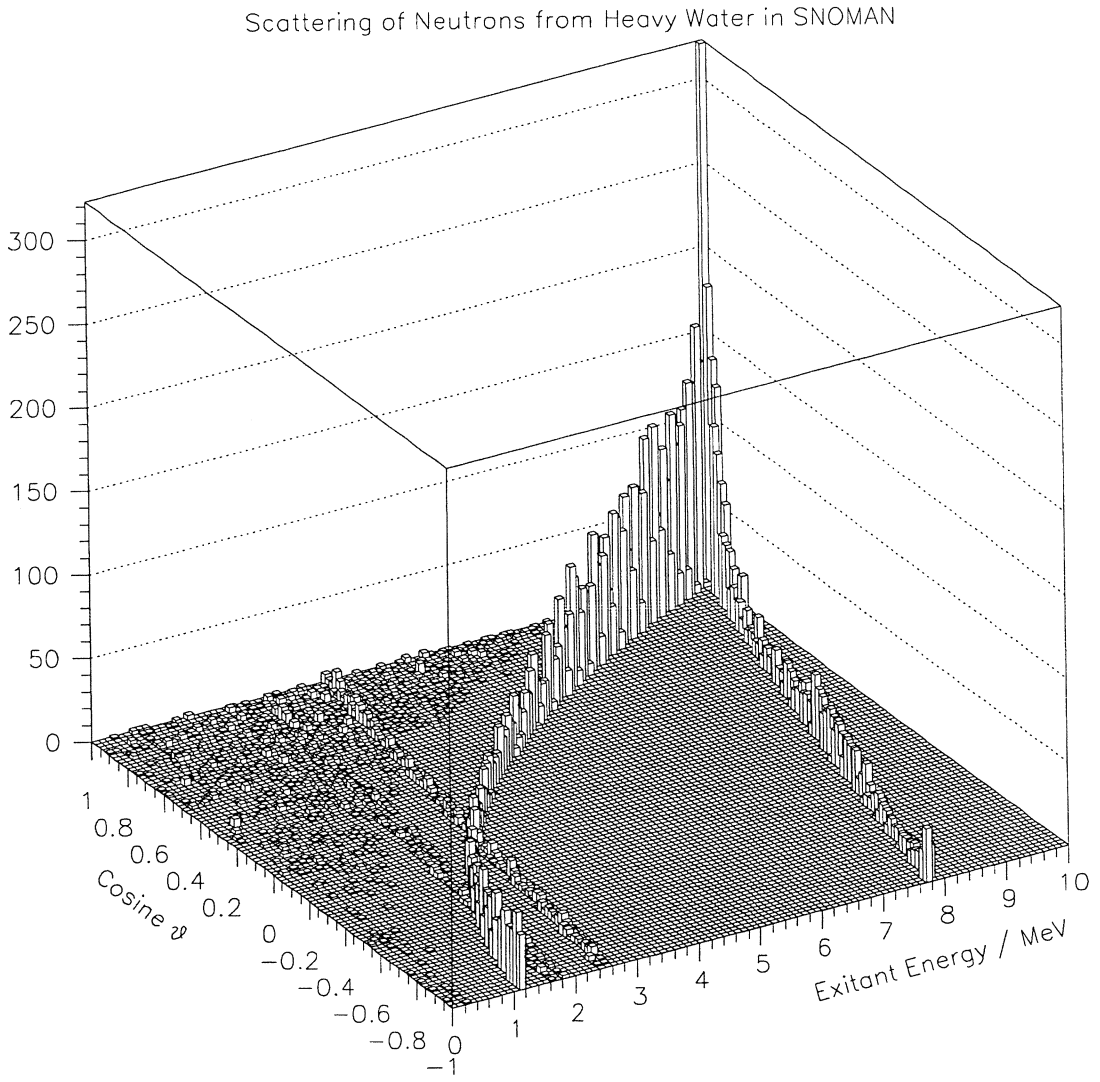

Figure 8.4: The energy-angle distribution from SNOMAN for 10MeV neutrons scattering from SNO quality heavy water.

that the SNOMAN program simulated the scattering from hydrogen and deuterium using S(α,β) tables (Section E.3.6) and the scattering from oxygen using the free-gas model (Section E.1.1) to determine the target's motion. 10000 neutrons were simulated, resulting in $\sim$ 22000 recorded interactions, or approximately $\sim$ 2.2 scatterings in each neutron history where the incident neutron energy lay in the narrow range (0.0249eV $\leq E_n <$ 0.0251eV).

The data collected from the 1keV point source was compared to data collected from the first interaction of neutrons emitted with energies uniformly distributed in the energy range (0.0249eV $\leq E_n <$ 0.0251eV). The simulated source was again positioned in the centre of the detector, and emitted neutrons isotropically into SNO quality heavy water. The data collected from the two simulations is shown in Figure 8.8. The results of the usual quantitative comparisons between the distributions are shown in Table 8.3. Note that the 'discrete' energy and angle distributions which arise as a result of the use of S(α,β) tables in neutron scattering reactions with hydrogen and deuterium below 4.46eV have acquired a width due to the range of input energies, and no longer fall naturally into bins. Therefore they are now compared using the Kolmogorov-Smirnov test rather than the χ^2 test.

Figure 8.8 and the data in Table 8.3 demonstrate that the simulation of neutron interactions in SNOMAN is not dependent on the number of previous reactions. In fact, the data presented here allows

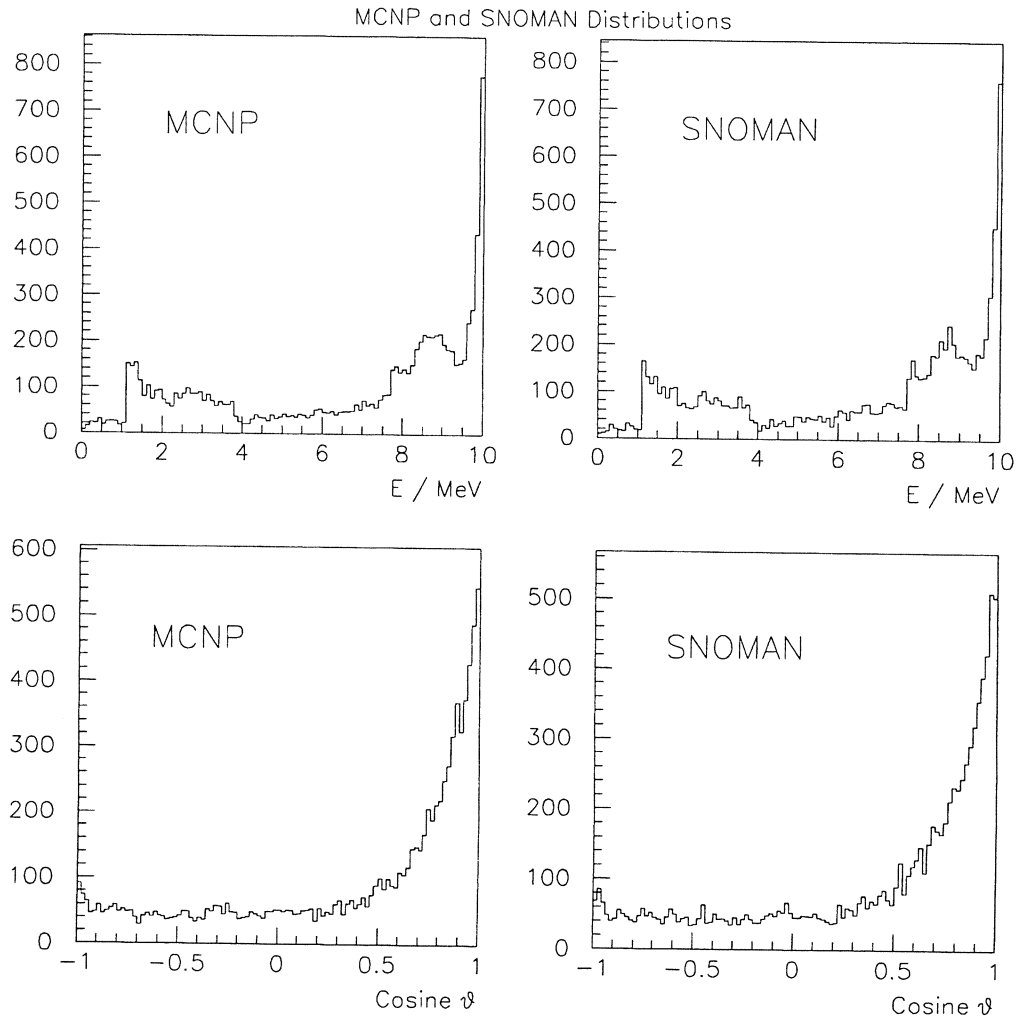

Figure 8.5: The separate energy and angle distributions from MCNP and SNOMAN for 10MeV neutrons scattering from SNO quality heavy water. The comparison of the SNOMAN and MCNP energy distributions gave $p = 6\%$, while the comparison of their $\cos\theta$ distributions gave $p = 36\%$.

a stronger conclusion to be drawn. The data shows that the final state energy, the cosine of the angle of scattering, the target, the reaction type, and the step length are independent of any and all previous interactions except in so far as those interactions result in the neutron being in a particular medium with a particular incident energy.

8.5 Representative Values from SNOMAN

In this section, it will be shown that SNOMAN does faithfully reproduce some of the more important cross sections. The demonstration will be restricted to thermal energies, which dominate the lifetime of neutrons in the SNO detector. This section is to some extent unnecessary, since the preceding section has shown that SNOMAN reproduces the results of MCNP, and the following section will show that the transport simulation in SNOMAN closely approximates to an analytical solution of the Boltzmann transport equation. However, it is felt that a simple demonstration of the accuracy of the SNOMAN code in reproducing well known results is desirable.

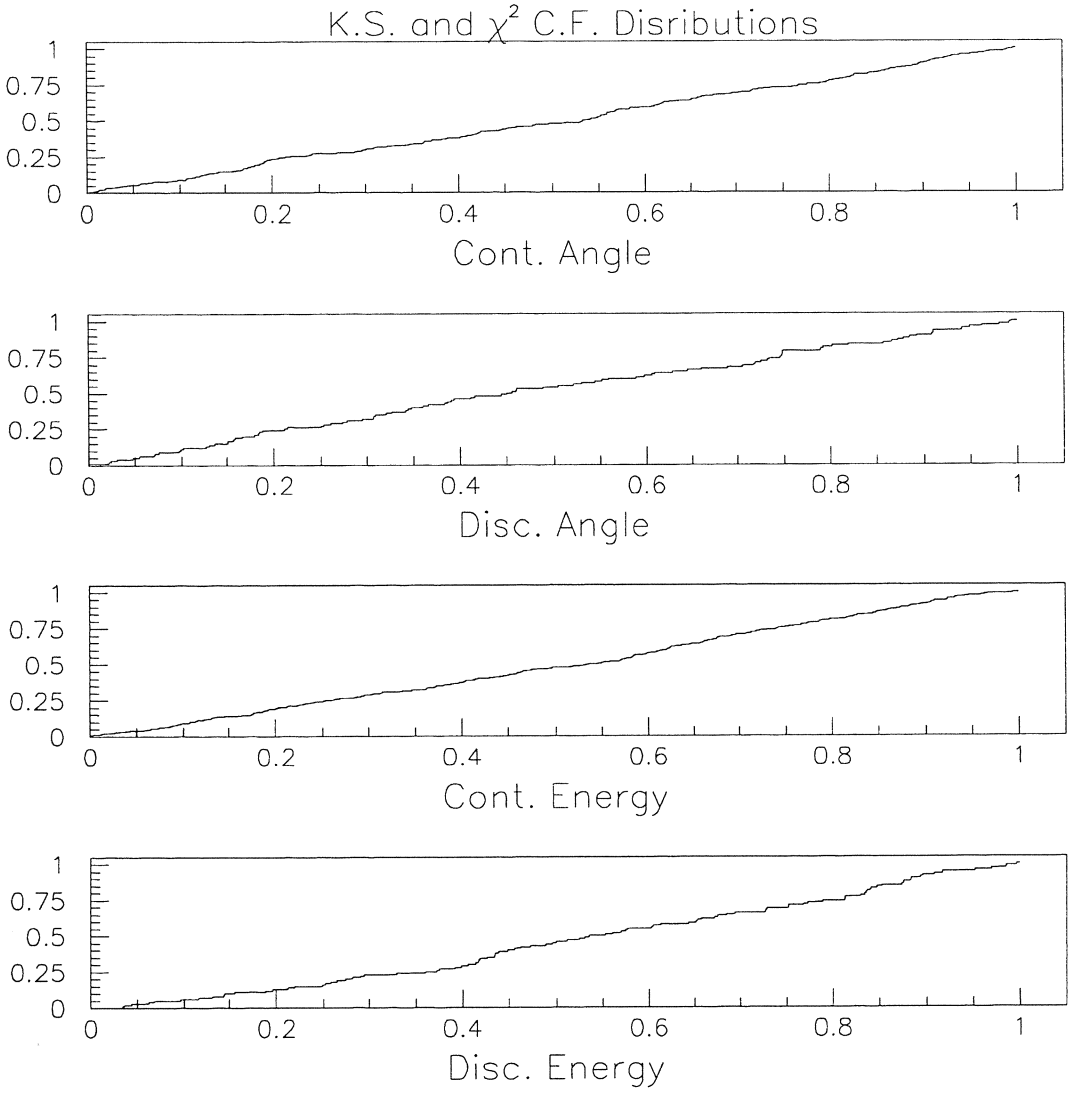

Figure 8.6: Kolmogorov-Smirnov and χ^2 test results. See the text for a detailed explanation.

Comparative Test Category	Result
Continuous Angle	0.60
Discrete Angle	0.70
Continuous Energy	0.40
Discrete Energy	0.09
Step Length	0.48
Reaction	0.62
Target	0.43
Amalgamated	0.78

Table 8.2: Results of the comparison between the distribution functions listed and the hypothesis that test results should be distributed uniformly between 0 and 1.

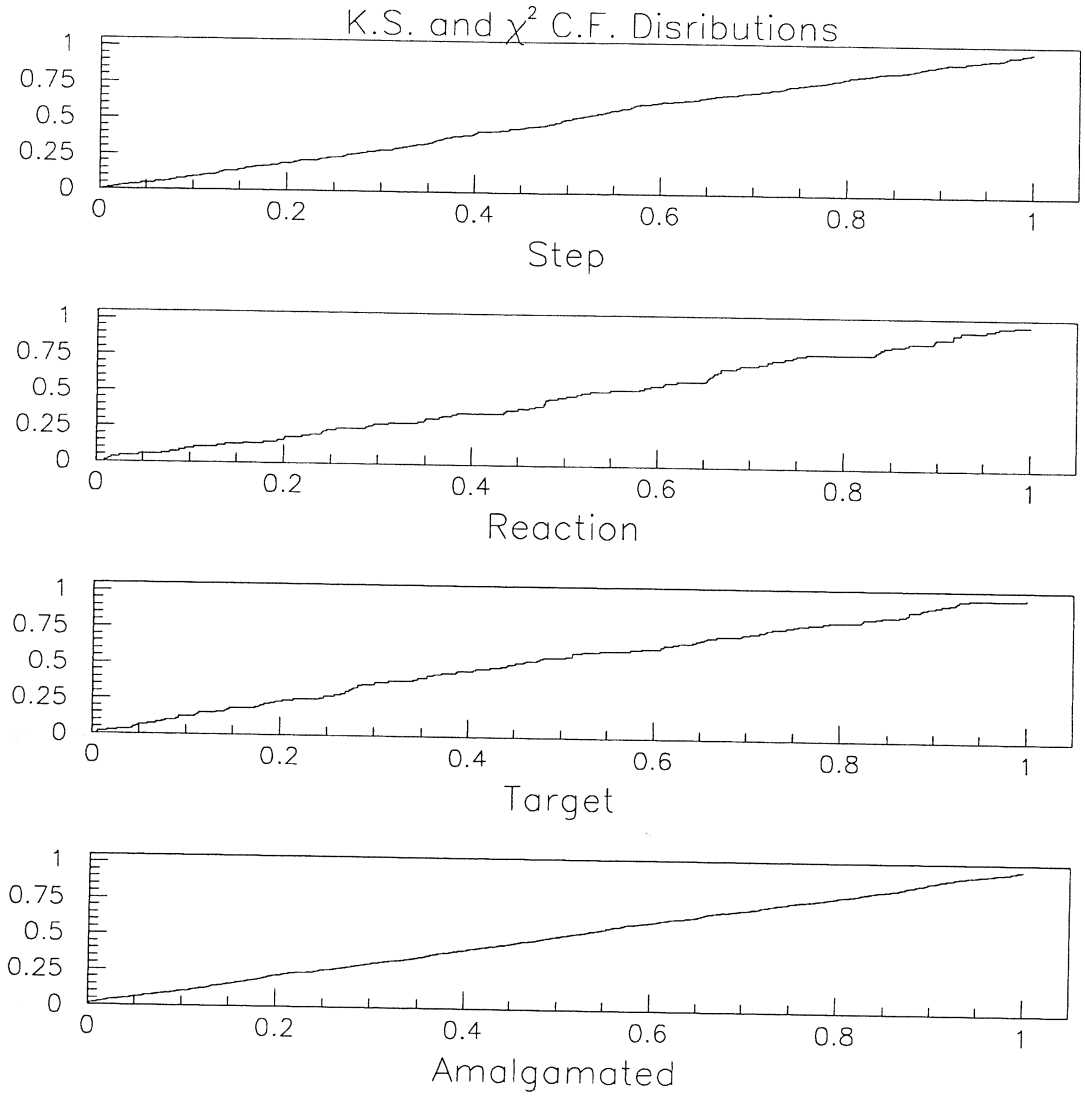

Figure 8.7: Kolmogorov-Smirnov and χ^2 test results. See the text for a detailed explanation.

Comparative Test Category	Result
Continuous Angle	0.35
Discrete Angle	0.05
Continuous Energy	0.11
Discrete Energy	0.92
Step Length	0.90
Target	0.86

Table 8.3: The results of the comparisons between the data obtained from neutron interactions in the energy range ($0.0249 \leq E_n < 0.0251$)eV after the thermalisation of neutrons from a 1keV source, and data obtained from the first interaction of neutrons from a source emitting neutrons uniformly in the same energy range. The comparison of reaction types (not shown) was trivial (only elastic scattering reactions occurred in the data sets).

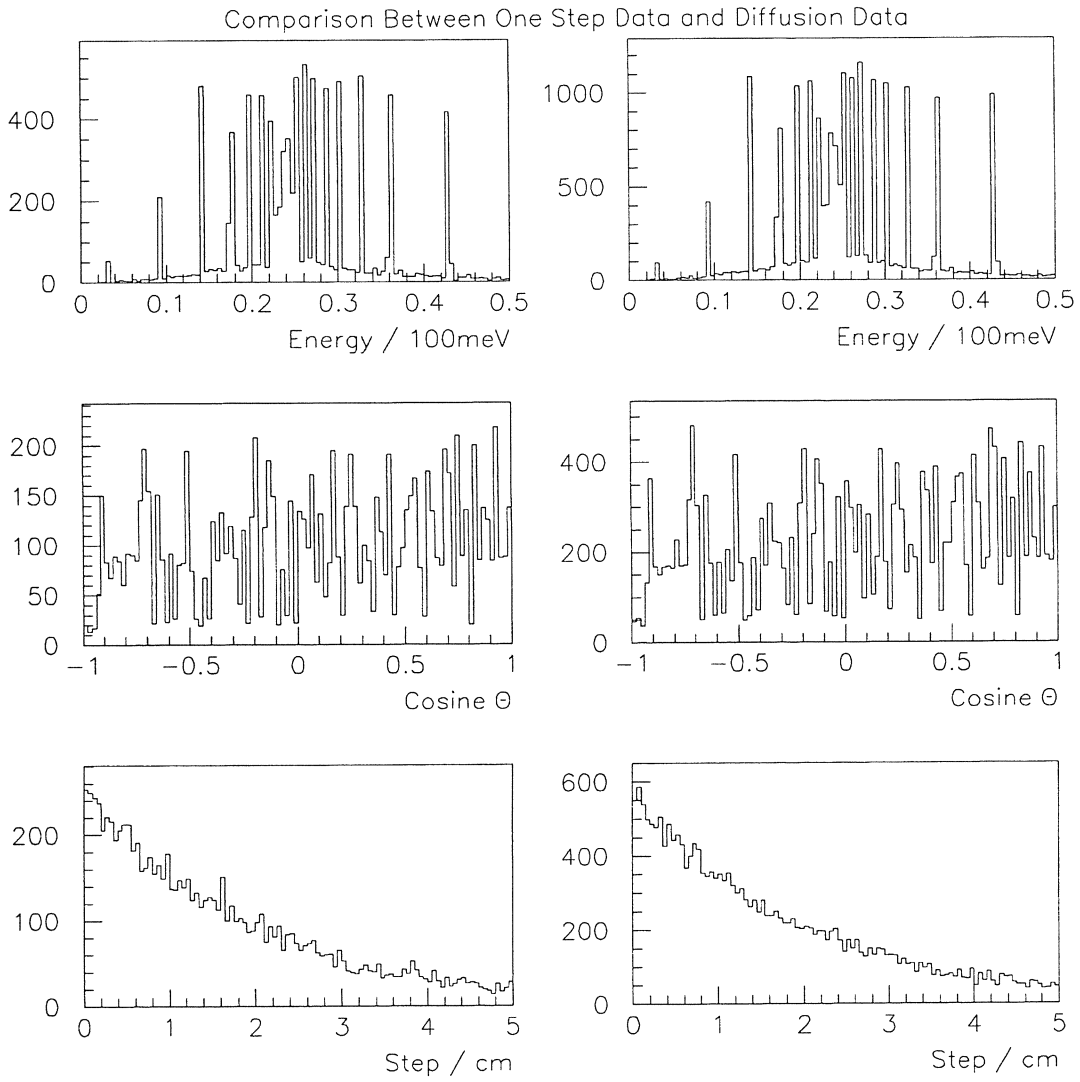

Figure 8.8: The graphs in the left column are those of the data obtained from the first interaction of neutrons with energies in the range $(0.0249 \leq E_n < 0.0251)$eV. The graphs in the right column are those with data obtained from neutrons with energies in the same range after their thermalisation from a 1keV source. The graphs are in excellent agreement (see Table 8.3).

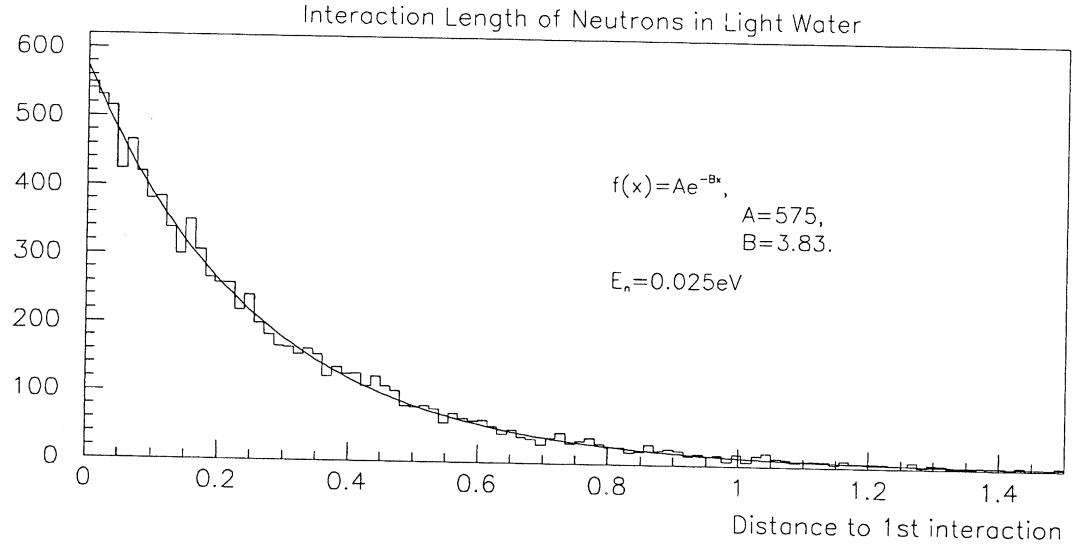

Figure 8.9: The neutron interaction length in H_2O. 0.033% ^{17}O was included in the simulation. The fitted interaction length is 0.261cm.

Medium	σ(SNOMAN) / b	σ(NNDC) / b
Light water	114.7 ± 2.6	112.2
Heavy water	15.10 ± 0.44	15.4
Rock salt	102.5 ± 3.6	104.4

Table 8.4: Comparison between cross sections inferred from SNOMAN and evaluated data from NNDC [129]. The NNDC data given here matches the evaluated experimental data to within 1%.

8.5.1 Interaction Lengths from the SNOMAN Program

The SNOMAN program was made to simulate a single scattering at an energy of 0.025eV. The step lengths and interactions were recorded. The number of events in each run was 10000. There were 3 runs, each with a different medium. The media used in the 3 runs were:

1. pure D_2O;
2. pure H_2O; and,
3. solid anhydrous $MgCl_2$.

A typical fit to the interaction length is shown in Figure 8.9. Table 8.4 compares the total cross section from SNOMAN with those of [123] and [129]. The total cross sections have been inferred from fitted interaction lengths using the relation $\lambda^{-1} = n\sigma_T$.

8.5.2 Partial Cross Sections from the SNOMAN Program

Partial cross sections for scattering and capture on particular elements can be calculated from the data collected in the SNOMAN runs of the previous section. The probability of a particular reaction occurring is related to the partial and total cross sections by the formula;

$$p_i = \frac{n_i \sigma_i}{\sum_j n_j \sigma_j}, \tag{8.8}$$

where $\sum_j n_j \sigma_j$ is the total cross section, and σ_i is the cross section for the ith interaction. The probability, p_i, that the ith interaction occurs is known from the data collected in the SNOMAN runs. It can be used to calculate the partial cross section for the ith interaction;

Interaction	σ(SNOMAN) / b	σ(NNDC) / b
Cl (total)	49.8 ± 1.9	50.5
Cl (n,γ)	33.1 ± 1.3	33.3
Mg (total)	3.0 ± 0.2	3.5
H (total)	55.4 ± 1.5	54.2
D (total)	5.7 ± 0.2	5.7
O (total)	3.7 ± 0.2	4.0

Table 8.5: Comparison between cross sections inferred from SNOMAN and evaluated data from NNDC [129].

$$\sigma_i = \frac{p_i}{n_i \lambda} , \tag{8.9}$$

where as before $\lambda^{-1} = \sum_j n_j \sigma_j$. Table 8.5 contains the partial cross sections that were inferred from the SNOMAN runs and also the evaluated cross sections from [129].

Capture cross sections for ^{1}H and ^{2}H have not been included in Table 8.5 because these captures occur so infrequently that the margin of statistical error on the inferred cross section trivially includes the figure from the evaluated data of [129]. The agreement between the cross sections inferred from SNOMAN and those obtained elsewhere is pleasing.

8.6 Comparison Between SNOMAN and the Diffusion Equation

Boltzmann's transport equation for the time development of the neutron flux is well known [128, Chapter 9]. For monoenergetic neutrons in the steady state the transport equation becomes;

$$\Omega \bullet \nabla_x f(\mathbf{x}, \Omega) + \Sigma(\mathbf{x}) f(\mathbf{x}, \Omega) = \int d\Omega' f(\mathbf{x}, \Omega') \Sigma_s(\mathbf{x}, \Omega' \rightarrow \Omega) + S(\mathbf{x}, \Omega) , \tag{8.10}$$

where $f(\mathbf{x}, \Omega)$ is the flux of neutrons at $\mathbf{x}$ into solid angle Ω, $\Sigma(\mathbf{x})$ is the macroscopic interaction cross section at x, $\Sigma_s(\Omega' \rightarrow \Omega)$ is the macroscopic partial cross section for scattering from solid angle Ω' into Ω at x, and $S(\mathbf{x}, \omega)$ is the neutron source strength. Consider an isotropic point source at the origin in a infinite uniform medium. Equation 8.10 reduces to;

$$\Omega \bullet \nabla_x f(\mathbf{x}, \Omega) + \Sigma f(\mathbf{x}, \Omega) = \int d\Omega' f(\mathbf{x}, \Omega') \frac{\Sigma_s}{4\pi} + \frac{S_0}{4\pi} \delta(\mathbf{x}) . \tag{8.11}$$

Σ is the macroscopic interaction cross section, Σ_s the macroscopic scattering cross section, and S_0 the point source strength. δ is the Dirac delta function. A solution to Equation 8.11 can be found [128, Chapter 8];

$$\Phi(r) = \frac{S_0 \beta}{4\pi D r} e^{-\kappa r} + \frac{S_0}{4\pi r^2} e^{-\Sigma' r} , \tag{8.12}$$

where;

$$\Sigma' = \frac{5\Sigma}{4} , \tag{8.13}$$

$$\beta = 1 - \frac{4\Sigma_a}{5\Sigma} , \tag{8.14}$$

$$D^{-1} = 3 \sum_i \Sigma_i (1 - \overline{\mu}_i) , \tag{8.15}$$

$$\kappa = \sqrt{\frac{\Sigma_a}{D}} . \tag{8.16}$$

The calculation of the diffusion constant D involves a sum over the isotopes present in the medium (here enumerated through the index i). $\overline{\mu}_i$ is the mean scattering cosine of the ith isotopic species. Due to

Medium	Σ	Σ_a	Σ/Σ_a
D_2O	0.4899	3.8963×10^{-5}	12574
SNO D_2O	0.4923	5.6440×10^{-5}	8723
Salted D_2O	0.4924	8.8758×10^{-4}	555
H_2O	3.4724	1.9797×10^{-2}	175

Table 8.6: The ratio Σ/Σ_a changes by several orders of magnitude with changes in the constitution of the transport medium, but Σ/Σ_a never falls below 10. $E = 4k_bT/\pi$ throughout.

the spherical symmetry inherent in the problem, the neutron flux $f(\mathbf{x}, \Omega)$ has been replaced by $\Phi(r)$, which is just the flux through unit surface area a radial distance r from the neutron source. The solution consists of an immediate or transient part $\propto e^{-\Sigma' r}/r^2$, due to neutrons arriving at r without having been scattered, and an asymptotic part $\propto e^{-\kappa r}/r$, representing the diffusion of thermal neutrons. The immediate solution is small except very close to the source, where it is dominant. The solution presented in Equation 8.12 is approximate, being valid only in the limit $\Sigma_a \ll \Sigma$, where Σ_a is the macroscopic absorption cross section, and Σ is the macroscopic total cross section as before. In fact, the exact and approximate distributions are quite close to one another, their difference, for $\Sigma/\Sigma_a > 10$, never exceeding more than about 1% [128, Chapter 8]. It is shown in Table 8.6 that none of the important media in SNO fall below $\Sigma/\Sigma_a > 10$.

Equation 8.12 contains just three parameters, which are the diffusion constant, the absorption cross section, and the total cross section. The selection of a single velocity to represent all neutrons and from which Σ and Σ_a are determined is achieved by demanding that the decay constant at that velocity be the same as that for the Maxwellian distribution. This is because the velocity distribution of the neutrons is Maxwellian when $\Sigma \gg \Sigma_a$. The appropriate neutron velocity is that at which $E_n = 4k_BT/\pi$ [128, Ch.8]. Circumstances in SNO exist in which Σ_a is sufficiently large that the neutron velocity distribution is no longer approximately Maxwellian. This occurs in the light water. In this case, because $\Sigma_a \propto 1/v$, the proportion of neutrons with low velocities is reduced. The resulting neutron distribution will not be discussed here, except to note that it can be approximated by using cross sections for neutrons with energies greater than kT, modelling an upward shift in the representative neutron energy, and indicating that the neutron distribution is no longer in thermal equilibrium with the transport medium.

Equation 8.12 is not in a suitable form for comparison with results obtained from the SNOMAN program, which will most easily yield the neutron capture rate as a function of r. The neutron capture rate in unit volume at radius r is $\Sigma_a\Phi(r)$; and hence the capture rate as a function of r is;

$$\Psi(r) = \int \Sigma_a \Phi(r) r^2 dr d\theta d\phi \,, \tag{8.17}$$

$$\Psi(r) = \frac{\Sigma_a S_0 \beta}{D} r e^{-\kappa r} + \Sigma_a S_0 e^{-\Sigma' r} \,. \tag{8.18}$$

The rate as a function of r may be used to define a cumulative distribution function, which will be used in later KS tests. The normalised cumulative distribution function is;

$$\text{C.D.F.} = \frac{1}{S_0} \int_0^R \Psi(r) dr \,, \tag{8.19}$$

$$= \frac{\Sigma_a \beta}{D\kappa^2} \left(1 - (1 + \kappa R) e^{-\kappa R}\right) + \frac{\Sigma_a}{\Sigma'} \left(1 - e^{-\Sigma' R}\right) \,. \tag{8.20}$$

8.6.1 Results from SNOMAN

The SNOMAN program was used to simulate an isotropic source of neutrons in thermal equilibrium with the local medium at 294°K. Transport through 4 media was simulated, and in each case Σ and Σ_a were obtained from SNOMAN at $E_n = 4k_BT/\pi = 0.032$eV, as was D. The four media were D_2O with an isotopic content of ^{17}O of 0.055% by weight (known as pure D_2O), D_2O not only with ^{17}O but also 0.08% H_2O by weight (SNO quality D_2O), an 0.2% salt solution of SNO quality D_2O (Salted D_2O), and light water (with 0.033% ^{17}O by mass). In pure and SNO quality D_2O, neutrons diffuse sufficiently far that n-capture on the acrylic vessel distorts the results obtained from SNOMAN with respect to those

obtained analytically. The acrylic vessel was effectively excluded from these SNOMAN simulations by increasing the density of the media by a factor of 10. Σ and Σ_a were altered accordingly. The positions of thermal neutron captures were recorded. The results are shown in Figures 8.10 and 8.11, where the appropriate solutions of the diffusion equation from Equation 8.18 are also shown.

Kolmogorov-Smirnov and χ^2 tests were used to compare the SNOMAN distribution with the diffusion equation capture distribution function (Equation 8.19). In the cases where neutrons are transported through D_2O (pure or SNO quality), the agreement between the two independent solutions of the diffusion equation (one an analytical approximation, the other a Monte Carlo estimate) is acceptable, given $\overline{\mu}$ is provided for each isotope. If it is assumed that $\overline{\mu} = 0$ for all isotopes, there is no agreement between the two distributions. This is not surprising, since for all the isotopes in SNOMAN $\overline{\mu} \neq 0$. Table 8.7 summarises both the input values and the results of the comparative tests. The differences between the probabilities returned by the K.S. test and χ^2 test in each case are attributed to the the systematic nature of the deviation of SNOMAN from the diffusion equation, which are penalised more heavily by the Kolmogorov-Smirnov test because it compares two cumulative distribution functions than by the χ^2 test which does not attempt to retain information about the ordering of bins. In general, the probabilities are low, indicating that SNOMAN does not exactly reproduce the diffusion equation. This is to be expected, since SNOMAN attempts an approximation to an exact simulation of neutron transport, whereas the diffusion equation is a monoenergetic equation which uses average, rather than energy dependent, scattering angles.

SNOMAN differs most from the diffusion equation when neutrons are transported through light water. The difference is not great (see Figure 8.11), but the statistical comparisons indicate that the capture distribution for neutrons in light water from SNOMAN is not the same as that from the diffusion equation. In this case the maximum difference between the cumulative distribution functions of the two data sets remains small, at 3.7%, indicating that the local difference between the two functions is likely to be less than 1%, and certainly less than the 3% error ascribed to MCNP (and hence SNOMAN) by Wang *et al.* [104]. As described in the preceding section, the neutron capture distributions in light water can be reproduced approximately by using a higher-than-thermal energy in the one-velocity diffusion equation. This method can be used to produce satisfactory results for light water, but further discussion is not warranted here. It is important to note that 88.6% of all neutrons are captured within 10cm of thermalisation in the light water, and 99.5% are captured within 20cm. These facts, together with the detector's estimated position resolution of 20cm, imply that the differences between SNOMAN and the diffusion equation are least important where they are greatest. Where the neutron can propagate great distances before capture (in the heavy water), SNOMAN reproduces the diffusion equation well.

8.7 Conclusion

The SNOMAN program has been shown to produce results exactly in accordance with those of MCNP when both programs are operated with equal precision. The statistical tests that were applied to differentiate between results from the SNOMAN program and those from the MCNP program were unable to find any evidence for the existence of any such distinction after 2.64 million data elements were collected from each program.

Strictly interpreted, the comparisons between MCNP and SNOMAN confirm that they reproduce the same distributions only for their first scatterings. Additional data has been presented to show that scattering data in a restricted energy range culled from the first simulated neutron interaction in the SNOMAN program is the same as scattering data culled from interactions after thermalisation in the same medium in the same energy range. This demonstrates that the production of scattering distributions

Medium	Σ (cm^{-1})	Σ_a (cm^{-1})	D (10^{-1} cm)	Δ (%)	P(K.S.) (%)	P(χ^2) (%)
Pure D_2O	0.4899	3.896×10^{-5}	7.582	1.6	1.5	11
SNO D_2O	0.4923	5.644×10^{-5}	7.548	2.3	0.01	0.3
Salted D_2O	0.4924	8.876×10^{-4}	7.576	1.6	1.5	56
H_2O	3.4724	1.980×10^{-2}	1.174	3.7	low	low

Table 8.7: The results of K.S. and χ^2 tests for the comparison of SNOMAN data and the diffusion equation. Δ is the maximum difference between the cumulative distribution functions of the two data sets, the statistic that is used in the K.S. test. See text for further discussion.

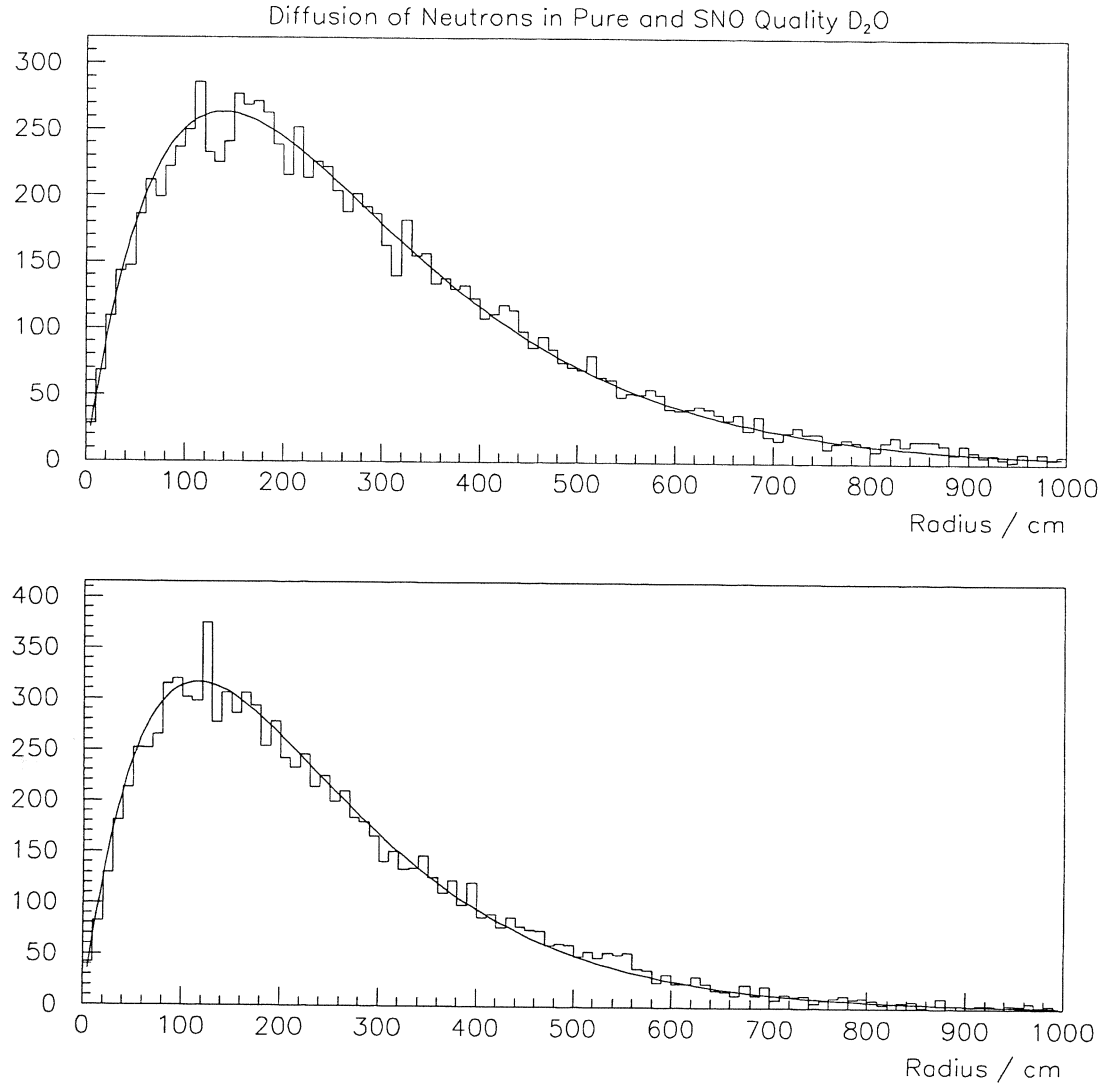

Figure 8.10: The plots show neutron capture rate as a function of r within the detector, normalised to 10000 events. The transport medium in the upper plot is pure D_2O, and in the lower plot it is SNO quality D_2O. See text for more details.

by SNOMAN is dependent only upon the neutron's incident energy and the transport medium, and does not depend upon the number or type of previous interactions, except in so far as they define the incident neutron's energy and the transport medium. This is due to the modular data driven design of the SNOMAN program. Is it therefore reasonable to suppose that the SNOMAN program reproduces the MCNP scattering distributions throughout the simulation of a neutron's history.

The SNOMAN program has also been shown to reproduce representative cross sections at thermal energies, and to match the diffusion equation closely in the limit $\Sigma \gg \Sigma_a$. SNOMAN reproduces the long range behaviour of neutrons in all the important SNO media well. Significant deviations from the diffusion equation occur only in light water, where the small diffusion length of the neutrons ($L = 2.4$cm) means that they will not be observable in the SNO detector which has a position resolution of ~ 20cm.

MCNP (and hence SNOMAN) has been shown by Wang *et al.* [104] to predict the absolute number of neutrons captured in an experiment involving neutron thermalisation with an accuracy which is at worst 3%. At the same time, Wang *et al.* showed that that the ratio of the numbers of neutrons captured predicted by MCNP in related experimental setups was accurate to within 0.3%. There is no reason to suspect that the situation will be worse in the SNO detector.

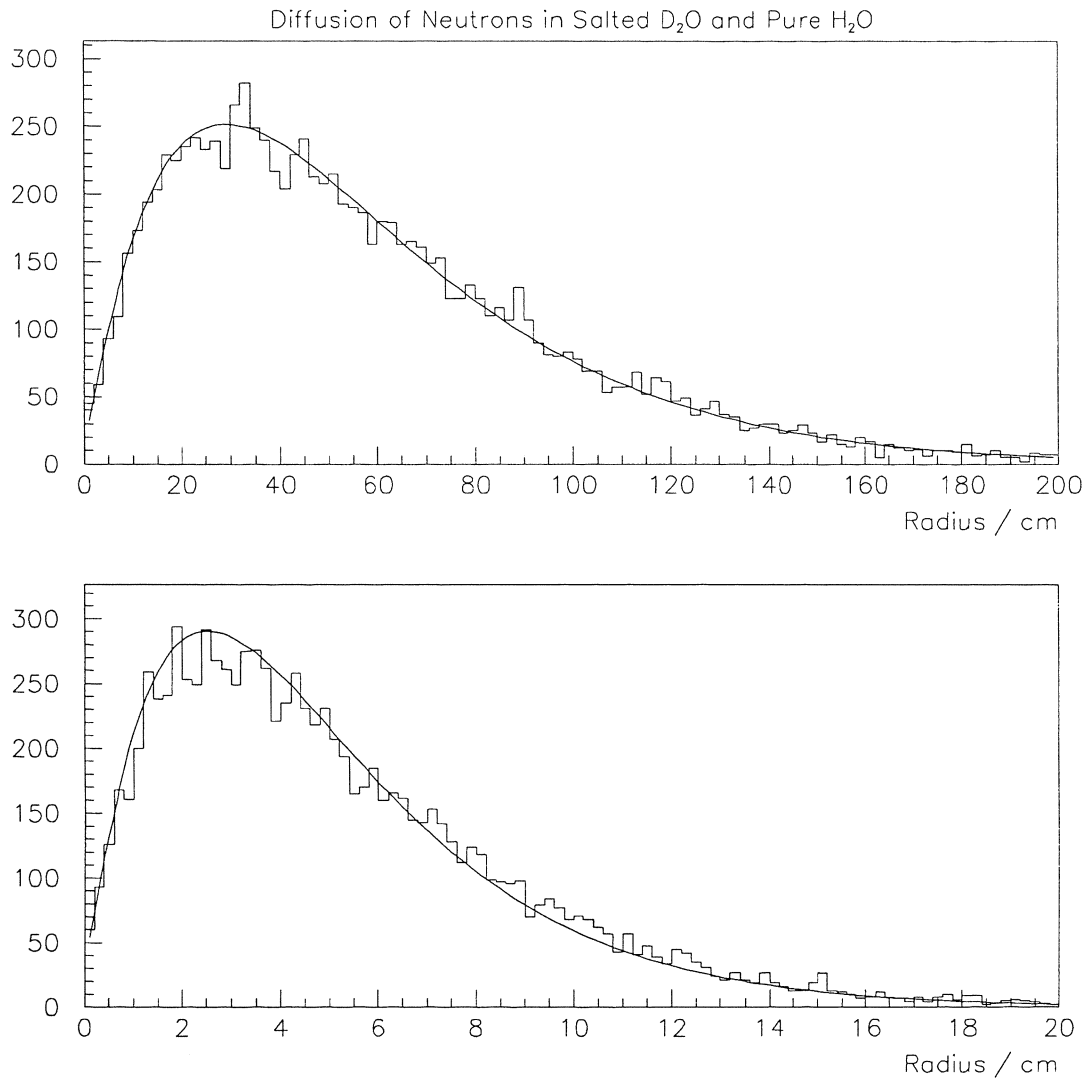

Figure 8.11: The plots show neutron capture rate as a function of r within the detector, normalised to 10000 events. The transport medium in the upper plot is salted D_2O, and in the lower plot it is H_2O. See text for more details.

SNOMAN has been verified to work well, both in reproducing the detailed results of MCNP and simple experimental cross sections, and in predicting the results of an experiment, and in correctly modelling the transport behaviour of thermal neutrons in circumstances described by the diffusion equation. The SNOMAN program can be used with confidence to predict the neutron transport properties of the SNO detector.

Chapter 9

Neutron Transport in the Sudbury Neutrino Detector

9.1 Introduction and Purpose

Chapter 5 concerned the accurate modelling of the photodisintegration cross section for the SNOMAN program. Chapters 6 $\rightarrow$ 8 dealt with the requirements for a neutron transport code for use in the Sudbury Neutrino Experiment, and the selection, installation, and testing of that code.

In this chapter, the now neutron-complete SNOMAN code will be used to make predictions about the generation and transport of neutrons within the SNO detector. The calculations include an estimate of the rate of photodisintegration from ^{214}Bi and ^{208}Tl in the heavy water, the light water, and the acrylic vessel and a breakdown of neutron capture probabilities in a number of circumstances. In addition, it will be shown that the principle sources of both signal and background neutrons fall into two categories, members of which cannot be distinguished in SNO. The SNO experiment will add $MgCl_2$ to the D_2O. The quantity of salt to be added has been considered using one year of simulated detector data. Based upon a minimisation of the uncertainty in the neutral current rate a minimum of 1 tonne of salt is required.

9.1.1 Statistical Note

In Chapter 8, it was noted that multinomial statistics govern binned distributions where the total number of events are fixed. This has a significant effect on the error in the content of a bin only where the number of bins is small or where the content of that bin is a significant fraction of the total number of events. In any case where the number of events of a single bin is small compared to the total number of events in the distribution, multinomial statistics approach Poisson statistics [103].

All the data on photodisintegration backgrounds in the SNO detector that is presented in this chapter is subject to Poisson statistics when it is binned. This is because the number of photodisintegration events is small compared to the number of ^{208}Tl or ^{214}Bi events that must be simulated to obtain them.

The data relating to neutron capture from neutral current events is also subject to Poisson statistics when it is binned. This would be approximately true merely because the number of bins used is large (typically 100) and the events are well distributed among all the bins, but in fact it is exactly true. This is because all the NC neutron data presented in this chapter has been gathered in runs where the total number of events was allowed to vary according to Poisson statistics. It is shown in Appendix F that the combination of a multinomial distribution (bins) and a Poisson event total leads to Poisson statistics in all the bins. It is usual for experimental data to be gathered in this regime - the measurement of a radioactive half life is a good example.

All the bins in all the distributions presented in this chapter are subject to Poisson statistics. This point is made here to avoid needless repetition later on.

9.2 Photodisintegration Rates from Backgrounds in the SNO Detector

Photodisintegration of the deuteron by high energy γ-rays from ^{208}Tl and ^{214}Bi decays are the major background to the measurement of the neutral current rate in the SNO detector. In this section, the

probabilities that a deuteron photodisintegration will occur as a result of a thalium or bismuth decay will be calculated. There are six distinct sources of background which are ^{208}Tl in the heavy water, light water, and acrylic vessel, and ^{214}Bi in the heavy water, light water, and acrylic vessel. The SNOMAN program was run for each distinct background.

The backgrounds were assumed to be uniform throughout their respective media. This assumption is justified for the backgrounds present in the D_2O, which will be subject to turbulent mixing, and for backgrounds in the light water which flows continuously away from the acrylic vessel and toward the PSUP. The assumption has been made for backgrounds in the acrylic because no better information is available, and because it is both a good approximation to the most likely scenario and also the worst case scenario in which the background is uniformly distributed in θ and ϕ, and hence differs from the neutral current signal only in r. More complex analysis of a position dependent background which may occur in the acrylic vessel must wait until data to that effect is available, and in any case such an analysis will include a uniformly distributed component such as the one assumed here.

The SNOMAN simulation used to determine the photodisintegration probabilities did not include either the belly plates or the acrylic vessel neck. This meant that the acrylic vessel was simulated as a perfect sphere. This absence of the neck from the simulation is not expected to have a significant effect, since it occupies only about 0.4% of the solid angle visible from the centre of the detector. The absence of the belly plates will affect the probability that a $2 \rightarrow 3$MeV γ-ray generated in the light water reaches the D_2O. The area of the acrylic vessel covered by the belly plates is estimated to be 13.3%. Assuming that the attenuation length for γ-rays in water is similar to that in the acrylic vessel (4.34m^{-1} for 2.6MeV γ-rays), and that the belly plates are on average twice as thick as a standard AV tile (11.0cm as opposed to 5.5cm thick), the number of high energy γ-rays penetrating through a belly plate without interaction is 78.7% of the number penetrating through a standard AV tile without interaction. Therefore the probability that high energy γ-rays originating in the light water will photodisintegrate a deuteron is overestimated by $\sim$ 3%. It will be shown that the number of photodisintegrations due to γ-rays from the light water is very small compared to those from other sources, and hence that the crude correction given here is more than sufficient. The PMT 'grey disk' simulation was also used. The 'grey disk' simulation simplifies the treatment of photons incident upon a photomultiplier, and has been shown to be functionally equivalent to a full PMT simulation.

Only 2.07% of the decays of ^{214}Bi result in γ-rays of more than 2.2MeV. To accelerate the collection of results, the decay scheme used to simulate ^{214}Bi in SNOMAN was truncated so that only those decays containing a γ-ray of 2.2MeV or greater remained. The fraction of decays causing photodisintegrations was amended accordingly. No such correction was made for ^{208}Tl, whose decays all proceed via a 2.6MeV γ-ray.

The γ-rays emitted from ^{208}Tl and ^{214}Bi decays in the light water are highly likely to be attenuated before reaching the acrylic vessel because the attenuation coefficient for 2.6MeV and 2.2MeV γ-rays is 4.34m^{-1} and 4.62m^{-1} respectively and the light water extends from the acrylic vessel at 6.06m radius to the PSUP at 8.5m radius. The photodisintegration rate in the light water was calculated using an active volume of light water extending from the surface of the acrylic vessel out to 6.56m radius only. This reduced the time taken to simulate γ-rays by a factor of $\sim$ 6.5. A correction factor was calculated by finding the intensity of γ-rays passing from outside (larger r) through the surface of a spherical shell of radius R from a γ-ray source uniformly distributed throughout a water volume from R to $R+r$. If the intensity is $I(r)$, then the correction factor is $F(r) = I(\infty)/I(r)$, i.e. $F(6.56)$. The intensity was evaluated separately for 2.6 and 2.2MeV γ-rays, and γ-rays that scatter and still retain more than 2.2MeV were crudely accounted for. The correction factors are 1.10 for 2.6MeV γ-rays, and 1.08 for 2.2MeV γ-rays.

9.2.1 Probability of Photodisintegration

The photodisintegration probability for one of the six sources described earlier in this section is given by;

$$P = \frac{n}{N} FAGB \ , \tag{9.1}$$

where n is the number of photodisintegrations that occurred in the simulation, F is the branching fraction (1 for ^{208}Tl decays, 0.0207 for ^{214}Bi decays), A is the correction factor given in the preceding section, G is the geometric correction that must be made to compensate for the fact that only a limited volume of light water was used to estimate the d(γ,n)p probability, and B is the correction for the neglect of the belly plates in the simulation. The factors A and G are 1 for decays in the acrylic and heavy water. Table 9.1 gives the results of the SNOMAN simulation.

	Thalium			Bismuth		
Location	D_2O	AV	H_2O	D_2O	AV	H_2O
Events simulated ($/10^7$)	1	3	1	1	2	1
D disintegrations	21076	22095	1485	15428	10891	1012
Branching factor	1			2.075%		
Attenuation factor	1		1.10	1		1.08
Geometric factor	1		0.1521	1		0.1521
Belly plate factor	1		0.971	1		0.971
P(D disintegration) $\times 10^5$	201.8	73.65	2.412	3.201	1.130	0.03349
σ(P) $\times 10^5$	1.4	0.50	0.068	0.026	0.011	0.00114

Table 9.1: Photodisintegration probability per nuclear decay for the six distinct backgrounds (^{208}Tl and ^{214}Bi in D_2O, H_2O, and the acrylic vessel). The error presented is the 1σ statistical error. Systematic errors are discussed in the text.

Nucleus	Thorium			Uranium		
Location	D_2O	AV	H_2O	D_2O	AV	H_2O
Mass of nucleus	232.038g			238.029g		
Decay rate of nucleus	4.95×10^{-11}yr^{-1}			1.54×10^{-10}yr^{-1}		
Branching fraction	0.36			1		
Contamination 10^{-15}g/g	3	250	10	30	1000	100
P(D disintegration) $\times 10^5$	201.8	73.65	2.412	3.201	1.130	0.03349
Mass of medium / tonnes	1000	30	1668	1000	30	1668
Rate / year	280	256	19	374	132	22
σ(Rate / yr)	2.8	2.6	0.5	4.2	1.6	0.7

Table 9.2: The rate of photodisintegrations in the SNO detector. The systematic error the the yearly rate is everywhere 5% as discussed in the Section 9.2.1. See text for further explanation.

9.2.2 Photodisintegration Rates in the SNO Detector

The rate of photodisintegrations due to thorium nuclei distributed uniformly in either the heavy water, light water or acrylic vessel is determined from the equation;

$$R = P\lambda \frac{MCN_A}{m} F \ , \tag{9.2}$$

where λ is the decay rate of thorium, N_A is Avogadro's number, F is the fraction of thorium nuclei whose decay cascade includes ^{208}Tl, the only photodisintegration capable nucleus in the thorium decay cascade, C is the mass of thorium per gram of material, m is the mass of 1 mole of thorium, and P is the probability that the decay of a ^{208}Tl nucleus will results in the photodisintegration of a deuteron in the heavy water. This probability is averaged over the appropriate material volume. A similar equation can be written for the rate of photodisintegrations due to contamination of detector materials by uranium, which decays via the photodisintegrating nucleus ^{214}Bi.

The mass of the acrylic vessel is 30 tonnes. The mass of the light water sandwiched between the acrylic vessel and the PSUP is 1668 tonnes. The mass of the heavy water is 1000 tonnes. The rate of photodisintegrations from the 6 different sources in the SNO detector is shown in Table 9.2.

9.3 Similarity Between Neutron Capture Distributions in the SNO Detector

In this section it will be shown that it is not possible to distinguish between certain neutron capture distributions after 1 year of SNO data taking. Neutron capture distributions were produced for the 6 photodisintegration backgrounds (^{208}Tl and ^{214}Bi in the light water, the acrylic vessel, and the heavy water) and for the neutral current signal at 5 salt concentrations which were 0%, 0.1%, 0.2%, 0.3%, and

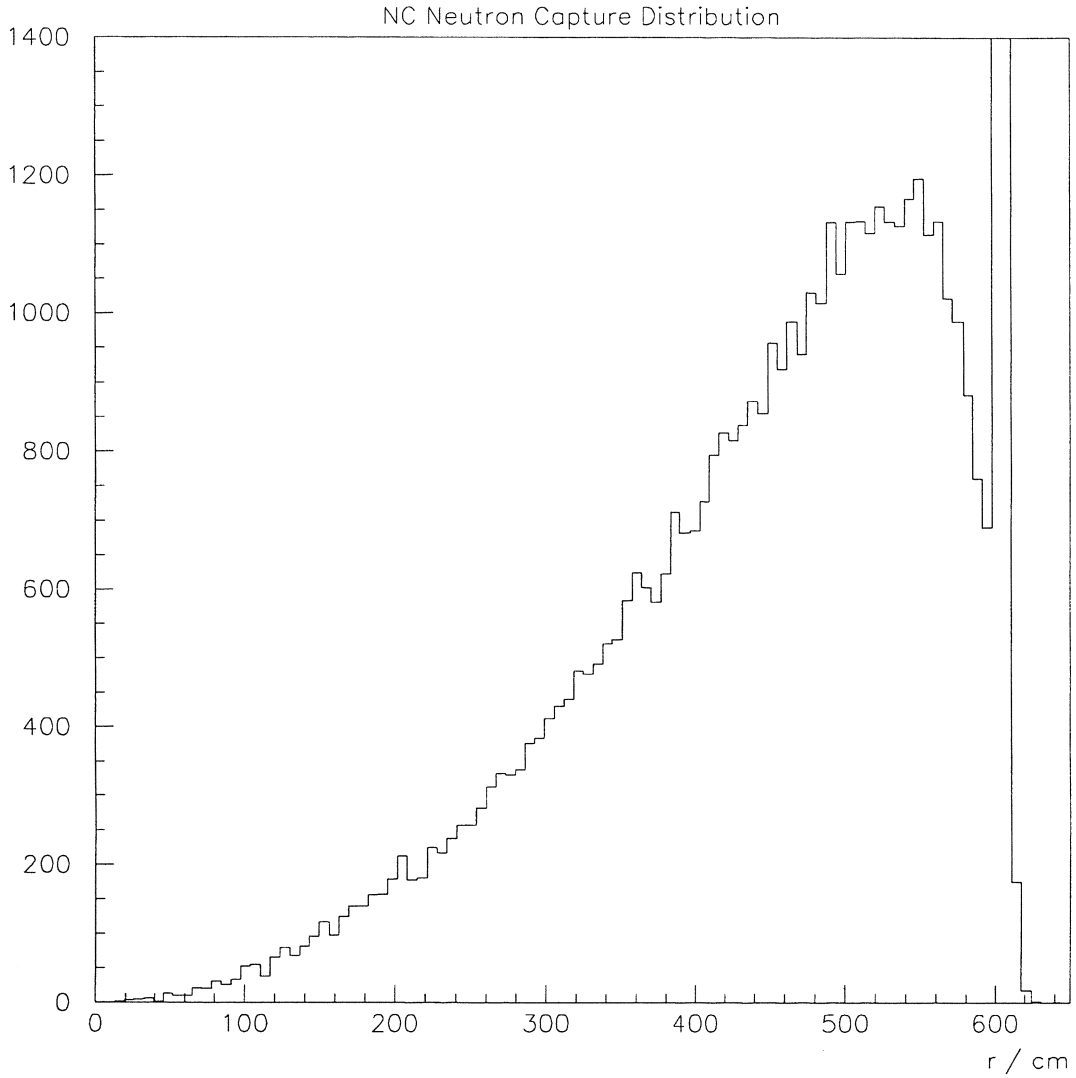

Figure 9.1: The r capture distributions of NC neutrons in an 0.2% heavy water salt solution in the SNO detector, as simulated in SNOMAN. The number of events simulated was 50266. The distribution below $r = 500$cm reflects the increase in the volume of the detector with increasing r ($V \propto r^3$). The fall in capture rate above $r = 500$cm and the large spike at $r \simeq 600$ are both due to the absorption of neutrons via the ^{1}H(n,γ)^{2}H reaction in the acrylic vessel.

0.4%. The range of values used for the salt concentration is discussed in Section 9.5.1. The simulation of the SNO detector included the acrylic vessel neck, but did not include the belly plates. The PMT 'grey disk' simulation was used. The radius of the capture position of each neutron was recorded. The β-γ decay events in the D_2O were assumed to be uniformly distributed throughout the D_2O volume, as were the β-γ events in the acrylic vessel and separately, the light water. An NC neutron r_{capture} distribution is shown in Figure 9.1. In the figure the importance of an accurate n-transport simulation is evident; the fraction of neutrons that capture on the acrylic vessel increases as the events that generate them approach the AV, while the number of NC events goes as r^3. Hence the accurate simulation of neutron transport increases in importance as the AV is approached.

The number of events in each of the seven categories expected during 1 year of the SNO detector's operation is shown as a function of salt concentration in Table 9.3. These numbers have been calculated under the assumption that only neutron capture events in which at least 60 PMTs are hit and which reconstruct inside 7m will be used in any analysis of the SNO experiment. The probability that these

Event	Location	Salt Concentration				
		0.0%	0.1%	0.2%	0.3%	0.4%
NC(SSM/MSW)	D_2O	473.9	2218.0	2413.1	2520.7	2578.4
NC(SSM/3)	D_2O	158.0	739.3	804.4	804.2	859.5
^{208}Tl decay	D_2O	24.2	113.3	123.3	128.7	131.7
	AV	3.7	49.5	55.8	65.0	70.7
	H_2O	0.3	3.7	4.2	4.9	5.3
^{214}Bi decay	D_2O	32.3	151.4	164.7	172.0	176.0
	AV	1.9	25.6	28.8	33.6	36.5
	H_2O	0.3	4.1	4.9	5.7	6.2

Table 9.3: The yearly event rate for the neutral current signal and photodisintegration backgrounds as a function of salt concentration. The figures have been calculated under the assumption that 60 or more PMTs were hit and that the event vertex was fitted using the time fitter to be within 7m of the centre of the acrylic vessel. The effects of the cuts have been deduced from data presented in Tables 9.5, 9.4, and 9.6.

conditions are satisfied has been calculated from the distributions obtained in Section 9.4. The number of events expected in each event category is just the product of $P(\text{NHITs} \geq 60, \text{RFIT} \leq 700)$ and the total number of neutrons produced by events in that category. The number of events produced by γ-decay sources is shown in Table 9.2. The number of NC events is shown in Table 2.1. The time fitter was used to fit the event vertex because it is not yet known how fitters will be selected and used to deal with SNO data, and the time fitter is the minimal standard for SNO event fitters.

A sample distribution simulating one year of SNO data taking was obtained by randomly selecting n_i events from the N_i that were simulated in SNOMAN for the ith distribution ($n_i < N_i$, and n_i taken from Table 9.3). The value of N_i was allowed to vary like a Poisson variable of mean 50000 in the SNOMAN simulations used to gather the NC event distributions. The Kolmogorov-Smirnov test for the comparison of two binned distributions was used to compare all the r capture distributions arising from signal and background events in the D_2O to one another, and to compare all the r capture distributions from background sources in the acrylic and light water to one another.

The reader is reminded that the result of the K.S. test for the comparison of two distributions is a number which represents the probability that two distributions drawn from the same parent distribution are as different of more different than the two distributions that have been compared. The probabilities for all the comparisons that have been described were uniformly distributed between 0 and 1. This means that no two distributions which were compared could be told apart on a statistical basis. This conclusion is the result of both the similarity of the distributions and the low statistics that will be available to a binned distribution of neutron background events in SNO. Thus, none of the different classes of events in the D_2O could be distinguished from one another, and none of the different classes of events outside the D_2O could be distinguished from one another. This leads directly to the classification of all neutron events as either 'internal' or 'external' to the D_2O. This conclusion is evidently reliant on the uniformity of the distribution of photodisintegration causing decays in the three media. Typical internal and external distributions are shown in Figure 9.2.

This conclusion is more general than it at first appears. This is because a neutron event is observed in the SNO detector via the γ-rays released in either the $^2H(n,\gamma)^3H$ or the $^{35}Cl(n,\gamma)^{36}Cl$ capture reaction. All of the information from an event is contained in the number, timing, and spatial distribution of PMT hits, the distributions of which are fixed by the capture position and the characteristics of the γ-rays released as a result of the neutron capture. Therefore, since their r capture distributions cannot be told apart, there can be no mechanism which can be used to distinguish between neutron capture distributions from NC events and n-capture distributions from photodisintegrations caused by ^{214}Bi and ^{208}Tl decays distributed uniformly throughout the D_2O. There is also no mechanism for distinguishing between n-capture distributions from photodisintegrations caused by either ^{214}Bi or ^{208}Tl decays distributed uniformly throughout either the acrylic vessel or the light water. These conclusions are based upon 1 year of data taking in SNO.

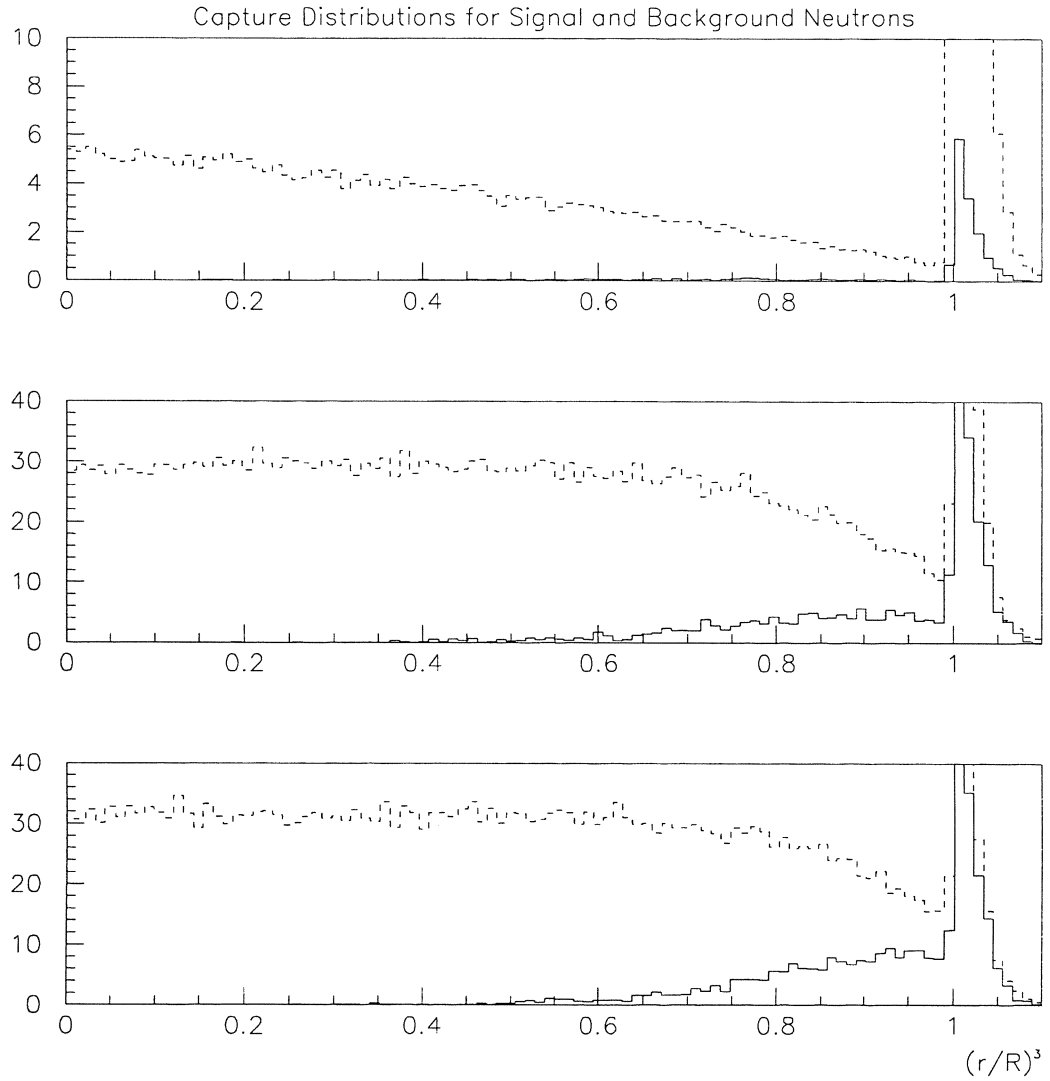

Figure 9.2: The sum of the NC, ^{214}Bi and ^{208}Tl distributions and the sum of the acrylic and light water ^{214}Bi and ^{208}Tl distributions, for no salt (top), 0.2% (middle), and 0.4% (bottom) D_2O salt solutions. The distributions have been scaled to represent 1 years worth of data taking in SNO. The high level of detail occurs because the distributions used have been scaled from data sets representing about 10 years of data in SNO.

9.4 Neutron Capture Probabilities in the SNO Detector

All neutrons end their lives in the SNO detector through (n,γ), (n,p), or (n,α) capture reactions. In this section, results obtained from SNOMAN showing the probability that a neutron will capture onto a specific nucleus through one of these reactions will be presented as a function of salt concentration. In addition, the probability that the major (n,γ) reactions satisfy a $\geq$ 50 or $\geq$ 60 NHIT and $r_{\text{fitted}} \leq$ 7m cut is presented in Table 9.6. In that table, the difference between the probability that an internal neutron survives the standard analysis cut and the probability that an external neutron survives the same cut is explained by the slight position dependence of the energy response of the SNO detector. The importance of the 50 $\rightarrow$ 60 NHIT region is clear.

Following the discussion in Section 9.3, neutron capture probabilities were determined for only two data sets, one of which was used to represent the internal source n-capture distributions and the other the external source n-capture distributions. The NC distribution was chosen to represent the class of source that is internal to the D_2O, and acrylic vessel ^{208}Tl events were chosen to represent the class of

Capture Reaction	Salt Concentration				
	0.0%	0.1%	0.2%	0.3%	0.4%
$^{1}H(n,\gamma)^{2}H$	60.72 ± 0.44	18.21 ± 0.21	12.47 ± 0.17	9.93 ± 0.15	8.46 ± 0.13
H_2O	7.45 ± 0.13	2.94 ± 0.08	2.18 ± 0.07	1.93 ± 0.06	1.62 ± 0.06
AV	35.86 ± 0.31	12.34 ± 0.17	8.44 ± 0.13	6.76 ± 0.12	5.90 ± 0.11
D_2O	17.41 ± 0.20	2.93 ± 0.08	1.85 ± 0.06	1.24 ± 0.05	0.93 ± 0.04
$^{2}H(n,\gamma)^{3}H$	29.93 ± 0.28	5.30 ± 0.10	3.01 ± 0.08	2.02 ± 0.06	1.53 ± 0.06
$^{X}C(n,\gamma)^{X+1}C$	0.27 ± 0.02	0.09 ± 0.01	0.06 ± 0.01	0.07 ± 0.01	0.04 ± 0.01
$^{16}O(n,\gamma)^{17}O$	5.23 ± 0.10	0.93 ± 0.04	0.58 ± 0.03	0.37 ± 0.03	0.27 ± 0.02
$^{17}O(n,\alpha)^{12}C$	3.80 ± 0.09	0.67 ± 0.04	0.33 ± 0.03	0.28 ± 0.02	0.21 ± 0.02
$^{X}Mg(n,\gamma)^{X+1}Mg$		0.08 ± 0.01	0.08 ± 0.01	0.07 ± 0.01	0.06 ± 0.01
$^{35}Cl(n,\gamma)^{36}Cl$		73.84 ± 0.50	82.49 ± 0.54	86.26 ± 0.57	88.51 ± 0.57
$^{35}Cl(n,p)^{36}Cl$		0.85 ± 0.04	0.94 ± 0.04	0.95 ± 0.04	0.89 ± 0.04
Other	0.05 ± 0.01	0.05 ± 0.01	0.03 ± 0.01	0.04 ± 0.01	0.02 ± 0.01

Table 9.4: The termination fraction for neutron histories that are classed as arising from internal sources. A breakdown of the $^{1}H(n,\gamma)^{2}H$ reaction is given by location. The 'Other' category represents those neutrons which are generated in the neck of the acrylic vessel, and which initially walk vertically upward to be captured on nuclei not found in the inner three media of the detector. See the accompanying text for further discussion.

Capture Reaction	Salt Concentration				
	0.0%	0.1%	0.2%	0.3%	0.4%
$^{1}H(n,\gamma)^{2}H$	90.28 ± 2.28	60.96 ± 1.85	52.04 ± 1.64	49.18 ± 1.55	43.13 ± 1.41
H_2O	18.33 ± 0.81	12.92 ± 0.71	13.01 ± 0.70	12.40 ± 0.67	11.06 ± 0.63
AV	66.65 ± 1.83	46.34 ± 1.53	38.22 ± 1.34	36.03 ± 1.26	31.52 ± 1.16
D_2O	5.33 ± 0.41	1.70 ± 0.25	0.81 ± 0.17	0.75 ± 0.16	0.55 ± 0.13
$^{2}H(n,\gamma)^{3}H$	6.60 ± 0.46	2.40 ± 0.29	1.62 ± 0.24	1.11 ± 0.19	0.97 ± 0.18
$^{X}C(n,\gamma)^{X+1}C$	0.39 ± 0.11	0.17 ± 0.08	0.10 ± 0.06	0.16 ± 0.07	0.19 ± 0.08
$^{16}O(n,\gamma)^{17}O$	1.54 ± 0.22	0.49 ± 0.13	0.41 ± 0.12	0.10 ± 0.06	0.26 ± 0.09
$^{17}O(n,\alpha)^{12}C$	1.18 ± 0.19	0.35 ± 0.11	0.30 ± 0.10	0.07 ± 0.05	0.19 ± 0.08
$^{35}Cl(n,\gamma)^{36}Cl$		35.15 ± 1.28	45.08 ± 1.49	48.99 ± 1.54	54.67 ± 1.66
$^{35}Cl(n,p)^{36}Cl$		0.49 ± 0.13	0.37 ± 0.11	0.36 ± 0.11	0.55 ± 0.13
$^{X}Mg(n,\gamma)^{X+1}Mg$			0.07 ± 0.05	0.03 ± 0.03	0.03 ± 0.03

Table 9.5: The termination fraction for neutron histories that are classed as arising from external sources. A breakdown of the $^{1}H(n,\gamma)^{2}H$ reaction is given by location. See the accompanying text for further discussion.

source external to the D_2O. These choices of representative event types were made because they are the distributions which are simulated most quickly by the SNOMAN program, yielding the largest number of neutrons per event (one to one in the case of NC events). The neutron capture simulations were run for the usual 5 salt concentrations of 0.0%, 0.1%, 0.2%, 0.3%, and 0.4%. These simulations included the acrylic vessel neck. The capture probabilities are shown in Tables 9.4 and 9.5.

The errors shown in Tables 9.4 and 9.5 are purely statistical. The systematic error is estimated in accordance with the results of Section 8.3, where it was shown that absolute values are determined at the 3% level by MCNP (SNOMAN). The fraction of internal-source neutron histories that are terminated by the $^{35}Cl(n,\gamma)^{36}Cl$ capture reaction when 2 tonnes of salt have been added to the heavy water is thus;

$$82.49 \pm 0.54(\text{stat.}) \pm 2.47(\text{sys.}) \; . \tag{9.3}$$

Neutron capture probabilities were also determined for the D_2O+poison scenario in which 300kgs of $LiNO_3$ is added to the D_2O, and for D_2O+NCDs. The results are shown in Table 9.7. When the NC poison is present in the D_2O, only $0.80 \pm 0.04\%$ of NC neutrons results in ≥ 50 NHITs in the detector, and only $0.39 \pm 0.03\%$ result in 60 NHITs or more. The light production above 50 NHITs in the poison

Category	Reaction	Probability (%)	
		$\geq$ 50 NHIT	$\geq$ 60 NHIT
Internal n	$^{2}H(n,\gamma)^{3}H$	62.4 ± 0.7	28.6 ± 0.4
	$^{35}Cl(n,\gamma)^{36}Cl$	77.8 ± 0.3	52.6 ± 0.2
External n	$^{2}H(n,\gamma)^{3}H$	56.4 ± 4.7	24.3 ± 2.8
	$^{35}Cl(n,\gamma)^{36}Cl$	74.1 ± 1.5	50.9 ± 1.2

Table 9.6: The probability that a neutron capturing via the $^{2}H(n,\gamma)^{3}H$ or $^{35}Cl(n,\gamma)^{36}Cl$ reactions survives a 50 or 60 NHIT cut. The probabilities are subject to reconstruction inside 7m. See test for details.

Capture Reaction	Loc.	Poison	NCDs
$^{1}H(n,\gamma)^{2}H$		7.17 ± 0.12	34.89 ± 0.21
	H_2O	1.47 ± 0.05	4.94 ± 0.06
	AV	5.03 ± 0.10	22.72 ± 0.16
	D_2O	0.66 ± 0.03	7.23 ± 0.08
$^{2}H(n,\gamma)^{3}H$	D_2O	1.19 ± 0.04	12.23 ± 0.11
$^{X}C(n,\gamma)^{X+1}C$	D_2O	0.03 ± 0.01	0.16 ± 0.01
$^{16}O(n,\gamma)^{17}O$	D_2O	0.21 ± 0.02	2.10 ± 0.04
$^{17}O(n,\alpha)^{12}C$	D_2O	0.16 ± 0.01	1.63 ± 0.04
$^{6}Li(n,\alpha)^{3}H$	D_2O	91.01 ± 0.59	
$^{14}N(n,\gamma)^{15}N$	D_2O	0.17 ± 0.02	
$^{3}He(n,p)^{3}H$	NCDs		46.07 ± 0.24
$^{X}Ni(n,\gamma)^{X+1}Ni$	NCDs		2.83 ± 0.05
Other		0.04 ± 0.01	0.07 ± 0.01

Table 9.7: The termination fraction for neutron histories from internal sources with NCDs and the neutron poison ($LiNO_3$) in the D_2O. See test for details.

run is entirely due to the $^{2}H(n,\gamma)^{3}H$ reaction.

The mean time taken for an NC neutron to reach thermal energies is 125ns. D_2O additives have little effect on the high energy interaction cross section (see Chapter 6) and therefore the mean thermalisation time is expected to be correct to within 10% when salt and poison are present in the D_2O. The time to capture is not expected to remain the same when either salt, poison, or the NCDs are added to the D_2O. Table 9.8 lists the mean capture times for these scenarios.

The capture times are important in SNO for 2 reasons. A lookback analysis has been envisaged that would distinguish between NC neutrons and β-γ background neutrons. The technique would rely upon a coincidence between the captured background neutron (which would trigger the detector) and the β-decay that must have preceded it. The neutron would have to have been reconstructed within 4m of the centre of the acrylic vessel and the β-decay within 50cm of the neutron event. The analysis is complicated by the number of ^{40}K and PMT β-γ decay events that occur in the detector ($0.07ms^{-1}$ in the case of ^{40}K and $6ms^{-1}$ in the case of ^{214}Bi PMT β-γs) which can mimic the position and energy of the lookback β-decay event, but in principle it could provide an additional method of assessing the neutral current background. The lookback analysis would be assisted by increased salt concentrations, which would shorten the time taken for neutron capture and hence the time window used in the analysis, and in addition, increase the number of neutrons capturing within 50cm of the β-γ event that preceded them. Higher salt concentrations would also increase the ^{40}K content of the D_2O.

The mean capture time is also important in the design of the ^{252}Cf source. The source is essentially a very small quantity of ^{252}Cf in the shape of a disc implanted in a liquid scintillator within an acrylic sphere less than 10cm in diameter. The recoil nuclei from a ^{252}Cf fission excite the scintillator, and the resulting light may be used to provide a fission event trigger. If the light is allowed to escape the acrylic sphere, then further ^{252}Cf fission events may mimic the neutron capture signal. This undesirable feature can be investigated using SNOMAN to model the ^{252}Cf source.

Scenario	Mean Time to Capture
D_2O	31.6ms
D_2O+1 tonne $MgCl_2$	7.0ms
D_2O+2 tonnes $MgCl_2$	4.0ms
D_2O+3 tonnes $MgCl_2$	2.8ms
D_2O+4 tonnes $MgCl_2$	2.2ms
D_2O+300kg $LiNO_3$	1.6ms
D_2O+ NCDs	15.4ms

Table 9.8: The mean time to capture for NC neutrons in the SNO detector. No error is shown since the time to capture is strongly position dependent. For comparison, the mean time to thermalisation is 125ns.

9.5 Analysis of the NC/CC Ratio As A Function of Salt Concentration

9.5.1 Introduction

One of the main goals of the SNO experiment is to determine the ratio of the flux of all neutrinos through the SNO detector to the flux of electron neutrinos through it. This requires the measurement of the neutral current (NC) and charged current (CC) rates. The NC and CC rates in SNO can be extracted using a simple analysis of the SNO data. It is the aim of this section to show the effect of the salt concentration and backgrounds upon the significance of such an analysis, and hence to recommend a salt concentration for use in SNO.

Five salt concentrations were used in the analysis. They were 0%, 0.1%, 0.2%, 0.3%, and 0.4%. The absolute maximum salt concentration that could be SNO is set by the limits on the D_2O desalination process; there are two 60 tonne tanks and the maximum concentration of the brine solution that can be achieved is 5% and so the maximum concentration of $MgCl_2O$ in the SNO D_2O is 0.6%. However, it has been stated [49] that 0.4% is the maximum concentration that could easily be achieved and that the lower the salt concentration the easier the desalination process will be. The concentrations that were investigated were restricted to the range $0 \rightarrow 0.4\%$ for this reason. The number of salt concentrations at which data was obtained was limited by the computer time available.

To compare the analysis of data obtained at one salt concentration to the analysis of data obtained at another, a measure of significance must be defined. Unfortunately the flux ratio F_{ν_x}/F_{ν_e}, which is 1 in the standard model of particle physics, is not directly determined in SNO. However, the NC and CC rates are related to the flavour and energy dependent neutrino fluxes through the detector;

$$\mathrm{NC} = \sum_{x=e,\mu,\tau} \int F_{\nu_x}(E_{\nu_x})\sigma(E_{\nu_x})\,G\,dE_{\nu_x} \text{ , and ,} \tag{9.4}$$

$$\mathrm{CC} = \int F_{\nu_e}(E_{\nu_e})\sigma(E_{\nu_e})H(E_{\nu_e})dE_{\nu_e} \text{ ,} \tag{9.5}$$

$$\tag{9.6}$$

where NC is the neutral current event rate in SNO, CC is the charged current event rate, and e, μ, and τ represent the three neutrino flavours, F is a neutrino flux, E is a neutrino energy, σ is a neutrino interaction cross section in the SNO detector, G is the probability of detecting a neutral current event (which is independent of neutrino energy), and H is the probability of detecting a charged current event. The NC and CC rates in the SNO detector have been determined for the SSM and best fit MSW scenario using SNOMAN. Define R_{model} to be the ratio of the SSM-normalised NC and CC rates and the rate for a model scenario in the SNO detector;

$$R_{\mathrm{model}} = \frac{\mathrm{NC_{model}}/\mathrm{NC_{SSM}}}{\mathrm{CC_{model}}/\mathrm{CC_{SSM}}} \,. \tag{9.7}$$

Clearly if the SSM is taken as the model, $R_{\mathrm{SSM}} = 1$. However, $R_{\mathrm{MSW}} > 1$, due to the deficit of electron-neutrino CC events in the MSW model when it is compared to the SSM case. If R can be accurately determined to be greater than 1, neutrino oscillations will have been observed in SNO. The significance

of the difference between R_{MSW} and 1 depends upon the accuracy with which the quantities NC and CC can be determined from SNO data. The significance of an analysis is defined to be;

$$S = \frac{R_{\mathrm{MSW}} - 1}{\sigma(R_{\mathrm{MSW}})} , \tag{9.8}$$

and is it intended to be a crude indicator of the statistical significance of a value for R different from 1.

9.5.2 The Analysis

The simplest analysis that could be used in SNO to obtain the NC and CC rates is a four parameter fit of signal and background distributions in four dimensions to data obtained directly from SNO. The number of parameters required is small because a 60 NHIT threshold will be used in the analysis. Such a high threshold means that only four types of event are present in the data. These are internal neutron events (IN), CC events, electron scattering events (ES) and external neutron events (EN). A 60 NHIT threshold is also the worst case scenario expected in SNO. Note that the results of Section 9.3 that all neutron events (with certain caveats) can either be classed as arising from a distribution like NC neutrons in SNO (internal neutrons) or like ^{208}Tl in the acrylic vessel (external neutrons) have been taken advantage of. All neutrino events have been simulated under the assumption that the MSW distortion to the ν_x energy spectrum will be small above 60 NHITs, and hence that neutrino oscillations cannot be detected by looking for the distortions. This is not an unlikely circumstance; most of the spectral distortions occur at low energies (below 60 NHITs).

Both neutral current events and ^{208}Tl and ^{214}Bi events in the D_2O contribute to the internal neutron distributions. It will be assumed that there is no way of determining the contribution of the D_2O backgrounds to the internal neutron rate in the SNO detector by data analysis. This is not true; Chen [56] [57] [58] has shown that it is possible to estimate the number of ^{208}Tl and ^{214}Bi events in the SNO detector at the 10% level using a pattern recognition algorithm, and the steeply rising number of background events at low NHIT is also a function of the concentrations of these two nuclei in the heavy water, but neither of these techniques has been verified to work and be robust against all systematics at this stage. Hence, for the purpose of this analysis, it will be assumed that the concentration of the contaminating ^{208}Tl and ^{214}Bi nuclei can only be determined by chemical assay with an accuracy at the 10% level.

The fit is four dimensional, following Wark [143]. The four dimensions used are r_{fitted}, NHITs, β_1, and $\cos\theta_{\mathrm{sun}}$. With the exception of NHITs, each of these values is obtained by fitting an event with the time fitter (r_{fitted}, $\cos\theta_{\mathrm{sun}}$) and the grid fitter/event classifier (β_1). The β_1 parameter is equal to the mean value of $\cos\theta_{ij}$ where θ_{ij} is the angle between the ith and the jth PMT hits. β_1 is a measure of the isotropy of an event (^{35}Cl(n,γ)^{37}Cl events are more isotropic than CC and ES events).

The analysis will be a standard minimisation of χ^2;

$$\chi^2 = \sum_{i=1}^{4}\sum_{j=1}^{100} \frac{\left(\sum_{k=1}^{4} a_k D_{ijk} - Y_{ij}\right)^2}{\left(\sum_{k=1}^{4} a_k^2 \sigma^2(D_{ijk}) + \sigma^2(Y_{ij})\right)} , \tag{9.9}$$

where the sum over i is a sum over 4 dimensions, the sum over j is a sum over the number of bins (always 100), and the sum over k is a sum over the 4 parameters to be fitted (the a_k). D_{ijk} is the jth bin of the kth distribution in the ith dimension (D_{ijk} might represent the jth bin of the electron scattering distribution in r, for example). D_{ijk} is normalised such that $\sum_{j=1}^{100} D_{ijk} = 1$. Poisson statistics have been assumed for the D_{ijk} before normalisation. The distribution representing 1 year of data in the SNO detector is Y_{ij}, and it formed from the distribution E_{ijk} as follows;

$$Y_{ij} = \sum_{k=1}^{4} n_k E_{ijk} \tag{9.10}$$

It is the aim of the analysis to obtain the n_k. The E_{ijk} are obtained in the same way but separately from the D_{ijk}. The fits were carried out using the Levenberg-Marquardt algorithm for finding non-linear least squares from [80]. The algorithm needed to be modified to evaluate χ^2 according to Equation 9.9.

The n_k were determined from Tables 2.1, 9.3, 9.4, 9.5, and 9.6, except that at the time of the analysis, the AV ^{208}Tl rate of Table 9.3 was believed to be a factor of 4 higher than that listed. Several analyses were completed in which the internal and external background rates (the sum of all the photodisintegration backgrounds internal to the D_2O and external to the D_2O respectively) were varied. Low and high rates differ from the standard rate by a factor of $\sqrt{10}$. The number of events in each event category that

Category	Event	Salt Concentration (%)				
		0.0	0.1	0.2	0.3	0.4
Signal	CC	3397	3397	3397	3397	3397
	ES	535	535	535	535	535
	NC	474	2218	2413	2521	2578
Background (n's)	D_2O	57	265	288	301	308
	AV	17	224	252	294	319
	H_2O	1	8	9	11	12

Category	Regime	Salt Concentration (%)				
		0.0	0.1	0.2	0.3	0.4
Internal neutrons	Low	492	2302	2504	2616	2675
	Std.	531	2483	2701	2822	2886
	High	654	3056	3324	3473	3552
External neutrons	Low	7	73	83	96	105
	Std.	18	232	261	305	331
	High	57	734	825	964	1047

Table 9.9: The number of events expected in 1 year of SNO data taking, as a function of salt concentration. Best fit MSW effect assumed. See text for details.

contributed to the total distribution is given in Table 9.9. Table 9.9 is divided into two halves. The first half lists the number of signal and background events expected in SNO at ≥ 60 NHITs and $r_{\text{fitted}} \leq 700$. The second half of the table gives the number of internal neutron events and the number of external neutron events in three background regimes.

9.5.3 Obtaining the Data

The distributions required to evaluate Equation 9.9 were obtained by direct simulation of 1 year's worth of data taking in SNO using the SNOMAN program. SNOMAN was run once for each of the four event types (IN, EN, CC, and ES). The IN and CC events were distributed uniformly throughout the D_2O. The ES events were simulated uniformly in the D_2O and H_2O. The EN events were simulated uniformly throughout the acrylic vessel.

Each event in SNOMAN was fitted using the time fitter and the grid fitter/event classifier to obtain values for the four variables described in Section 9.5.2 (r_{fitted}, NHIT, β_1, and $\cos\theta_{\text{sun}}$). The data was subject to a cut; an event must produce ≥ 60 hits in the detector, and must be reconstructed by the time fitter inside a 7m radius of the centre of the acrylic vessel. The purpose of the 60 NHIT cut was to restrict the scope of the analysis carried out here to just four event types. The purpose of a 7m cut rather than a 6m cut was to allow events that occur inside the acrylic vessel but which reconstruct just outside it (due to a non-zero fitter resolution) to be included in the analysis.

Int.	Ext.	Salt Concentration (%)				
		0.0	0.1	0.2	0.3	0.4
Low	Low	3313 ± 48	3238 ± 68	3333 ± 69	3293 ± 69	3260 ± 71
	Std.	3319 ± 47	3196 ± 69	3354 ± 70	3289 ± 70	3258 ± 72
	High	3304 ± 48	3212 ± 71	3331 ± 72	3291 ± 73	3291 ± 75
Std.	Low	3314 ± 48	3243 ± 69	3311 ± 70	3288 ± 70	3268 ± 71
	Std.	3320 ± 47	3200 ± 70	3334 ± 71	3283 ± 71	3265 ± 72
	High	3304 ± 48	3215 ± 72	3312 ± 73	3288 ± 74	3297 ± 75
High	Low	3313 ± 48	3190 ± 71	3321 ± 72	3290 ± 73	3268 ± 74
	Std.	3319 ± 48	3175 ± 72	3344 ± 73	3284 ± 74	3265 ± 75
	High	3304 ± 49	3191 ± 74	3319 ± 75	3290 ± 76	3296 ± 78

Table 9.10: The CC rate reported by the χ^2 analysis (1 year of SNO data simulated).

Int.	Ext.	Salt Concentration (%)				
		0.0	0.1	0.2	0.3	0.4
Low	Low	509 ± 26	498 ± 30	523 ± 30	482 ± 30	473 ± 30
	Std.	509 ± 26	494 ± 30	526 ± 31	480 ± 30	483 ± 31
	High	510 ± 26	495 ± 31	510 ± 32	476 ± 32	459 ± 33
Std.	Low	508 ± 26	501 ± 30	519 ± 31	481 ± 30	472 ± 31
	Std.	508 ± 26	497 ± 30	523 ± 31	478 ± 31	482 ± 31
	High	510 ± 27	498 ± 31	507 ± 32	475 ± 32	460 ± 33
High	Low	511 ± 27	486 ± 31	524 ± 32	485 ± 31	470 ± 32
	Std.	511 ± 27	492 ± 31	527 ± 32	483 ± 32	481 ± 32
	High	512 ± 27	492 ± 32	512 ± 33	480 ± 33	459 ± 34

Table 9.11: The ES rate reported by the χ^2 analysis (1 year of SNO data simulated).

Int.	Ext.	Salt Concentration (%)				
		0.0	0.1	0.2	0.3	0.4
Low	Low	471 ± 32	2422 ± 81	2399 ± 84	2569 ± 86	2765 ± 88
	Std.	476 ± 32	2423 ± 82	2414 ± 85	2666 ± 86	2787 ± 90
	High	468 ± 32	2348 ± 89	2361 ± 90	2550 ± 94	2709 ± 98
Std.	Low	473 ± 33	2439 ± 86	2418 ± 90	2574 ± 92	2750 ± 94
	Std.	478 ± 33	2432 ± 87	2431 ± 91	2670 ± 91	2770 ± 96
	High	469 ± 33	2361 ± 94	2378 ± 95	2552 ± 99	2695 ± 103
High	Low.	471 ± 38	2393 ± 120	2359 ± 127	2592 ± 131	2767 ± 134
	Std.	476 ± 38	2438 ± 120	2370 ± 128	2689 ± 131	2787 ± 136
	High	467 ± 38	2357 ± 126	2328 ± 131	2572 ± 137	2714 ± 141

Table 9.12: The NC rate inferred from the χ^2 analysis (1 year of SNO data simulated). The NC rate is obtained by subtracting the internal background rate from the internal neutron rate reported by the χ^2 analysis. The internal photodisintegration background is assumed to be known at the 10% level by chemical assay.

9.5.4 Results

The results of the χ^2 analysis are displayed in Tables 9.10, 9.11, 9.12, 9.13, and 9.14. Figure 9.3 shows the individual CC, IN, ES, and EN contributions to 1 year of simulated SNO data (an 0.2% salt solution was simulated). The general results and trends in the fit are;

1. that the χ^2 per degree of freedom was always between 0.9 and 1.1; and,
2. that the number of CC and NC events are correctly reported to within 1σ, but that they are always low;
3. that the number of ES events is correctly reported to within 2σ, but that they are always low, especially at high salt concentrations; and,
4. that the number of EN events is very poorly estimated for low rates (< 100 events per year), but otherwise an acceptable estimate is made; and,
5. that the significance of the NC/CC ratio deduced from the analysis is always > 7; and,
6. that the significance of the NC/CC ratio rises steeply between 0 and 0.1% salt concentrations and slowly thereafter; and,
7. that the significance of the NC/CC ratio is a strong function of the quantity of background internal to the D_2O at salt concentrations of 0.1% and above; and,
8. that the significance of the NC/CC ratio is a weak function of the quantity of photodisintegration capable nuclei in the AV and H_2O.

Int.	Ext.	Salt Concentration (%)				
		0.0	0.1	0.2	0.3	0.4
Low	Low	7 ± 20	-52 ± 53	59 ± 57	105 ± 58	12 ± 56
	Std.	7 ± 17	153 ± 56	200 ± 55	216 ± 57	211 ± 57
	High	68 ± 24	707 ± 65	867 ± 65	1002 ± 67	1004 ± 66
Std.	Low	6 ± 20	-78 ± 53	68 ± 58	108 ± 59	21 ± 57
	Std.	6 ± 18	136 ± 57	209 ± 56	222 ± 58	222 ± 58
	High	68 ± 24	688 ± 66	875 ± 66	1004 ± 68	1012 ± 67
High	Low.	6 ± 20	42 ± 59	109 ± 60	78 ± 61	2 ± 59
	Std.	7 ± 18	162 ± 60	254 ± 58	193 ± 60	203 ± 61
	High	67 ± 24	723 ± 68	908 ± 68	973 ± 70	990 ± 69

Table 9.13: The EN rate reported by the χ^2 analysis (1 year of SNO data simulated).

Int.	Ext.	Salt Concentration (%)				
		0.0	0.1	0.2	0.3	0.4
Low	Low	8.9 ± 2.0	16.5 ± 1.7	15.0 ± 1.6	15.9 ± 1.6	16.8 ± 1.6
	Std.	9.0 ± 2.0	16.4 ± 1.7	15.0 ± 1.6	16.6 ± 1.6	16.7 ± 1.6
	High	8.6 ± 1.9	14.7 ± 1.6	13.8 ± 1.6	14.5 ± 1.6	15.0 ± 1.6
Std.	Low	8.7 ± 1.9	15.9 ± 1.7	14.4 ± 1.6	15.1 ± 1.6	15.9 ± 1.6
	Std.	8.9 ± 2.0	15.8 ± 1.7	14.4 ± 1.6	15.8 ± 1.6	15.8 ± 1.6
	High	8.5 ± 1.9	14.3 ± 1.6	13.4 ± 1.6	13.9 ± 1.6	14.3 ± 1.6
High	Low	7.6 ± 1.8	12.0 ± 1.6	10.5 ± 1.5	11.4 ± 1.5	12.1 ± 1.5
	Std.	7.7 ± 1.8	12.3 ± 1.6	10.5 ± 1.5	12.0 ± 1.5	12.1 ± 1.6
	High	7.4 ± 1.7	11.3 ± 1.6	10.0 ± 1.5	10.9 ± 1.5	11.2 ± 1.5

Table 9.14: The significance, S, as a function of the internal (Int.) and external (Ext.) backgrounds and the salt concentration. The error on the significance is purely statistical.

The general trend for underestimating the number of events in each distribution means that the number of events reported by the fit is smaller than the number that took place. Wark [143] carried out a similar fit which also underestimated the total number of hits (by 0.7%). The effect is believed to be the result of assuming Gaussian statistics in where Poisson statistics actually apply. A more advanced analysis will be required for the SNO data when it becomes available. The number of events reported here are too low at the 1.5% level. This will be ignored in the present discussion.

The simple analysis carried out here is successful because each of the four event types can be distinguished from the others in at least 1 of the four fitted dimensions. For example;

1. the CC events distribution can be distinguished from the IN distribution using the NHITs variable and/or the β_1 variable and/or the $\cos\theta_{\text{sun}}$ variable.

2. The forward peaked ES event distribution can be distinguished from the CC and (IN+EN) distributions using the $\cos\theta_{\text{sun}}$ variable.

3. The IN and EN distributions can only be told apart using the r_{fitted} variable. This partly explains the weakness of the χ^2 fit in estimating EN.

In fact, the distributions are sufficiently different that the fit can be successfully accomplished with any three of the 4 fit dimensions. Only the absence of the r_{fitted} distributions has significant effect on the outcome; in this case IN and EN cannot be distinguished in any way (they are covariant).

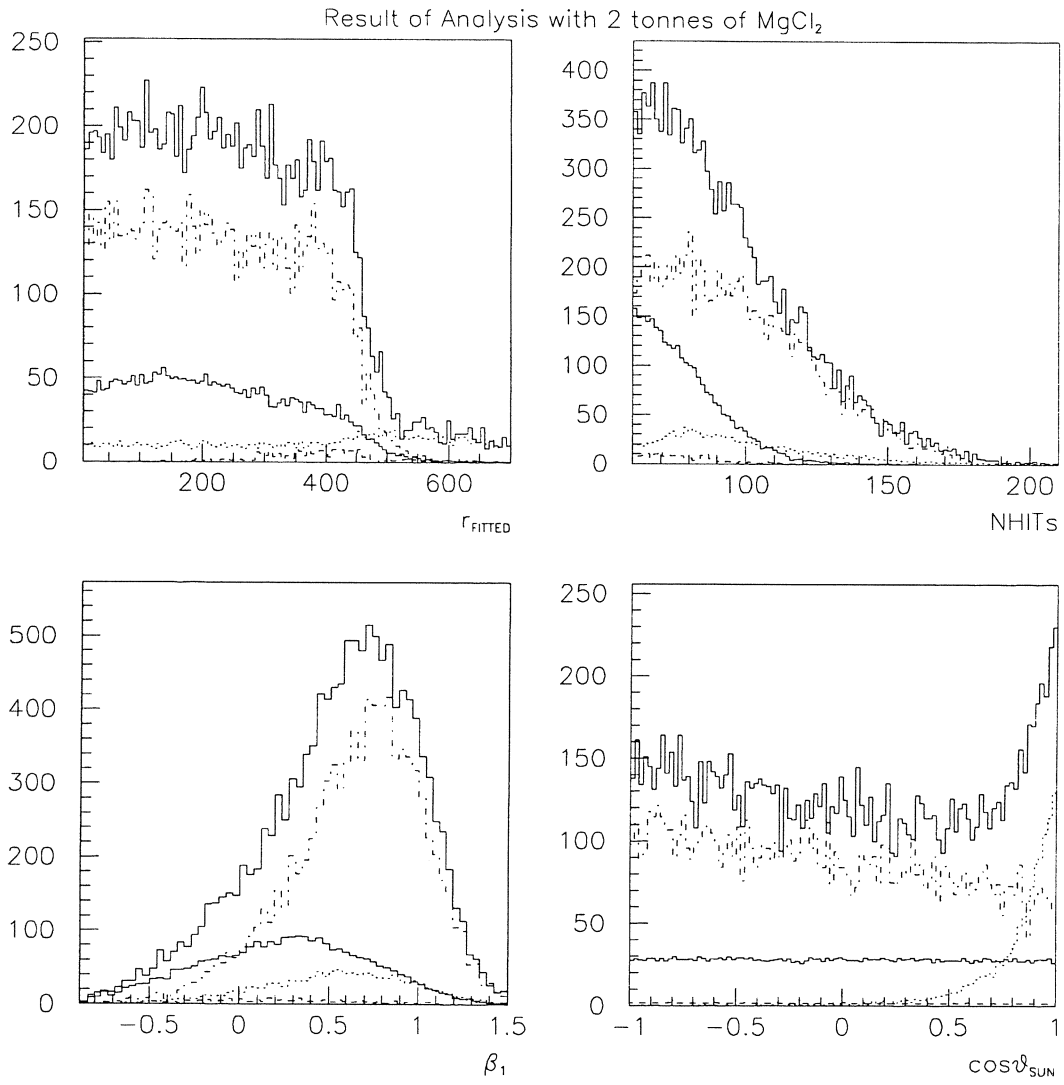

Figure 9.3: The result of the χ^2 fit for standard internal and external backgrounds and 2 tonnes of $MgCl_2$. The distributions are, in order of magnitude largest to smallest in the fitted r plot; 1 year of SNO data, CC events, IN events, ES events, and EN events.

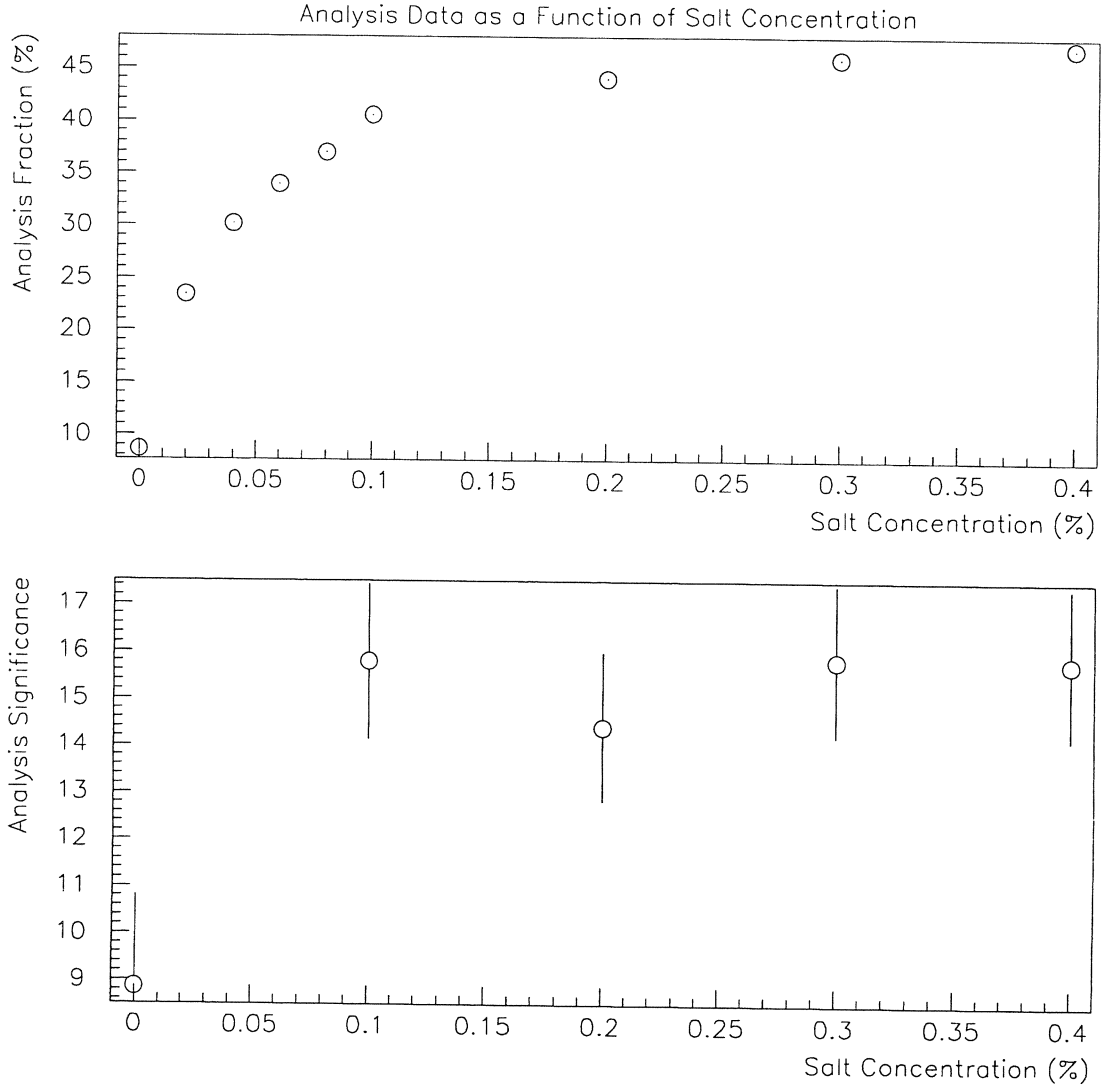

Figure 9.4: S is crudely proportional to the NC rate. The analysis fraction is the fraction of NC events in the SNO detector which can be detected above a 60 NHIT threshold and which reconstruct inside 7m. Below 0.1%, S is expected to fall.

The significance S varies rapidly with salt concentration in the region $0 \rightarrow 0.1\%$. The quantity varying most rapidly with the salt concentration in the region of $0 \rightarrow 0.1\%$ salt conc. is the NC rate. Making the approximation that the variation in the NC rate and in its error determine the variation in S, it is possible to show that $S \propto \sqrt{\mathrm{NC}/(1 + A.\mathrm{NC})}$, where $A \propto 5 \times 10^{-4}$. Therefore S can be expected to vary like NC. S and NC are plotted against salt concentration in Figure 9.4. The figure illustrates that where all quantities are slowly varying (above 0.1% salt concentration), S is also slowly varying. It is also clear that, although no analysis has been completed to determine S for salt concentrations between 0% and 0.1%, since S can crudely be expected to vary like the NC rate it is expected to fall immediately below 0.1%.

9.6 Discussion of Results

The χ^2 analysis that has been carried out implies that the SNO detector will be very sensitive to differences in the NC/CC ratio from 1. There are some caveats. The analysis has assumed that the event distributions in r_{fitted}, NHITs, β_1, and $\cos\theta_{\text{sun}}$ are known to a high precision. This requires that the electron and γ-ray calibrations be successful, and be modelled very well by SNOMAN. Wark [143] has investigated the sensitivity of the analysis presented here to a number of systematic errors (although only 2 salt concentrations were used, 0 and 2 tonnes). The most serious systematic error is a miscalibration of the energy response of the detector, where a shift of 2 PMT hits (which is much larger than expected in SNO) can almost eliminate NC/CC ratios different from 1. The most significant error from the point of view of neutron transport and the estimation of the NC rate in SNO is an error in the r_{fitted} distributions for IN and EN events used in the χ^2 analysis. This is because the two event types differ only in their r_{fitted} distributions. This error would be particularly significant when the number of EN events becomes large. The neutron calibration source (^{252}Cf) is particularly important in this regard, and it must be made to approach the acrylic vessel as closely as possible when calibrating in salted D_2O, since the IN neutron distribution is changing rapidly in this region.

There are several ways in which the presence of systematic errors in the χ^2 analysis might be detected. The most basic are;

1. to exclude each variable in turn from the χ^2 analysis. This cannot be used to eliminate the energy dependence of the analysis, since β_1 is not energy-independent (high energy electrons spend a larger fraction of their life travelling in a straight line than low energy electrons).

2. To compare the analysis of the whole detector with analyses involving the $0 \rightarrow 4$m region and the $5 \rightarrow 6$m region.

3. To compare analyses with different NHIT thresholds (generally higher).

All of these techniques will be used in the analysis of SNO data.

An analysis such as the one presented here will be used on SNO data. It will be more difficult to complete because of the difficulty in calibrating the events distributions that are required. This means that the significance levels found here cannot be expected of the SNO data, mainly due to systematic uncertainties that will be generally independent of salt concentration. However, the behaviour of the significance S as a function of salt concentration can be expected to be similar to that found here, and therefore it is possible to make a recommendation regarding the salt concentration. There is no benefit to the statistical significance of a χ^2 fit when salt concentrations are increased above 0.1%. Below 0.1%, the significance is expected to fall continuously until 0% salt concentration is reached. At 0% the significance is sufficient in the absence of large systematic errors to indicate an NC/CC ratio different from 1, but this concentration cannot be recommended because β_1 can no longer be used to distinguish IN and CC events. A salt concentration of 0.1% is recommended by this analysis for use in SNO, although if the lookback analysis is to be used, higher salt concentrations may be preferable.

9.7 Conclusion of Thesis

In this thesis, work done by the author on the SNO experiment has been presented. Most of the work has revolved the incorporation of neutron transport into the SNO Monte Carlo, SNOMAN, with some other work on verification and component testing.

The measurements of the angular performance of the SNO PMT and concentrator were used to verify Lay's Monte Carlo model [63] of the photomultipliers. Lay's model agrees well with the data at the 2% level. The agreement between the experimental data and Lay's model of the bin experiment gives some confidence that the behaviour of the PMTs will be well modelled in the SNO Monte Carlo. These results were first presented in a paper by Lay and Lyon [96].

The photodisintegration cross section was fitted to a simple theory (near threshold) and to data ($\rightarrow$ 20MeV) with errors of the order of 1% for γ-ray energies below 18MeV. The required change to the γ-ray interaction cross section in SNOMAN can be made without modifying the EGS4 code which calculates that cross section, and without introducing any approximations.

The n-transport requirements of any model of the SNO detector have been investigated. The dominance of low energy NC interactions and light nuclei in SNO mean that thermal transport must be modelled accurately in SNOMAN. The most significant nuclei are the H, D, and O nuclei which all contribute to scattering at thermal energies, and the ^{6}Li, ^{35}Cl and ^{3}He nuclei which dominate capture whenever they are present. The ^{13}C and ^{18}O nuclei in SNO can be neglected as can the ^{17}O nucleus provided the ^{17}O(n,α)^{14}C reaction is explicitly catered for. The effects on n-transport of the isotopic exchange of hydrogen with deuterium in the SNO heavy water were shown to be negligible.

MCNP has been found to be accurate at the 3% level [104] in circumstances similar to those found in the SNO experiment and was selected for use in SNOMAN. Because MCNP and SNOMAN are very different programs, MCNP was rewritten for use in SNOMAN. The SNOMAN n-transport code was then shown to reproduce the results of MCNP. In addition the SNOMAN program has also been shown to reproduce representative cross sections at thermal energies, and to match the diffusion equation closely in the limit $\Sigma \gg \Sigma_a$. The n-transport code will be used extensively in the analysis of SNO data.

The photodisintegration code written for SNOMAN by this author was used to determine the probabilities that ^{214}Bi and ^{208}Tl decays in the D_2O, AV, and H_2O result in the photodisintegration of a deuteron, and hence to estimate the number of photodisintegration events that are expected in the SNO detector. This is vitally important because these events mimic the neutral current signal in SNO.

SNOMAN was used to determine the r_{fitted}, NHITs, β_1, and $\cos\theta_{\text{sun}}$ distributions for neutrons in SNO for 5 salt concentrations from 0 $\rightarrow$ 0.4%. These were used with the charged current and elastic scattering distributions to construct the distributions expected from 1 years data taking in SNO, assuming MSW event rates. A simple χ^2 analysis was carried out, and the significance of the analysis was found to fall below and be constant above salt concentrations of 0.1%. A minimum salt concentration of 0.1% should be used in the SNO detector.

In addition to the work on SNOMAN, the author has also designed a test tank facility in collaboration with N. Jelley. The facility will be used to monitor detector component corrosion in ultra pure light water. The purpose of the test tanks is to mimic water purity, temperature, and flow conditions in the PSUP region of the SNO detector as closely as practicable in order to allow the testing of components similar to those in place in the SNO detector. The purity and flow conditions will be matched very closely. The temperature in the test tanks will be approximately 4°C higher than those in the SNO cavity.

Appendix A

The Uranium and Thorium Decay Chains

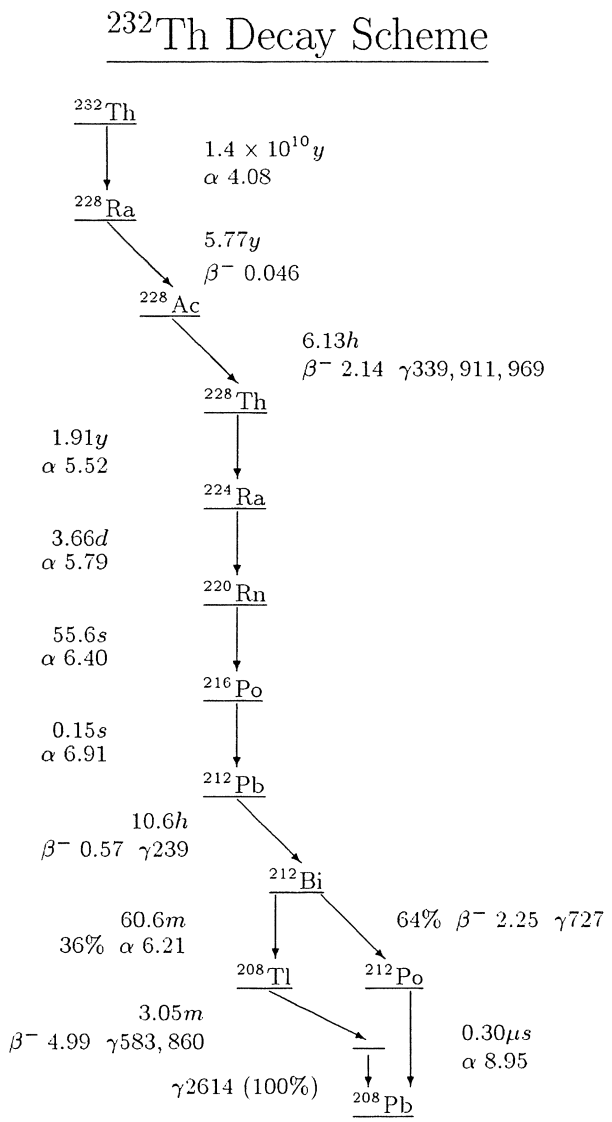

Figure A.1: The Thorium decay scheme [145]. Half lives and Q-values (in MeV) of α and β^- decays and energies (in keV) of important γ radiations are given.

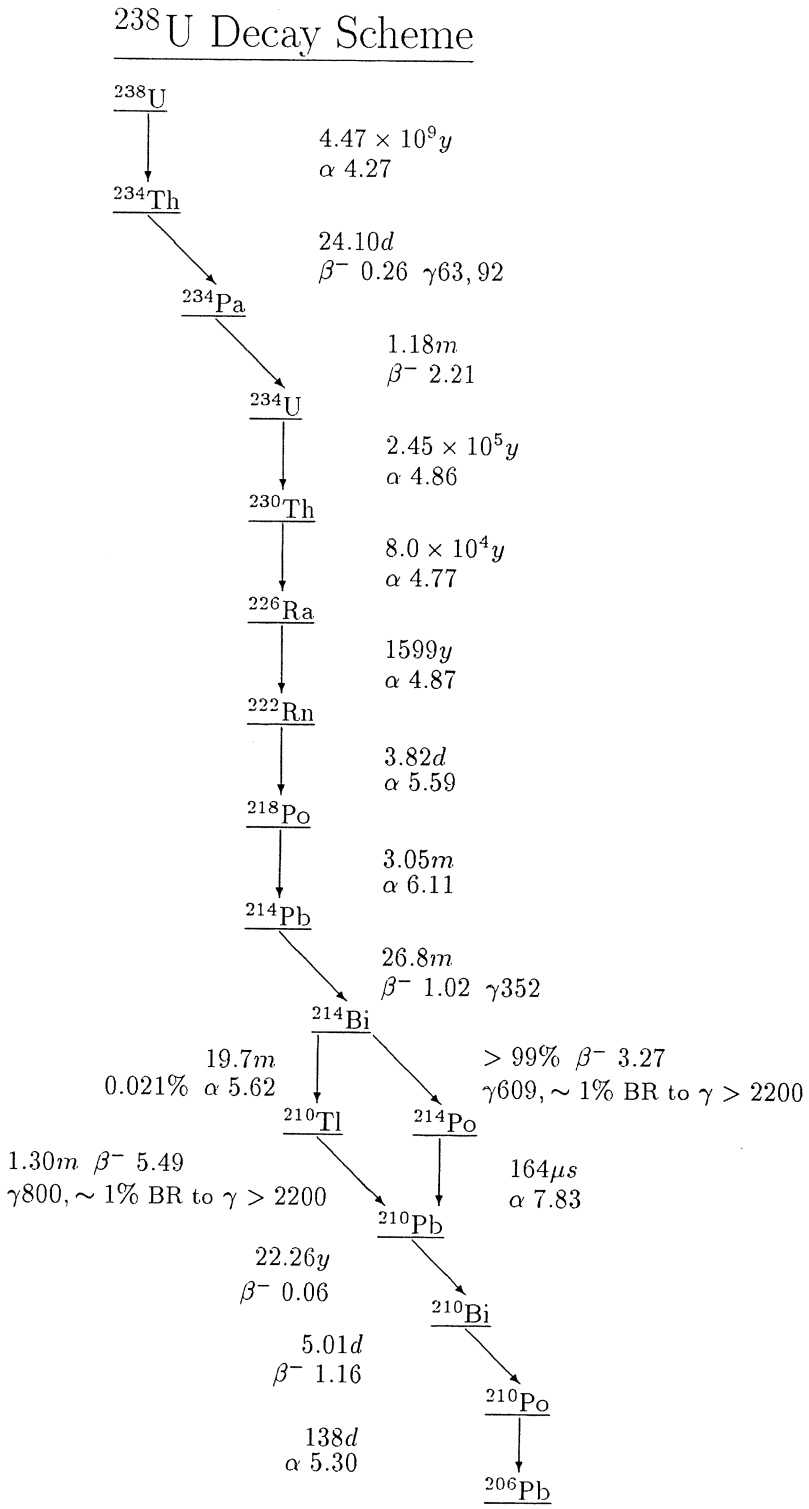

Figure A.2: The Uranium decay chain [145]. Half lives and Q-values (in MeV) of α and β^- decays and energies (in keV) of important γ radiations are given.

Appendix B

Heat Transfer in Multi-Layered Cylindrical Systems Undergoing Cooling by Free Convection

B.1 Introduction

The pipe and test tanks of Chapter 4 are subject to heating by their environment. This appendix will determine the temperature change in the water in the pipe and in the test tanks which occurs as a result of the heating.

In Section B.2 empirical relations and data are presented which describe heat transfer by free convection from the surface of the pipe and the surfaces of the test tanks. Empirical relations and data will also be presented for the heat transfered to the pipe by forced convection from the water flowing through it. Sections B.3 and B.4 present the calculations of the temperature change in the pipe and the mean temperature in the tanks.

B.2 Heat Transfer by Free and Forced Convection

B.2.1 Heat Transfer by Free Convection

In general, it is not possible to solve analytically for the heat transferred from a surface by free convection in a physical system, and empirical relations are used instead. This section aims to introduce the dimensionless numbers that characterise fluid properties in free convection and their relationship to the film coefficient (also known as the heat transfer coefficient). These relations are used later in this appendix to determine the heat lost from the test tanks and the pipe bringing water to them.

Several dimensionless numbers are useful in empirical free-convection heat flow calculations. The first, the Grassof number, represents the ratio of buoyancy forces to viscous forces in free flow convection. It is defined as;

$$\mathrm{Gr} = \frac{g\beta(T_w - T_\infty)x^3}{\nu^2}\ , \tag{B.1}$$

where g is the acceleration due to gravity, β is the convective fluid's volume coefficient of expansion, and ν is its kinematic viscosity. T_w is the temperature of the surface that is being heated (cooled) by free convection, whilst T_∞ is the bulk temperature of the convective fluid. x is the magnitude of the characteristic dimension of the convective surface. For pipes in air, $x = d$, where d is the outer diameter of the pipe.

The second dimensionless number, the Prandtl number, is defined as $\mathrm{Pr} = \nu/\alpha$, and it is the ratio of the thicknesses of the hydrodynamic and thermal boundary layers. Here $\alpha = k/\rho c$ is the thermal diffusivity of the convective fluid, k is its thermal conductivity, ρ is its density and c its specific heat capacity.

The third dimensionless number is the Nusselt number. Empirically, the Grassof and Prandtl numbers can be related to the average value of the Nusselt number in a variety of circumstances through the equation [109] (overleaf);

$$\overline{\mathrm{Nu}}_f = C(\mathrm{Gr}_f \mathrm{Pr}_f)^m \ , \tag{B.2}$$

where Nu, Gr, Pr, are the Nusselt, Grassof, and Prandtl numbers, respectively. The subscript f indicates that the dimensionless numbers are evaluated at the film temperature which is defined as $T_f = (T_w + T_\infty)/2$. Empirical data on C and m is available for a range of geometries and Rayleigh numbers (Ra = GrPr).

The heat transfer q per unit area through a surface exposed to a convective fluid is related to the film coefficient f by [111][109];

$$q = f(T_w - T_\infty) \ , \tag{B.3}$$

where the definitions of T_w and T_∞ are unchanged. The film coefficient is just the heat transfered per unit area per unit temperature difference. The average value of the film coefficient is directly related to the average value of the Nusselt number, $\overline{f}x/k = \overline{\mathrm{Nu}}_x$, and therefore it is empirically related to the Grassof/Prandtl numbers;

$$\overline{f} = \frac{k}{x} C(\mathrm{Gr}_f \mathrm{Pr}_f)^m \ . \tag{B.4}$$

The free convection film coefficient is temperature dependent, that dependence residing in the Grassof number. The empirical relation of Equation B.4 can now be used to determine the heat transfer coefficient (film coefficient) f from the Grassof and Prandtl numbers, provided C and m are known. Fortunately, many experiments in free convection have been done which report values of C and m. These have been tabulated for a number of surfaces of different geometry in both vertical and horizontal orientations by Holman [109].

The free convection Grassof and Prandtl numbers for the pipe of Chapter 4 vary with the thickness of the insulation that is envisaged. For a pipe in air at approximately 15°C whose outer diameter varies between 6.7cm and 19.9cm, their product (the Rayleigh number, Ra) always lies in the range $10^4 \rightarrow 10^7$. In this range Holman [109] recommends values for C and m for a horizontal pipe as follows; $C = 0.48$ and $m = 1/4$.

Holman [109] states that a vertical cylinder such as that represented by the side of the test tanks may be treated as a vertical flat plate for the purposes of free convection when the ratio of its diameter to its height satisfies the condition;

$$\frac{D}{L} \geq \frac{35}{\mathrm{Gr}_L^{1/4}} \ , \tag{B.5}$$

where D is the diameter of the cylinder, L is the height of the cylinder, and Gr_L is the Grassof number formed with the height of the cylinder as the characteristic dimension. For the cylinder of Chapter 4,

$$\frac{D}{L} = 3.4 \ , \tag{B.6}$$

$$\frac{35}{\mathrm{Gr}_L^{1/4}} = 0.2 \ , \tag{B.7}$$

and so the inequality of Equation B.5 is satisfied, and hence the vertical cylinder may be treated as a vertical flat plate.

The free convection Rayleigh number for the cylinder of Chapter 4 lies in the range $10^4 \rightarrow 10^9$. In this range Holman [109] recommends values for C and m for a vertical flat plate as follows; $C = 0.59$ and $m = 1/4$. The Rayleigh number for the upper surface of the cylinder, a circular horizontal plate, is in the range $10^5 \rightarrow 10^{11}$. In this range Holman [109] recommends values for C and m for the upper surface of a cooled horizontal plate of $C = 0.27$ and $m = 1/4$.

C and m have now been determined for all the surfaces in the test tanks and the pipe bringing water to them which are exposed to the free motion of air, and hence heated by free convection. The dependence of the free convection film coefficients on temperature is slight; they vary only slowly with changes in T. The next section will move on to the forced convection that takes place in the water pipe leading to the test tanks.

B.2.2 Heat Transfer by Forced Convection

If cold water is forced into a warm pipe heating will occur. The physics in this section applies to the long horizontal pipe of Chapter 4 that carries water to the test tanks. Forced convection in conditions of laminar flow (see Chapter 4) is dealt with by Kay and Crawford [110]. They state that in the case of laminar fluid flow in a smooth circular tube with fully developed velocity and temperature profiles (away from the mouth of the tube) and an exponentially varying heat flux (see later in this appendix), there is an indirect empirical relationship between the Nusselt number and that flux. For a heat flux q (the heat transfer per unit are per unit time) of the form;

$$q = q_0 \exp\left(-\frac{1}{2}nz\right) , \tag{B.8}$$

Kay and Crawford give a relationship due to Shah and London [111] who have found that n is related to the Nusselt number by the equation;

$$\begin{aligned} \mathrm{Nu}_d &= 4.3573 + 0.0424n - 2.8368 \times 10^{-4}n^2 \\ &\quad +3.6250 \times 10^{-6}n^3 - 7.6497 \times 10^{-8}n^4 \\ &\quad +9.1222 \times 10^{-10}n^5 - 3.8446 \times 10^{-12}n^6 , \end{aligned} \tag{B.9}$$

this latter equation being accurate to 3% in the range $-51.36 < n < 100$. Once the Nusselt number is known the film coefficient, which is a constant in the circumstances of forced convection presented here, can be obtained from it using the usual relation $f'd/k = \mathrm{Nu}_d$, where d is the pipe inner diameter, and f' and k are defined in Section B.2.1. The relationship between the heat transferred, q, and its coefficient f', is now;

$$q = f'(T_w - T_m) , \tag{B.10}$$

where T_m is defined as the mean (velocity-averaged) temperature of the fluid in the tube.

Unfortunately $q \propto f \propto \mathrm{Nu}_x = F(q)$, where $F(q)$ is only a convenient notational device for emphasising the difficulty in using the equations given in this section for a calculation from first principles. This is because of the difficulty in evaluating either q, f, or Nu_x. Later in this appendix, this problem is overcome by searching for a value for n that satisfies all the relationships given here.

B.3 Heat Loss in the 30m Horizontal Pipe

The temperature of the water delivered to the test tanks is dependent on the heat transferred to the water from the environment during its journey down the 30m pipe that delivers water to the test tanks. Throughout this discussion, the pipe shall be assumed to be everywhere horizontal: this is in fact not the case, but the vertical sections of pipe are short compared with the length of the remainder, and therefore they will be neglected in this treatment. Note that a temperature rise in the pipe of less than 1°C will be considered low enough for the operation of the test tanks. This is not only because the temperature rise in the test tanks is larger than 1°C, but also because the calculations made here are idealised, and hence cannot be expected to yield results that are applicable to the test tank facility to much better than 30%. Rather, these calculations have been made to show the feasibility of the operation of the test tanks.

In this section the heat transferred to the water from the environment will be calculated and the temperature rise inferred for a variety of water velocities and insulation thicknesses. The heat transferred to a horizontal pipe varies depending on whether the fluid flow is laminar or turbulent. The Reynolds number associated with the slow flow of the water through the pipe that supplies the test tank facility is;

$$Re = \frac{\rho v d}{\mu} \tag{B.11}$$

$$= 309.1 \tag{B.12}$$

where ρ is the density of the fluid (1g cm^{-1}), v is the mean velocity of the water in the pipe (1.59cm s^{-1}), d is the diameter of the pipe (2.54cm), and μ is the dynamic viscosity of water at 10 °C (which is 1.307×10^{-3}Pa s). The water velocity is that required to supply the 3 test tanks with enough water in order to simulate the flow rate in the PSUP region of the SNO detector. Munson, Young and Okiishi [107] state that fluid flow is expected to be laminar in a pipe whenever $Re \leq 2100$, and hence the water

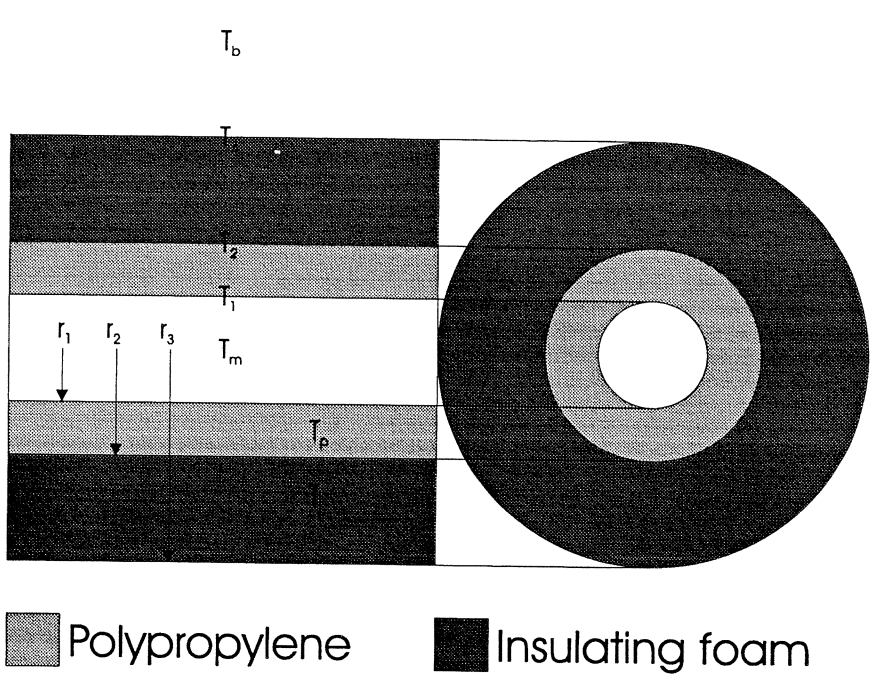

Figure B.1: A schematic of the pipe. r_1 is the pipe's inner radius, r_2 its outer radius. r_3 is the outer radius of the insulation material. T_m is the velocity-averaged mean temperature of the water. T_1 is the temperature of the water-polypropylene boundary, T_2 is that of the polypropylene-insulator boundary. T_3 is that of the insulator-air boundary, and T_b is the bulk temperature of the air.

in the pipes will be in the laminar flow regime for water velocities of up to approximately 7 times the nominal value.

Heat transfer from the air to the pipe is due to the free convection of air around the pipe. 'Free convection' here refers to the buoyant motion of the air due to local variations in the density that result from heating. This heating is by conduction from neighbouring volumes of air or the surface of the pipe. Heat transfer in the pipe is by conduction through the polypropylene and the insulation. This conduction carries heat radially inward to the water and along the pipe. Heat enters the water in the pipe from the plastic by forced convection. Forced convection is the process by which heat traverses a fluid whose velocity profile is, to a good approximation, fixed. Here it is assumed that the velocity profile of the water in the pipe is unaffected by the temperature profile that develops as the water is heated. Once again, heat is transferred locally by conduction. Convection cannot occur along the pipe, and will not occur in the transverse (vertical) direction because of the small dimensions of the pipe (its inner diameter will be 1.58cm).

B.3.1 An Equation for the Local Heat Loss in a Horizontal Pipe

It is the goal of this section to present a physical model of the heat lost from an insulated horizontal pipe. Good thermal contact between the pipe and the insulation is assumed throughout. The relationships given in Sections B.2.1 and B.2.2 between the free and forced heat transfer coefficients and the heat transferred will be used to provide boundary equations. The system is illustrated in Figure B.1. The heat equation [109] is;

$$mc\frac{\partial T}{\partial t} = \nabla.(k\nabla T) + Q \ . \tag{B.13}$$

m is the mass of the element, c is its specific heat, T is its temperature, k is its thermal conductivity, and Q is the heat generated within the element. This treatment will be concerned solely with the radial heat transfer through the pipe materials, neglecting the comparatively slow longitudinal heat transfer, and

hence the problem will reduce to one of a one-dimensional nature. In the steady state, for a cylindrically symmetric system, and for $Q = 0$, $\partial^2 T/\partial z^2 = 0$, Equation B.13, in cylindrical polar coordinates, is;

$$\frac{1}{r}\frac{\partial}{\partial r} r \frac{\partial T}{\partial r} = 0 \tag{B.14}$$

The solution to this equation takes the form $T(r) = A + B\ln(r)$ where A and B are constants whose values are set using the boundary conditions. The physical system consists of two concentric cylinders in contact with one another. The inner cylinder is made of polypropylene (plastic), the outer cylinder is an insulating material. The labels w, p, i, and a refer to the water, plastic, insulating material and the air. The inner, contact, and outer radii of the cylinders are r_1, r_2, and r_3, respectively. The boundary conditions represent the equality of temperature at a boundary, and are $T_p(r_1) = T_1$, $T_p(r_2) = T_i(r_2) = T_2$, and $T_i(r_3) = T_3$. The boundary conditions are also definitions for the quantities T_1, T_2, and T_3. These boundary conditions yield expressions for the solutions to Equation B.14 in the polypropylene and the insulating material;

$$T_p(r) = T_1 + \frac{T_2 - T_1}{\ln(r_2/r_1)} \ln(r/r_1) \ , \tag{B.15}$$

$$T_i(r) = T_2 + \frac{T_3 - T_2}{\ln(r_3/r_2)} \ln(r/r_2) \ . \tag{B.16}$$

The thermal conductivities of polypropylene and the insulating foam are k_p and k_i. The areas A_2 and A_3 are defined as $A_2 = 2\pi r_2$, and $A_3 = 2\pi r_3$, and are perimeters, or areas per unit cylinder length. Using these definitions, the remaining boundary conditions, which represent equality of heat flow, or conservation of energy flux through a boundary, can be stated;

$$f'(T_m - T_1) = -k_p \left.\frac{\partial T_p}{\partial r}\right|_{r_1} \ , \tag{B.17}$$

$$-k_p \left.\frac{\partial T_p}{\partial r}\right|_{r_2} = -k_i \left.\frac{\partial T_i}{\partial r}\right|_{r_2} \ , \tag{B.18}$$

$$-k_i \left.\frac{\partial T_i}{\partial r}\right|_{r_3} = f(T_3 - T_\infty) \ . \tag{B.19}$$

where $q = -kA\nabla T$ follows from Fourier's law of heat conduction [111]. In the first and last equations, Equations B.17 and B.19, empirical relations for the heat flux in the circumstances of forced and free convection have been utilised. These relations are discussed in Sections B.2.2 and B.2.1, where f and f', the free and forced heat transfer coefficients, were introduced. T_m is the velocity-averaged water temperature. T_∞ is the bulk temperature of the air around the pipe. k_p is the thermal conductivity of plastic, and k_i is that of the insulating foam.

From Equations B.16 to B.19 and their associated definitions, it follows that the heat lost per unit length of the pipe, q, is [112];

$$\frac{q}{2\pi} = \frac{t_m - t_\infty}{\frac{1}{r_1 f'} + \frac{\ln(r_2/r_1)}{k_p} + \frac{\ln(r_3/r_2)}{k_i} + \frac{1}{r_3 f}} \ . \tag{B.20}$$

Equation B.20 is the principal result of this section. It describes the heat lost radially from a section of the pipe of unit length provided T_m, f, and f' can be found. Note that T_∞ is a known boundary condition, and the other quantities are known material properties or dimensions. Note also that if the very slight hidden dependence of q on T which resides in f is ignored, then q is a linear function of T_m.

At and near the mouth of the 30m pipe of Chapter 4, the temperature of the water has not risen above that of the SNO cavity and therefore $T_m = 10°\mathrm{C}$. With this in mind, and the $f'(n) = \mathrm{Nu}_d(n)k/d$ dependence of the forced convection film coefficient $f'(n)$ made explicit, the heat transfer near the mouth of the pipe, q_0, is;

$$\frac{q_0}{2\pi} = \frac{t_m - t_\infty}{\frac{1}{r_1 f'(n)} + \frac{\ln(r_2/r_1)}{k_p} + \frac{\ln(r_3/r_2)}{k_i} + \frac{1}{r_3 f}} \ . \tag{B.21}$$

B.3.2 Heat Loss in a Pipe of 30m Length

This section will use the relations developed in the previous sections to determine the temperature change in the water flowing through the 30m pipe. The heat flux into the pipe is expected to vary exponentially with distance, as are all the temperatures in the pipe; this is because the change in temperature of an element of water flowing down the pipe is a linear function of the heat transfer per unit length, q, which is in turn a linear function of the temperatures. This latter fact is a consequence of the repeated application of boundary conditions to the fundamental heat transfer equations. The relationship between q and T_m (the velocity-averaged temperature of the fluid in the pipe) for the horizontal pipe in question is derived in in its entirety in B.20. It is approximately equivalent to $q \propto AT_m + B$. The exponential dependence of the water temperature and heat flux on distance is evident in

$$\frac{\Delta T_m}{\Delta z} \propto q \propto AT_m + B \ . \tag{B.22}$$

Using Equation B.8, the heat loss per unit area per unit time is defined to be $q = q_0 \exp(-\frac{1}{2}nz)$, where n has yet to be determined. The mean temperature change of the water in the pipe over a distance d due to the heat loss through the walls is then;

$$\delta T_m = \frac{-q(z)\delta z \delta t}{\pi r^2 \delta z \rho c} \ , \tag{B.23}$$

$$\delta T_m = \frac{-q(z)\delta z}{\pi r^2 \rho c v} \ , z = vt \ , \tag{B.24}$$

$$\int_{T_m(0)}^{T_m(d)} dT = \int_0^d \frac{-q(z)}{\pi r^2 \rho c v} dz \ , \tag{B.25}$$

$$T_m(d) - T_m(0) = \frac{-q_0}{\pi r^2 \rho c v} \int_0^d \exp(-nz/2) dz \ , \tag{B.26}$$

$$T_m(d) - T_m(0) = \frac{-2q_0}{n\pi r^2 \rho c v} (\exp(-nd/2) - 1) \ , \tag{B.27}$$

where v is the mean velocity of the water in the pipe. Using the fact that $T_m(z)$ varies exponentially in the manner of the heat flux, and applying the boundary conditions $T_m(0) = T_0$ and $T_m(\infty) = T_\infty$ leads to;

$$T_m(z) = T_\infty - (T_\infty - T_0) \exp(-\frac{1}{2}nz) \ . \tag{B.28}$$

Equations B.27 and B.28 can in their turn be used to find an equation for n;

$$n = \frac{2q_0}{(T_\infty - T_0)\pi r^2 \rho c v} \ . \tag{B.29}$$

Unfortunately, q_0 is itself dependent on n, as is shown in Equation B.21, and hence Equation B.29 must be solved numerically. A program has been written to search for a consistent value of n. The program repeatedly bisects ever smaller intervals whilst searching for a change in sign of the function

$$f(n) = n - \frac{2q_0}{(T_\infty - T_0)\pi r^2 \rho c v} \ . \tag{B.30}$$

The program halts when the width of the interval is smaller than 10^{-6}, which when considered as the sole error gives a negligible maximal error in $T_m(d)$ of;

$$\Delta T = \left[\frac{d}{2}(T_\infty - T_0)\exp(-nd/2)\right] \Delta n < 0.0005°\mathrm{K} \ . \tag{B.31}$$

Once an appropriate value for n has been found, the change in the velocity-averaged temperature can be found from Equation B.28. Table B.1 gives T_d as a function of v, the water velocity, and x, the insulating foam's thickness.

Water exits the SNO cavity at 10°C. Without any mechanism to actively cool the water, controlling the temperature at which it arrives at the test tank facility must be achieved by the use of insulation and increased water flow rates. Given the range of values presented in Table B.1, a 1°C rise in temperature is attainable with a flow velocity of $\sim$ 6cm s^{-1} and 0.5cm of foam insulation.

	0cm	0.5cm	×2	×3	×4	×5	×6	×7	×8
1.54cm s^{-1}	288.0	286.8	286.3	285.9	285.6	285.5	285.3	285.2	285.1
×2	285.7	285.1	284.7	284.5	284.4	284.3	284.2	284.1	284.1
×3	284.9	284.4	284.2	284.0	283.9	283.9	283.8	283.8	283.7
×4	284.4	284.1	283.9	283.8	283.7	283.7	283.6	283.6	283.6
×5	284.2	283.9	283.7	283.6	283.6	283.5	283.5	283.5	283.4
×6	284.0	283.7	283.6	283.5	283.5	283.4	283.4	283.4	283.4
×7	283.8	283.6	283.5	283.5	283.4	283.4	283.4	283.3	283.3
×8	283.7	283.5	283.5	283.4	283.4	283.3	283.3	283.3	283.3
×9	283.7	283.5	283.4	283.4	283.3	283.3	283.3	283.3	283.2
×10	283.6	283.4	283.4	283.3	283.3	283.3	283.2	283.2	283.2

Table B.1: $T_m(d)$ as a function of water velocity and the radial thickness of the insulation.

Throughout this evaluation, it has been assumed that the air flow around the pipe could be considered as entirely due to natural convection. The worst-case scenario, which is rapid turbulent motion of the air near the pipe, can be simulated by assuming that the surface of the pipe is at a constant temperature of 25°C. Even in this circumstance, the temperature rise can be limited to 1°C by using 1cm of insulation and flowing the water at $\sim$ 9cm s^{-1} (calculations not shown). This result shows that the heat transferred is minimally dependent on atmospheric conditions around the pipe, and indirectly justifies the neglect if the T dependence of the free convection film coefficient, f.

It has also been assumed that the pipe is far from other objects, where far in this context means a distance $\gg$ 1cm, the approximate thickness of the convective boundary layer around the pipe [109]. In reality, the pipe is supported next to a mine corridor wall, and it is likely to be near to other pipework. The effects of such crowding cannot be quantitatively anticipated here, but the large range of water flow velocities and foam thicknesses presented in the results of Table B.1 that lead to a water temperature rise in the pipe of less than 1°C imply that by adjusting the water flow velocity and insulation thickness, a temperature rise limited to a maximum of 1°C can be achieved.

This author conservatively recommends that 1cm of foam insulation is used, and the water velocity adjusted until the temperature rise in the pipe is less than 1°C. The velocity required is expected to be between 4 and 6 times the minimum required rate.

B.4 Heat Loss in the Test Tanks

In the preceding section, Section B.3, it has been shown that it is reasonable to expect a temperature rise in the pipework leading up to the tank of no more than 1°C (to 11°C). It is the aim of this section to determine the average temperature of the water in the test tanks. Once the water has entered the test tanks, its flow rate slows considerably, the average vertical water velocity in the tanks being 3.7×10^{-4}cm s^{-1} (or approximately 1.3cm hr^{-1}). The test tanks will be lagged with 5cm of Instapak-Floral foam insulation [108]. The flow rate of the water will be assumed to be negligible in the calculations that follow.

B.4.1 Heat Transfer Through the Sides of the Test Tanks

It is the goal of this section to present a physical model of the heat lost from the sides of the test tanks of Chapter 4. The system under consideration will be cylindrical and vertical in nature, and undergoing free convection at its outer surface. There is no forced convection, and it will be assumed that the inner surface of the cylinder is at the same temperature as the water it is in contact with, and that that temperature is representative of the bulk of the water inside a test tank. This is an approximation based upon the slow heating in the tanks. As a result of the change in boundary conditions at the inner surface of the cylinder, this problem is somewhat simpler than that considered in Section B.3.1; there is one fewer boundary conditions (Equation B.17 is no longer applicable), and one fewer variable to eliminate (T_1 is now a boundary value, and equal to T_w, the bulk water temperature). In all other respects, the physics is the same as before. The heat flux through a vertical cylinder (a test tank) per unit height, q, is [112];

$$\frac{q}{2\pi} = \frac{t_w - t_\infty}{\frac{\ln(r_2/r_1)}{k_p} + \frac{\ln(r_3/r_2)}{k_i} + \frac{1}{r_3 f}} , \tag{B.32}$$

where r_1 is now the inner radius of the test tanks, r_2 is the outer radius of those tanks and the inner radius of the insulation, and r_3 is the outer radius of the insulation on the test tanks. The thermal conductivities have the same definitions as they did in Section B.3.1. The film coefficient f now refers to the heat lost by free convection from the sides of the test tanks. The rate of heat loss from the top and bottom surfaces of the test tanks will be determined in the next section.

B.4.2 Heat Transfer Through The Top and the Bottom of the Test Tanks

This section is applicable to the heat conducted out of the lid and floor of the test tanks of Chapter 4. The floor of the tank is shielded by insulating material from the floor proper: a good thermal contact is assumed. The lid suffers heat loss by free convection. Once again it is assumed that the inner surface of the lid and floor of the test tanks is at the same temperature as the bulk of the water. The solution to the heat equation, Equation B.13, for a layered system of 2 regions with 3 parallel boundaries, representing an acrylic plate and a layer of insulation material, is;

$$T_p = T_1 + \frac{T_2 - T_1}{x_2 - x_1}(x - x_1) , \tag{B.33}$$

$$T_i = T_2 + \frac{T_3 - T_2}{x_3 - x_2}(x - x_2) , \tag{B.34}$$

where T_1 is the temperature of the polypropylene in contact with the water, T_2 is the temperature of the polypropylene in contact with the insulating foam, and T_3 is that of the insulating foam in contact with the floor. $x_2 - x_1$ is the thickness of the polypropylene, $x_3 - x_2$ is that of the insulating foam. In the steady state, the heat conducted through the foam must be the same as that conducted through the polypropylene (there are no heat sinks) and hence, from Fourier's law of heat conduction [111] and Equations B.33 and B.34;

$$q = -k_p \frac{T_2 - T_1}{x_2 - x_1} = -k_i \frac{T_3 - T_2}{x_3 - x_2} , \tag{B.35}$$

where k_p is the thermal conductivity of the polypropylene plastic, and k_i is that of the foam insulator. q is the heat conducted per unit area per unit time. Equations B.33, B.34, and B.35 are sufficient to find a solution for the floor of the tank provided it is assumed that the insulation around the tank is in good thermal contact with the ground; then the heat transferred per unit area per unit time is;

$$q = \frac{T_3 - T_1}{\frac{x_2 - x_1}{k_p} + \frac{x_3 - x_2}{k_i}} . \tag{B.36}$$

q is a linear function of $T_3 (= T_\infty)$ and $T_1 (= T_w)$.

The lid of the tank is insulated like the floor, but here heat transfer by free convection will occur. Equations B.33, B.34 and B.35 are still valid, but now T_3 is the temperature of the insulating foam in contact with the air, and T_∞ is the bulk air temperature. There is one further boundary condition involving a film coefficient;

$$q = -k_i \frac{T_3 - T_2}{x_3 - x_2} = -f(T_\infty - T_3) , \tag{B.37}$$

Using Equations B.33, B.34, B.35, and B.37, q, the heat transfer per unit time per unit area for the tank lid, can be found;

$$q = \frac{T_\infty - T_1}{\frac{x_2 - x_1}{k_p} + \frac{x_3 - x_2}{k_i} + \frac{1}{f}} . \tag{B.38}$$

B.4.3 The Average Temperature of the Water in the Test Tanks

If it is assumed that the temperature difference between the top and the bottom of a test tank is small, then there will be little convective heat transfer through the water, and conductive heat transfer will dominate. In addition, the water tank will be well described by a single temperature. In the steady state, the net heat flow into the tank must be balanced by the heat absorbed or released by any changes in temperature of the water therein;

$$Mc\frac{\partial T}{\partial t} = Q - mc(T - T_0) = 0 \ , \tag{B.39}$$

where T is the temperature of the water, M is the mass of the water in the test tank, c is the specific heat capacity of water, m is the mass of cold water flowing into the tank each second, $T_0 = 11°\mathrm{C}$ is the temperature of that water, and Q is the heat gained through the walls of the tank. Q is the sum of the heat transfers given in Equations B.32, B.36, and B.38, which give the heat lost through the sides and the bottom and top of the test tanks, respectively. Hence, from Equation B.39;

$$T = \frac{T_0 + AT_\infty + BT_\infty + CT_{\mathrm{floor}}}{1 + A + B + C} \ , \tag{B.40}$$

$$A = \frac{2\pi L}{mc\left(\frac{1}{fr_3} + \frac{\ln(r_3/r_2)}{k_i} + \frac{\ln(r_2/r_1)}{k_p}\right)} \ , \tag{B.41}$$

$$B = \frac{\pi r_2^2}{mc\left(\frac{1}{f'} + \frac{x_3 - x_2}{k_i} + \frac{x_2 - x_1}{k_p}\right)} \ , \tag{B.42}$$

$$C = \frac{\pi r_2^2}{mc\left(\frac{x_3 - x_2}{k_i} + \frac{x_2 - x_1}{k_p}\right)} \ . \tag{B.43}$$

In Equations B.40 $\rightarrow$ B.43, T_∞ is the bulk temperature of the air, and T_{floor} is the temperature of the insulator in contact with the floor in the test tank installation. f is the film coefficient for heat transfer through the insulator-air interface at the sides of the test tank, f' is that for heat transfer from the horizontal lid on the test tank. The remaining symbols are as defined earlier in this appendix.

Equation B.40 cannot be solved in a straightforward manner for the value of T because the film coefficient, f, is a slowly varying function of the temperature of the insulator-air boundary that in turn depends upon T at equilibrium. A computer program was written to find a consistent value for T. Consistent in this context means a value of T that, having been used to calculate f, is the the T of Equation B.40. A consistent value was found to be

$$T = 287°\mathrm{K} \ . \tag{B.44}$$

To observe how sensitive the quantity T is to the values calculated for the film coefficients, they were allowed to vary by a factor of 10. The results were;

$$\frac{T}{°\mathrm{K}} = 287^{+0.4}_{-1.7} \ . \tag{B.45}$$

This result is very encouraging, since it implies that significantly higher values for the heat transfer coefficients, f and f', do not induce a significant rise in the equilibrium temperature of the test tanks. It also implies that the temperature dependence of the film coefficients could have been neglected without introducing any significant error. This is consistent with the conclusions drawn in support of the results presented in Section B.3. Other sources of error in this calculation include:

1. poor thermal contact between the polypropylene and the insulator foam;
2. poor thermal contact between the insulator foam and the floor; and,
3. the floor temperature has been wrongly estimated.

Item (1) can be excluded because the insulator is foam based, and will actually be sprayed into a drum surrounding the polypropylene tanks. Item (2) cannot be excluded, but poor thermal contact makes heat transfer into the test tanks more difficult, and so the average temperature in the tanks would be expected to fall as a result. Item (3) also cannot be excluded, but the maximum likely temperature has been used throughout (25°C), and again this means that the final temperature of the test tank has probably been overestimated.

B.5 Physical Quantities

This section presents the values of the physical constants, the pipe, tank, and insulation dimensions, and the boundary conditions that have been used to obtain the results of Chapter 4 from the material presented in this appendix.

B.5.1 Free Convection

For air:

The acceleration due to gravity is 9.81m s^{-2}.
The volume coefficient of expansion is 3.67×10^{-3}
The thermal conductivity of air is 2.41×10^{-2}W m^{-1} K^{-1}.
The density of air is 1.255kg m^{-3}.
The heat capacity of air 1008J kg^{-1}.
The dynamic viscosity of air is 18.2×10^{-6}kg m^{-1} s^{-1}.
The kinematic viscosity of air is $1.45 \times 10^{-5}m^2$ s^{-1}.
The thermal diffusivity of air is $1.91 \times 10^{-5}m^2$ K^{-1} s^{-1}.

B.5.2 The Supply Pipe

For water:

The density of water is $\rho_w = 1$g cm^{-3}.
Its thermal conductivity is $k_w = 57.5$W cm^{-1} K^{-1}.
Its heat capacity is $c_w = 4.19$J g^{-1}.

For the insulated pipe:

The inner radius of the pipe is $r_1 = 1.29$cm.
The outer radius of the pipe is $r_2 = 3.36$cm.
The outer radius of the insulating foam is r_3, and may take values in the range $3.36 \rightarrow 8.44$cm.
The thermal conductivity of the acrylic is $k_p = 12$W cm^{-1} K^{-1}.
The thermal conductivity of the insulating material is $k_i = 4.3$W cm^{-1} K^{-1}.
$T_\infty = 25°$C is the temperature of the bulk of the air that cools the pipe through free convection.

B.5.3 The Test Tanks

The height of the test tank is 0.99m.
The vertical flow rate of the water in the tanks is 3.7×10^{-4}cm s^{-1}, arising from an inflow of water of 2.69cm^3 s^{-1}
The inner radius of the 0.72 tonne tank is $r_1 = 0.483$m.
The outer radius of the 0.72 tonne tank is $r_2 = 0.492$m.
The thickness of the foam used to insulate the tank is approximately 2 inches, making the outer radius of the insulating foam,r_3, 0.543m.

Appendix C

Probability Distributions and Sampling Methods: Step Lengths

C.1 Introduction

Section C.2 of this appendix demonstrates how the random numbers generated by a computer (an approximation to uniform deviates) can be used to sample from an exponential distribution. Section C.3 gives a derivation of the exponential distributions relevant to particle propagation. Section C.4 shows how essentially the same distributions can be derived for a particle with multiple interactions.

In Section C.5 a proof is presented showing that if two step lengths are independently sampled from exponential step length distributions, picking the interaction and distance associated with the shortest sampled value reproduces the distribution of step lengths expected if the interaction probabilities underlying the two step length distributions are used to sample from a single multiple interaction distribution. Section C.6 concludes this appendix.

C.2 The Transformation Method: Sampling from the Exponential Distribution

Suppose that uniform deviates in the range $(0, 1]$ can be generated:

$$P(x)dx = dx \;\; 0 < x \leq 1 \tag{C.1}$$

$$= 0 \;\; x \leq 0,\; x > 1\,. \tag{C.2}$$

This probability distribution is normalised to 1 at $x = 0$:

$$\int_0^1 dx\, P(x) = 1\,. \tag{C.3}$$

Now if y is some function of x, $y(x)$, then the probability of obtaining a particular value of y can be expressed as

$$|P(y)dy| = |P(x)dx| \tag{C.4}$$

$$P(y) = P(x)\left|\frac{dx}{dy}\right|\,. \tag{C.5}$$

Now consider the particular function $y(x) = -(1/\lambda)\ln(x)$. The probability distribution function $P(y)$ can be found by applying Equation C.5:

$$P(y) = \lambda e^{-\lambda y}\,. \tag{C.6}$$

These results were first seen by the author of this work in 'Numerical Recipes in FORTRAN', [80]. They indicate that by transforming uniform deviates x according to the prescription $y(x) = -(1/\lambda)\ln(x)$, values of y are generated that are distributed in the same manner as they would have been if they were drawn from a population whose probability distribution function was $P(y) = \lambda e^{-\lambda y}$.

C.3 The Probability Distribution for Particle Propagation

Consider a particle whose probability of undergoing a discrete interaction per unit distance is λ. Write the probability that the particle travels a distance x without suffering an interaction as $P(x)$. Suppose that the probability of travelling an additional distance y after having travelled a distance x is independent of x, specifically $P(x+y) = P(y|x)P(x) = P(y)P(x)$. This supposition is in agreement with the intuitive idea that in an infinite homogeneous medium, if a particle travels some distance in some time, and neither the condition of the particle nor that of the medium is altered in this time (excepting that the particle undergoes spatial translation, which is unimportant in an infinite medium), then the future prospects for the particle should be the same as they were when it started out. It follows from these definitions and conditions that

$$\begin{aligned} P(x+\delta x) &= P(x)P(\delta x) && \text{(C.7)} \\ &\simeq P(x)(1-\lambda\delta x)\,, && \text{(C.8)} \end{aligned}$$

Where the approximate equality is satisfied as an equality in the limit $\delta x \to 0$. Now $P(x+\delta x)$ can be expressed through a Taylor expansion as

$$P(x+\delta x) = P(x) + \frac{dP(x)}{dx}\delta x + \frac{1}{2!}\frac{d^2P(x)}{dx^2}\delta x^2 + \frac{1}{3!}\frac{d^3P(x)}{dx^3}\delta x^3 + \cdots\,. \tag{C.9}$$

Therefore

$$-P(x)\lambda\delta x = \frac{dP(x)}{dx}\delta x + \frac{1}{2!}\frac{d^2P(x)}{dx^2}\delta x^2 + \frac{1}{3!}\frac{d^3P(x)}{dx^3}\delta x^3 + \cdots\,. \tag{C.10}$$

In the limit that $\delta x \to 0$

$$\frac{dP(x)}{P(x)} = -\lambda dx\,. \tag{C.11}$$

Integrating, normalising so that $P(0) = 1$,

$$\begin{aligned} \int_0^{P(x)} \frac{dP(x)}{P(x)} &= -\int_0^x dx\,\lambda\,, && \text{(C.12)} \\ \ln P(x) &= -\lambda x\,, && \text{(C.13)} \\ P(x) &= e^{-\lambda x}\,. && \text{(C.14)} \end{aligned}$$

Recall that $P(x)$ is the probability that a particle travels a distance x without interaction. Another useful function is $P'(x)$ which is the probability that a particle travels a distance x and then interacts immediately (at x). $P'(x)$ is calculated from $P(x)$ through

$$\begin{aligned} P'(x)\delta x &= P(x)\overline{P(\delta x)} && \text{(C.15)} \\ &= e^{-\lambda x}\lambda\delta x\,, && \text{(C.16)} \\ P'(x) &= \lambda e^{-\lambda x}\,. && \text{(C.17)} \end{aligned}$$

If $P(x)$ is the probability that a particle travels a distance x without interaction, the notation $\overline{P(x)}$ is intended to be probability that a particle does not travel a distance x without interaction (the overbar is intended to remind the reader of the logical operator NOT). The expression $\overline{P(\delta x)} = \lambda\delta x$ arises from the definitions of $P(x)$ and λ that are given at the beginning of this section, in the limit that $\delta x \to 0$. Note that because of the manner in which $P'(x)$ has been derived, the expected normalisation condition

$$\int_0^\infty dx\,P'(x) = 1 \tag{C.18}$$

is satisfied in a natural way.

$P(x)$ and $P'(x)$ differ algebraically only by a constant factor (λ), and because this factor can be introduced by demanding that a normalisation condition is met, the two appear to be used interchangeably in the literature. It has been shown that they differ radically in their meaning, and it is for this reason that the author of this work wishes to make the distinction clear. The method used here also has the advantage of introducing the normalisation condition on $P'(x)$ in a very natural way. Note that $P'(x)$ is the probability distribution function for x. In summary:

1. $P(x)$ is the probability that a particle travels a distance x without interaction.
2. $P'(x)$ is the probability that a particle travels to an interaction a distance x away. It is also the probability distribution function for x.

The method that shall be used to sample from the probability distribution function $P'(x)$ has been described in the previous section.

C.4 A Particle with Multiple Interactions

Consider a particle which undergoes several distinct discrete interactions. If there are N such interactions, and if the probability that the particle is subject to the ith such interaction per unit distance is λ_i, then

$$\begin{aligned} P_M(x+\delta x) &= P_M(x).P_M(\delta x) && \text{(C.19)} \\ &= P(x)_M(1-\lambda_1\delta x-\lambda_2\delta x-\cdots-\lambda_N\delta x) && \text{(C.20)} \\ &= P(x)_M(1-\sum_{i=1}^{N}\lambda_i\,\delta x) && \text{(C.21)} \\ &= P(x)_M(1-\lambda_T\delta x)\,. && \text{(C.22)} \end{aligned}$$

λ_T is defined by a comparison of the two last expressions. From here, proceed just as earlier to derive the expression

$$\begin{aligned} P_M(x) &= e^{-\lambda_T x} && \text{(C.23)} \\ &= e^{-(\sum_{i=1}^{N}\lambda_i)x}\,. && \text{(C.24)} \end{aligned}$$

$P_M(x)$ here has the same meaning as $P(x)$, but it applies to a particle that suffers multiple interactions. It is just as easy as before to find a function $P'_M(x)$, again exactly analogous to $P'(x)$. Once a step length is sampled from the distribution, it remains to select which interaction ended the particle's progress. Clearly, since each interaction occurs with a probability λ_i per unit distance, the ith will be selected with a probability λ_i/λ_T.

The probability function $P_M(x)$ is similar to that of the previous section, as might have been expected upon writing $\lambda = \lambda_T = \sum_{i=1}^{N}\lambda_i$. Another way this result might have been anticipated is by direct consideration of the probability that a particle might travel a distance x without suffering any of the N interactions whose interaction probabilities per unit distance are given by λ_i:

$$\begin{aligned} P_M(x) &= \prod_{i=1}^{N} P_i(x) && \text{(C.25)} \\ &= \prod_{i=1}^{N} e^{-\lambda_i x} && \text{(C.26)} \\ &= e^{-(\sum_{i=1}^{N}\lambda_i)x}\,. && \text{(C.27)} \end{aligned}$$

C.5 Independent Sampling to Obtain a Distribution

Consider a particle with two discrete interactions, labelled by 1 and 2. These two (multiple) interactions result in the probability distribution function governing the selection of a path length

$$P'_{1,2}(x) = (\lambda_1+\lambda_2)e^{-(\lambda_1+\lambda_2)x}\,. \qquad \text{(C.28)}$$

By ignoring the existence of first one interaction and then the other, two single interaction probability functions can be derived:

$$\begin{aligned} P'_1(x) &= \lambda_1 e^{-\lambda_1 x}\,, && \text{(C.29)} \\ P'_2(x) &= \lambda_2 e^{-\lambda_2 x}\,. && \text{(C.30)} \end{aligned}$$

The probability functions $P(x)$ and $P'(x)$ have the meanings described in earlier sections. It shall be shown that it is possible to independently sample two step lengths from the two independent distributions $P'_1(x)$ and $P'_2(x)$, and by choosing the shorter of the two step lengths, reproduce the distribution $P'_{1,2}(x)$.

For clarity: consider the circumstance in which a step length is sampled from the probability distribution $P'_1(x)$, giving x_1, and the step length x_2 is independently sampled from the distribution $P'_2(x)$. Interaction 1 is to be chosen if x_1 is shorter than x_2, and interaction 2 is chosen if the reverse case occurs. The case where $x_1 = x_2$ is ignored, since the mathematical probability for such an event is vanishing. The distance to the interaction is to be x_1 if interaction 1 has been chosen, and x_2 if interaction 2 has been chosen.

Consider the independent sampling method outlined, and calculate the probability that $x_1 = x < x_2$ from the probability functions $P_1(x)$ and $P_2(x)$:

$$\begin{aligned} P'(x_1 = x < x_2)\delta x &= P_1(x)P_2(x)\overline{P_1(\delta x)}P_2(\delta x) \ , & \text{(C.31)} \\ &= P_1(x)P_2(x)\left[1 - P_1(\delta x)\right]P_2(\delta x) \ , & \text{(C.32)} \\ &= P_1(x)P_2(x)\lambda_1\delta x\left[1 - \lambda_2\delta x\right] \ , & \text{(C.33)} \\ &= P_1(x)P_2(x)\lambda_1\delta x - \vartheta(\delta x^2) \ , & \text{(C.34)} \end{aligned}$$

and hence, in the limit $\delta x \to 0$,

$$\begin{aligned} P'(x_1 = x < x_2) &= P_1(x)P_2(x)\lambda_1 & \text{(C.35)} \\ &= \lambda_1 e^{-(\lambda_1+\lambda_2)x} \ . & \text{(C.36)} \end{aligned}$$

The notation $\overline{P(x)}$ represents the probability that the particle interacts in a distance x (the overbar is logically equivalent to the NOT function) where $P(x)$ is, as usual, the probability that no interaction occurs in the same distance. The derivation of Equation C.34 can be repeated for the second interaction to find

$$\begin{aligned} P'(x_2 = x < x_1) &= P_1(x)P_2(x)\lambda_2 & \text{(C.37)} \\ &= \lambda_2 e^{-(\lambda_1+\lambda_2)x} \ . & \text{(C.38)} \end{aligned}$$

The probability distribution function for x (where x is the distance travelled before interaction) in the independent sampling regime is therefore

$$\begin{aligned} P'_I(x) &= P'(x_1 = x < x_2) + P'(x_2 = x < x_1) & \text{(C.39)} \\ &= (\lambda_1 + \lambda_2)e^{-(\lambda_1+\lambda_2)x} \ , & \text{(C.40)} \end{aligned}$$

where $P'(x_1 = x < x_2)$ and $P'(x_2 = x < x_1)$ are understood as mutually exclusive independent possibilities (the case where $x_1 = x_2$ is ignored). It is now obvious that $P'_I(x)$ is equivalent to $P'_{1,2}(x)$.

It is also possible to show that interaction 1 is picked the appropriate fraction of the time. To prove this consider the probability of selecting interaction 1, given that an interaction has occurred after a distance x:

$$\begin{aligned} P'_1(x)|P'_I(x) &= \frac{P'(x_1 = x < x_2)}{P'(x_1 = x < x_2) + P'(x_2 = x < x_1)} & \text{(C.41)} \\ &= \frac{P_1(x)P_2(x)\lambda_1}{P_1(x)P_2(x)\lambda_1 + P_1(x)P_2(x)\lambda_2} & \text{(C.42)} \\ &= \frac{\lambda_1}{\lambda_1 + \lambda_2} \ . & \text{(C.43)} \end{aligned}$$

Naturally, a similar result can be derived for interaction 2,

$$P'_2(x)|P'_I(x) = \frac{\lambda_2}{\lambda_1 + \lambda_2} \ . \qquad \text{(C.44)}$$

Note that the results of Equations C.43 and C.44 are independent of x. This is just what is required of the independent sampling method if it is to match the standard method (outlined in the previous section) for

selection of an interaction. It is now obvious that interactions 1 and 2 are picked with the same relative probabilities in the independent sampling regime as they are when using the ordinary sampling method.

The results of Equations C.36,C.38,C.43, and C.44 demonstrate that the independent sampling method gives identical results to the standard method (outlined in the previous section) for selection of an interaction and step length for a particle suffering two interactions. These results are not approximate, they are analytically exact. The independent sampling method can be easily generalised to more than two interactions, but a moment's thought reveals the weakness of the independent method: a single random number is required for each interaction for which a step length is sampled, while in the standard method, two random numbers are all that are ever needed.

C.6 Conclusions

A mechanism for utilising uniform deviates in sampling from an exponential probability distribution has been described. The probability distribution function for the distance travelled by a particle suffering one or many discrete interactions has been shown to be an exponential function of the distance. The independent sampling method has been shown to reproduce the results of the standard sampling method. This last result is not approximate, it is analytically exact.

In the context of the SNOMAN program, and the photodisintegration extension to the EGS4 code, the analytical equivalence of the independent sampling method to the standard sampling mechanism is important. It means that the true distribution of γ-ray interaction lengths is appropriately sampled without any change being made to the EGS4 code.

Appendix D

Formal Theory of Deuteron Photodisintegration At Low Energies

D.1 Introduction

In this appendix a simple theory of deuteron photodisintegration via the electric dipole interaction is given. In addition errors on σ_{E1} and σ_{M1} will be derived at and near the threshold for the d(γ,n)p process. This derivation was found in Arenhövel and Sanzone [69].

D.2 Electric Dipole Cross Section for Deuteron Photodisintegration Using a Delta Function Potential Model

For sufficiently low energy γ-rays incident upon a deuteron, the precise details of the behaviour of the nuclear wavefunction inside the nucleus are not expected to matter in the calculation of σ_{E1} because of the small size of the nucleus compared to the wavelength of the γ-ray. The long range form of the nuclear wavefunction does matter, and it can be approximated very well and simply by a δ function potential, which gives rise to a nuclear wavefunction $\propto \exp(-\alpha r)/r$ where $\alpha = \sqrt{M\epsilon}$, and r is the radial coordinate, M is the average mass of a nucleon within the deuteron, and ϵ is the binding energy of the deuteron. This is the same form as would be derived from a better potential model such as a square well potential, but the normalisation of the wavefunction external to the nucleus is not that which would arise from such a potential. As a result, the cross section that is calculated using the δ function potential is correct in its form, but incorrect in its absolute magnitude (it is too low). To correct for the limitations of the δ function potential, effective range theory is used. This allows n-p scattering data to provide the required overall normalisation external to the nucleus.

In the dipole approximation, the differential absorption cross section of a photon incident upon a deuteron is given by

$$\frac{d\sigma}{d\Omega} = 2\pi^2 e^2 \omega k M |\boldsymbol{D}_{fi}.\boldsymbol{\varepsilon}|^2 \ , \tag{D.1}$$

where $\boldsymbol{D}_{fi} = \langle f|\hat{\boldsymbol{D}}|i\rangle$ denotes the dipole transition matrix element between the deuteron bound state and the continuum, and $\boldsymbol{\varepsilon}$ is the photon polarisation vector. The average nucleon mass is denoted by M, and ω is the frequency of the incident photon, and k is the wavelength of an exiting nucleon in the centre of momentum.

To describe the nucleon-nucleon force the potential

$$V(r) = -V_0\delta(r) \tag{D.2}$$

is used, which represents a spin-independent zero-range force. The justification for this is that in the limit in which the photon wavelength is very large compared to the range of the nuclear potential the details of the force involved are not expected to matter. The bound state solution for the nuclear wavefunction is ($\hbar = 1$);

$$\psi_s^0(r) = \sqrt{\frac{\alpha}{2\pi}}\frac{e^{-\alpha r}}{r} \ , \tag{D.3}$$

where α is related to the binding energy of the deuteron, ϵ, through $\alpha = \sqrt{M\epsilon}$. It is well known that for moderate energies the P-state wave function may be replaced by that of a free particle, and this shall be done for the final state wavefunction of the nucleon. The electric dipole matrix element, after inserting a free plane wave as the final state wavefunction of the nucleons, is

$$\boldsymbol{D}_{fi} = \frac{1}{2(2\pi)^{3/2}} \int d^3r \, e^{-i\boldsymbol{k}.\boldsymbol{r}} \boldsymbol{r} \psi_s^0(r) \ . \tag{D.4}$$

This integral is of the form

$$\int d^3r \, f(r, r\cos\theta)\, \boldsymbol{r} \ . \tag{D.5}$$

Define $\hat{\boldsymbol{r}}_{\|}$ as a unit vector in the direction of $\boldsymbol{k}$, and $\hat{\boldsymbol{r}}_{\perp}$ through the equation

$$\boldsymbol{r} = r\cos\theta\, \hat{\boldsymbol{r}}_{\|} + r\sin\theta\, \hat{\boldsymbol{r}}_{\perp} \ , \tag{D.6}$$

where θ is the angle between $\boldsymbol{r}$ and $\boldsymbol{k}$, and $\hat{\boldsymbol{r}}_{\perp}$ is then a function of $\boldsymbol{r}$. Using these definitions of the parallel and perpendicular unit vectors, Equation D.5 can be expressed as

$$\begin{aligned} \int dr\, d\theta\, d\phi\, f(r, r\cos\theta)\, \boldsymbol{r} \quad &= \quad \int dr\, d\theta\, d\phi\, f(r, r\cos\theta)\, r\cos\theta\, \hat{\boldsymbol{r}}_{\|} + \\ & \qquad \int dr\, d\theta\, d\phi\, f(r, r\cos\theta)\, r\sin\theta\, \hat{\boldsymbol{r}}_{\perp} \ . \end{aligned} \tag{D.7}$$

Now the second integral on the right hand side of Equation D.7 vanishes, because for each vector $\hat{\boldsymbol{r}}_{\perp}$ there is a vector $\hat{\boldsymbol{r}}'_{\perp} = -\hat{\boldsymbol{r}}_{\perp}$ that contributes to the integral with the same weight, but with the opposite sign. It is now clear that the integral in Equation D.4 is equivalent to the much simpler integral

$$\boldsymbol{D}_{fi} = \frac{\hat{\boldsymbol{k}}}{2(2\pi)^{3/2}} \int dr\, d\theta\, d\phi\, r^2 \sin\theta\, e^{-ikr\cos\theta} r\cos\theta\, \psi_s^0(r) \tag{D.8}$$

$$= \frac{\sqrt{\alpha}}{2\pi}\frac{\hat{\boldsymbol{k}}}{2} \int dr\, d\theta\, r^2 \sin\theta\, \cos\theta\, e^{-ikr\cos\theta} e^{-\alpha r} \ . \tag{D.9}$$

After some simple but long-winded algebra, this integral can be seen to be equal to

$$\boldsymbol{D}_{fi} = i\frac{\sqrt{\alpha}}{\pi}\frac{\boldsymbol{k}}{(\alpha^2 + k^2)^2} \ , \tag{D.10}$$

where $\boldsymbol{k}$ is the final-state relative momentum $\boldsymbol{k} = (\boldsymbol{p}_p - \boldsymbol{p}_n)/2$, and is related to the photon energy ω by the equation $k = \sqrt{M(\omega - \epsilon)}$ or by $\alpha^2 + k^2 = M\omega$. Substituting the expression from Equation D.10 into Equation D.1, averaging over all photon polarisations, and integrating over solid angle returns the cross section for deuteron photodisintegration through an electric dipole transition, which is

$$\sigma_{\text{E1}} = \frac{8\pi}{3}\frac{e^2}{\alpha^2}\frac{(\gamma - 1)^{3/2}}{\gamma^3} \ , \tag{D.11}$$

where the definition $\gamma = \omega/\epsilon$ has been used. Note that if an electromagnetic interaction of the form $-\boldsymbol{j}.\boldsymbol{A}$ had been used, where $\boldsymbol{j}$ denotes the one body current and $\boldsymbol{A}$ is the vector potential of the electromagnetic field, the same result would have been achieved. This is demonstrated by Blatt and Weisskopf [70, Chapter XII and Appendix B].

Comparison with experiment shows that the shape of the cross section is quite well reproduced even at energies above $\simeq$ 10MeV where one would not expect it to be in view of the use of a simplified delta-function potential model. However, the overall magnitude of the cross section is incorrect by a factor of approximately 1.7 - the theoretical result is much too low. Effective range theory can be used to correct for the normalisation of the wavefunction that arises from the use of the δ function potential.

D.2.1 Effective Range Theory in Deuteron Photodisintegration

In this section effective range theory, as described by Bethe [66], will be used to find an appropriate normalisation for the wavefunction of the deuteron. This will be used to correct the cross section for the electric dipole.

In the standard effective range theory, used in describing low energy nucleon-nucleon scattering, complications arise because of the variation of the initial and final state wavefunctions with the energy of the incident nucleons. When considering the deuteron bound state, such complications are completely unnecessary, since there is no variation in the wavefunctions because only a single energy is permitted! In what follows, a simpler, much faster derivation can be achieved by considering $u_1 = u_2$ and $\chi_1 = \chi_2$ right from the start. However, such a derivation would be specific to the bound neutron-proton triplet state (the deuteron), and would not be sufficient to identify the effective range measured in scattering experiments with that used here.

Consider the radial Schrödinger equation for an S state. If $\phi(r)$ is the radial wavefunction, $u_1 = r\phi(r)$, and u_1 satisfies the equation

$$\frac{d^2u_1}{dr^2} + k_1^2 u_1 - V(r)u_1 = 0 \ , \tag{D.12}$$

where $V(r)$ is the modified potential energy, related to the true potential by $V(r) = \frac{1}{M}V'(r)$. It is clear that at a different energy corresponding to k_2, the function u_2 also satisfies an equation similar to that of Equation D.12. Multiply Equation D.12 by u_2 and the corresponding equation for u_2 by u_1, subtract the second from the first and integrate. The result is

$$\left[u_2\frac{du_1}{dr} - u_1\frac{du_2}{dr}\right]_0^R = (k_2^2 - k_1^2)\int_0^R dr\, u_1u_2 \ . \tag{D.13}$$

Equation D.13 shall not be used directly to obtain the principal result of effective range theory, instead the comparison functions $\chi_1(r)$ and $\chi_2(r)$ are introduced. They are particular solutions of Equation D.12 when $V(r) = V_0\delta(r)$, and are normalised to 1 at $r = 0$. The algebraic forms for χ_1 and χ_2 are

$$\chi_1(r) = e^{-k_1 r} \ , \tag{D.14}$$
$$\chi_2(r) = e^{-k_2 r} \ . \tag{D.15}$$

The comparison functions are intended to represent the long range behaviour of the functions $u(r)$. The comparison functions $\chi_1(r)$ and $\chi_2(r)$ also satisfy a relationship similar to that of $u_1(r)$ and $u_2(r)$ in Equation D.13:

$$\left[\chi_2\frac{d\chi_1}{dr} - \chi_1\frac{d\chi_2}{dr}\right]_0^R = (k_2^2 - k_1^2)\int_0^R dr\, \chi_1\chi_2 \ . \tag{D.16}$$

By taking the difference of these last equations, Equations D.13 and D.16, it is found that

$$\left[\chi_2\frac{d\chi_1}{dr} - \chi_1\frac{d\chi_2}{dr} - u_2\frac{du_1}{dr} + u_1\frac{du_2}{dr}\right]_0^R = (k_2^2 - k_1^2)\int_0^R dr\,(\chi_1\chi_2 - u_1u_2) \ . \tag{D.17}$$

Now consider just the left hand side of Equation D.17. If R is chosen to be large compared to the range of the nuclear forces involved, then the functions $u(r)$ approach the comparison functions $\chi(r)$, and there is no contribution from the upper limit. In addition, $u_1(0) = u_2(0) = 0$, so there is no contribution from the u terms at the lower limit. On the right hand side, the upper limit of the integral can be extended such that $R = \infty$ for just the same reason that there was no contribution to the upper limit from the terms on the left hand side, that is, for sufficiently large r the functions $u(r)$ approach the comparison functions $\chi(r)$, and therefore there will be no addition to the integral as $R \to \infty$ from an initially large value. These considerations make the Equation D.17 equivalent to the expression

$$\left[\chi_1\frac{d\chi_2}{dr} - \chi_2\frac{d\chi_1}{dr}\right]_0 = (k_2^2 - k_1^2)\int_0^\infty dr\,(\chi_1\chi_2 - u_1u_2) \ . \tag{D.18}$$

Now take the special case $k_1 = 0$. Take the subscript 0 to refer to the zero energy functions, and drop the subscript 2 altogether. This results in the relations $u_0 = u_1$, $\phi_0 = \phi_1$, $k = k_2$, $u = u_2$, and $\phi = \phi_2$. Resolving the left hand side of Equation D.18, it is found that

$$\frac{1}{k} = \int_0^\infty dr\,(\chi_0\chi - u_0 u)\ , \tag{D.19}$$

where the integral clearly has the dimensions of a length. The functions $\chi_0(r)$ and $u_0(r)$ only differ inside the range of the nuclear forces. The same is also true of $\chi(r)$ and $u(r)$. In addition, for small k, the function χ_0 differs very little from χ, and u_0 very little from u, because the the potential energy is very much larger than k^2 and kr is small. This means that a good approximation to Equation D.19 can be achieved by replacing χ by χ_0 and u by u_0. The result is

$$\frac{1}{2}r_0 = \int_0^\infty dr\,(\chi_0^2 - u_0^2)\ . \tag{D.20}$$

This integral quantity can be identified as the effective range, see Bethe [66], or Jelley [67, Section 7.1]. The principal approximation that has been repeatedly used in deriving the expression involving the effective range in Equation D.20 is that all the energies involved are small. This is true in the case of the deuteron bound state, where the nucleons are bound by approximately 2.22MeV.

The next step is to identify the wavefunction that was used in deriving the electric dipole cross section for deuteron photodisintegration with the modified radial model function $\chi_0(r)$:

$$\psi_0(r) = \frac{1}{4\pi}\frac{\chi_0(r)}{r}\ . \tag{D.21}$$

$u_0(r)$ is intended to approach the model function $\chi_0(r)$ as $r \to \infty$, as is required by effective range theory, and bears a similar relationship to the real radial wavefunction as does the model function $\chi_0(r)$ to $\psi_0(r)$. Now the normalisation condition for the radial function $u_0(r)$ can be found, given that $\int_0^\infty dr\,\chi_0^2(r) = 1/2\alpha$:

$$\int dr\,u_0^2 = \int dr\,\chi_0^2 - \int dr\,(\chi_0^2 - u_0^2)\ , \tag{D.22}$$

$$= \frac{1}{2\alpha} - \frac{r_0}{2}\ , \tag{D.23}$$

$$= \frac{(1-\alpha r_0)}{2\alpha}\ , \tag{D.24}$$

and therefore

$$N_u^2 = \frac{N_\chi^2}{(1-\alpha r_0)}\ . \tag{D.25}$$

where N_u and N_χ are the long range or extra-nuclear normalisation factors for the u and χ wavefunctions which are themselves just the the radial parts of the true potential and delta function potential wavefunctions, respectively.

D.2.2 Conclusion

Now that the true normalisation of the radial wavefunction is known, it is possible to correct the electric dipole cross section to account for it. The electric dipole cross section, modified by the results of effective range theory, is

$$\sigma_{\mathrm{E1}} = \frac{8\pi}{3}\frac{e^2}{\alpha^2}\frac{(\gamma-1)^{3/2}}{\gamma^3(1-\alpha r_t)}\ , \tag{D.26}$$

where r_t is the n-p triplet effective range.

D.3 The Errors on the Derived Cross Sections

This section shall provide an evaluation of the accuracy of the photoelectric and photomagnetic interaction cross sections of Chapter 5. The equations 5.2 and 5.3 contain only experimental observables, which are subject to measurement errors. Under the assumption that these errors are drawn from a Gaussian distribution, it is possible to derive simple expressions for the overall error associated with the cross sections σ_{E1} and σ_{M1}. The magnitudes of these random errors can then be compared to the error arising

from neglect of exchange effects in the magnetic interaction cross section to establish the overall error associated with the calculated cross section near the threshold for deuteron photodisintegration. The error for σ_{E1} is

$$\frac{V(\sigma_{\mathrm{E1}})}{\sigma_{\mathrm{E1}}^2} = \frac{9}{4}\frac{V(\gamma)}{(\gamma-1)^2} + 9\frac{V(\gamma)}{\gamma^2} + 4\frac{V(\alpha)}{\alpha^2} + \frac{r_t^2 V(\alpha) + \alpha^2 V(r_t)}{(1-\alpha r_t)^2} , \tag{D.27}$$

where $V(x)$ is the variance of the quantity x, related to the Gaussian error by the expression $V(x) = \sigma^2(x)$. The magnitudes of the individual errors are

$$\begin{aligned} r_t &= 1.759\mathrm{fm} \pm 0.005\mathrm{fm} , & \text{(D.28)} \\ \epsilon &= 2.224644\mathrm{MeV} \pm 0.000046\mathrm{MeV} , & \text{(D.29)} \\ M &= \frac{1}{2}(m_p + m_n) = 938.91897\mathrm{MeV}/c^2 \pm 0.00020\mathrm{MeV}/c^2 , & \text{(D.30)} \\ a_s &= -23.748\mathrm{fm} \pm 0.010\mathrm{fm} , & \text{(D.31)} \end{aligned}$$

where these numbers have been taken from Dumbrajs *et al.* [81, NN Scattering], and the Review of Particle Properties [82], and a_s is included because it is used later. Both $\alpha = \sqrt{M\epsilon}$ and $\gamma = \omega/\epsilon$ are dependent on either or both of M and ϵ. Now, the errors on M and ϵ are negligible when compared to the error in r_t, and therefore any terms containing the variances on those quantities in Equation D.27 will be neglected. This assumption renders the error associated with σ_{E1} energy-independent. With this in mind, Equation D.27 becomes

$$\begin{aligned} \frac{V(\sigma_{\mathrm{E1}})}{\sigma_{\mathrm{E1}}^2} &\simeq \frac{\alpha^2 V(r_t)}{(1-\alpha r_t)^2} , & \text{(D.32)} \\ \frac{\mathrm{Error}(\sigma_{\mathrm{E1}})}{\sigma_{\mathrm{E1}}} &\simeq 0.00195 & \text{(D.33)} \\ &\simeq 0.2\% . & \text{(D.34)} \end{aligned}$$

The error for σ_{M1} is more difficult to calculate. During the calculation it is necessary to choose an energy at which the error is to be evaluated. The calculation is greatly simplified by an appropriate choice of that energy, in particular if $k = \alpha$. This corresponds to choosing an incident γ-ray energy very near the peak of the deuteron photodisintegration cross section, and while it renders the estimate of the random error on σ_{M1} strictly valid at only one energy, it does give an indication of the approximate magnitude of the error elsewhere. Neglecting the errors of small relative magnitude once again:

$$\frac{V(\sigma_{\mathrm{M1}})}{\sigma_{\mathrm{M1}}^2} = \left(\frac{r_t\alpha^2}{Q} - \frac{2\alpha}{Q} - \frac{2\alpha^2 a_s}{R}\right)^2 V(a_s) + \left(\frac{\alpha}{S} + \frac{a_s\alpha^2}{Q}\right)^2 V(r_t) , \tag{D.35}$$

where Q, R, and S are defined thus:

$$\begin{aligned} Q &= 1 - \alpha a_s + \alpha^2 a_s r_t/2 , & \text{(D.36)} \\ R &= 1 + \alpha^2 a_s^2 , & \text{(D.37)} \\ S &= 1 - \alpha r_t . & \text{(D.38)} \end{aligned}$$

With the choice $k = \alpha$, and retaining only errors on the singlet scattering length and the triplet effective range (which are comparatively large), the estimate for the error on σ_{M1} becomes

$$\frac{\mathrm{Error}(\sigma_{\mathrm{M1}})}{\sigma_{\mathrm{M1}}} \simeq 0.08\% . \tag{D.39}$$

Whilst this error has not been derived at the threshold for photodisintegration, it does give an indication of the magnitude of the error that can be expected there.

Appendix E

MCNP in SNOMAN: N-Transport and Sampling

E.1 The Transport Mechanism in MCNP

Fundamentally, MCNP's neutron transport conforms to the standard analogue Monte Carlo procedure outlined in Chapter 7. The general algorithm used by MCNP for processing a nuclear collision at non-thermal energies is as follows [88]:

1. a collision type is selected;
2. the energy and direction vector of the target nucleus are sampled;
3. the collision data is identified as centre-of-momentum or target-at-rest data. The neutron's energy and direction vector are adjusted accordingly;
4. the final state neutron's scattering angle is sampled based upon the data provided for the selected collision type and nucleus;
5. the final state neutron's energy is calculated (if there is a one-to-one correspondence between scattered angle and energy as in elastic scattering), or sampled, or partly sampled and partly calculated, based upon the scattering angle and data provided for the selected collision type and nucleus;
6. the final state neutron's direction vector in the centre-of-momentum or target-at-rest frame are calculated from its scattering angle.
7. the final state neutron's energy and direction vector are transformed to the laboratory frame from the centre-of-momentum or the target-at-rest frame.
8. (The processes $2 \rightarrow 7$ are repeated for each final state neutron).

The methods used in Items 1 through 7 are described later in this appendix. Neutron collisions at energies below 4.6eV can be handled differently. For a small number of nuclei, collisions at thermal energies are handled using an accurate S(α,β) treatment described in Section E.3.6. That treatment is available only for very light nuclei (hydrogen and deuterium) where molecular effects cannot be ignored.

MCNP models all of its physics using data drawn from nuclide specific data tables that must be provided. These tables provide partial and total interaction cross sections as a function of neutron energy, and energy-angle spectra for the emerging neutrons, as well as other interaction data. There is a wide choice of tables that may be provided to MCNP depending on the nature of the problem that is to be solved, upon the accuracy desired in the results, and the time available. The best, i.e. most accurate tables are the continuous energy evaluations, and SNOMAN makes use of these. The data tables typically cover neutron interactions in the energy range from $10^{-11} \rightarrow$ 20MeV. The cross sections are stored as a set of paired data elements, (E_i,σ_i). Linear interpolation is used to evaluate the cross section between tabulated points. Enough pairwise points are included in a cross section to ensure that the linear interpolation reproduces the evaluated cross sections to within 1%.

Nuclear collisions that result in just one final state neutron are handled as accurately as the data made available to the MCNP program will allow. Neutron collisions with more than one neutron in the

final state are handled approximately. This is because the data provided to MCNP in this circumstance is in the form of an all-outgoing-neutron average energy-angle distribution. The MCNP program steps through the process-list given above, using the data provided to it. The result is that no quantity that is correlated between final state neutrons is sampled correctly in an individual collision. For example, the energy spectrum of a large number of neutrons from an (n,2n) collision is correct, but the energy spectra of two neutrons emerging from a single collision is not. Indeed, in this example, energy and momentum are conserved on average, but not in an individual collision.

The approximate nature of the handling by MCNP of multiple final state neutron collisions is not a cause for concern in the computational evaluation of the SNO detector. This is because this evaluation is dominated by single outgoing neutron scattering events. Indeed, the only significant exception is the ^{2}H(n,2n)^{1}H reaction, which has Q-value of -2.225MeV and a negligible cross section for neutrons with energies below 4.1MeV. Hence this reaction is only important during the use of the high energy detector calibration sources.

E.1.1 Thermal Motion and Molecular Effects

When the kinetic energy of the neutron is much greater than that of the target, and the target is heavy, the thermal motion of the target can be ignored. In practice, in MCNP, the thermal motion of the target is neglected provided $E_n > 400kT$, and the target is not ^{1}H. Otherwise the motion of the target is sampled from the distribution;

$$P(V,\mu) \propto \sqrt{v^2 + V^2 - 2vV\mu}\; V^2 e^{-\beta^2 V^2}\;, \tag{E.1}$$

where v is the speed of the incident neutron, V is that of the target, μ is the angle between the neutron's velocity vector and the target's, and $\beta^2 = A/2kT$. A is the mass of the target nucleus, k is Boltzmann's constant, and T is the temperature of the medium. The assumptions made in the derivation of this probability distribution are given in Section E.3.2. This free-gas method is a thermal interaction model that results in a good approximation to the thermal flux spectrum in a variety of applications [88].

This free-gas approximation breaks down when molecular effects become significant. This is the case when the kinetic energy of a neutron becomes comparable to that energy binding either hydrogen or deuterium into the water molecule. The light target nucleus can no longer be considered free. This is because there is insufficient energy available to the neutron to break the molecular binding of the light target nucleus without a significant change in the energy of the incident neutron. In this low target mass, low energy limit, the free gas approximation is no longer applicable to elastic scattering. The neutron now behaves as if it were scattering from a light nuclear target with the mass of the entire molecule to which it is bound and this greatly increases the elastic scattering cross section, which takes the form [99];

$$\sigma(\theta) = \frac{\mu^2}{4\pi^2\hbar^2}\left|\int \psi^*_{\text{final}} S \psi_{\text{initial}} \delta\tau\right|^2 \tag{E.2}$$

The factor μ is the reduced mass, $\mu = m_n m/(m_n + m)$, which rises from about $\frac{1}{2} \rightarrow 1$ as the mass m rises from 1 (in units of the neutron's mass) for high energy neutrons incident upon hydrogen in the light water, to approximately 18 as the incident neutron's energy becomes increasingly small when compared to the binding energy of the target proton. The effect of this change in the reduced mass is that the elastic scattering cross section rises by about a factor of 4 as the neutron's energy falls to well below thermal energies. The moderating effects of the light nuclei in the water are also reduced due to the larger effective mass of the target nuclei. In addition, the target now has internal degrees of freedom, and can be inelastically scattered into rotational and vibrational final states, which is reflected in the inelastic scattering cross section.

The several effects of atomic binding are explicitly taken account of in MCNP by the provision of thermal S(α,β) tables (Section E.3.6). Each table is applicable to a single nuclear species in a single molecule, and is intended to provide a complete description of thermal scattering for that nuclear species. An S(α,β) table achieves this by providing cross sections and energy dependent final state distributions for the elastic and inelastic scattering of neutrons at energies below 4.46eV. In MCNP, tables of this kind are available for H in H_2O, H in polyethene (an acrylic substitute for the purposes of the SNOMAN simulation), and D in D_2O. The inclusion of these tables in the SNOMAN program is sufficient to cover the thermal behaviour of neutrons when scattering from all the significant light nuclei in the SNO detector.

Medium	Nuclear Species
Heavy water	^{1}H,^{2}H,^{16}O,^{17}O*
Light water	^{1}H,^{16}O,^{17}O*
Acrylic vessel	^{1}H,^{12}C,^{16}O,^{17}O*
Norite	^{16}O,^{17}O*,^{23}Na,Mg,^{27}Al, Si,K,Ca,Fe
Nickel	Ni
Stainless steel	Fe,Cr,Mn,Ni
Pyrex	^{16}O,^{17}O*,^{23}Na,^{27}Al,Si,K,^{10}B, ^{11}B
Air	^{14}N,^{15}N,^{16}O,^{17}O*,Ar
Aluminium	^{27}Al
Kevlar	^{1}H,^{12}C,^{14}N,^{15}N,^{16}O, ^{17}O*
Ba-Fe-Feroxdur	^{16}O,^{17}O*,Fe,^{138}Ba
Counter gas	^{3}He,^{12}C,^{19}F

Table E.1: The nuclear content of the SNO media. The * reminds the reader that the ^{17}O nucleus is represented only by a data table for the (n,α) interaction. See text for further explanation.

E.2 Media and Choice of Data Tables for MCNP

There are several media through which neutrons can be propagated in the SNOMAN program. Each medium represents a material or substance or an approximation to a material or substance contained within the SNO experiment. The media most relevant to neutron transport are the heavy water, the light water, and the acrylic vessel. All the media in SNO, and the nuclear species making up those media, are shown in Table E.1. Table E.2 shows which MCNP data tables have been associated with which nuclei in the SNOMAN program.

Table E.2 is included for the convenience of SNO collaboration members who may be involved in working on aspects of neutron transport in the SNO experiment. At the time of writing, the group at Los Alamos responsible for maintaining and updating the MCNP code have released a new set of data tables that should be preferred for use with the MCNP program. These tables are indicated in the column marked "to be used", and will be incorporated into the SNOMAN program when they have been obtained.

SNOMAN attempts to simulate media containing an element using data appropriate to the abundances of the natural isotopes. There are two ways that this can be done. Either:

1. a 'natural' data table can be used, or,

2. a number of correctly weighted isotopic data tables can be used.

'Natural' data tables are constructed so as to simulate neutron transport through a naturally occurring mix of the isotopes of a single nuclear species. Examples given in Table E.2 include Mg, Cl, Fe, and Ni. Greater accuracy can be obtained using a number of isotopic data tables. A switch from natural tables to isotopic tables will be made for O, N, Cr, Fe, and Ni when the data is obtained.

Note that thermal energy tables are provided for the lighter nuclei ^{1}H and ^{2}H. These tables are used to simulate the transport of neutrons at thermal energies ($\sim$ 0.025eV), for the reasons discussed in Section E.1.1. The poly.01t table is intended for use in simulating transport through polyethylene, but will be used in SNOMAN in simulating thermal transport through the acrylic vessel (which is not polyethylene but polymethylmethacrylate). The poly.01t table has been used because it is applicable to the simulation of neutron scattering from hydrogen nuclei which are part of a hydrocarbon molecule, and it the only table of this kind available.

The lack of any thermal tables for the simulation of scattering at thermal energies from the ^{6}Li and ^{7}Li nuclei is not felt to present any difficulty. This is because the lithium nuclei will be present in very small numbers (2.66×10^{18}cm^{-3} compared with 6.66×10^{22}cm^{-3} for deuterium in heavy water), and the scattering cross section on ^{6}Li is 2.9b at thermal energies, compared with 4.3b for deuterium and 4b from oxygen. The ^{7}Li cross sections are even smaller. Scattering from a lithium nucleus is therefore expected to occur on average no more than once in every $\sim$ 130000 nuclear collisions ($130000 n_{^{6}\mathrm{Li}} \sigma_{n,n}(^{6}\mathrm{Li}) \simeq n_{\mathrm{H_2O}} \sigma_{n,n}(\mathrm{H_2O})$). It is now obvious that the incorrect simulation of elastic and inelastic scattering at thermal energies from the lithium isotopes present at low concentrations in the SNO detector will have

Nuclear Species	Data tables	
	used now	to be used
^{1}H	1001.60c	1001.60c
	lwtr.01t*	lwtr.01t*
	poly.01t*	poly.01t*
^{2}H	1002.55c	1002.55c
	hwtr.01t*	hwtr.01t*
^{3}He	2003.60c	2003.60c
^{4}He	2004.50c	2004.60c
^{6}Li	3006.50c	3006.60c
^{7}Li	3007.55c	3007.60c
^{10}B	5010.50c	5010.60c
^{11}B	5011.56c	5011.60c
^{12}C	6000.50c	6000.60c
^{14}N	7014.50c	7014.60c
^{15}N	none	7015.60c
^{16}O	8016.50c	8016.60c
^{17}O	none**	8017.60c
^{19}F	9019.50c	9019.60c
^{23}Na	11023.50c	11023.60c
Mg	12000.50c	12000.60c
^{27}Al	13027.50c	13027.60c
Si	14000.50c	14000.60c
Cl	17000.50c	17000.60c

Nuclear Species	Data tables	
	used now	to be used
Ar	18000.35c	18000.35c
K	19000.50c	19000.60c
Ca	20000.50c	20000.60c
Cr	24000.50c	none
^{50}Cr	none	24050.60c
^{52}Cr	none	24052.60c
^{53}Cr	none	24053.60c
^{54}Cr	none	24054.60c
Mn	25055.50c	25055.60c
Fe	26000.55c	none
^{54}Fe	none	26054.60c
^{56}Fe	none	26056.60c
^{57}Fe	none	26057.60c
^{58}Fe	none	26058.60c
Ni	28000.50c	none
^{58}Ni	none	28058.60c
^{60}Ni	none	28060.60c
^{61}Ni	none	28061.60c
^{62}Ni	none	28062.60c
^{64}Ni	none	28064.60c
Ba	56138.50c	56138.60c

Table E.2: The data tables used in the transport simulation. A * indicates that the table is used to simulate neutron transport at thermal energies. The ** reminds the reader that the ^{17}O nucleus is represented only by a data table for the (n,α) interaction. See text for further explanation.

no effect on the results of the transport process. Note that the capture cross section is not different for free and bound lithium nuclei (see Section 6.7.2).

In Chapter 6 it was shown that because ^{17}O has scattering cross section similar to that of ^{16}O, and because it is present in very small numbers, neutron scattering due to ^{17}O can be neglected in all media. This is not the case for the ^{17}O(n,α)^{14}C capture interaction, which has a much larger thermal neutron capture cross section (235mb) than other nuclei present in the D_2O, with the exception of hydrogen. Therefore this interaction should be included in SNOMAN. Unfortunately, MCNP do not provide a nuclear table specific to ^{17}O, and hence the cross section for (n,α) capture must be obtained from elsewhere. This has been achieved, and the data used in SNOMAN to calculate the ^{17}O(n,α)^{14}C was taken from the National Nuclear Data Centre maintained by Brookhaven National Laboratory, USA [129].

E.3 Sampling Processes in MCNP

E.3.1 Selection of Target and Collision Type

Consider a medium in which there are n different nuclear species, each with uniform density distribution. The ith nuclide has a density n_i per unit volume and a total cross section $\sigma_i(E)$. The jth nuclide is selected for a collision using a uniform deviate ϵ from the interval [0,1) and the neutron's laboratory energy, E, if;

$$\sum_{k=1}^{j-1} n_k\sigma_k(E) < \epsilon \sum_{k=1}^{n} n_k\sigma_k(E) \leq \sum_{k=1}^{j} n_k\sigma_k(E) \ . \tag{E.3}$$

$n_k\sigma_k(E)$ represents the macroscopic cross section at the laboratory neutron energy, E.

Once the jth collision nuclide has been selected, the collision type must be chosen. This is done through the following algorithm:

1. neutron capture is sampled;

2. either an S(α,β) treatment is available, or;

3. an elastic or an inelastic collision is selected;

4. if an inelastic collision is selected, one is chosen from those available.

The various cross sections are calculated using the laboratory energy of the incident neutron. The sampling of an inelastic collision is carried out using a random uniform deviate, ϵ, from the interval [0,1). The ith cross section is σ_i and the jth reaction is picked from the n available if;

$$\sum_{k=1}^{j-1} \sigma_k(E) < \epsilon \sum_{k=1}^{n} \sigma_k(E) \leq \sum_{k=1}^{j} \sigma_k(E) \ . \tag{E.4}$$

E.3.2 Transformation from the Laboratory Frame

Collision data is available in either the centre-of-momentum (COM) or the target-at-rest (TAR) frame. The energy of the incident neutron is transformed from the laboratory (LAB) frame into one of these frames before any collision can be resolved.

Nuclear Target Velocity

The effective elastic cross section, σ_s^*, for a nuclear target whose energies are distributed thermally is;

$$\sigma_s^*(E) = \frac{1}{v_n} \int \int \sigma_s(v_r) v_r P(V) dV \frac{d\mu}{2} \ , \tag{E.5}$$

where V and v_n are the nuclides' LAB speed and the neutron's LAB speed respectively. μ is the cosine between the neutron and the target's velocity vector. $\sigma_s(v_r)$ is the elastic scattering cross section as a function of the relative velocity v_r. v_r is the neutron-target relative velocity;

$$v_r = \sqrt{v_n^2 + V^2 - 2 v_n V \mu} \ . \tag{E.6}$$

p(V) in Equation E.5 is the probability density function for the Maxwellian distribution of target velocities. The implied probability distribution of target velocities as a function of V and μ from Equation E.5 is;

$$P(V,\mu) = \frac{\sigma_s v_r P(V)}{2\sigma_s^*(E) v_n} \ . \tag{E.7}$$

If it is assumed that the variation of $\sigma_s(v_r)$ with V can be ignored, then $P(V,\mu)$ is a function of v_r and $P(V)$ only. The justification for the assumption is as follows:

1. for light nuclei, $\sigma_s(v_r)$ is only slowly varying with V, and;

2. for heavy nuclei, where $\sigma_s(v_r)$ can vary rapidly with V, the effects of moderation are minimal.

Hence $P(V,\mu) \propto v_r P(V)$, and the target energy (velocity) and incident scattering cosine are sampled accordingly for an elastic collision.

The sampled target velocity is correctly distributed only for elastic collisions. However, the only significant thermal reactions for the isotopes occurring in the SNO experiment are absorption and elastic scattering. Inelastic scattering occurs only at energies above an MeV, where the target velocity can be safely neglected. Therefore the correction to the dynamics of a scattering process due to the motion of the target is significant only in elastic scattering in the SNO experiment, where the calculation described here is correct.

Transformation to the Target-At-Rest Frame

The transformation from the laboratory (LAB) frame to the target-at-rest (TAR) frame are carried out as follows;

1. the target's speed and relative direction cosine are sampled as is described in the previous section.
2. The target's velocity vector is calculated from the its speed and relative direction cosine and the direction of motion of the incident neutron. This includes the random selection of the azimuthal component of the target's angular motion.
3. The target's velocity vector is subtracted from that of the incident neutron, whose energy is adjusted accordingly.

Note that because the neutron is considered as a purely non-relativistic particle, the neutron has the same energy in the target-at-rest frame as it does in the centre-of-momentum frame. Therefore no additional transformation is required.

Transformation from the Centre-of-Momentum Frame

The energy and scattering angle in the centre-of-mass frame are related to those in the target-at-rest frame by the equations;

$$E'_t = E'_c + \left[\frac{E + 2\mu_c(A+1)\sqrt{EE_c}}{(A+1)^2}\right] , \tag{E.8}$$

and;

$$u_t = \mu_c\sqrt{\frac{E'_c}{E'}} + \frac{1}{A+1}\sqrt{\frac{E}{E'}} , \tag{E.9}$$

where;

E'_t is the final state neutron TAR energy;
E'_c is the final state neutron COM energy;
E is the incident TAR energy;
μ_c is the COM scattering cosine;
μ_t is the TAR scattering cosine;
A is the mass of the target nucleus divided by the mass of the neutron.

E.3.3 Sampling of Angular Distributions

The direction of emitted particles is sampled in the same way for most elastic and inelastic collisions. The cosine between incident and final state particle directions, μ, is sampled for angular collision tables in the collision nuclide's cross-section library. The angular distribution tables consist of 32 equiprobable cosine bins, and are given at a number of different incident neutron energies. The cosines are either in the centre-of-momentum or target-at-rest system, depending on the type of reaction. If E is the incident neutron energy, and E_n the energy of table n and E_{n+1} the energy of table $n+1$, then a value of μ is sampled from table $n+1$ with a probability $(E - E_n)/(E_{n+1} - E_n)$ and from table n with a probability $(E_{n+1} - E)/(E_{n+1} - E_n)$. A uniform random deviate ϵ from the interval [0,1) is then used to select the ith cosine bin such that $32\epsilon < i \leq 32\epsilon + 1$. The value of μ is then computed from;

$$\mu = \mu_i + (32\epsilon - i)(\mu_{i+1} - \mu_i) . \tag{E.10}$$

E.3.4 Sampling of Energy Distributions

There are a great many data formats and accompanying sampling methods that can be used to provide a distribution for a final state neutron's energy. In most cases, a collision will be of a particular type (for example elastic, or inelastic, or fission), and the most efficient or convenient way to store and sample data for that type of collision has been used. Just two sampling methods are demonstrated here; they are elastic and inelastic scattering, which are the most common neutron interactions in the SNO detector at non-thermal energies.

E.3.5 Elastic Scattering

The scattered neutron's energy is calculated based upon the scattering cosine, which must be sampled first. The energy is;

$$E_o = \frac{1}{2}E_i\left[(1-\alpha)\mu_c + 1 + \alpha\right] , \tag{E.11}$$

$$= E_i\left[\frac{1+A^2+2A\mu_c}{(1+A)^2}\right] , \tag{E.12}$$

where E_o is the final state energy, E_i is the incident energy, and μ_c is the scattering angle. These three quantities are all centre-of-momentum quantities. $\alpha^{1/2} = (A-1)/(A+1)$, where A is the relative mass of the target.

Inelastic X(n,n')X* Scattering

Here the final state angle and energy are unrelated in the computer simulation. In this approximate treatment, the angle is sampled as usual (see Section E.3.3) and the energy is calculated from;

$$E_o = \left(\frac{A}{A+1}\right)^2\left[E_i - \frac{Q(A+1)}{A}\right] , \tag{E.13}$$

where E_i and E_o are the incident and outgoing energies of the neutron, A is the mass of the nucleus in units of the neutron's mass, and Q is the Q-value of the inelastic collision, $E_i \geq Q$.

E.3.6 Thermal Collisions

The S(α,β) thermal scattering treatment is a complete representation (including rotational and vibrational effects) of thermal neutron scattering by molecules and crystalline solids. Inelastic scattering and elastic scattering from a lattice are provided for. If both exist for a particular nuclear species, inelastic scattering is chosen with a probability $\sigma_i/(\sigma_i+\sigma_e)$, and elastic scattering occurs otherwise. This thermal scattering treatment allows for representation of scattering by multi atomic molecules. This is important in SNOMAN, where scattering from the H nucleus in H_2O and D nucleus in D_2O are handled in this manner.

In the thermal regime, all collisions are carried out in the laboratory frame. Neither the target-at-rest, nor the centre-of-momentum frame are used. An inelastic collision is any collision where in general, $E_o \neq E_i$. An elastic collision is one where $E_o = E_i$.

The key to the success of the S(α,β) mechanism is its generality and simplicity. No assumptions are made about the target whatsoever. All that is provided is a tabulated total cross section as a function of the incident energy E_i, and probability distributions for the final state energy, E_o, as a function of E_i, and the cosine of the final state scattering angle as a function of both E_i and E_o.

Inelastic Collisions

For inelastic collisions, the distribution of final state energies is represented by a set of equally-probable final state energies (typically 16 or 32 such energies exist) for each member of a grid of initial energies from an upper limit of typically 4.6eV down to 10^{-5}eV, along with a set of angular data for each initial and final energy. The selection of the final energy E' given an initial energy E can be characterised by sampling from the distribution;

$$p(E'|E_i < E \leq E_{i+1}) = \frac{1}{N}\sum_{i=1}^{N}\delta\left[E' - \rho E_{i,j} - (1-\rho)E_{i+1,j}\right] , \tag{E.14}$$

where E_i and E_{i+1} are adjacent energies on the energy grid, and;

$$\rho = \frac{E_{i+1} - E}{E_{i+1} - E_i} . \tag{E.15}$$

N is the number of equally probable final state energies, and $E_{i,j}$ is the jth discrete final energy for incident energy E_i.

There are two allowed schemes for the selection of a scattering cosine following the selection of a final energy and final energy index j. In each case, the (i,j)th set of angular data is associated with the energy transition $E_i \rightarrow E' = E_{i,j}$.

In the first method for the selection of scattering cosine, the data consist of equally probable discrete cosines $\mu_{i,j,k}$ for $k = 1, \ldots, \nu$, ν typically 4 or 8. An index k is selected with probability $1/\nu$ and μ, the scattering cosine, obtained by the relation;

$$\mu = \rho\mu_{i,j,k} + (1-\rho)\mu_{i+1,j,k} \ . \tag{E.16}$$

In the second method, the data consist of bin boundaries of equally probable cosine bins. In this case random linear interpolation is used to select either the ith or the $i+1$th data set, with ρ being the probability to select the ith, associated with E_i. If there are ν bins, each has a probability $1/\nu$ of being selected, and the scattering cosine μ is then sampled uniformly from within the chosen bin.

Elastic Collisions

For elastic scattering, the two angular representations used in inelastic thermal scattering can be used in elastic thermal scattering were the data have been derived by an incoherent approximation. If this is the case, then elastic scattering is treated in the same way as inelastic scattering, except that $E_o = E_i$.

For elastic scattering for which the data have been derived in a coherent approximation, a completely different representation occurs. In this case, the data actually stored are the set of parameters D_k, where;

$$\begin{aligned} \sigma_e &= D_k/E \text{ for } E_k \leq E < E_{k+1} \ , \\ \sigma_e &= 0 \text{ for } E < E_1 \ . \end{aligned}$$

and E_k are Bragg energies derived from the lattice parameters. For incident energy E such that $E_k \leq E \leq E_{k+1}$;

$$P_i = D_i/D_k \text{ for } i = 1, \ldots, k \tag{E.17}$$

represents a discrete cumulative probability distribution that is sampled to obtain index i, representing scattering from the ith Bragg edge. The scattering cosine is the derived from the relationship;

$$\mu = 1 - 2E_i/E \ . \tag{E.18}$$

Artificial Boundaries in the S(α,β) Tables

In Chapter 8, Section 8.4.3, it was noted that there are artificial boundaries within in the S(α,β) tables. In that section, their effect upon the comparisons between MCNP and the SNOMAN program were examined. Equations E.14 and E.16 are the prime causes of the artificial boundaries in the inelastic scattering treatment. It is clear that where the incident neutron energy E (correctly represented in MCNP) satisfies the inequality

$$E_i < E \leq E_{i+1} \ , \tag{E.19}$$

whilst $E + \delta E$ satisfies

$$E_{i+1} < E + \delta E \leq E_{i+2} \ , \tag{E.20}$$

where δE is the error in the representation of the initial energy E made by the SNOMAN program, the selection of outgoing energies will be different in the two programs.

It is important to realise that the artificial energy boundaries that arise from the crude nature of the representation of the S(α,β) scattering matrix do not have any measurable effect upon the macroscopic predictions regarding neutron transport made by the MCNP program. This is because any effect that the energy and angle boundaries have upon a single collision is quickly 'washed out' by subsequent scatterings.

Appendix F

From Binomial to Poisson Statistics

Frodesen *et al.* give a proof [103, Section 4.4.3] which shows that when two variables are related in a binomial distribution, and their sum has a Poisson distribution, then they are in fact Poisson. The proof is simply extended to the multinomial case here.

Let n be the total number of events whose distribution is Poisson;

$$n = b_1 + b_2 + b_3 + \ldots + b_{r-1} + b_r \ , \tag{F.1}$$

where there are r categories or "bins", and where the probability of an event falling into the ith bin is p_i;

$$1 = p_1 + p_2 + p_3 + \ldots + p_{r-1} + p_r \ . \tag{F.2}$$

The probability of obtaining the distribution defined in F.1 and F.2 is obtained from the multinomial distribution;

$$M(b : n, p) = \frac{n!}{b_1!b_2!b_3! \cdots b_r!} p_1^{b_1} p_2^{b_2} p_3^{b_3} \cdots p_{r-1}^{b_{r-1}} p_r^{b_r} \ , \tag{F.3}$$

whilst the probability of obtaining n events is governed by the Poisson distribution whose mean in ν;

$$P(n : \nu) = \frac{1}{n!} \nu^n \exp(-\nu) \ . \tag{F.4}$$

The joint probability of the $r + 1$ variables, b_1, b_2, b_3, ..., b_r, b_{r-1}, n, is just the product of M and P is Q;

$$\begin{aligned} Q(b, n : p, \nu) &= M(b : n, p) P(n : \nu) \ , & \text{(F.5)} \\ &= \left(\frac{n!}{b_1!b_2!b_3! \cdots b_r!} p_1^{b_1} p_2^{b_2} p_3^{b_3} \cdots p_{r-1}^{b_{r-1}} p_r^{b_r} \right) \left(\frac{1}{n!} \nu^n \exp(-\nu) \right) \ , & \text{(F.6)} \end{aligned}$$

which is easily decomposed, using F.1 and F.2, so that it takes the form;

$$\begin{aligned} Q(b, n : p, \nu) &= \left(\frac{1}{b_1!} (\nu p_1)^{b_1} \exp(-\nu p_1) \right) \left(\frac{1}{b_2!} (\nu p_2)^{b_2} \exp(-\nu p_2) \right) \ldots \\ &\quad \ldots \left(\frac{1}{b_{r-1}!} (\nu p_{r-1})^{b_r} \exp(-\nu p_{r-1}) \right) \left(\frac{1}{b_r!} (\nu p_r)^{b_r} \exp(-\nu p_r) \right) \ . \end{aligned} \tag{F.7}$$

Clearly, the final distribution is just the product of the probabilities associated with a series of Poisson distributions of mean νp_i. In other words, if the probability associated with the ith bin is p_i, and the number of events is held fixed, the distribution of events in that bin is governed by multinomial statistics. But when the total number of events is allowed to vary according to the Poisson distribution, the distribution of the number of events in the ith bin is also Poisson, with mean νp_i.

Appendix G

Running the Verification Procedure

The verification procedure which was used to compare the transport mechanism of SNOMAN to that of MCNP, from which it was taken, is important to the SNO collaboration. It is described here in detail. The verification procedure was constructed to be wholly automated. This appendix describes that procedure to illustrate the magnitude of the task at hand. The verification procedure's main aims were;

1. to run SNOMAN and MCNP using equivalent run files; and then,
2. to extract and store data for the purposes of comparison; and then,
3. to statistically compare stored MCNP and SNOMAN data; and then,
4. to systematically record the results; and then,
5. to repeat the process in 6 different media, at 12 different energies, and 5 times over;
6. all the while ensuring that different random number sequences are used.

The number of the tests and the systematic variations over the set of tests lead to the writing of programs and command files to carry them out. The importance of writing a small number of programs to complete a large number of tests is that a small subset of the tests can be used to iron the errors out of the suite of programs and command files used to carry out the tests; if the test procedure is then error free it will remain so.

The steps in carrying out a single test sweep (of which there were 5 in all) are;

1. to choose a random number seed for the entire process (the pre-initialisation stage);
2. to generate the run files for the SNOMAN and MCNP programs;
3. to distribute the run files (the initialisation stage);
4. to run SNOMAN and MCNP with their appropriate run files and collect the results (the run stage); and,
5. to use the data from of each pair of MCNP and SNOMAN runs to carry out statistical tests on the distributions therein, and to record the results of the tests (the statistical stage).

A complex directory structure was created to facilitate the test procedure. The details of this structure will not be described except to say that each comparative run of MCNP and SNOMAN was given its own directory labelled by medium and energy. These directories are known collectively as test home directories. There were 72 home directories, covering the 6 media and 12 energies.

Each test run begins with the pre-initialisation stage where a seed file is read from a control directory and copied to the initialisation directory. The initialisation stage begins by reading in this file, and by writing out a control file for each of the SNOMAN and MCNP runs. This control file is then read and converted into either a SNOMAN or an MCNP command file. The control files specify the medium, energy, random number seed sequence, and number of events to simulate (the number of events was distributed like a Poisson variable with a mean value of 10000). The initialisation sequence ends when all the command files have been written to their home directories.

The run stage is a sequence of events carried out for the command files in each home directory. The MCNP command file is copied from the directory into the MCNP program directory. The MCNP

program is then run, and the data files resulting from the run are copied back into the appropriate home directory. The process is repeated for the SNOMAN command file. Once this process has been repeated for all the home directories, the statistical stage begins.

The statistical stage is a sequence of events that are carried out for each home directory. The run data files from both SNOMAN and MCNP are copied from their home directory into the statistical test program directory. Once they are there, another computer program is run which extracts each of the seven test distributions, which are continuous energy, continuous angle, discrete energy, discrete angle, step length, reaction type, and target identity, to separate input data files. Each pair of SNOMAN and MCNP data files is then compared using either a Kolmogorov-Smirnov or χ^2 statistical test. The test result is written to a distribution specific file (of which there are 7). Once all 7 comparisons are completed, the test results are then copied back to the appropriate home directory. Once this sequence has been repeated for all the home directories, the test run proper ends.

After each full test run, the ground must be prepared for the next, which will utilise the same filenames for much of the test sequence, and will therefore overwrite the results of all the previous test runs if action is not taken. To prevent this occurrence, the data files from SNOMAN and MCNP in each medium and energy specific home directory were renamed to reflect which test run they came from (for example, the SNOMAN results ntuple file is renamed SNOMAN.NTP $\rightarrow$ SNOMAN3.NTP after the 3rd full test run). The results of each of the seven statistical comparisons were then appended to one of seven appropriate run results files. The home directories are then ready for the next run to begin.

After all 5 test runs are completed, a typical home directory would contain the following files;

```
ANGLE_DISC.ALL      SNOMAN1.NTP      VERTEX1.DAT
ANGLE_CONT.ALL      SNOMAN2.NTP      VERTEX2.DAT
ENERGY_DISC.ALL     SNOMAN3.NTP      VERTEX3.DAT
ENERGY_CONT.ALL     SNOMAN4.NTP      VERTEX4.DAT
REACTION.ALL        SNOMAN5.NTP      VERTEX5.DAT
STEP.ALL            SNOMAN.CMD
TARGET.ALL          INPUT.DAT
```

The .ALL files each contain the five probabilities that are the results of the comparative tests from the five test runs. The SNOMAN1.NTP $\rightarrow$ SNOMAN5.NTP files are the data files output from the SNOMAN program, containing the first output energy, scattering angle, target, reaction, and step distance for $\sim$ 10000 neutrons. The VERTEX1.DAT $\rightarrow$ VERTEX5.DAT files are the data files output from MCNP, which contain the same distributions. The numbers $1 \rightarrow 5$ indicate which from which run the data was obtained. The file INPUT.DAT is the command file for the 5th run of the MCNP program. The file SNOMAN.CMD is the command file for the 5th run of the SNOMAN program.

There are many advantages accrued from carrying out the statistical tests in this way. The principal advantage is that genuine coding errors which prevent the the SNOMAN program from reproducing the results of MCNP can be located using the test results. This is because MCNP (and hence SNOMAN) uses different code subroutines to propagate neutrons in different energy regimes and different materials. The distribution of any very poor results $P < 10^{-10}$, for example) of the comparisons between MCNP and SNOMAN can then be examined together with the data files that lead to those poor results. This often allowed the author of this thesis to narrow the search for the location of the error in SNOMAN to a single routine. The test suite use to search for errors in SNOMAN was the same as that given here, but it was executed just once, not five times.

Once the SNOMAN program was believed to be error free, the test suite was executed again in the form given here (5 runs). The results from those runs are the results presented in this thesis, and which show SNOMAN to reproduce the transport calculations of MCNP very well. The number of runs was increased to 5 to improve the test suites' sensitivity to differences between SNOMAN and MCNP. None were located.

Bibliography

[1] R. Davis Jr., D. S. Harmer, and K. C. Hoffman, Search for Neutrinos from the Sun, Phys. Rev. Lett. 20 (1968) 1205-1209.

[2] B. T. Cleveland, T. Daily, R. Davis Jr., J. Distel, K. Lande, C. K. Lee, P. Wildenhain, and J. Ullman, Update on the Measurement of the Solar Neutrino Flux with the Homestake Chlorine Detector, Nucl. Phys. B (Proc. Suppl.) 38 (1995) 47-53.

[3] K. Lande, Results reported to the Neutrino '96 conference on behalf of the Homestake collaboration, (proceedings to be published).

[4] K. S. Hirata *et al.* , Real-Time, Directional Measurement of the ^{8}B Solar Neutrinos in the Kamiokande II Detector, Phys. Rev. D 44 (1991) 2241-2260.

[5] K. Nakamura, Recent Results from Kamiokande Solar Neutrino Observations, Nucl. Phys. B (Proc. Suppl.) 31 (1993) 105-110.

[6] N. Hata and P. Langacker, Solar Model Uncertainties, MSW Analysis, and Future Solar Neutrino Experiments, Phys. Rev. D 50 (1994) 632-660.

[7] Y. Suzuki, Kamiokande Solar Neutrino Results, Nucl. Phys. B (Proc. Suppl.) 38 (1995) 54-59.

[8] Y. Totsuka, Kamiokande and Super-Kamiokande, Nucl. Phys. B (Proc. Suppl.) 48 (1996) 547-556.

[9] Y. Suzuki, Results reported to the Neutrino '96 conference on behalf of the Kamiokande collaboration, (proceedings to be published).

[10] P. Anselmann *et al.* , Solar Neutrinos Observed by GALLEX at Gran Sasso, Phys. Lett. B 285 (1992) 376-389.

[11] P. Anselmann *et al.* , GALLEX Solar Neutrino Observations: Complete Results for GALLEX II, Phys. Lett. B 357 (1995) 237-247.

[12] P. Anselmann *et al.* , First Results from the ^{51}Cr Neutrino Source Experiment with the GALLEX Detector, Phys. Lett. B 342 (1995) 440-450.

[13] T. Kirsten, Results reported to the Neutrino '96 conference on behalf of the GALLEX collaboration, (proceedings to be published).

[14] J. N. Abdurashitov *et al.* , Results from SAGE, Phys. Lett. B 328 (1994) 234-248.

[15] J. N. Abdurashitov *et al.* , Results from SAGE, Nucl. Phys. B (Proc. Suppl.) 48 (1996) 299-303.

[16] S. R. Elliot *et al.* , Preliminary Results from the Russian-American Gallium Experiment Cr-neutrino Source Measurement, Nucl. Phys. B 48 (1996) 370-374.

[17] V. N. Gavrin, Results reported to the Neutrino '96 conference on behalf of the SAGE collaboration, (proceedings to be published).

[18] A. Alimonti *et al.* , A New Solar Neutrino Detector, Nucl. Phys. B 32 (1993) 149-155.

[19] F. J. Rogers and C. A. Iglesias, Science 263 (1994) 50.

[20] N. Grevasse and A. Noels, Phys. Scripta T47 (1993) 133.

[21] W. A. Dziembowski, P. R. Goode, A. A. Pamyatnykh and R. Sienkiewicz, A Seismic Model of the Sun's Interior, Astrophys. J. 432 (1994) 417-426.

[22] C. R. Proffitt, Effects of Heavy-Element Settling on Solar Neutrino Fluxes and Interior Structure, Astrophys. J. 425 (1994) 849-855.

[23] A. A. Thoul, J. N. Bahcall and A. Loeb, Element Diffusion in the Solar Interior, Astrophys. J. 421 (1994) 828-842.

[24] J. N. Bahcall, Neutrino-Electron Scattering and Solar Neutrino Experiments, Rev. Mod. Phys. 59 (1987) 505.

[25] J. N. Bahcall and R. K. Ulrich, Solar Models, Neutrino Experiments, and Helioseismology, Rev. Mod. Phys. 60 (1988) 297.

[26] J. N. Bahcall, Neutrino Astrophysics, Cambridge University Press, 1989.

[27] J. N. Bahcall and M. H. Pinsonneault, Standard Solar Models, with and without Helium Diffusion, and the Solar Neutrino Problem, Rev. Mod. Phys. 64 (1992) 885.

[28] J. N. Bahcall, Two Solar Neutrino Problems, Phys. Lett. B 338 (1994) 276-281.

[29] J. N. Bahcall and A. Glasner, Solar Neutrinos: Sensitivity to Pre-Main-Sequence Evolution and to the Depth of the Convection Zone, Astrophys. J. 437 (1994) 485-490.

[30] J. N. Bahcall and M. H. Pinsonneault, With an Appendix on the Age of the Sun by G. J. Wasserburg, Solar Models with Helium and Heavy-Element Diffusion, Rev. Mod. Phys. 67 (1995) 781.

[31] J. N. Bahcall and A. Ulmer, Temperature Dependence of Solar Neutrino Fluxes, Phys. Rev. D 53 (1996) 4202.

[32] J. N. Bahcall, in a paper presented to the Neutrino '96 conference (proceedings to be published).

[33] J. N. Bahcall, M. H. Pinsonneault, S. Basu, and J. Christensen-Dalsgaard, Are Standard Solar Models Reliable, pre-print.

[34] G t'Hooft, Prediction for the Neutrino-Electron Cross-Sections in Weinberg's Model of Weak Interactions, Phys. Lett. B 37 (1971) 195-196.

[35] S. Turck-Chiéze and I. Lopes, Toward a Unified Classical Model of the Sun: On the Sensitivity of Neutrinos and Helioseismology to the Microscopic Physics, Astrophys. J. 408 (1993) 347-367.

[36] V. Castellani *et al.* , Neutrino from the Sun: Experimental Results Confronted with Solar Models, Phys. Rev. D 50 (1994) 4749.

[37] S. Parke, Status of the Solar Neutrino Puzzle, Phys. Rev. Lett. 74 (1995) 839.

[38] S. P. Mikheyev and A. Y. Smirnov, Resonant Amplification of ν Oscillations in Matter and Solar-Neutrino Spectroscopy, Nuovo Cimento C9 (1986) 17.

[39] L. Wolfenstein, Phys. Rev. D 20 (1979) 2634.

[40] S. P. Rosen, An Introduction to Neutrino Oscillations and the Solar Neutrino Problem, Presented at the TASI Meeting, Santa Fe, New Mexico.

[41] N. Hata and P. Langacker, Solar Model Uncertainties, MSW Analysis, and Future Solar Neutrino Experiments, Phys. Rev. D 50 (1994) 632.

[42] M. Doi and K. Kubodera, Astrophysical Neutrino Reactions on the Deuteron, Phys. Rev. C 45 (1992) 1988.

[43] S. Ying, W. C. Haxton, and E. M. Henley, Charged- and Neutral-Current Solar-Neutrino Cross-Sections for Heavy-Water Čerenkov Detectors, Phys. Rev. C 45 (1992) 1982.

[44] J. N. Bahcall, K. Kubodera, and S. Nozawa, Neutral Current Reactions of Solar and Supernova Neutrinos on Deuterium, Phys. Rev. D 38 (1988) 1030.

[45] J. V. Jelley, Čerenkov Radiation, Pergammon Press, London (1958).

[46] C. Athanassopoulos *et al.* , Candidate Events in the Search for $\overline{\nu}_\mu \rightarrow \overline{\nu}_\tau$ Oscillations, Phys. Rev. Lett. 75 (1995) 2650-2653.

[47] J. Hill, An Alternative Analysis of the LSND Neutrino Oscillation Search Data on $\overline{\nu}_\mu \rightarrow \overline{\nu}_\tau$, Phys. Rev. Lett. 75 (1995) 2654-2657.

[48] Bodman *et al.* , Results from the KARMEN Neutrino Experiment, Nucl. Phys. A 553 (1993) 831-834.

[49] D. Sinclair, Carlton University, private communication with, 1995.

[50] R. M. Barnett *et al.* , Review of Particle Physics, Phys. Rev. D 54 (1996) 1.

[51] A. Burrows, Neutrinos from Supernova Explosions, Ann. Rev. Nucl. and Part. Sci. 40 (1990) 181.

[52] A. Burrows, D. Klein, R. Ghandi, The Future of Supernova Neutrino Detection, Phys. Rev. D 45 (1992) 3361.

[53] A. Burrows, D. Klein, R. Ghandi, Supernova Neutrino Bursts, the SNO Detector, and Neutrino Oscillation, Nucl. Phys. B (Proc. Suppl.) 31 (1993) 408.

[54] C. Bratton *et al.* , Neutrinos from SN1987A in the IMB Detector, NIM A264 (1988) 28-31.

[55] K. Hirata *et al.* , Observation in the Kamiokande II Detector of the Neutrino Burst from Supernova SN1987A, Phys. Rev. D 38 (1988) 448-458.

[56] X. Chen, Monte Carlo Study of Beta-Gamma Backgrounds from ^{208}Tl and ^{214}Bi, SNO-STR-96-003.

[57] X. Chen, Neural Network and Statistical Study of the ^{208}Tl and the ^{214}Bi Decay Events in SNO, SNO-STR-96-004 (1996).

[58] X. Chen, A Systematic Study of the Background Analysis Using SNOMAN Code, SNO-STR-96-005, (1996).

[59] M. Thorman, private communication, 1996.

[60] M. E. Moorhead *et al.* , ^{6}Li Neutron Poison for SNO, SNO-STR-95-056 (1995).

[61] J. Chadwick and M. Goldhaber, Nature 134 (1934) 237.

[62] H. A. Bethe and R. Peierls, Proc. Roy. Soc. A148 (1935) 146.

[63] M. D. Lay, D. Phil. Thesis, Creation and Detection of Ĉerenkov Light in the Sudbury Neutrino Observatory, June 1994.

[64] M. D. Lay, Energy Response and PMT Backgrounds in SNO, SNO-STR-97-015 (1996).

[65] Walter R. Nelson, Hideo Hirayama and David W. O. Rogers, The EGS4 Code System, SLAC-Report-265, December 1985.

[66] H. A. Bethe, Theory of Effective Range in Nuclear Scattering, Phys. Rev. 76 (1949) 38-50.

[67] N. A. Jelley, Fundamentals of Nuclear Physics, 1990.

[68] H. A. Bethe and C. Longmire, The Effective Range of Nuclear Forces, II. Photo Disintegration of the Deuteron, Phys. Rev. 77 (1950) 647-654.

[69] H. Arenhövel and M. Sanzone, Photodisintegration of the Deuteron, Springer-Verlag, 1991.

[70] John M. Blatt and Victor F. Weisskopf, Theoretical Nuclear Physics, (1952).

[71] N. Austern and R. G. Sachs, Interaction Effects on Radiative Transitions in Nuclei, Phys. Rev. 81 (1951) 710-716.

[72] N. Austern, Evaluation of the Interaction Effect in n-p Capture, Phys. Rev. 92 (1953) 670-674.

[73] N. Austern and E. Rost, Evaluation of the Interaction Effect in n-p Capture, Phys. Rev. 117 (1960) 1506-1510.

[74] H. P. Noyes, The Interaction Effect in n-p Capture, Nucl. Phys. 74 (1965) 508-532.

[75] A. E. Thorlacius and Harold W. Fearing, Phenomenological fit to deuteron photodisintegration data in the medium energy region, Phys. Rev. C 33 (1986) 1830-1833.

[76] M. P. DePascale *et al.* , A Critical Review of the Deuteron Photodisintegration Data Between 10 and 120 MeV, Phys. Lett. 119B (1982) 30-34.

[77] E. De Sanctis *et al.* , Differential cross section for the $^2H(\gamma,p)n$ reaction between 100 and 225 MeV, Phys. Rev. C 34 (1986) 413-423.

[78] P. Rossi *et al.* , Bidimensional fit to $^2H(\gamma,p)n$ cross-section values between 20 and 440 MeV, Phys. Rev. C 40 (1989) 2412-2415.

[79] J. F. Marshall and E. Guth, Photo Disintegration of the Deuteron at High Energies, Phys. Rev. 78 (1950) 738.

[80] Press, Teukolsky, Vetterling, Flannery, Numerical Recipes in FORTRAN, 2nd Ed. (1992).

[81] O. Dumbrajs *et al.* , Compilation of Coupling Constants and Low Energy Parameters, Nucl. Phys. B216 (1983) 277-335.

[82] Review of Particle Properties, Phys. Rev. D50 (1994) 1173.

[83] Sudbury Neutrino Observatory Proposal, SNO-87-12 (October 1987).

[84] Sudbury Neutrino Observatory, Collection of Annexes in Support of the Main Proposal, SNO-87-12 (November 1987).

[85] S. D. Ellis and J. N. Bahcall, Neutrino Absorption by Deuterium, Nucl. Phys. A114 (1968) 636.

[86] J. N. Bahcall, K. Kubodera, S. Nozawa, Neutral-current reactions of solar and supernova neutrinos on deuterium, Phs. Rev. D38 (1988) 1030.

[87] A. J. F Siegert, Phys. Rev. 52 (1937) 787.

[88] MCNP4A, A Monte Carlo N-Particle Transport Code System, Radiation Shielding Information Center, Los Alamos National Laboratory, November 1993.

[89] The SNOMAN User's Manual, Version 2.09, August 1995.

[90] The SNOMAN Programmer's Manual, Version 2.09, August 1995.

[91] R. J. Boardman, D. Phil. Thesis, The Detection of Čerenkov Radiation from Neutrino Interactions, June 1992.

[92] M. E. Moorhead, D. Phil. Thesis, Reflectors in Čerenkov Detectors, June 1992.

[93] RCA Photomultiplier Handbook, R. W. Engstrom, RCA Solid State Division, Electro Optics and Devices, Lancaster, 1980.

[94] M. D. Lay, Parameterisation of the Angular Response of the R1408 Hamamatsu Eight-inch Photomultiplier Tube to be used in the Sudbury Neutrino Observatory, accepted for publication by Nucl. Inst. Meth.

[95] G. Doucas *et al.* , Light Concentrators for the Sudbury Neutrino Observatory, submitted to Nucl. Inst. Meth.

[96] M. D. Lay and M. J. Lyon, An Experimental and Monte Carlo Investigation of the R1408 Hamamatsu 8-inch Phototube and Associated Concentrator to be used in the Sudbury Neutrino Observatory, to be published in Nucl. Inst. Meth.

[97] B. Davison, Neutron Transport Theory, 1957.

[98] W. Marshall and D. H. Wilkinson, Theory of Thermal Neutron Scattering, Oxford University Press, 1971.

[99] Enrico Fermi, Nuclear Physics, The University of Chicago Press, 1949, reprinted 1974.

[100] E. D. Earl and P. Y. Wong, Calculations of Neutron Transport in the SNO Vessel, Collection of Annexes in Support of the Main Proposal (for the Sudbury Neutrino Observatory), November 1987.

[101] Wilhelmy, Skensved, and Lowry, private communications among, recieved December 1995.

[102] F. James, A Review of Pseudorandom Number Generators, Computer Physics Communications, 60 (1990) 329.

[103] Frodesen, Skjeggestad, and Tofte, Probability and Statistics in Particle Physics, Universiteforlaget, 1979.

[104] J. C. Wang, G. L. Jensen, J. B. Czirr, A Test Of MCNP With A Li-6-Glass Moderating Neutron Detector, Nuclear Science and Engineering, 113 vol. 1 (1993) 77-85.

[105] R. H. Olsher, H. H. Hsu, W. F. Harvey, Benchmarking the MCNP Mote-Carlo Code with a Photon Skyshine Experiment, Nuclear Science and Engineering, 114 vol. 3 (1993) 219-227.

[106] P. G. Laky, N. Tsoulfanidis, Neutron Fluence at the Pressure-Vessel of a Pressurized-Water Reactor Determined by the MCNP Code, Nuclear Science and Engineering, 121 vol. 3 (1995) 433-447.

[107] B. R. Munson, D. F. Young, and T. H. Okiishi, Fundamentals of Fluid Mechanics, John Wiley and Sons, 1990.

[108] Private communication, Technical Data Sheet, Instapak-Floral CFC Free Floral Foam, received March 1996.

[109] J. P. Holman, Heat Transfer, 7th Edition, McGraw Hill, 1992.

[110] W. M. Kay and M. E. Crawford, Convective Heat and Mass Transfer, 3rd Edition, McGraw Hill, 1993.

[111] R. K. Shah and A. K. London, Laminar Flow Forced Convection in Ducts, Advances in Heat Transfer, Academic Press, New York, 1978.

[112] Chapman, Fundamentals of Heat Transfer, Macmillan Publishing, 1987.

[113] G. Doucas, Report on the Effects of Water Vapour Exposure on the SNO Connectors, 1996, unpublished.

[114] G. Doucas, Oxford, private communication, 1996.

[115] Louis McGarry, Salvador Gil, and Chris Waltham, Reflectivity Tests of Aged Ambrite from First OCLI Production Run, 1992, unpublished.

[116] Louis McGarry,Report on Ageing of DCA Samples from OCLI's August Production Run, 1993, unpublished.

[117] R. Newman, Honours Thesis, Corrosion of Dielectric Coated Aluminium in the Sudbury Neutrino Observatory, March 1995.

[118] Morley, engineer-on-site at Sudbury, private communication with, 1995.

[119] A. J. Noble, Editor, and the SNO Water Group, Scientific Review of SNO Water Systems, 1996.

[120] S. Gil, G. A. Clarke, L. McGarry and C. Waltham, Determination of Absolute Specular Reflectivities in Liquid Medium with Variable Angle of Incidence, Applied Optics, Vol. 34, No. 4 (1995) 695.

[121] P. W. Atkins, Physical Chemistry, Oxford, 1990.

[122] S. J. Brice, D. Phil. Thesis, Monte Carlo and Analysis Techniques for the Sudbury Neutrino Observatory, 1996.

[123] Donald J. Hughes and John A. Harvey, Neutron Cross Sections, Brookhaven National Laboratory, July 1955.

[124] Emilio Segre, Nuclei and Particles, An Introduction to Nuclei and Subnuclear Physics, W. A. Benjamin, Inc., 1965.

[125] J. Klein, using data from K. Kubodera and S. Nozawa, International Journal of Modern Physics, E3, 101-148, and data from personal communications between R. Van de Water and K. Kubodera and S. Nozawa.

[126] M. G. Bowler, Effects of Electron Scattering on Čerenkov Light Production, Nuclear Instruments and Methods (accepted for publication).

[127] M. G. Bowler and M. D. Lay, Angular Distribution of Čerenkov Light from Electrons Both Produced and Stopping in Water, Nuclear Instruments and Methods (accepted for publication).

[128] Alvin M. Weinberg and Eugene P. Wigner, The Physical Theory of Neutron Chain Reactors, The University of Chicago Press, 1958.

[129] Data made available for public use by FTP to the National Nuclear Data Center, Brookhaven National Laboratory, USA.

[130] N. N. Greenwood and A. Earnshaw, Chemistry of the Elements, Pergammon Press 1984.

[131] L. D. Landau and E. M. Lifshitz, Statistical Mechanics, Pergammon Press, 1959.

[132] F. Ajzenberg-Selove, Energy Levels of Light Nuclei $A = 5 - 10$, Nucl. Phys. A 413 (1984) 1.

[133] F. Ajzenberg-Selove, Energy Levels of Light Nuclei $A = 5 - 10$, Nucl. Phys. A 490 (1988) 1.

[134] F. Ajzenberg-Selove, Energy Levels of Light Nuclei $A = 13 - 15$, Nucl. Phys. A 523 (1991) 1.

[135] S. Mughabghab, M. Divadeenam, N. Holden, Neutron Cross Sections, Volume 1, Neutron Resonance Parameters and Thermal Cross Sections, Part A, $Z = 1 - 60$, National Nuclear Data Centre, Brookhaven National Laboratory, Academic Press, 1981.

[136] V. McLane, C. Dunford, P.Rose, Neutron Cross Sections, Volume 2, Neutron Cross Section Curves, National Nuclear Data Centre, Brookhaven National Laboratory, Academic Press, 1981.

[137] D. Tilley, H. Weller, C. Cheeves, Energy Levels of Light Nuclei, $A = 16 - 17$, Nucl. Phys. A 564 (1993) 1-184.

[138] F. Ajzenberg-Selove, Energy Levels of Light Nuclei $A = 18 - 20$, Nucl. Phys. A 475 (1987) 1-198.

[139] A. Sayres, K. Jones, C. Wu, Phys. Rev. 122 (1961) 1853.

[140] B. Sur, private communication, 1995.

[141] G. Breit and E. Wigner, Capture of Slow Neutrons, Phys. Rev. 49 (1936) 519.

[142] The Chemical Rubber Company Handbook of Chemistry and Physics, 1995-1996, 76th edition, CRC Press.

[143] M. G. Bowler *et al.* , Some Monte Carlo Studies of the Added Salt Option, SNO internal document prepared by the University of Oxford, 1996.

[144] ZEBRA, CERN Program Library Long Writeups Q100/Q101.

[145] A.P. Ferraris, D. Phil. Thesis, Oxford (1992).

[146] A. G. Wright, Sources of Noise in Photomultipliers, Thorn EMI Electron Tubes Ltd., 1988.

[147] H. R. Krall (1967) IEEE Trans. NS, 14, 455.